Alma Mater Studiorum – Università di Bologna

DOTTORATO DI RICERCA IN

CHIMICA

Ciclo XXIX

Settore Concorsuale di afferenza: 03/B1

Settore Scientifico disciplinare: CHIM/03

CARBON BASED HYBRID NANOSTRUCTURES FOR ADVANCED FUNCTIONAL MATERIALS

Presentata da: Matteo Di Giosia

Coordinatore Dottorato

Prof. Aldo Roda

Relatore

Prof. Marco Montalti

Correlatori

Prof. Giuseppe Falini

Prof. Matteo Calvaresi

Esame finale anno 2017

Dedicated to my
cousin Massimo

CONTENTS

ABSTRACT

In nature, carbon exists under different allotropic forms: graphite, diamond and amorphous that show very different physicochemical properties. In the last thirty years many of new carbon nanoallotropes were produced, showing a variety of size, shape, aspect ratio and dimensionality.
All the carbon based nanomaterials (CNMs) are highly hydrophobic, which make them unsuitable for most of the applications in water and organic solvents. Aggregation phenomena significantly reduce the high performances displayed by the single nanostructure. Two main strategies allow to overcome this bottleneck: the chemical functionalization with hydrophilic functional groups or the non-covalent interaction between CNMs and amphiphilic molecules.
The aim of this thesis has been to produce different carbon-based hybrid nanostructures to preserve the peculiar properties of CNMs and use them for advanced application in nanomedical and technological fields.
In the first project, the potential application of fullerene (C_{60}) as sensitizer for photodynamic therapy was explored. Monodispersity of fullerenes is the key feature for its potential application in this field. Noncovalent approach was used to disperse C_{60} in water, taking advantage from the surfactant-like properties of the proteins. C_{60}@lyszoyme hybrid was used as model system to study the stability of fullerene in physiological conditions and to assess its ability to produce reactive oxygen species upon irradiations.
The second subject of my research concerned the study of interactions between fluorescent nanodiamonds (FNDs) and plasma proteins. FNDs show potential applications as probe for bioimaging but their tendency to aggregate in physiological environments is the main limit for their application. In this study, a procedure to keep monodispersed FNDs in relevant biological fluids was optimized and the composition of FNDs protein corona was extensively characterized. This project was carried out at Center for BioNano Interactions (UCD), in the group lead by prof. Kenneth Dawson.
The third project was addressed to the manufacturing of graphene based calcite nanocomposite. Both covalent (graphene oxide) and non-covalent (graphene/biomolecules adducts) approaches were used to disperse graphene in water. Following a biological inspired synthetic procedure, it was possible to incorporate the 2D materials within a 3D crystal lattice, producing a nanocomposite possessing several new properties.

CHAPTER 1

CARBON BASED NANOMATERIALS

INTRODUCTION

Carbon is widely diffused in nature. It is one of the main component of living matters, as proteins, lipids and carbohydrates. Carbon dioxide is essential for the photosynthesis. An entire discipline is dedicated to the study of the component containing carbon: organic chemistry. The peculiar ability of carbon atoms to build covalent bonds with other carbon atoms using different hybridization states or with nonmetallic elements confers them the possibility to build up a wide range of structures, from simple molecules to complex nanostructures[1].

Carbon exists in nature under different allotropic forms: graphite, diamond and amorphous. Despite they are composed by the same atoms they show very different properties, extensively studied by inorganic chemists.

i. Diamond is a transparent electrical insulator and the hardest known material, constituted by tetrahedral sp^3 carbon atoms which form a unique crystal lattice.
ii. Graphite is a black opaque soft material with high electrical conductivity. It's constituted by stacked graphene monolayers held together by Van der Waals interactions. Each graphene layer consist of sp^2 carbon atoms organized in a two-dimensional hexagonal lattice.

The empty space between organic molecules and natural carbon materials has been recently filled by a range of new nanomaterials (Figure 1).

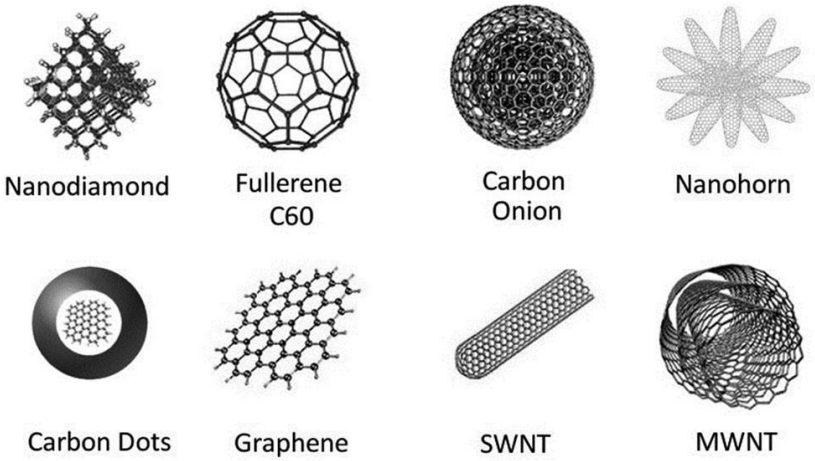

Figure 1. Representative structures of known carbon nanoallotropes.[2]

The discovery of C_{60} fullerene reported in 1985[3] by Richard E. Smalley, Robert F. Curl, and Harold W. Kroto can be considered as the starting point of the carbon nanomaterials (CNMs) development.

C_{60} is a discrete molecule and consists of 60 sp^2 carbon atoms arranged as hexagons and pentagons to form a spherical (truncated icosahedral) structure, as an old fashioned soccer ball. The name was an homage to Buckminster Fuller, whose geodesic domes it resembles. Fullerenes are the smallest stable carbon nanostructures and lie on the boundary between molecules and nanomaterials.

The following important step in the carbon nanomaterials happened six years later, with the discovery of carbon nanotubes (CNTs) by Iijima.[4,5] Because of the differences of the size, shape and aspect ratio, CNTs properties results completely different from fullerenes.

The discoveries and the successive characterization of fullerenes and CNTs permitted to synthetize new carbon based nanostructures with different size and architecture, such as single-walled carbon nanohorns (SWCNH), onion-like carbon (OLC), bamboo-like nanotubes *etc*.

The most recently isolated CNM is graphene, the single layer of graphite. It was predicted[6] and identified[7] decades ago but it was isolated and characterized in 2004 by Andre Geim and Konstantin Novoselov.[8] Since that moment to now more sub-structure (few atoms) and super-structure (assemblies) of graphene was identified, showing different properties from graphene.

All these carbon nanoallotropes can be classified as members of the same group: their basic structure consist of sp^2 carbon atoms arranged in a hexagonal network. From a theoretical

perspective, graphene sheets are regarded as the 2D building blocks of these carbon allotropes:[9] they can be wrapped up to form 0D fullerenes, rolled up to establish the cylindrical structure of 1D carbon nanotubes, or stacked to form 3D graphite (Figure 2). Size and shape make each object unique, but they share similar properties within the subgroups, such as level of conductivity, mechanical strength, chemical reactivity and optical properties. All CNMs are highly hydrophobic, which make them unsuitable for most of the applications in water and organic solvents.

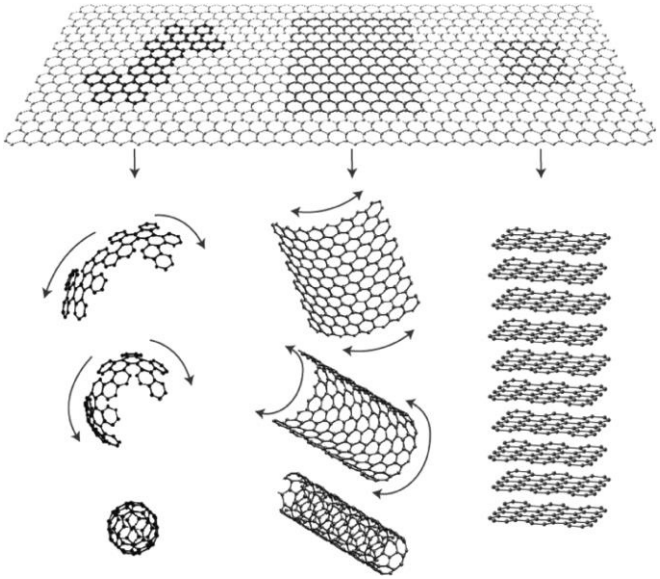

Figure 2. Graphene as a building block of a fullerene, carbon nanotube, and graphite.[9]

The other group of carbon nanostructures (CNSs) contains sp^3 based carbon atoms. Nanodiamonds consist primarily of tetrahedral C sp^3 while carbon dots are composed by variable percentage of sp^3 and sp^2 carbon atoms.

1.1 0D Carbon Nanoallotropes: Fullerenes, Nanodiamonds and Other Structures

Fullerenes are closed hollow cages constituted by sp^2 hybridized carbon atoms organized into 12 pentagons and a variable number of hexagons, depending by the total number of carbon atoms. A

fullerene with 20+2*n* carbon atoms contains *n* hexagons. C_{60} is a spherical molecule with an external diameter of 0.71 nm. Its chemical properties are very similar to the common organic molecules. However, it is considered the smallest stable carbon nanostructure and a representative molecule for CNPs. It shows the shape of a truncated icosahedron containing 12 pentagons and 20 hexagons. Despite its composition of 60 sp^2 carbon atoms, their arrangement is not planar but rather pyramidalized: sp^3 bonding component must be present in the essentially sp^2 carbons. The presence of pentagons is fundamental to introduce the curvature and hence, allowing closing of the cage. Two different kind of bond are identified on C_{60}, connecting C atoms common to hexagon - hexagon and hexagon - pentagon pairs.[1] Nevertheless, C_{60} contains a single carbon atom type, as showed experimentally by ^{13}C-NMR (Figure 3a).[10] Using the Fast Atom Bombardment (FAB) ionization technique, it is possible to analyze the mass spectrum of C_{60}, containing the single peak at m/z = 720 corresponding to C_{60}^+(Figure 3b).[10] The optical properties of fullerenes are strictly dependent by the size and shape of each fullerene. In toluene, C_{60} appears violet instead of C_{70} which is red (Figure 3c).[11,12] For larger fullerenes the color shifts from yellow to green as their size increase.

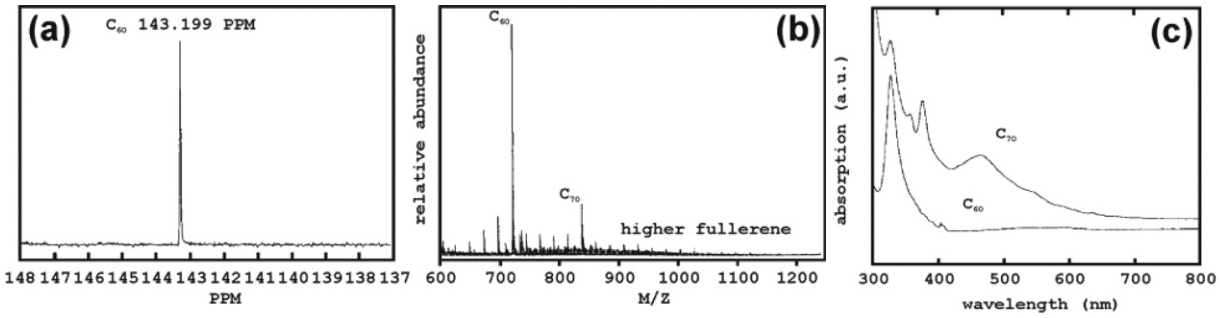

Figure 3. (a) ^{13}C NMR spectrum of pure C_{60} in deuterated benzene. (b) Mass spectrum of the toluene extract of fullerene soot, which consists primarily of C_{60} and C_{70}. (c) UV − Vis spectra of C_{60} and C_{70} in hexane.[10]

Raman and FTIR are also used to characterize bare and functionalized fullerenes. Fullerenes have the main advantage to be treated as a common organic molecule and can be characterized by standard analytic techniques.

Nanodiamonds (NDs) were first produced in USSR in 1960s[13] by detonation, but in 1990s a number of important breakthroughs permitted to focus the interest on these particles:[14]

i. Colloidal suspension of 4-5 nm diamond particles became available;[15]
ii. Fluorescent nanodiamonds (FNDs) were used as a non-toxic alternative to quantum dots (QDs) for bio-imaging; [16,17]
iii. NDs based magnetic sensors were developed;[18]
iv. Functionalization of NDs surface[19,20] allowed the applications in different field, in particular as a theranostic platform;[21–23]
v. New environmental friendly purification techniques permitted to produce high pure NDs in large volume at low cost; [24,25]

Diamond is an outstanding material in many respects, and NDs inherits most of the superior properties of bulk diamond and delivers them at the nanoscale. These properties include superior hardness and Young's modulus, biocompatibility, optical properties and fluorescence, high thermal conductivity and electrical resistivity, chemical stability and the resistance to harsh environments.

Up to date, different approaches were developed to synthetize NDs. Detonation technique,[26] laser ablation[27] and especially high-energy ball milling of high-pressure high-temperature (HPHT) synthetic diamond microcrystals are commercially used.[28]

Graphite is the most stable form of carbon at ambient temperature and pressure and diamond is metastable. Despite the small energy difference between the two forms (0.02 eV per atom), they are separated by an high energy barrier (0.4 eV per atom) so high temperature and high pressure are required to interconvert graphite to diamond. At the nanoscale, however, the carbon phase diagram must also include the cluster size as a third parameter because Gibbs free energy depends by surface energy (Figure 4).[26,29]

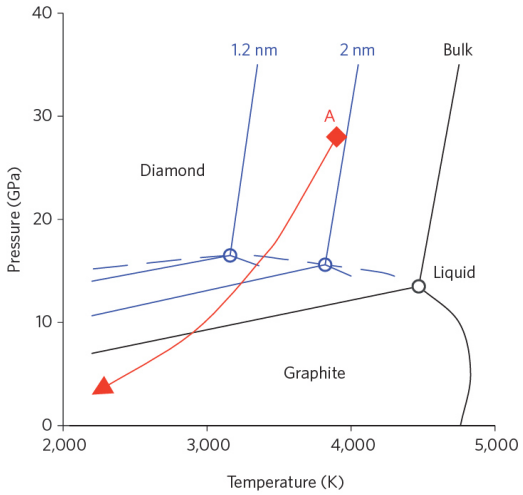

Figure 4. Phase diagram showing that the most stable phase of carbon is graphite at low pressures, and diamond at high pressures, with both phases melting when at temperatures above 4,500 K (with the precise melting temperature for each phase depending on the pressure). The phase diagrams for nanoscale carbon are similar, but the liquid phase is found at lower temperatures. During detonation, the pressure and temperature rise instantaneously, reaching the Jouguet point (point A), which falls within the region of liquid carbon clusters of 1–2 nm in size for many explosives. As the temperature and pressure decrease along the isentrope (red line), carbon atoms condense into nanoclusters, which further coalesce into larger liquid droplets and crystallize. When the pressure drops below the diamond–graphite equilibrium line, the growth of diamond is replaced by the formation of graphite.[26]

At the nanoscale, morphology play an important role in the stability of nanodiamonds by influencing surface reconstruction and sp^2 carbon formation. The surface of sp^3 clusters is stabilized either by terminations with functional groups and sp^2 carbon atoms shell (Figure 5).[30] The identity of the organic functional groups depends on the chemical conditions applied during the purification. FTIR and Raman spectra of NDs are powerful tools which give important information about their structure and surface composition.[24]

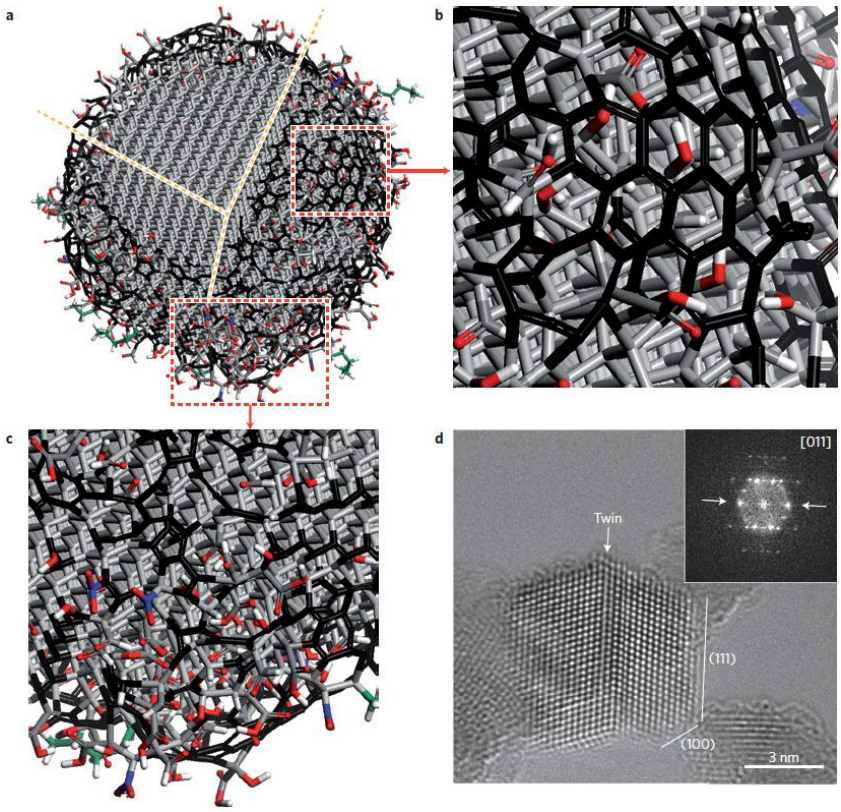

Figure 5. Structure of a single nanodiamond particle. (a) Schematic model illustrating the structure of a single ~5-nm nanodiamond after oxidative purification. The diamond core is covered by a layer of surface functional groups, which stabilize the particle. The surface can also be stabilized by the conversion of sp^3 carbon to sp^2 carbon. (b,c) Close-up views of two regions of the nanodiamond shown in a. The sp^2 carbon (shown in black) forms chains and graphitic patches (b). The majority of surface atoms are terminated with oxygen-containing groups (oxygen atoms are shown in red, nitrogen in blue). Some hydrocarbon chains (green) and hydrogen terminations (hydrogen atoms are shown in white) are also seen. (d) TEM acquisition of a faceted NDs. The inset is a fast Fourier transform of the micrograph, which shows the highly ordered diamond core.[25]

The other 0D structure displayed a lot of interest in the last decade. The most studied and promising particle are Carbon dots (C-dots), Graphene quantum dots (GQDs) and Onion-like carbon (OLC).

Carbon dots are very small nanoparticle (2-10 nm), composed by an high oxygen content and consist of variable ratio of graphitic and turbostratic carbon.[31–34] They contain mostly sp^3-hybridized carbon and are usually of amorphous nature. The double character of C-dots was clearly identified by X-ray diffraction (XRD) pattern.[34] Raman analysis shows the characteristic D and G bands and by the relative intensity is possible to demonstrate that they have high content of sp^3 carbon atoms.[34] Hydroxyl, carboxyl and epoxy groups are the main functional groups identified

by FTIR experiments (Figure 6).[34] What make them so interesting is their strong photoluminescence which depends by their structural properties (size and surface functionalization) and the excitation wavelength.[35]

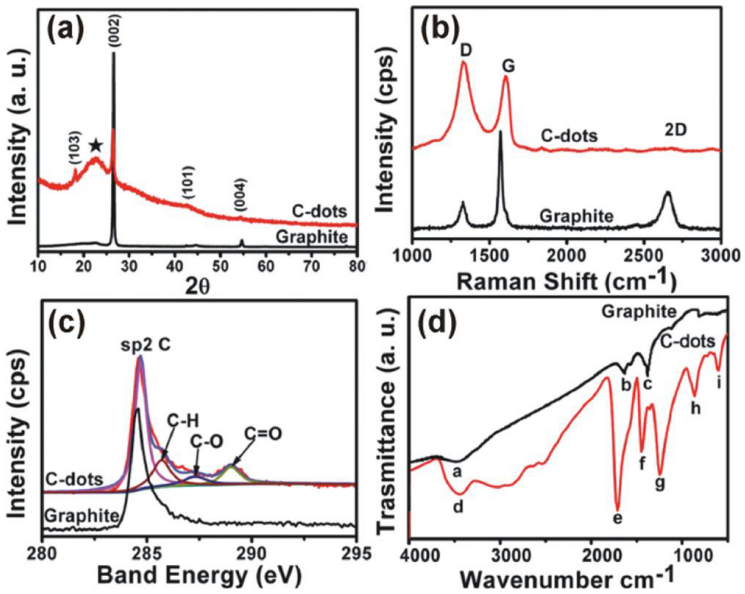

Figure 6. (a) XRD patterns, (b) Raman spectra (λ_{ex} = 633 nm), (c) C 1s XPS spectra, and (d) FTIR spectra of graphite and carbon dots.[34]

Graphene quantum dots (GQDs) are obtained by cutting graphene monolayer into small fragments with dimensions between 2 and 20 nm. GQD are mainly composed by sp^2-hybridized carbons and they are crystalline.[36] However, they usually consist of more than one layer of graphene, based on the structure of the graphenic nanosheet precursors. When the size of graphene sheets decrease below 100 nanometers, quantum confinement and edge effects become significant, particularly if one of their dimensions fall below 10 nm.[37] Contrary to large graphene sheets, GQDs have a nonzero band gap. This size-dependent behavior confers them peculiar electronic and optical properties:[38] changing their size, shape, geometry and the nature of the edges it is possible to tune the band gaps. UV-Vis absorption spectrum is similar to graphene oxide and the emission in very intense between 400 and 600 nm (Figure 7).[39] Raman spectra are similar to graphene but the main difference is about the relative intensity of I_D/I_G ratio which is higher than graphene because there is a large number of sp^3 carbons at the edges respect to sp^2 carbons "core".[39]

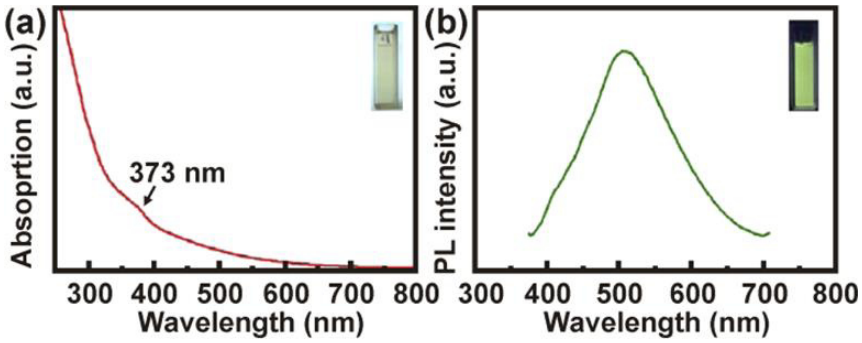

Figure 7. (a) UV − Vis and (b) photoluminescence emission spectra of GQDs.

Onion-like carbon structure can be considered as a giant fullerene which enclose a series of progressively smaller fullerenes. They are produced by graphitization of NDs and have shown potential applications in energy storage, lubricant, composites and catalysis.[1]

1.2 1D Carbon Nanoallotropes: Carbon Nanotubes and Nanohorns

Carbon Nanotubes (CNTs) are based on hexagonal lattice of sp^2 carbon atoms such as a graphene sheet but with the edges fused to form a cylindrical tube with high aspect ratio (length-to-diameter ratio). Single-walled carbon nanotubes (SWCNTs) have a diameter of around 0.4-2 nm which consists of a single graphenic sheet rolled on himself. More than one rolled sheet of graphene produce multi-wall carbon nanotubes (MWCNTs) and their diameters depend by the number of layers in the walls of the cylindrical structure. The aspect ratio of CNTs can be more than 10,000 and so they are considered the most anisotropic materials ever produced.[1]

The way in which graphene monolayer is rolled up to form a cylinder confer specific properties to CNTs; apart from diameter and length, it determine chirality of the tube (the angle between the hexagons and the nanotube axis).[40] Depending on the chirality, carbon atom around the circumference of the tube are arranged in different ways:[41]

i. armchair
ii. zigzag
iii. chiral

The electrical properties of CNTs are governed by their diameter and chirality. Armchair structure (n = m) display metallic behavior if the diameter is higher than a threshold value (the energy gap in the semiconducting tube is proportional to diameter $^{-1}$). Chiral nanotubes with m ≠ n and m – n is a multiple of 3 are semiconducting. The other tube are considered moderate semiconductors (Figure 8).[41]

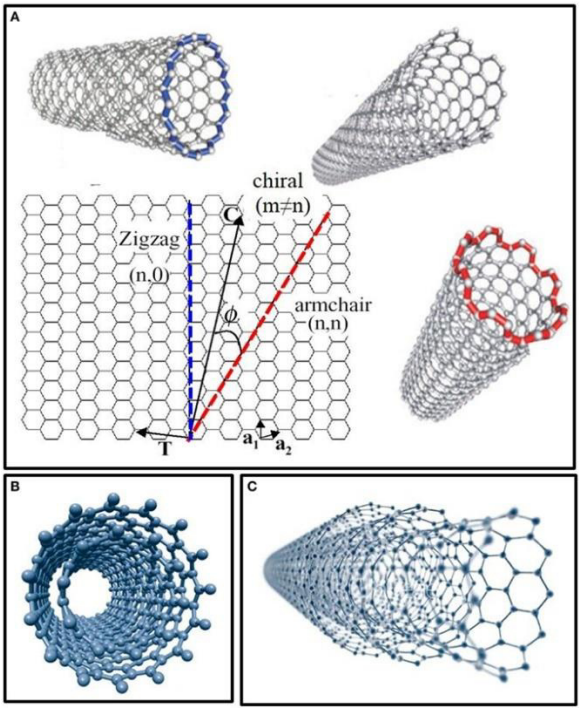

Figure 8. Structure and models of carbon nanotubes in function of their number of walls. (A) Single-walled carbon nanotubes (SWNTs) structures in function of their chirality (zigzag, armchair, and chiral). (B) Model of double-walled carbon nanotubes (DWNTs). (C) Structure of multi-walled carbon nanotubes (MWNTs) made up of several concentric shells.[41]

The drawback of the high aspect ratio and the high specific surface area of CNTs is the strong tendency to stick together, indeed, they are not singly dispersible also in organic solvents; they are strongly held together in bundles by significant Van der Waals interaction.[42,43] Also CNTs show the characteristic G and D bands in Raman spectroscopy and the relative intensity gives information about the defects abundance. The typical Raman spectra of CNTs show the low-energy modes known as “radial breathing mode” (150 – 350 cm^{-1}) which is a fingerprint for the tube diameter, and it only occurs in SWCNTs.[44]

Carbon nanohorns are lobule-like/conelike structures constituted by a single graphene sheet. They are commonly found in spherical aggregates of 100 nm approximately, and resemble dahlia flowers (Figure 1). The medium size of each single walled nanohorn (SWNH) is 1-2 nm at the tip and 4-5 nm at the base of the cone.[45] Similarly to CNTs, cutting a wedge from graphene and connecting the edges in a seamless fashion it is possible to obtain a SWNH. The opening angle of the wedge is called the declination angle and is defined as $n(\pi/3)$, where $0 \leq n \leq 6$ (for n=0 and n=6 correspond a 2D structure like graphene and 1D structure like nanotube, respectively).[45] Considering geometrical rules, nanohorns contain exactly 5 pentagons close the tip and they are classified considering the relative positions of carbon pentagons at the apex which determine the morphology of the terminating cup (Figure 9). Similarly to the previous CNPs, also these structures show the characteristic D and G Raman bands.

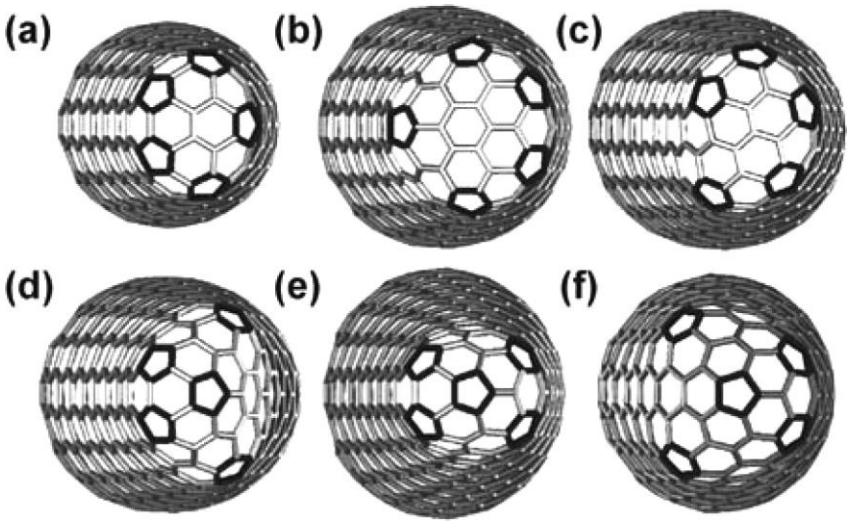

Figure 9. Examples of the end structure of an SWNH when all pentagons are located (a−c) at the conical shoulder or (d−f) at the apex.[45]

1.3 2D Carbon Nanoallotropes: Graphene and its Derivatives

Graphene is the building block of graphite. Each carbon atom is sp^2 hybridized so it is able to make covalent σ bonds with 3 carbon neighbor, creating a robust honeycomb lattice.[9,46] The unhybridized p orbitals, perpendicular to the planar sheet of graphene, interact altogether creating an extensive π conjugated system, conferring to graphene an aromatic character. The unique

organization of these sheets results on high strength and toughness, making graphene the strongest known material. The optical transmittance of single layer graphene is quasi-total but it drastically decreases for stacked layer.[46]

There are several methods to produce graphene, and in general the higher quality graphene require more expensive procedures. The quality of graphene depends by different factors, *in primis* by the amount of oxygen atom and the number of defects in the honeycomb lattice. The other parameter regards the number of the layer composing "graphene". Multilayer graphitic nanosheet consists of between 2 and 10 graphene monolayers and their properties are similar to graphene: it is possible to disperse it in organic solvents, forming stable and transparent suspensions.

Raman spectra of graphene contain an intense G band at 1580 cm^{-1} assigned to the E_{2g} phonon of the sp^2 carbon atoms, a D band at 1350 cm^{-1} due to the A_{1g} breathing mode vibration of the aromatic rings, activated only for the rings directly bound to sp^3 carbon atoms at defect sites and edges, and 2D band at 2700 cm^{-1} which is an overtone of D band. I_D/I_G ratio reflects the percentage of sp^3 carbons than it is an indication of the quality of graphene.[47,48]

Cutting a strip of the single layer graphene is possible to obtain a slightly different material. Practically, it can be produced unzipping CNTs to achieve **graphene nanoribbons**.[49] They are considered a one-dimensional sp^2-hybridized carbon strip with defined edges at which carbon atoms are not allowed to perform the 3rd C-C bond. As well as CNTs, it is possible to distinguish the carbon nanoribbons by the edge terminations: armchair, zigzag and chiral.[50]

Chemical conversion from graphite appears to be a much more efficient approach to bulk production of graphene sheets at low costs.[51] It consist in a fist stage chemical oxidation of graphite followed by ultrasonication and purification, obtaining a well-dispersed aqueous colloid of **graphene oxide** (GO). The functional groups introduced by the oxidation treatments (carboxyl, epoxy, carbonyl and hydroxy) favor the water compatibility and prevent the re-stacking of the sheets, thanks to the net negative surface charge.[51] GO which is electrically insulating, can be converted to conducting graphene by chemical reduction (Figure 10). Chemical converted graphene (CCG) is still stable in water and partially recovers the conductive properties of graphene. This approach permits to produce significant amount of graphene with low costs, at the expense of the quality which is significantly lower than physical exfoliation approach.[51]

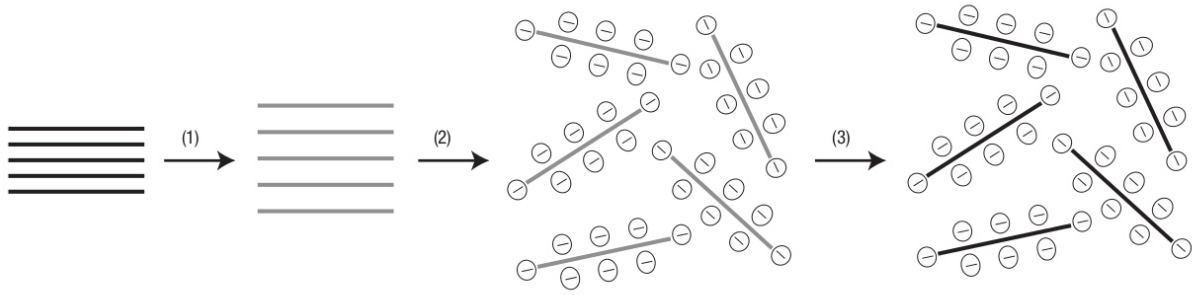

Figure 10. 1) Oxidation of graphite (black) to graphite oxide (grey) with greater interlayer distance. 2) Exfoliation of graphite oxide in water by sonication to obtain GO colloids that are stabilized by electrostatic repulsion. 3) Controlled conversion of GO colloids to conducting graphene colloids through chemical reduction.[51]

1.4 Protein and Carbon Based Nanomaterial Hybrids

Integrating carbon nanomaterials with biological systems to form hybrid functional assemblies is an innovative research area with great promise for medical, nanotechnology, and materials science applications. The specifics of molecular recognition and catalytic activity of proteins combined with the mechanical and electronic properties of CNMs provides opportunities to understand and develop new nanomachines, sensors, or any of a number of other molecular assemblies. Researchers know relatively little about the structure, function, and spatial orientation of proteins noncovalently adsorbed on CNMs, yet because the interaction of CNMs with proteins depends strongly on the tridimensional structure of the proteins.[52]

1.4.1 Surface Chemistry of CNMs and Proteins

Four types of interactions control the binding of proteins to CNMs:

i. Van der Waals interactions. The large number of protein-CNM contacts makes the total Van der Waals (VdW) force dominant. The entity of interaction between amino acids (AA) and CNMs can be assessed using the refractive index of the individual AA, which is related to the VdW interaction.[53] Aromatic residues show the highest values: formation of π-π

stacks between these residues and the surface of the CNMs play the most important role in the protein-CNMs binding.[54,55] Tryptophan possesses the highest affinity for CNMs, followed by tyrosine, phenylalanine, and histidine.[56]

ii. Hydrophobic interactions. Hydrophobicity originates from excluding the ordered water molecules from a nonpolar surface. These interactions tend to minimize the nonpolar surface area by clustering hydrophobic groups and avoiding the exposure to hydrophilic media. AA with a hydrophobic side chain tend to bind to the surface of the CNMs reducing the interfacial energy with the water interface (hydrophobic effect). Other than the aromatic AA, aliphatic residues such as leucine, isoleucine, methionine, and valine play a major role in hydrophobic interactions.[57,58]

iii. Amphiphilicity. Experimentally, some peptides whose residues are mostly hydrophilic can also strongly bind onto the CNMs.[55] Molecular dynamic simulations revealed that polar residues such as glutamine, asparagine, aspartic acid, glutamic acid, arginine, and lysine may provide significant contributions to the binding of proteins onto CNMs.[58,59] Hydrophobic aliphatic chains of these residues interact with the CNMs surface, whereas the hydrophilic groups point out toward water, generating what were defined as surfactant-like interactions. [58,60]

iv. Electrostatic interactions are quantitatively smaller than the previous ones but can alter significantly the electronic properties of CNMs.[61,62] Positively charged residues (arginine and lysine, in particular) can interact with the CNT via the classic cation-π interactions. When a net charge is not present in the residue, a charge-transfer mechanism may still occur.

1.4.2 Spatial Arrangements and Peptide Sequence Contribution on CNMs-Protein Interactions

The presence of AA with a strong tendency to bind CNMs does not suffice to guarantee binding of peptides or proteins to CNMs. Proteins with similar contents of residues bind CNMs differently.[63,64] The presence of amphiphilicity in peptides or proteins is a prerequisite to disperse CNMs efficiently.[65] Screening of peptides demonstrated that only amphiphilic peptides with

hydrophobic residues at the center or at one end of the sequence form stable dispersions of peptide-CNM conjugates. Proteins with similar percentages of hydrophobic, aromatic, and polar residues show different binding behaviors.[63]

The reason is their different three-dimensional arrangement. The higher the content of interacting residues on the surface of the protein, the higher is the efficacy of protein binding to CNMs.[63] There is also a significant role of shape complementarity as the discriminating factor to control binding between carbon nanoobjects and proteins.[66]

1.4.3 CNMs – Protein Applications in Nanotechnology

Dispersion of CNMs by Proteins. To obtains a stable dispersions of CNMs is one of the most important prerequisites for their technological exploitation.[67–70] The noncovalent approaches are attractive because they preserves the peculiar properties of CNMs, while improving their dispersibility.[69,71]

Amphiphilic molecules, surfactants, synthetic polymers, biopolymers, DNA, and short peptides were used to disperse CNMs.[69] In recent years, also proteins have become widely used as CNTs-dispersing agents. [63,72–74] Proteins are naturally amphiphilic. Taking advantage of this feature may avoid complicated synthetic procedures or the use of organic solvents. Most proteins are also pH-responsive, which is an advantage for system manipulation.[74] Steric hindrance and electrostatic repulsion are two of the major mechanisms active in the dispersion of CNMs in protein solutions.

Sorting CNMs. Protocols were developed to sort different CNTs according to different geometric characteristics, electronic properties, and chirality of each sub-groups.[75] These methodologies are effective but have some important shortcomings, such as complex separation processes, special equipment requirements, and difficulties for achieving mass production. [76]

Most of the drawbacks were overcome using proteins.[77] For example, lysozyme was shown to bind preferentially and to disperse CNTs with larger diameters, which, realized an efficient large-scale fractionalization and enrichment of large diameter CNTs.[78]

CNMs as Support for Enzyme Immobilization. The high surface area of CNMs (especially CNTs and graphene) makes them ideal candidates to support enzymes.[79] These hybrids possess

properties of soluble and immobilized enzymes, which confer them useful attributes such as low mass transfer resistance, high activity, stability and reusability.[80]

An important behavior is require for this application: active site of the protein should be located away from the interaction area of the protein with the CNM.

CNM-Enzyme Hybrids as Functional Materials. Highly active and stable polymer-nanotube-enzyme composites were prepared. [81] In these composites, enzymes both disperse CNTs in the matrix and perform their natural catalytic activity, while CNTs both support the enzyme in the polymeric matrices and improve the mechanical properties of the material.[81]

Proteins Assemble Ordered Hierarchical Objects. Proteins can integrate nanoscale objects in an ordered and hierarchical manner. Amphiphilic R-helical peptides were designed to control assembly of peptide-coated nanotubes into supramolecular structures.[82]

Peptide sequences were designed for organize themselves into a tubular structure surrounding the CNTs. The geometrically defined, virus-like coating created by these peptides converts the smooth surfaces of CNMs into richly textured, multilayered surfaces with long-range order, capable of directing the assembly of gold nanoparticles into helical arrays along the CNT axis (Figure 11).[83]

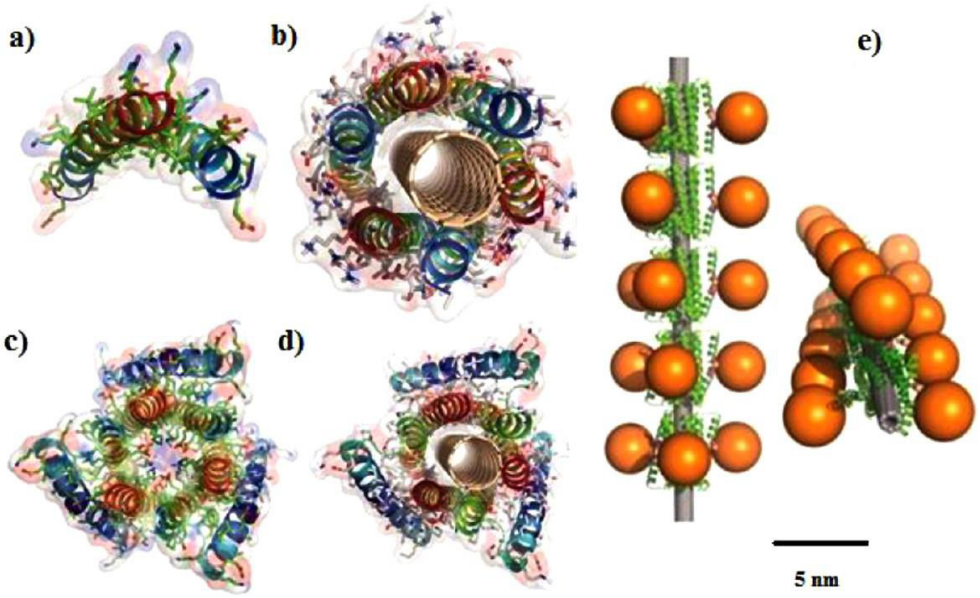

Figure 11. (a) Crystal structure of de novo designed helical assembly protein HexCoil-Ala (PDB 3S0R). (b) Model structure of HexCoil-Gly with a (3,8) CNT. (c) Crystal structure of the native inner ring of helices of a domain-swapped helical protein called DSD (PDB 1G6U). (d) Model of DSD-Ala with a (3,8) SWNT. (e) Computational model of gold nanoparticles grown on cysteine-modified DSD-Gly hexamers wrapped around individual CNT complex.[83]

1.4.4 CNMs – Protein Applications in Biology and Medicine

Targeted Carriers for Therapeutic and Imaging Materials. Some CNMs' ability to pass cellular membranes[84] can allow them to shuttle cargoes from the extracellular matrix into the cells with great potential for drug delivery applications.

CNMs themselves are usable in cancer therapies including photodynamic[70,85,86], photothermal[87] and photoacoustic[88] therapy. CNMs also show promise against a variety of pathogens for their strong antimicrobial activity.[89]

Nonspecific cell targeting of CNMs remains a barrier to delivery applications. The CNMs surface can be decorated with proteins or antibodies[73,74,90] and, for hollow CNMs, it is possible to load in their interior a variety of cargoes, including materials of medical interest for diagnostic such as Fe_2O_3 nanoparticles or Gd^{3+} ions for magnetic resonance imaging (MRI), I_2 molecules for X-ray computed tomography (CT) imaging, and radionuclides (86Y, 211At,and 225Ac) for emission tomography (PET and SPECT) or R-radioimmunotherapy.[91,92]

These hybrid constructs can provide the basis for theranostics, offering a platform for the development of candidates for simultaneous diagnosis and targeted delivery to specific sites in the body.

Immunization with Biofunctionalized CNMs. They are able to present peptides attached to their surface with the correct conformation for recognition without perturbing the secondary structure of the peptide.[93] Peptide antigens are poorly immunogenic, and conjugation to protein carriers is usually necessary to improve antibody production. Protein carriers are intrinsically immunogenic, and the antibodies generated by them present low specificity. Decoration of CNMs with B and T cell peptide epitopes generated a multivalent system that induced strong immune responses.[94]

Protein-CNMs hybrid bioscaffold. CNMs can be incorporated in proteic bioscaffolds, providing structural reinforcement as well as imparting novel properties, such as electrical conductivity, in tissue engineering.[91]

CNMs as Substrates for Cell Growth and Neural Interfacing Applications. CNMs functionalized with cell adhesion peptides or proteins are promising candidates for next generation cell-growth substrates since they support cell adhesion, growth, and differentiation.[95,96] Functionalization of CNMs with extracellular matrix (ECM) proteins, such as fibronectin or collagen, produce effective platforms to control cell adhesion. [95,96]

Proteins That Detect CNMs. Erlanger and co-workers generated IgG antibodies in mice that bind specifically to C_{60}.[97] The same monoclonal antibody recognizes and binds specifically to CNTs. X-ray crystallography of its Fab fragment showed that the binding cavity is a cluster of hydrophobic residues.

CNM Alteration of Protein Functioning. A toxicological profile of CNMs has emerged during the last years. One of the main aspects involves CNMs interaction with proteins. CNMs may interfere directly with protein functions. More studies reported that fullerenes and C_{60} can block ion channel proteins (Figure 12).[98]

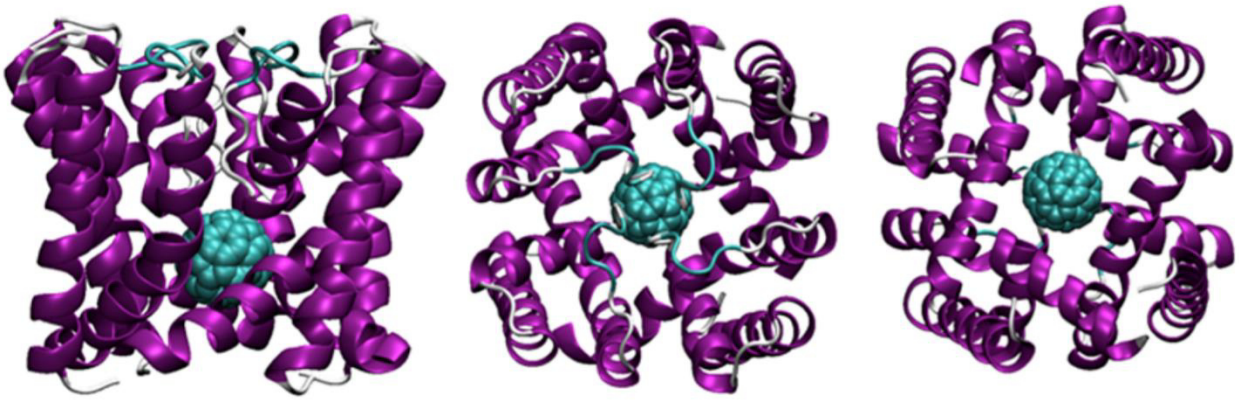

Figure 12. Docked complex. Left: front view. Middle: top view. Right: bottom view.[98]

Protein Biocompatible CNMs Coating. CNMs toxicity can be completely alleviated by chemical functionalization;[70,99,100] in the same way, encapsulation by protein may control and decrease the overall CNMs cytotoxicity.[76] Well-dispersed CNMs are less toxic than their agglomerates. Protein binding also alters the cellular interaction pathways of CNMs. Binding of blood proteins to the CNMs surface results in reduced cytotoxicity of these hybrids. The coating of CNMs with proteins can confer on them a new biological identity,[101] defining their recognition by cells of the innate immune system, which may affect CNMs cellular uptake and recovery biodistribution and toxicity.

1.4.5 CNMs – Protein for Sensing Applications

Electrochemical Sensors. Hybrid systems obtained by conjugating redox proteins with CNMs have potential in bioelectronics and biosensing.[102] Redox proteins produce processable signals in response to biological events, environment modifications, or optical absorption. For example, CNTs can increase protein loading and assist electron transfer to the electrode.[102]

Detection of Proteins and Biorecognition Events. Proteins carry charged groups that, upon adsorption, can electrostatically gate a semiconducting CNTs. The gating was exploited for protein detection in solution with direct electronic readout. The shift in conductivity allowed estimating the number of adsorbed proteins.[61]

Catalytic activity of enzymes can be monitored. Choi et al.[103] attached a single T4 lysozyme molecule to a CNTFET device. In their single-molecule enzymatic reaction assay, lysozyme dynamics was monitored revealing the conformational motions of the enzyme active site during enzymatic reaction turnover (Figure 13). Molecular motions created changes in electrostatic potentials that were converted into dynamically changing electron fluxes, identifying the hydrolytic events.

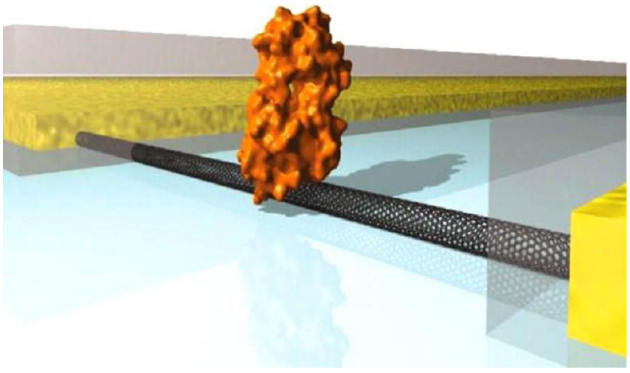

Figure 13. Tethering a single lysozyme molecule to a CNTFET produces a stable, high-bandwidth transducer for protein motion.[103]

CONCLUSIONS

Carbon based nanomaterials and proteins differ greatly. CNMs are simple 0D, 1D or 2D objects made of carbon atoms and characterized by outstanding mechanical, electrical and optical properties.

Proteins are “soft materials”, with a huge assortment of chemical-physical features and offering an wide variety of shapes and sizes. They can be considered nanomachines able to “sense” the presence of molecules or to assemble or disassemble molecular size components with incredible efficiency or to be structural or “active mechanical” components of an organism.

The development of hybrid CNM-protein systems potentially combines the peculiar properties of the single components and may drive fundamental technological advancements in different fields such as nanotechnology, medicine, materials science and biology.[52]

REFERENCES

1. Georgakilas, V., Perman, J. A., Tucek, J. & Zboril, R. *Broad Family of Carbon Nanoallotropes: Classification, Chemistry, and Applications of Fullerenes, Carbon Dots, Nanotubes, Graphene, Nanodiamonds, and Combined Superstructures*. *Chemical Reviews* **115,** (American Chemical Society, 2015).
2. Baptista, F. R., Belhout, S. A., Giordani, S. & Quinn, S. J. Recent developments in carbon nanomaterial sensors. *Chem. Soc. Rev.* **44,** 4433–4453 (2015).
3. Kroto, H. W., Heath, J. R., O'Brien, S. C., Curl, R. F. & Smalley, R. E. C60: Buckminsterfullerene. *Nature* **318,** 162–163 (1985).
4. Iijima, S. & Ichihashi, T. Single-shell carbon nanotubes of 1-nm diameter. *Nature* **363,** 603–605 (1993).
5. Iijima, S. Helical microtubules of graphitic carbon. *Nature* **354,** 56–58 (1991).
6. Wallace, P. R. The Band Theory of Graphite. *Phys. Rev.* **71,** 622–634 (1947).
7. Boehm., H. P., Clauss, A., Fischer, G. O. & Hofmann, U. Dünnste Kohlenstoff-Folien. *Zeitschrift für Naturforsch. B* **17,** 150–153 (1962).
8. Novoselov, K. S. Electric Field Effect in Atomically Thin Carbon Films. *Science (80-.).* **306,** 666–669 (2004).
9. Geim, A. K. & Novoselov, K. S. The rise of graphene. *Nat. Mater.* **6,** 183–191 (2007).
10. Lieber, C. M. & Chen, C.-C. in 109–148 (1994). doi:10.1016/S0081-1947(08)60578-0
11. Shigeru Deguchi, *, Rossitza G. Alargova, and & Tsujii, K. Stable Dispersions of Fullerenes, C60 and C70, in Water. Preparation and Characterization. (2001). doi:10.1021/LA010651O
12. Ruoff, R. S., Tse, D. S., Malhotra, R. & Lorents, D. C. Solubility of fullerene (C60) in a variety of solvents. *J. Phys. Chem.* **97,** 3379–3383 (1993).
13. Danilenko, V. V. On the history of the discovery of nanodiamond synthesis. *Phys. Solid State* **46,** 595–599 (2004).
14. Mochalin, V. N., Shenderova, O., Ho, D. & Gogotsi, Y. The properties and applications of nanodiamonds. *Nat. Nanotechnol.* **7,** 11–23 (2011).
15. Ozawa, M. Preparation and behavior of brownish, clear nanodiamond colloids. *Adv. Mater.* **19,** 1201–1206 (2007).
16. Chang, Y.-R. *et al.* Mass production and dynamic imaging of fluorescent nanodiamonds. *Nat. Nanotechnol.* **3,** 284–288 (2008).
17. Mochalin, V. N. & Gogotsi, Y. Wet chemistry route to hydrophobic blue fluorescent nanodiamond. *J. Am. Chem. Soc.* **131,** 4594–4595 (2009).
18. Maze, J. R. Nanoscale magnetic sensing with an individual electronic spin in diamond. *Nature* **455,** 644–647 (2008).
19. Krueger, A. Diamond nanoparticles: Jewels for chemistry and physics. *Adv. Mater.* **20,** 2445–2449 (2008).
20. Spitsyn, B. V. Inroad to modification of detonation nanodiamond. *Diam. Relat. Mater.* **15,** 296–299 (2006).
21. Shimkunas, R. A. *et al.* Nanodiamond-insulin complexes as pH-dependent protein delivery vehicles. *Biomaterials* **30,** 5720–8 (2009).
22. Purtov, K. V, Petunin, A. I., Burov, A. E., Puzyr, A. P. & Bondar, V. S. Nanodiamonds as

carriers for address delivery of biologically active substances. *Nanoscale Res. Lett.* **5,** 631–636 (2010).
23. Alhaddad, A. Nanodiamond as a vector for siRNA delivery to Ewing sarcoma cells. *Small* **7,** 3087–3095 (2011).
24. Osswald, S., Yushin, G., Mochalin, V., Kucheyev, S. O. & Gogotsi, Y. Control of sp2/sp3 carbon ratio and surface chemistry of nanodiamond powders by selective oxidation in air. *J. Am. Chem. Soc.* **128,** 11635–11642 (2006).
25. Shenderova, O. Surface chemistry and properties of ozone-purified detonation nanodiamonds. *J. Phys. Chem. C* **115,** 9827–9837 (2011).
26. Danilenko, V. V. Synthesis, Properties and Applications of Ultrananocrystalline Diamond. 181–198 (2005). doi:10.1007/1-4020-3322-2
27. Yang, G. W., Wang, J. B. & Liu, Q. X. Preparation of nano-crystalline diamonds using pulsed laser induced reactive quenching. *J. Phys. Condens. Mat.* **10,** 7923–7927 (1998).
28. Boudou, J.-P. *et al.* High yield fabrication of fluorescent nanodiamonds. *Nanotechnology* **20,** 235602 (2009).
29. Viecelli, J. A., Bastea, S., Glosli, J. N. & Ree, F. H. Phase transformations of nanometer size carbon particles in shocked hydrocarbons and explosives. *J. Chem. Phys.* **115,** 2730–2736 (2001).
30. Barnard, A. S., Russo, S. P. & Snook, I. K. Structural relaxation and relative stability of nanodiamond morphologies. *Diam. Relat. Mater.* **12,** 1867–1872 (2003).
31. Luo, P. G. *et al.* Carbon-based quantum dots for fluorescence imaging of cells and tissues. *RSC Adv.* **4,** 10791 (2014).
32. Chandra, S. *et al.* Synthesis, functionalization and bioimaging applications of highly fluorescent carbon nanoparticles. *Nanoscale* **3,** 1533 (2011).
33. Jiang, J. *et al.* Amino acids as the source for producing carbon nanodots: microwave assisted one-step synthesis, intrinsic photoluminescence property and intense chemiluminescence enhancement. *Chem. Commun.* **48,** 9634 (2012).
34. Ming, H. *et al.* Large scale electrochemical synthesis of high quality carbon nanodots and their photocatalytic property. *Dalt. Trans.* **41,** 9526 (2012).
35. Wang, Y. *et al.* Carbon quantum dots: synthesis, properties and applications. *J. Mater. Chem. C* **2,** 6921 (2014).
36. Zhu, X. *et al.* Hydrothermal synthesis of two photoluminescent nitrogen-doped graphene quantum dots emitted green and khaki luminescence. *Mater. Chem. Phys.* **147,** 963–967 (2014).
37. Ponomarenko, L. A. *et al.* Chaotic Dirac Billiard in Graphene Quantum Dots. *Science (80-.).* **320,** 356–358 (2008).
38. Ritter, K. A. & Lyding, J. W. The influence of edge structure on the electronic properties of graphene quantum dots and nanoribbons. *Nat. Mater.* **8,** 235–242 (2009).
39. Xie, M. *et al.* Blue and green photoluminescence graphene quantum dots synthesized from carbon fibers. *Mater. Lett.* **93,** 161–164 (2013).
40. Belin, T. & Epron, F. Characterization methods of carbon nanotubes: a review. *Mater. Sci. Eng. B* **119,** 105–118 (2005).
41. Tîlmaciu, C.-M. & Morris, M. C. Carbon nanotube biosensors. *Front. Chem.* **3,** 59 (2015).
42. Dai*, H. Carbon Nanotubes: Synthesis, Integration, and Properties. (2002). doi:10.1021/AR0101640
43. Bahr, J. L. *et al.* Dissolution of small diameter single-wall carbon nanotubes in organic

solvents? *Chem. Commun.* **67,** 193–194 (2001).
44. Costa, S., Borowiak-Palen, E., Kruszyńska, M., Bachmatiuk, A. & Kaleńczuk, R. J. Characterization of carbon nanotubes by Raman spectroscopy. *Mater. Sci.* **26,** (2008).
45. Berber, S., Kwon, Y.-K. & Tománek, D. Electronic and structural properties of carbon nanohorns. *Phys. Rev. B* **62,** R2291–R2294 (2000).
46. Ferrari, A. C. *et al.* Science and technology roadmap for graphene, related two-dimensional crystals, and hybrid systems. *Nanoscale* **7,** 4598–4810 (2015).
47. Ferrari, A. C. *et al.* Raman Spectrum of Graphene and Graphene Layers. *Phys. Rev. Lett.* **97,** 187401 (2006).
48. Wang, G. *et al.* Facile Synthesis and Characterization of Graphene Nanosheets. *J. Phys. Chem. C* **112,** 8192–8195 (2008).
49. Sinitskii, A., Dimiev, A., Kosynkin, D. V. & Tour, J. M. Graphene Nanoribbon Devices Produced by Oxidative Unzipping of Carbon Nanotubes. *ACS Nano* **4,** 5405–5413 (2010).
50. Terrones, M. *et al.* Graphene and graphite nanoribbons: Morphology, properties, synthesis, defects and applications. *Nano Today* **5,** 351–372 (2010).
51. Li, D., Müller, M. B., Gilje, S., Kaner, R. B. & Wallace, G. G. Processable aqueous dispersions of graphene nanosheets. *Nat. Nanotechnol.* **3,** 101–5 (2008).
52. Calvaresi, M. & Zerbetto, F. The devil and holy water: protein and carbon nanotube hybrids. *Acc. Chem. Res.* **46,** 2454–63 (2013).
53. McMeekin, T. L., Wilensky, M. & Groves, M. L. Refractive Indices of Proteins in Relation to Amino Acid Composition and Specific Volume. *Biochem. Biophys. Res. Commun.* **7,** 151 (1962).
54. Wang, S. *et al.* Peptides with Selective Affinity for Carbon Nanotubes. *Nat. Mater.* **2,** 196 (2003).
55. Brown, S., Jespersen, T. S. & Nygard, J. A Genetic Analysis of Carbon-Nanotube-Binding Proteins. *Small* **4,** 416 (2008).
56. Xie, H., Becraft, E. J., Baughman, R. H., Dalton, A. B. & Dieckmann, G. R. Ranking the Affinity of Aromatic Residues for Carbon Nanotubes by Using Designed Surfactant Peptides. *J. Pept. Sci.* **14,** 139 (2008).
57. Zuo, G., Kang, S.-G., Xiu, P., Zhao, Y. & Zhou, R. Interactions Between Proteins and Carbon-Based Nanoparticles: Exploring the Origin of Nanotoxicity at the Molecular Level. *Small* **9,** 1546 (2013).
58. Calvaresi, M., Hoefinger, S. & Zerbetto, F. Probing the Structure of Lysozyme-Carbon-Nanotube Hybrids with Molecular Dynamics. *Chem.—Eur. J.* **18,** 4308 (2012).
59. Yang, S.-T., Liu, y., Wang, Y.-W. & Cao, A. Biosafety and Bioapplication of Nanomaterials by Designing Protein–Nanoparticle Interactions. *Small* **9,** 1635 (2013).
60. Li, J., Garg, M., Shah, D. & Rajagopalan, R. Solubilization of Aromatic and Hydrophobic Moieties by Arginine in Aqueous Solutions. *J. Chem. Phys.* **133,** 54902 (2010).
61. Bradley, K., Briman, M., Star, A. & Gruner, G. Charge Transfer from Adsorbed Proteins. *Nano Lett.* **4,** 253 (2004).
62. Samarajeewa, D. R., Dieckmann, G. R., Nielsen, S. O. & Musselman, I. H. Modifying the Electronic Properties of Single-Walled Carbon Nanotubes Using Designed Surfactant Peptides. *Nanoscale* **4,** 4544 (2012).
63. Matsuura, K. *et al.* Selectivity of Water-Soluble Proteins in Single-Walled Carbon Nanotube Dispersions. *Chem. Phys. Lett.* **429,** 497 (2006).
64. Yu, T. *et al.* Recognition of Carbon Nanotube Chirality by Phage Display. *RSC Adv.* **2,** 1466

(2012).
65. Deshpande, M. S. & Mazumdar, S. Sequence Specific Association of Tryptic Peptides with Multiwalled Carbon Nanotubes: Effect of Localization of Hydrophobic Residues. *Biomacromolecules* **13,** 1410 (2012).
66. Calvaresi, M. & Zerbetto, F. Baiting Proteins with C $_{60}$. *ACS Nano* **4,** 2283–2299 (2010).
67. Guldi*, D. M. & Prato, M. Excited-State Properties of C60 Fullerene Derivatives. (2000). doi:10.1021/AR990144M
68. Stankovich, S. *et al.* Stable aqueous dispersions of graphitic nanoplatelets via the reduction of exfoliated graphite oxide in the presence of poly(sodium 4-styrenesulfonate). *J. Mater. Chem.* **16,** 155 (2006).
69. Premkumar, T., Mezzenga, R. & Geckeler, K. E. Carbon Nanotubes in the Liquid Phase: Addressing the Issue of Dispersion. *Small* **8,** 1299 (2012).
70. Da Ros, T. in *Twenty Years of Promises: Fullerene in Medicinal Chemistry* 1–21 (2008). doi:10.1007/978-1-4020-6845-4_1
71. Markovic, Z. & Trajkovic, V. Biomedical potential of the reactive oxygen species generation and quenching by fullerenes (C60). *Biomaterials* **29,** 3561–73 (2008).
72. Nepal, D. & Geckeler, K. E. Proteins and Carbon Nanotubes: Close Encounter in Water. *Small* **3,** 1259 (2007).
73. Karajanagi, S. S. *et al.* Protein-Assisted Solubilization of Single-Walled Carbon Nanotubes. *Langmuir* **22,** 1392 (2006).
74. Nepal, D. & Geckeler, K. E. pH-Sensitive Dispersion and Debundling of Single-Walled Carbon Nanotubes: Lysozyme as a Tool. *Small* **2,** 406–412 (2006).
75. Hersam, M. C. Progress Towards Monodisperse Single-Walled Carbon Nanotubes. *Nat. Nanotechnol.* **3,** 387 (2008).
76. Ge, C. *et al.* Binding of blood proteins to carbon nanotubes reduces cytotoxicity. *Proc. Natl. Acad. Sci. U. S. A.* **108,** 16968–73 (2011).
77. Calvaresi, M. *et al.* Fullerene sorting proteins. *Nanoscale* **3,** 2873 (2011).
78. Nie, H. *et al.* Diameter-selective dispersion of double-walled carbon nanotubes by lysozyme. *Nanoscale* **3,** 970 (2011).
79. Karajanagi, S. S., Vertegel, A., Ravi, A., Kane, S. & Dordick, J. S. Structure and Function of Enzymes Adsorbed onto Single-Walled Carbon Nanotubes. *Langmuir* **20,** 11594 (2004).
80. Asuri, P. *et al.* Increasing Protein Stability Through Control of the Nanoscale Environment. *Langmuir* **22,** 5833 (2006).
81. Pangule, R. C. *et al.* Antistaphylococcal Nanocomposite Films Based on Enzyme−Nanotube Conjugates. *ACS Nano* **4,** 3993–4000 (2010).
82. Gregg R. Dieckmann, *,† *et al.* Controlled Assembly of Carbon Nanotubes by Designed Amphiphilic Peptide Helices. (2003). doi:10.1021/JA029084X
83. Grigoryan, G. *et al.* Computational design of virus-like protein assemblies on carbon nanotube surfaces. *Science* **332,** 1071–6 (2011).
84. Höfinger, S. *et al.* A computational analysis of the insertion of carbon nanotubes into cellular membranes. *Biomaterials* **32,** 7079–7085 (2011).
85. Sharma, S. K., Chiang, L. Y. & Hamblin, M. R. Photodynamic therapy with fullerenes in vivo: reality or a dream? doi:10.2217/nnm.11.144
86. Mroz, P. *et al.* in 79–106 (2008). doi:10.1007/978-1-4020-6845-4_4
87. Montalti, M., Cantelli, A. & Battistelli, G. Nanodiamonds and silicon quantum dots: ultrastable and biocompatible luminescent nanoprobes for long-term bioimaging. *Chem.*

Soc. Rev. **44,** 4853–921 (2015).
88. Wang, L. V. & Hu, S. Photoacoustic Tomography: In Vivo Imaging from Organelles to Organs. *Science (80-.).* **335,** (2012).
89. Olivi, M. *et al.* Antimicrobial properties of graphene-like nanoparticles: coating effect on Staphylococcus aureus. *J. Nanoparticle Res.* **18,** 358 (2016).
90. Hu, W. *et al.* Protein Corona-Mediated Mitigation of Cytotoxicity of Graphene Oxide. *ACS Nano* **5,** 3693–3700 (2011).
91. Heister, E., Brunner, E. W., Dieckmann, G. R., Jurewicz, I. & Dalton, A. B. Are Carbon Nanotubes a Natural Solution? Applications in Biology and Medicine. *ACS Appl. Mater. Interfaces* **5,** 1870 (2013).
92. Kostarelos, K., Bianco, A. & Prato, M. Promises, Facts and Challenges for Carbon Nanotubes in Imaging and Therapeutics. *Nat. Nanotechnol.* **4,** 627 (2009).
93. Davide Pantarotto, †,‡ *et al.* Synthesis, Structural Characterization, and Immunological Properties of Carbon Nanotubes Functionalized with Peptides. (2003). doi:10.1021/JA034342R
94. Pantarotto, D. *et al.* Synthesis, Structural Characterization and Immunological Properties of Carbon Nanotubes Functionalized with Peptides. *J. Am. Chem. Soc.* **125,** 6160 (2003).
95. Harrison, B. S. & Atala, A. Carbon Nanotube Applications for Tissue Engineering. *Biomaterials* **28,** 344 (2007).
96. Cai, N. *et al.* Modulating Cell Adhesion Dynamics on Carbon Nanotube Monolayer Engineered with Extracellular Matrix Proteins. *ACS Appl. Mater. Interfaces* **2,** 1038 (2010).
97. Braden, B. C. *et al.* X-ray crystal structure of an anti-Buckminsterfullerene antibody fab fragment: biomolecular recognition of C(60). *Proc. Natl. Acad. Sci. U. S. A.* **97,** 12193–7 (2000).
98. Calvaresi, M., Furini, S., Domene, C., Bottoni, A. & Zerbetto, F. Blocking the Passage: C_{60} Geometrically Clogs K^+ Channels. *ACS Nano* **9,** 4827–4834 (2015).
99. Prato, M. Medicinal chemistry with fullerenes and fullerene derivatives. 663–669 (1999).
100. Ali-Boucetta, H. *et al.* Asbestos-like Pathogenicity of Long Carbon Nanotubes Alleviated by Chemical Functionalization. *Angew. Chem., Int. Ed.* **52,** 2274 (2013).
101. Walczyk, D., Bombelli, F. B., Monopoli, M. P., Lynch, I. & Dawson, K. A. What the Cell 'Sees' in Bionanoscience. *J. Am. Chem. Soc.* **132,** 5761–5768 (2010).
102. Kim, S. N., Rusling, J. F. & Papadimitrakopoulos, F. Carbon Nanotubes for Electronic and Electrochemical Detection of Biomolecules. *Adv. Mater.* **19,** 3214–3228 (2007).
103. Choi, Y. *et al.* Single-Molecule Lysozyme Dynamics Monitored by an Electronic Circuit. *Science (80-.).* **335,** (2012).

CHAPTER 2

FULLERENES@PROTEINS HYBRID SYSTEMS: SYNTHESIS, CHARACTERIZATION AND APPLICATIONS

INTRODUCTION

2.1 BIOMEDICAL APPLICATION OF FULLERENES

The unique physical and chemical features of C_{60}, the most representative member of the fullerenes family, have recently incited a considerable hope of its possible use in various fields of biomedicine.[1]

Many fullerene-based compounds with different biological targets have been synthesized, displaying a range of biological activities potentially useful in anticancer or antimicrobial (photodynamic and photothermal) therapy,[2] enzyme inhibition,[3] controlled drug delivery[4,5] and contrast-[6] or radioactivity-based[7] diagnostic imaging.

2.1.1 EXCITED-STATE PROPERTIES OF C_{60}

Pumping of the fullerene ground state (S_0) with UV or visible light leads to the population of the singlet excited state (S_1) as shown in Figure 1.

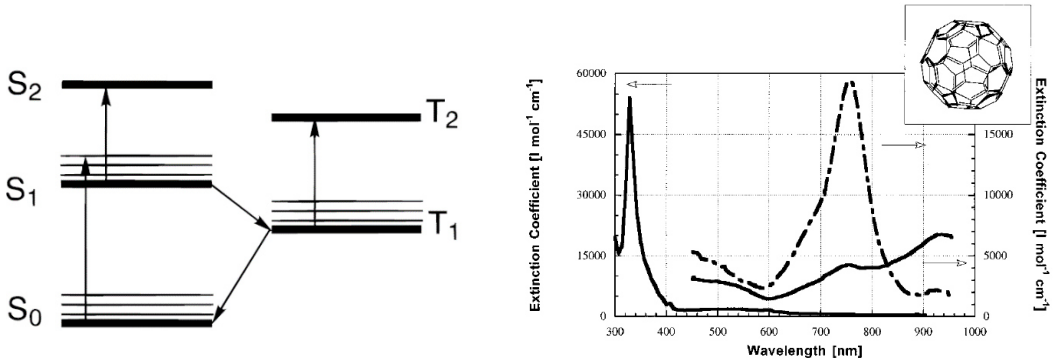

Figure 1. Left: Ground and excited states of fullerenes. Right: Ground-state absorption spectrum (solid line), transient singlet excited-state spectrum (solid line), and transient triplet excited-state spectrum (dashed line) following picosecond flash photolysis (355 nm) of C_{60} in oxygen-free toluene solution.[8]

The lifetime of this excited state is relatively short because C_{60} rapidly convert to the longer-lived triplet excited state (T_1, tens to hundreds of microseconds).[9] This process is a spin-forbidden intersystem crossing, showing a nearly unit yield. Fullerene C_{60} is an highly symmetric and rigid structure. The very small Stock shift demonstrate a little, if any, need for the adjustment of the fullerene singlet excited state to the solvent environment. While fluorescence show a moderate quantum yield, the phosphorescence is insignificant and hard to detect.[10]

The peculiar property of C_{60} concerns its ability to accept, reversibly, 6 electrons. The first reduction potential deeply depends by the solvent polarity.[11] In contrast to reduction, oxidation is more difficult and it is usually limited to one electron step which represents the highest oxidation state.[11]

It is possible to characterize the first reduction step of fullerene ($C_{60}^{\cdot -}$) observing the characteristic near-IR absorption band around 1080 nm.[12] This band permits to study electron-transfer (eT) processed by transient absorption spectroscopy.

Fullerenes are insoluble in water and in most of polar media. Chemical modification with water soluble functional groups is required to carry out any study. In polar solvent, the hydrophobic nature of fullerene leads them to cluster together, leaving the hydrophilic functional groups outside.[13] The degree of aggregation cannot be deduced by absorption spectra but the photophysical properties are significantly changed. The lifetime of the triplet excited state is sensitive to the environment. When fullerenes cluster into aggregates, it become subject to triplet-triplet annihilation and, consequently, the lifetime are drastically reduced (< 0.1 μs).[8]

The photophysical and electrochemical properties of functionalized fullerenes are strongly dependent by the number of functional group linked to the core.[14,15] In fact, monoadducts are more difficult to reduce than C_{60} itself, and the reduction process become more difficult as the number of addends increase.[14] More importantly, the triplet quantum yield significantly decrease as the number of pendant increase.[16]

2.1.2 Reactive Oxygen Species Generation

The application of fullerene in biomedical field requires the preservation of the long-lived triplet excited state. Thanks to this particular characteristic, fullerene can be used as photosensitizer: upon UV-Vis irradiation the triplet state can be quenched by ground state molecular oxygen to produce different reactive oxygen species (ROS).[2] The importance of ROS is bivalent because they can react with a wide range of biological targets and they are also involved in cellular signaling.[17] C_{60} can be used to generate cell-damage ROS and can be as cytotoxic anticancer/antimicrobial agent. The unique electron configuration of molecular oxygen, characterized by two single-occupied antibonding orbitals that contain electrons with parallel spins, give rise to three energetically close electronic states – the Σ triplet ground state and the excited Σ and Δ singlet states (Figure 2, right). The $O_2(^1\Delta_g)$ state, in which both electrons are paired in a single orbital has lower energy, but considerably longer lifetime than Σ excited state, and it is identified as the metastable O_2 species commonly known as singlet oxygen. Because of the extremely high oxidizing ability resulting from a removal of the spin restriction, singlet oxygen displays significant reactivity in a variety of chemical and biochemical reactions.[1]

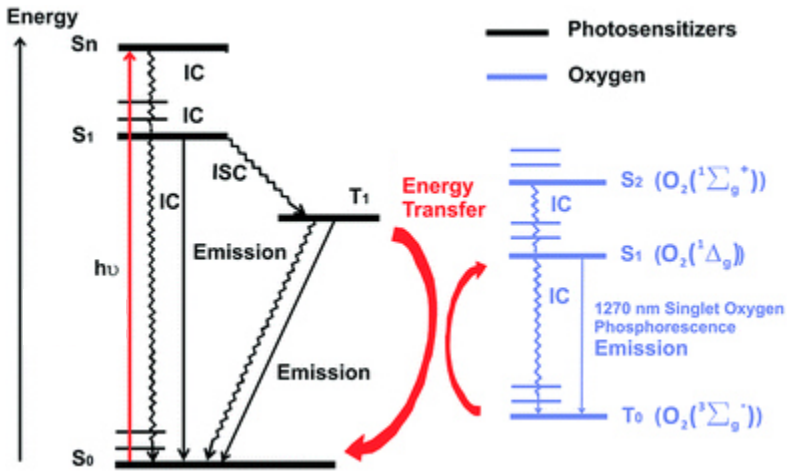

Figure 2. Energy diagram of the photosensitized singlet oxygen production[18]

The common way to produce singlet oxygen is photosensitation, which consists in the energy transfer to triplet ground state oxygen from an excited state molecule (sensitizer), formed by absorption of light in a specific wavelength region (Figure 2). Due to the particular electronic configuration of molecular O_2, singlet oxygen photosensitation is a highly favored process: the fact that the excitation energy of singlet and triplet oxygen is lower than triplet of the majority of organic molecule make it easy to find a suitable sensitizer.[1] Furthermore, because the transition between the triplet excited state of the sensitizer and the ground state in a spin-forbidden process, the excited state generally has long lifetime, allowing the complete quenching by O_2 in air saturated solutions.

The efficiency of a photosensitizer is measured by the quantum yield which consists in the number of $^1O_2$ produced per number of photon absorbed. Fullerene is extremely efficient as photosensitizer, its quantum yield in nonpolar solvents is close to the unity.[1] In general, fullerenes show an intense absorption band in the UV and a moderate absorption in visible range.[8] As mentioned before, singlet excited state (S_1) fullerenes rapidly convert to the long lived triplet state (T_1), where it can be efficiently quenched by triplet ground state molecular oxygen.

However, in the excited state, fullerene is also an excellent electron acceptor.[8] The resulting reduced fullerene triplet ($^3C_{60}^{\bullet-}$) can transfer one electron to molecular oxygen, forming superoxide anion $O_2^{\bullet-}$ and other reactive species. This mechanism is commonly observed in polar solvents, particularly in presence of electron donors (amines, NADH, reduced thiols *etc*).[19] These two

mechanisms to produce ROS, are classified as Type 1 and Type 2 (Figure 3), to identify electron transfer and energy transfer processes, respectively.

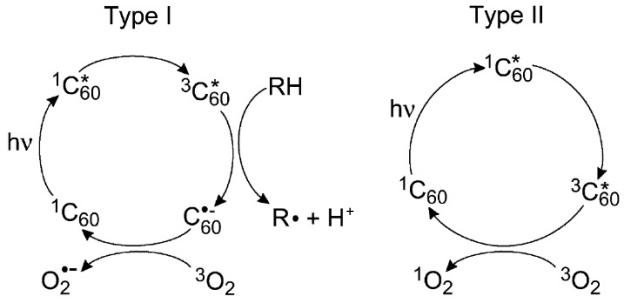

Figure 3. Schematic representation of Type I (electron transfer) and Type II (energy transfer) photochemical mechanisms (* denotes excited states of C_{60}).[1]

Type I mechanism in biological media can produce different reactive oxygen species. In presence of electron donors and oxidase enzymes, hydrogen peroxide (a stable ROS product) is formed upon superoxide dismutation. In presence of ferrous irons (available in biological environment as enzyme cofactor), Fenton reaction can occur (4), producing the high reactive hydroxyl radical and superoxide anion reduce the ferric ion (5, Haber-Weiss reaction) to close the cycle.[20]

1) $C_{60}^{*} + NADH \rightarrow 2C_{60}^{\cdot -} + NAD^{+} + H^{+}$
2) $C_{60}^{\cdot -} + O_2 \rightarrow C_{60} + O_2^{\cdot -}$
3) $2\ O_2^{\cdot -} + 2\ H^{+} \rightarrow O_2 + H_2O_2$
4) $H_2O_2 + Fe^{2+} \rightarrow OH^{\cdot} + OH^{-} + Fe^{3+}$
5) $Fe^{3+} + O_2^{\cdot -} \rightarrow Fe^{2+} + O_2$

Nowadays, there is still a debate about the mechanism of reactive oxygen species production by fullerenes. The most accepted interpretation is that both mechanisms can occur, but type I preferentially occurs in polar media and type II is commonly observed in organic solvents.[19,20] It is also hard to compare the results by literature, especially because different approaches were used to disperse/solubilize fullerenes in water (chemical functionalization,[16,21–23] incorporation in supramolecular structures,[24–27] solvent exchange method,[28,29] long-term stirring[30]).

In the last decade, fullerenes have gained considerable attention as potential photosensitizers for photodynamic therapy (PDT) of various diseases. Some advantages that fullerene possess over the traditional photosensitizer used in photodynamic therapy are:

i. Fullerenes are more photostable and demonstrate less photobleaching compared to the traditional synthetic dyes and tetrapyrroles;
ii. Fullerenes demonstrate to follow both the photophysical mechanisms while the traditional dyes show mainly the type II mechanism (singlet oxygen);
iii. The reactive oxygen species production yield is close to 1;

However the use of fullerene in PDT still presents important restrictions in their application due to:

i. Poor water solubility and low biocompatibility;
ii. Dependency of their properties and toxicity on the physiological environment and the related aggregation phenomena.

Monodispersity of fullerenes is the key feature for potential application in nanomedicine. Aggregation phenomena drastically decrease the long-lived triplet excited state lifetime, consequently reducing the ROS production efficiency.
Up to date two main approaches are followed to disperse fullerenes monomolecularly in water:

COVALENT. It is the most used method to prevent fullerene re-aggregation. The benefits obtained by functionalization are heavily payed by the decrease of the photophysical performances;[16]

NON-COVALENT. It requires the use of supramolecular hosts, that are amphipathic molecules able to specifically interact with a single fullerene and to screen it from the aqueous environment. Different family of surfactants are capable to interact with fullerenes but in all the cases they stabilize nanometric clusters of fullerene. The best host-guest interactions were found for calixarenes and cyclodextrin.[31,32] γ-cyclodextrin form a supramolecular system with fullerene (cyclodextrin-bicapped C_{60}, Figure 4) dispersing C_{60} in water, but it was experimentally observed

that they cluster into nanoparticles with a size ranging from tenths to several hundred of nanometers.[1,33]

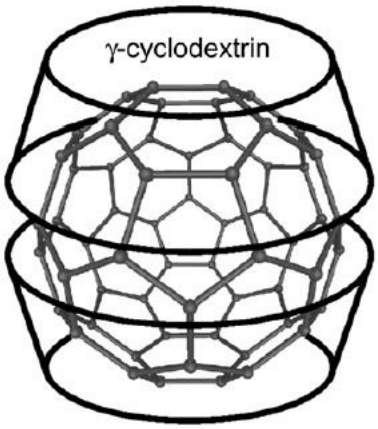

Figure 4. Schematic representation of γ-cyclodextrin-bicapped C_{60} supramolecular system.

In our group we recently showed that an alternative approach to host-guest interaction for fullerenes is possible. It was theoretically and experimentally demonstrated that proteins are potential tools to disperse fullerene in water.

2.2 First Evidence of C_{60}@Lysozyme 1:1 Adduct

The ability of C_{60} to interact with proteins is a very recent subject of study. There are different difficulties in the investigation of their interactions:

i. Because of its insolubility in water, fullerene is mainly used in derivative forms (fullerol, tris-malonate, tris-amine *etc.*);[4,34–38]
ii. The identification of fullerene binding site and subsequent proteins structural modification has been investigated only using indirect techniques;
iii. It is not clear if there is an interaction between the single fullerene with a protein or between fullerenes clusters with proteins.

The group where I spent my PhD research activity, for the first time, identified unambiguously in solution the protein – C_{60} binding pocket, using the NMR chemical shift perturbation analysis.[39]

Lysozyme (LSZ) was used as model protein. It is one of the less expensive, well characterized, stable, simple to crystallize and easy to genetically modify protein. Moreover, it is already known that lysozyme is able to disperse pristine single-wall carbon nanotubes in water.[40] A similar approach was used to produce the C_{60}@lysozyme hybrid system.

Upon sonication and supernatant collection, the UV-Vis spectrum revealed feature that belong to both components of the adduct, showing the characteristic absorption band of fullerene at 340 nm, and the convolution of both lysozyme (280 nm) and fullerene (265 nm) bands, which results in a sharper band with maximum at 271 nm.

Upon interaction, from circular dichroism (CD) analysis, the secondary structure of the protein did not appear significantly perturbed (Figure 5b) which means that sonication process and adduct formation (Figure 5a) did not cause a conformational change in the protein.

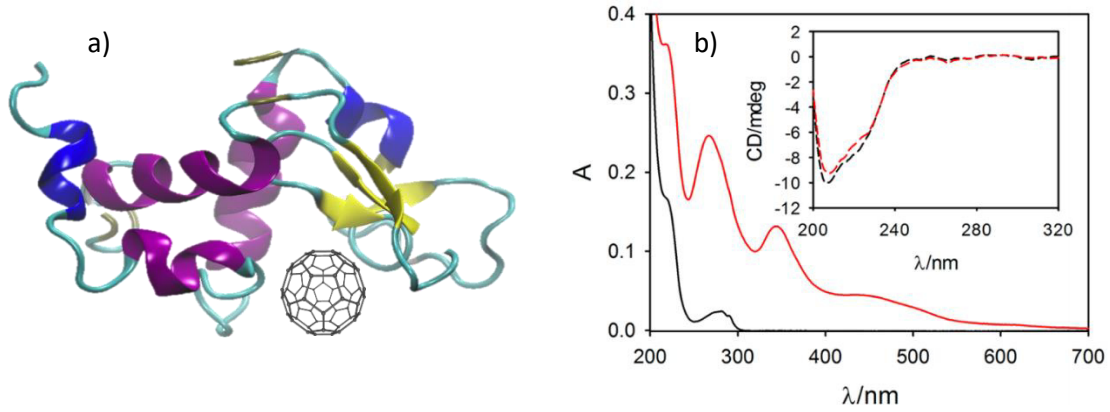

Figure 5. a) Tridimensional representation of C_{60}@LSZ hybrid. b) Spectroscopic characterization of C_{60}@LSZ hybrid. UV-visible spectra of monomeric LSZ protein (black line) and purified C_{60}@LSZ hybrid (red line). The inset shows the circular dichroism spectra of monomeric LSZ (black line) and C_{60}@LSZ hybrid (red line).[39]

Two-dimensional ^{1}H-^{15}N NMR experiments were conducted to detect changes in the chemical environment of all coupled H and N atoms of the protein upon formation of protein complexes (chemical shift perturbation analysis, CSP). Figure 6 shows the superposition of 2D ^{1}H-^{15}N HSQC spectra of free LSZ and C_{60}@LSZ hybrid. Each crosspeak represents a NH group of the protein backbone (one per amino acid residue, excluding Pro residues) and of a Trp indole ring. Even after complex formation the spectral resolution remained very high, indicating that the protein retained its folding. Only a few NH backbone groups underwent significant change in chemical shift upon binding to C_{60}, with the majority of them remaining unaffected. This finding indicated that the interaction of C_{60} with LSZ is very specific and affects only a few amino acids.

The residues that underwent the largest changes, not contiguous in the sequence (Figure 7a), cluster in a specific region of the three-dimensional structure of the protein (Figure 7b). These residues were most likely involved in the interaction with C_{60}.

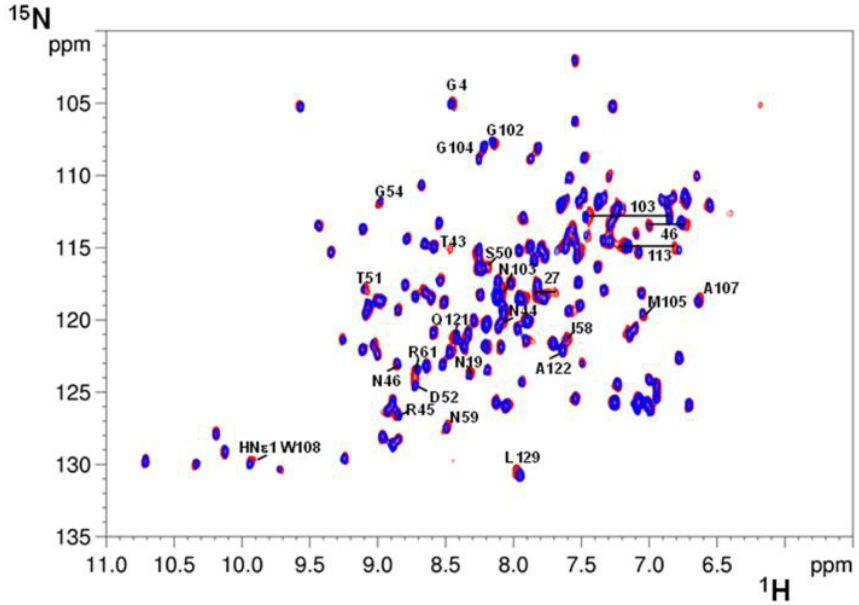

Figure 6. Superposition of 2D $^{1}H,^{15}N$ HSQC spectra of samples of free LSZ (blue) and C_{60}@LSZ hybrid (red). Black labels indicate cross-peak assignment of residues undergoing chemical shift perturbation upon interaction with C_{60}.[39]

A docking protocol[3] recently validated to detect fullerene-protein binding pockets, identified the same region of the NMR as the most likely binding site.

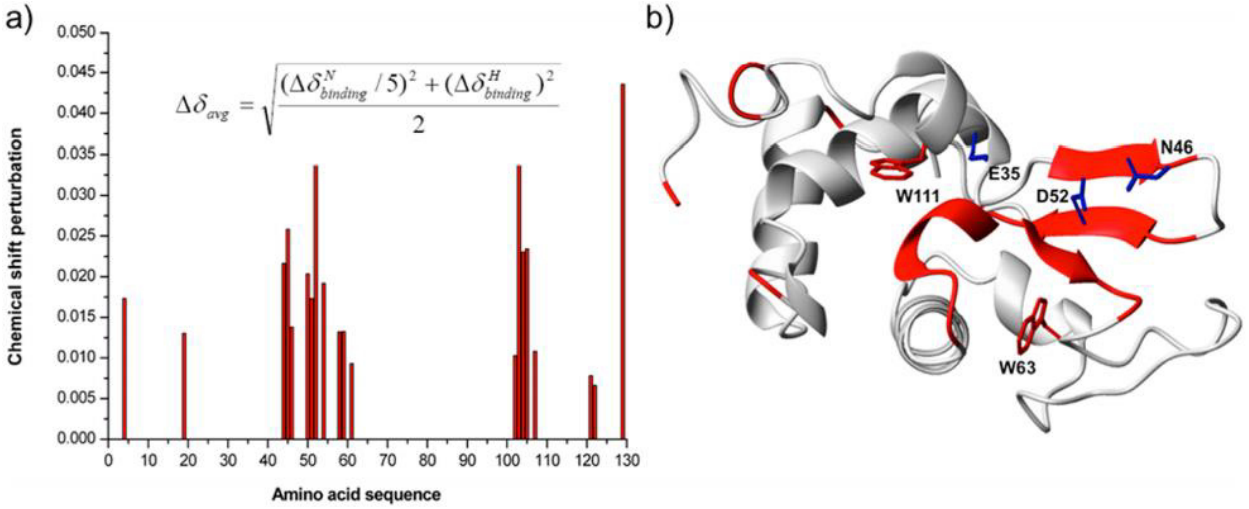

Figure 7. NMR chemical shift perturbation analysis of LSZ upon interaction with C_{60}. a) CSP is given by the weighted average chemical shift differences $\Delta\delta_{avg}$(HN) of cross-peaks in the $^{1}H,^{15}N$ HSQC spectra of free and bound LSZ (see equation embedded in the figure). b) 3D representation of the residues undergoing chemical shift changes (red region) upon C_{60} binding. [39]

Tryptophan quenching analysis showed that fullerene is able to completely quench the protein emission upon interaction with protein, demonstrating that all the LSZ molecule are present in solution as hybrid C_{60}@LSZ, and the stoichiometry of the adduct is 1:1.
For the first time using lysozyme and C_{60} as model systems and NMR chemical shift perturbation analysis, a protein-CNP binding pocket was identified unambiguously in solution and the effect of the binding, at the level of the single amino acid, was characterized by a variety of experimental and computational approaches.

AIM OF THE STUDY

The goal of this study is to achieve a stable and monodispersed fullerene@protein hybrid which can be used as sensitizer in photodynamic therapy.
The ability of lysozyme to disperse C_{60} in water was already demonstrated,[39] but the possible presence of aggregates, upon the interaction, cannot be excluded. To evaluate the limits where C_{60}@LSZ can be considered stable in aqueous media, an extensive characterization about different ionic strength and pH is required.
The monodispersion of fullerene in aqueous media is a necessary requirement for its use in photodynamic therapy, but the preservation of the photophysical properties of fullerene upon the interaction with the protein needs to be investigated.

2.3 C_{60}@LYSOZYME CHARACTERIZATION

C_{60}@LSZ adduct was synthetized and purified following the procedure described in the experimental section. These conditions were optimized to maximize the amount of C_{60}@lysozyme in water and, at the same time, to avoid proteins modification. Comparing the absorption spectra of pure LSZ and C_{60}@LSZ (Figure 8), it is possible to identify the presence of C_{60} from its diagnostic band centered at 340 nm.

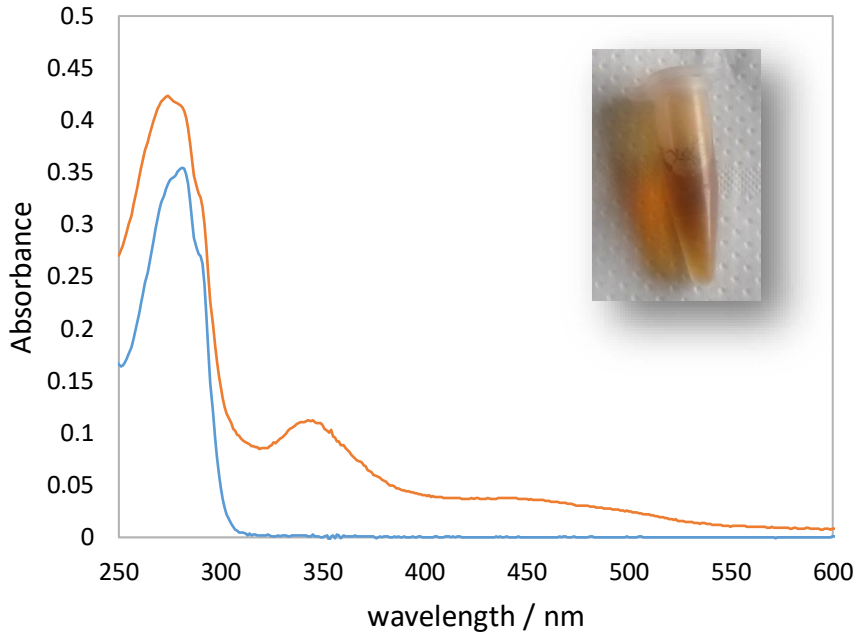

Figure 8. UV-Vis spectra of LSZ (blue) and purified C_{60}@LSZ hybrid (orange). Inset: picture of the purified C_{60}@LSZ hybrid solution.

2.3.1 ATOMIC FORCE MICROSCOPY

Atomic Force Microscopy (AFM) analysis (see appendix) were performed to detect the possible presence of aggregates into the C_{60}@LSZ dispersion. Comparing the topography of LSZ

(reference) and C_{60}@LSZ (sample) it is possible to affirm that in both the cases the systems were well monodispersed (Figure 9).

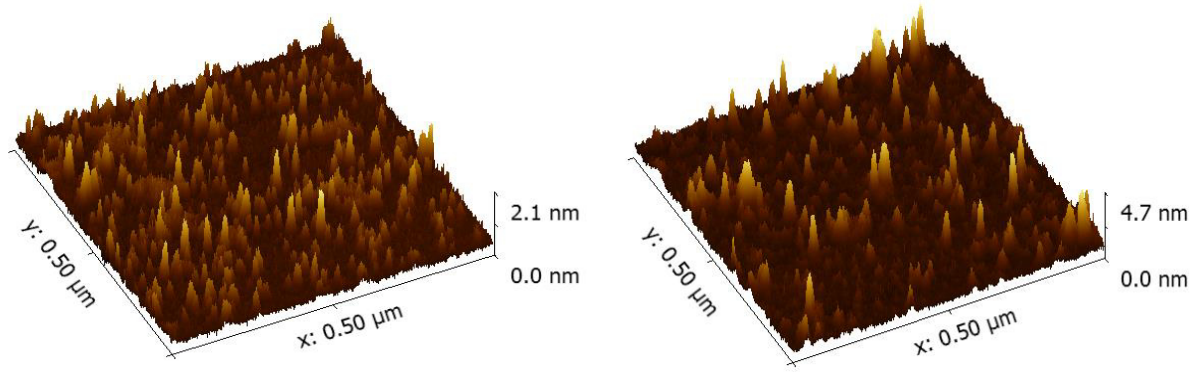

Figure 9. Topographic analysis performed by AFM using tapping-mode. Left: lysozyme. Right C_{60}@lysozyme.

The results perfectly matched the data found in literature in regard of AFM analysis performed on lysozyme (average sizes 3 x 3 x 4.5 nm).[41] A slight difference can be found between the two experiments: because of the introduction of the highly hydrophobic fullerene, the hybrid C_{60}@LSZ could rearrange its conformation over the hydrophilic surface to minimize the repulsive interactions. As a consequence, an increase of the medium height occurred, but the average size was still compatible to the regular sizes obtained from pure lysozyme.[41]

AFM analysis demonstrated that for high diluted sample, no drying effect were observed. Both the reference and the hybrid system were monodispersed. It is uncertain, but it cannot be excluded, the involvement of the surface on possible C_{60}@LSZ clusters disaggregation.

2.3.2 Cryo-Transmission Electron Microscopy

A different approach was used to evaluate the monodispersity of C_{60}@LSZ hybrid. Cryo-Transmission Electron Microscopy sample preparation consists in the instantaneous vitrification of the biological solution over the grid. This procedure prevents drying effects and surface related phenomena, allowing to “catch” an instantaneous condition of liquid solution.

A representative acquired image, shown in Figure 10, confirmed what was previously observed by AFM: each darker spot represents the single C_{60}@LSZ hybrid and no aggregate was found over the grid.

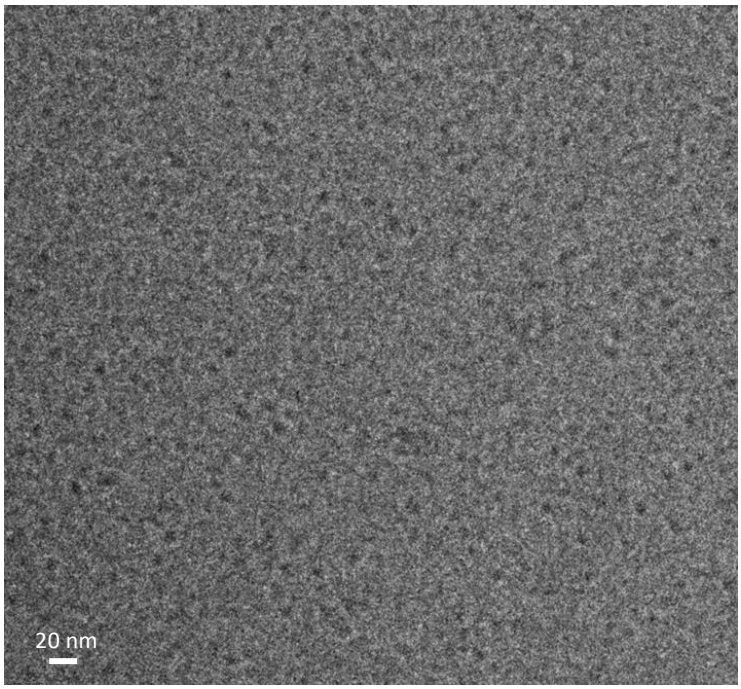

Figure 10. Cryo-TEM picture of vitrified C_{60}@LSZ 100 μM, supported on graphene oxide.*

*This measurement were conducted by our collaborator, prof. Nico Sommerdijk, at Laboratory of Materials and Interface Chemistry (Eindhoven University of Technology, Netherland).

2.3.3 High-Resolution Synchrotron Powder X-ray Diffraction Analysis

C_{60} fullerene exists as solid crystalline and the unit cell of solid C_{60} is known to be face-centered cubic (fcc). For most of applications in aqueous media, fullerene is used as nanocrystals (nC_{60} and nC_{70}, Figure 11) by means of solvent-exchange methods, surfactant assisted stabilization, supramolecular host-guest systems and mono-derivatization *etc* (see section 2.1.2).

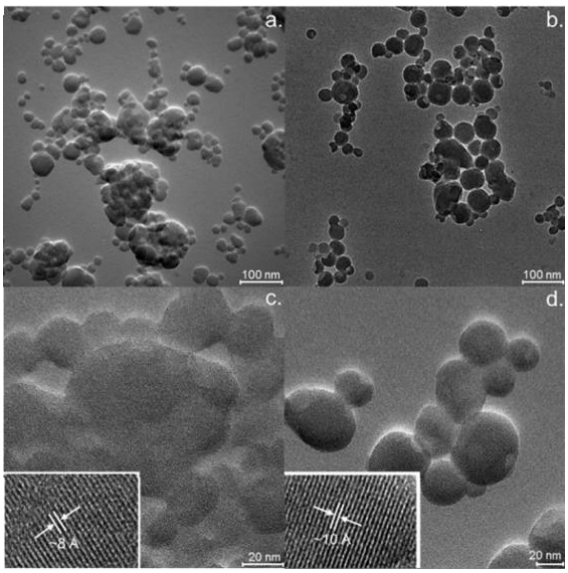

Figure 11. TEM images of (a and c) nC_{60} and (b and d) nC_{70}, including insets with magnified views depicting crystal lattice fringes. Inset: high-resolution lattice image of fullerene nanoparticles.[29]

X-ray powder diffraction (XRD) is the best technique which gives information about the possible presence of fullerene nanoclusters because over a minimum cluster size they show their typical diffraction pattern.

For aqueous dispersible fullerene nanocrystals (nC_{60}) produced by solvent exchange method, the diffraction pattern perfectly overlap the original diffraction pattern of solid C_{60} powder. A broadening effect associated to the nanocrystal peaks, highlights the reduced size of crystal domains respect to the starting material (Figure 12, left).

For what concerns the supramolecular host-guest system, in particular the γ-cyclodextrin, which is considered the best host molecule for C_{60}, there is a significant loss of peaks sharpness but it is still possible to assign each residual peak to the characteristic diffraction pattern of fullerene solid crystalline (Figure 12, right).

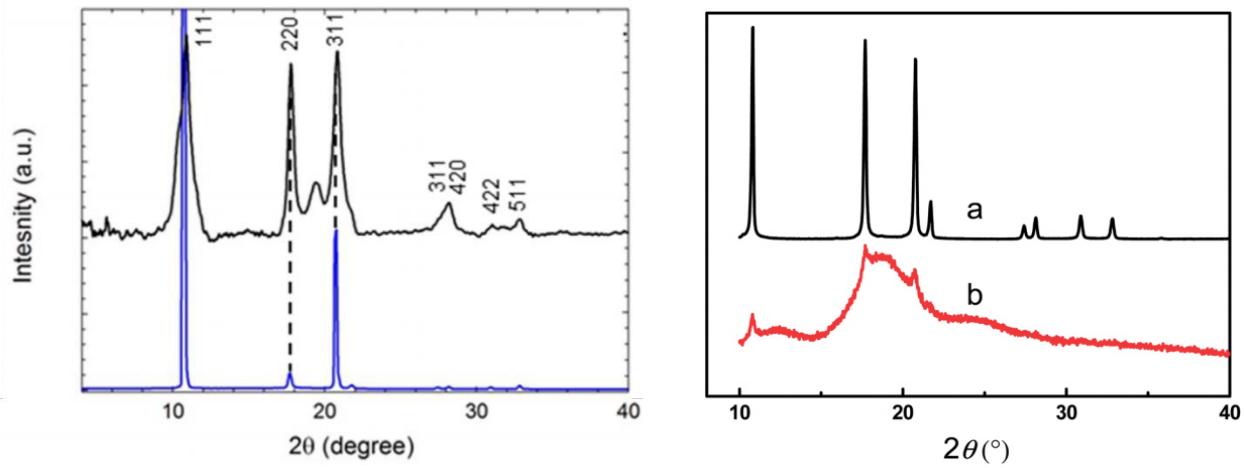

Figure 12. Left: Diffraction patterns of C_{60} (blue) and nC_{60} (black). [29] Right: Powder X-ray diffraction patterns of (a) C_{60} and (b) C_{60}@γ–cyclodextrin.[25]

In this work, the presence of C_{60}@LSZ aggregates was excluded by different microscopic techniques. To exclude also the possible presence of fullerene clusters in solid form, XRD analysis were performed.

Freeze-drying dehydration was carried out on C_{60}@LSZ solution. The resulting powder was analyzed by high-resolution synchrotron powder X-ray diffraction at a dedicated synchrotron beam line (HRPXRD, see experimental section).

Comparing the diffraction patterns of the C_{60}@LSZ (green), the negative reference of lyophilized lysozyme (blue) and the positive reference of C_{60} powder it can be observed that the lyophilized sample does not show any residual peak related to crystalline fullerene powder. Both lyophilized LSZ and C_{60}@LSZ result amorphous, as expected (Figure 13).

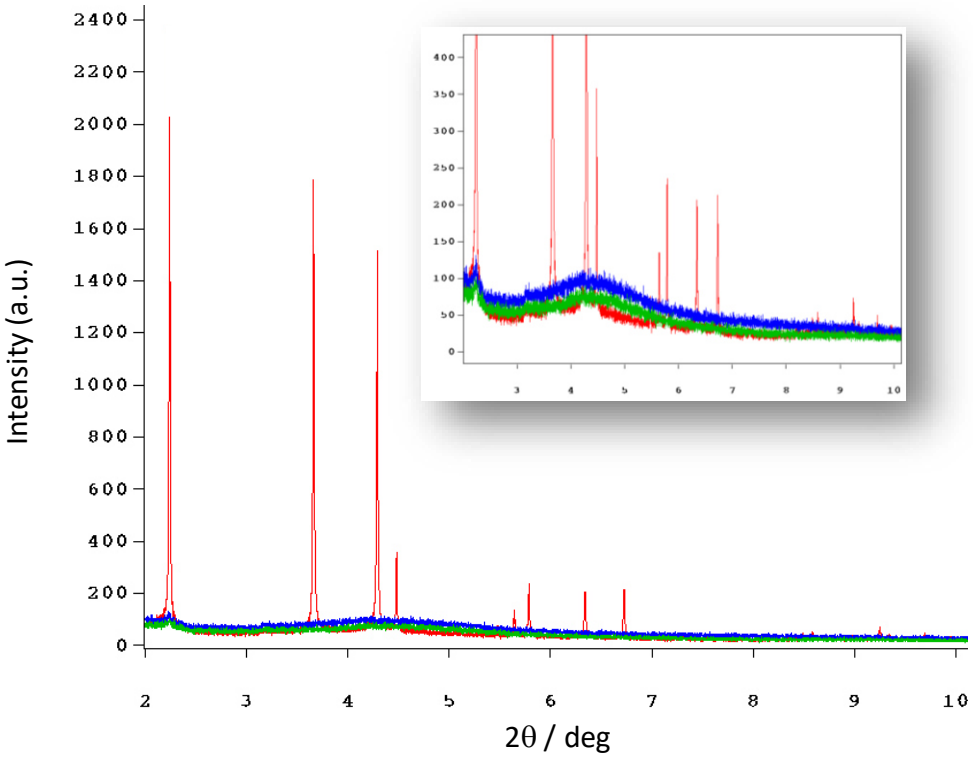

Figure 13. HRPXRD patterns of: C_{60}@LSZ powder (green), negative reference of lysozyme (blue), positive reference of C_{60} powder (red).

HRPXRD characterization demonstrated that:

i. there are no fullerene aggregates in C_{60}@LSZ hybrid system;
ii. it is possible to store fullerene single molecules as solid powder.

Freeze-drying dehydration is not a destructive treatment. On the contrary, re-dispersion of the powder in water was completely reversible. No precipitate was found upon dissolution and the standard characterization conducted on re-dispersed solution showed the same data (UV-Vis) obtained before the freeze-drying.

2.3.4 C_{60}@Lysozyme Stability in Aqueous Media

All the previous analysis were carried out on C_{60}@LSZ dispersed in milliQ water. In this section, a step further has been done, exploring the stability of the hybrid system at different pH and ionic strength conditions, to evaluate the limits where C_{60}@LSZ can be considered stable.

pH effect

To test the ability of lysozyme to disperse C_{60} at different pH, lysozyme solution was prepared and split in different tubes where each sample was set up at different pH (from 2.5 to 13). pH adjustment were set up using NaOH and HCl, respectively. In this way it is more difficult to reach a specific pH value but it is possible to exclude the influence of different buffers ions.

After fullerene powder addition, the adducts were prepared as per protocol. It was immediately evident that basic conditions destabilized the protein, in fact a white coagulation appeared for the highest pH value (pH 13).

Comparing the different samples by UV-Vis analysis (Figure 14) and following the absorbance at 340 nm (where the absorbance is proportional to the fullerene concentration) it was found that for all the acidic range of explored pH, lysozyme was able to disperse fullerene in water. The amount of fullerene dispersed was similar to that one obtained in pure water.

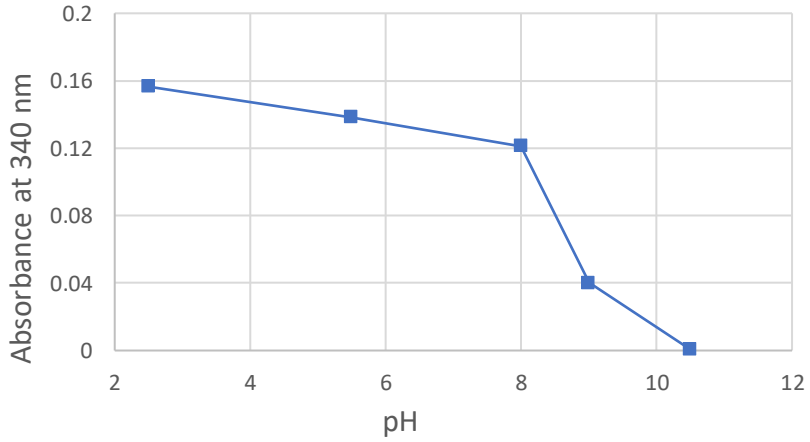

Figure 14. UV-Vis quantification of C_{60} dispersed in water by lysozyme at different pH values. Absorbance at 340 nm is diagnostic for fullerene.

During the sonication process, proteins undergo to a significant stress. In the specific case of lysozyme, which is a very compact and stable protein (it contains 4 disulfide bridges), it was already demonstrated that the sonication in milliQ water doesn't affect their structure and functionality.[39] A possible explanation to this behavior at different pH values is related to the colloidal nature of lysozyme: for a pH value closer to the isoelectric point of lysozyme (pI~11), where the net charge is zero, there is the minimal electrostatic repulsion among proteins which favors aggregation phenomena during the sonication.

To understand in which range of pH C_{60}@LSZ hybrid was stable, a single batch of the adduct was prepared as per protocol (in milliQ water), it was split in different aliquots and then, the pH of each solution was adjusted at different pH values (with HCl and NaOH), exploring the range from 1.5 to 13.

It can be noticed that for most of the pH values, the absorption spectra of C_{60}@LSZ hybrid resulted insensitive to the different environments. The absorption spectra acquired in the range from 1.5 to 9 are perfectly superimposable (Figure 15). Differently, for both the pH values 11 and 13, C_{60}@LSZ precipitates immediately after the pH adjustments.

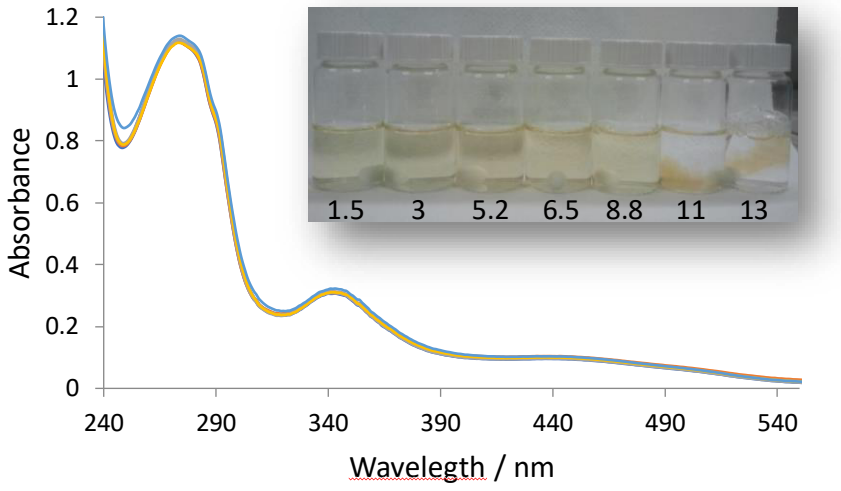

Figure 15. UV-Vis absorption spectra (overlapped) of C_{60}@LSZ obtained at the following pH values: 1.5, 3, 5.2, 6.5, 8.8. Inset: picture of the analyzed samples.

The hybrid C_{60}@LSZ stability is governed by LSZ properties. In fact, the minimum stability of the hybrid occurred for pH values close to the isoelectric point of the protein, where the net charge is not high enough to prevent the electrostatic repulsion, so aggregation took place.

ZETA POTENTIAL

A key feature for CNMs application in biological media is their ability to remain well suspended also in presence of electrolytes. Nowadays, it can be obtained a stable aqueous (pure water) dispersion of CNMs, especially upon chemical derivatization. But, in most of the cases, upon the addition of an electrolyte, the zeta-potential drop down, causing their aggregation.[42,43]

Ionic strength dependency of C_{60}@LSZ was evaluated through zeta potential analysis (see appendix). A wide range of electrolyte concentration was studied, from 1 μM to 1 M of sodium chloride (Figure 16).

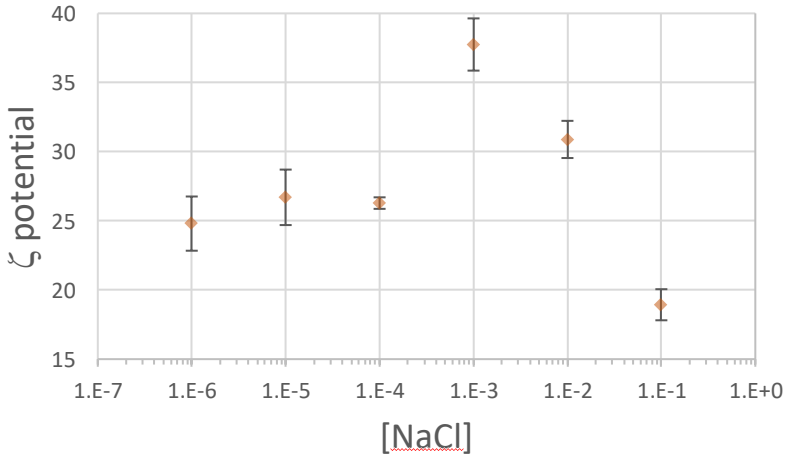

Figure 16. Ionic strength - zeta potential relation of C_{60}@LSZ, produced using different concentrations electrolyte (NaCl).

For low concentrations (1 μM – 100 μM), NaCl did not perturb the zeta potential of the hybrid system. For a salt concentration corresponding to the same (molar) concentration of C_{60}@LSZ,

there was a significant stabilization effect, commonly known as salting in. In fact, 1 mM of NaCl was the best compromise for C_{60}@LSZ stabilization.

C_{60}@LSZ resulted stable for higher ionic strength until 0.1 M of NaCl, where a lowering of zeta-potential occurred. This condition conferred metastability to the hybrid system, showing aggregation phenomena only after few hours. The high ionic strength causes a decrease of the solvating power of the salt ions (salting out), indeed, an instantaneous precipitation of C_{60}@LSZ occurred in presence of 1 M NaCl.

To compare the zeta potential with a standard reference, C_{60}@γ-cyclodextrin complex was prepared. The protocol optimized to produce C_{60}@LSZ was followed with the only difference about the stoichiometry (considering that fullerene is bicapped by cyclodextrin).

Comparing the absorption bands at 340 nm, it is possible to observe that γ-cyclodextrin is able to "solubilize" an amount of fullerene which is about 8 times lower respect to the lysozyme (Figure 17). Moreover, upon 1 mM of NaCl addition, the supramolecular system instantaneously precipitated, preventing the possibility to compare the zeta-potential characterization with C_{60}@LSZ.

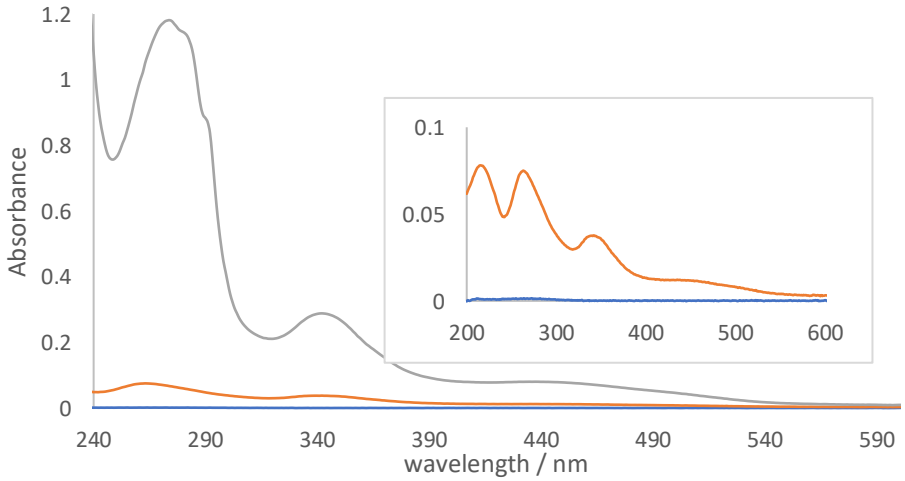

Figure 17. Absorption spectra of C_{60}@LSZ (grey), C_{60}@γ-cyclodextrin (orange) and γ-cyclodextrin (blue). Inset: magnification of C_{60}@γ-cyclodextrin and γ-cyclodextrin absorption spectra.

Evaluating the behavior of C_{60}@lysozyme in different pH and ionic strength conditions, it was found that the stability of the hybrid in aqueous media was governed by the protein. Further investigations were performed to check if fullerene properties as photosensitizer was still preserved, also upon binding with the protein.

2.4 Potential Application in Photodynamic Therapy

Among reactive oxygen species, hydrogen peroxide (H_2O_2) is the most important in regards to mitogenic stimulation or cell cycle regulation.[44] It has a relatively long lifetime (seconds to minutes) compared to the other ROS, whose lifetimes are only fractions of seconds. Consequently, H_2O_2 is less reactive than the other ROS, and it can easily transformed into water by catalase and peroxidase, making it an important messenger in ROS signaling cascade.[44]
On the other hand, H_2O_2 can be toxic to the cells because it is able to produce the highly reactive hydroxyl radical, which can initiate an H_2O_2-generated chain reactions. The relatively long-lived H_2O_2, produced from $O_2^{\cdot -}$, act as free radical carrier that can migrate long distances.
Considering the fundamental role of H_2O_2 as intermediate and as precursor of different ROS at the same time, and taking into account its long-lived lifetime, it is commonly used as representative species for ROS quantification. Moreover, for preliminary tests in buffers and unsupplemented media, hydrogen peroxide lifetime is even longer, because of the absence of catalase and oxidase enzymes.

There are a number of fluorogenic substrates to detect H_2O_2, which serve as hydrogen donors that have been used in conjunction with horseradish peroxidase (HRP) enzyme to produce intensely fluorescent products. While the list is quite extensive, the more commonly used substrates include diacetyldichloro-fluorescein, homovanillic acid and Amplex® Red. Apart from H_2O_2, specific dyes molecule are available to detect each specific ROS.[45]

2.4.1 TMB Test

A number of colorimetric substrates such as tetramethylbenzidine (TMB) and phenol red have also been used in conjunction with HRP to measure hydrogen peroxide concentrations through UV-Vis spectroscopy. In general, colorimetric means are less sensitive than fluorescent detection methods, but instrumentation costs are significantly lower than those required for fluorescence based

measurements, the results are more reproducible and they are particularly suitable for screening tests.

TMB test was used to study the ability of C_{60}@LSZ to produce hydrogen peroxide upon irradiation. A specific protocol, based on different existing procedure,[46] was developed (see experimental section). Using an excess of TMB, the absorption bands with maximums at 370 nm and 650 nm are diagnostic for H_2O_2. Absorption band centered at 650 nm was chosen as diagnostic band, to avoid the overlap with fullerene absorption tail (Figure 18).

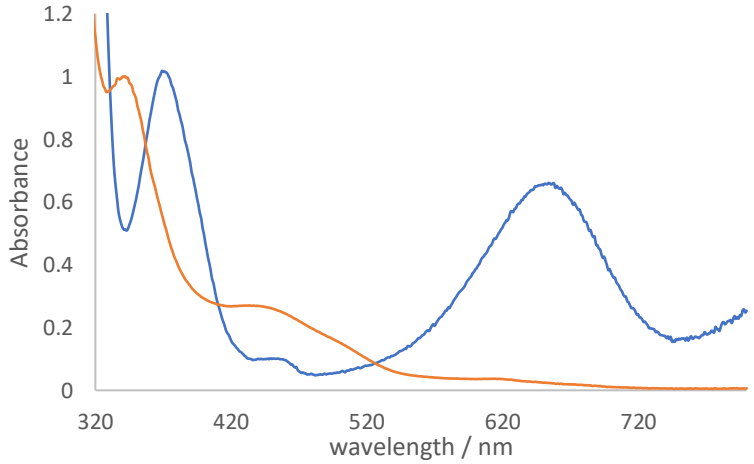

Figure 18. Absorption spectra of TMB one-electron oxidation product (blue) and C_{60}@LSZ complex (orange).

Preliminary tests were carried out using the high power visible light source. To evaluate a possible contribution of the dissolved oxygen, one set of experiments was performed saturating the solutions with oxygen gas. Lysozyme and sonicated lysozyme solutions were used as refences. Comparing the absorbance at 650 nm it was possible to find the best conditions to perform the next experiments (Figure 19).

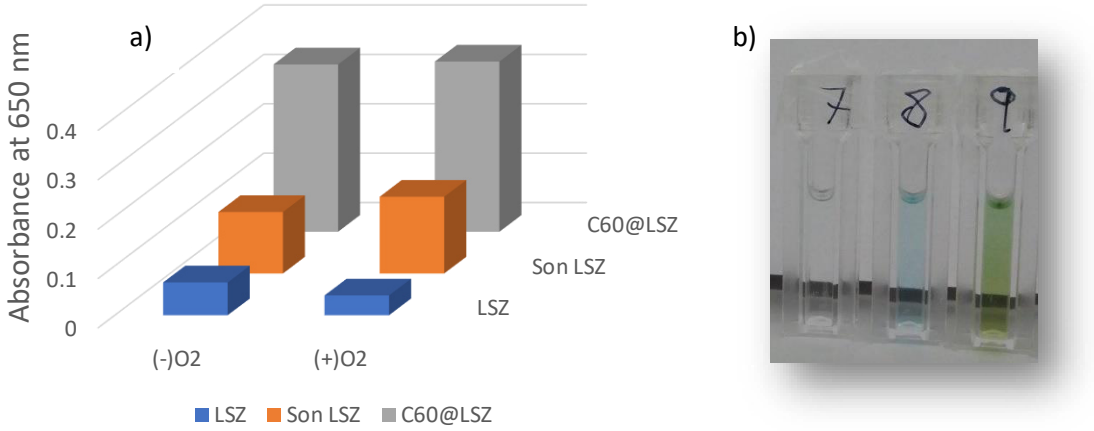

Figure 19. a) concentration of H_2O_2 produced upon irradiation of LSZ (blue), sonicated LSZ (orange) and C_{60}@LSZ (grey), estimated by the absorbance of the oxidized TMB (at 650 nm). The solutions were irradiated by a visible lamp with (+) and without (-) O_2 saturation. b) picture of the samples (without oxygen saturation) after irradiation. From left to right: LSZ, sonicated LSZ, C_{60}@LSZ.

Some consideration can be deduced from the results:

i. The solution of C_{60}@LSZ produced H_2O_2 only after irradiation;
ii. Oxygen saturated solutions did not enhance the amount H_2O_2 produced;
iii. Sonicated lysozyme showed a moderate amount of hydrogen peroxide;
iv. Irradiated lysozyme produced a negligible amount of H_2O_2 (close to the limit of detection).

Investigating the unexpected results about H_2O_2 production observed for sonicated LSZ samples, it was possible to understand the nature of this behavior. Hydrogen peroxide production did not significantly depend by the protein itself but it can be ascribed to the sonication process. This effect was also confirmed carrying out the same TMB test on sonicated water (positive control) and not sonicated water (negative control).

To exclude this nonspecific contribution of H_2O_2, centrifugal filtration washing step was performed upon sonication process. It consisted of successive washes of native and hybrid proteins, using a 3 kDa size pores membrane, to selectively removes H_2O_2. Upon the 3 washes, TMB test performed on the recovered protein solutions demonstrated that no more H_2O_2 was still detectable.

Following the optimized procedure, the production of H_2O_2 was evaluated as a function of the time for which C_{60}@LSZ was irradiated. H_2O_2 production were measured following the absorbance at 650 nm (Figure 20).

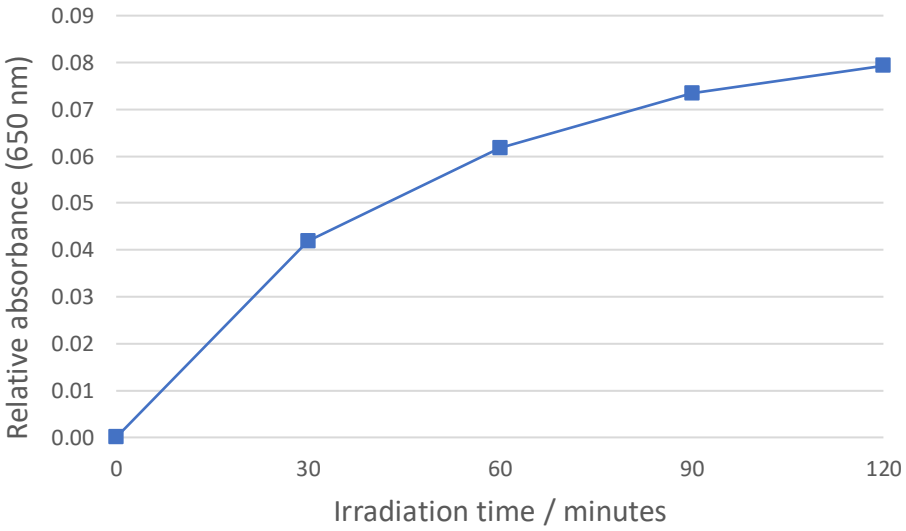

Figure 20. H_2O_2 production upon irradiation of C_{60}@LSZ solution, followed by mono-oxidized TMB absorption band (650 nm).

Based on the extinction coefficient of the mono-oxidized TMB species at 650 nm,[46] an estimated concentration of H_2O_2 produced by 100 μM of C_{60}@LSZ in water, after 2 hours of irradiation, corresponds to 15 μM.

Taking into account the stability of the C_{60}@LSZ hybrid in a wide explored range of pH, H_2O_2 production at different buffered pH conditions was also investigated. Here, a closer range was explored, from acidic to physiological pH. As well as the previous experiment, H_2O_2 produced after the irradiation was evaluated comparing the absorbance of the mono-oxidized TMB at 650 nm (Figure 21).

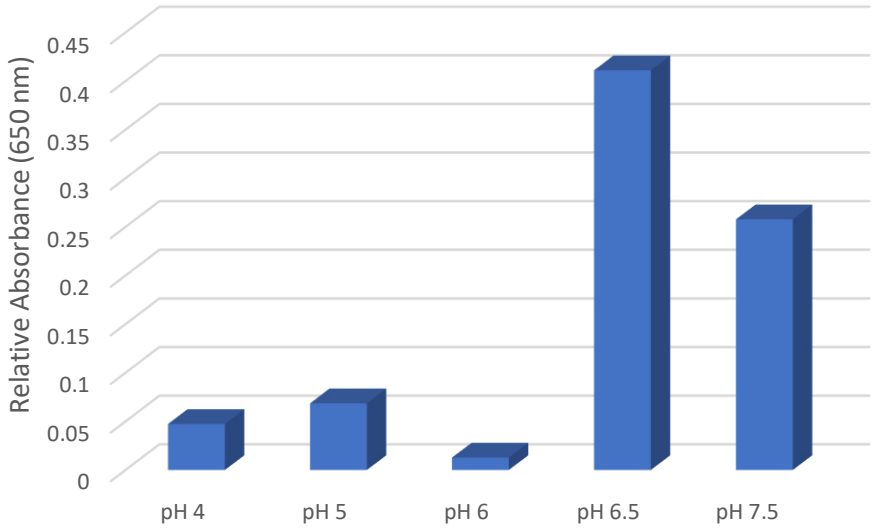

Figure 21. H_2O_2 production upon irradiation of C_{60}@LSZ solution at different pH values, followed by mono-oxidized TMB absorption (650 nm). Buffers: glycine pH 4, sodium citrate pH 5, sodium malonate pH 6, HEPES pH 6.5, HEPES pH 7.5 .

An essential role of pH conditions was identified by this characterization. Lower pH values showed a net decrease of hydrogen peroxide concentration, while for pH closer to the neutrality (HEPES), the H_2O_2 detected were significantly higher.

The pH-dependency of H_2O_2 production is still not completely understood. However, this characterization showed that in physiological conditions and (only) upon irradiation, C_{60}@LSZ hybrid was able to produce H_2O_2.

H_2O_2 is an intermediate for most of the ROS species. Even if its quantification underestimate the effective amount of ROS produced, it is useful to understand how different experimental setups can influence the ROS production efficiency.

We selected a UV-Vis quantification method because it is the most versatile and reproducible approach. In addition, TMB test doesn't show a significant background signal and gives the opportunity to use a wide range of absorption spectra to quantify the H_2O_2.

2.4.2 Singlet Oxygen Emission

Singlet oxygen detection can be performed using different approaches (fluorescent probes, EPR, NIR emission). Near infrared fluorescence of singlet oxygen has the main advantage to be a direct measurement (it does not require chemical reactions with specific probes) and it is not sensitive to the other ROS.

Compared to C_{60} dispersed in toluene, the emission band of C_{60}@LSZ (Figure 22) was slightly red-shifted (~5 nm) and its relative intensity resulted 7.5 times lower. Different polarity of the solvents (and consequently, the relative solubility of molecular oxygen) significantly affected the fluorescence intensity.

However, this qualitative analysis showed that type II mechanism of ROS production is also involved, demonstrating one more time that protein assisted dispersion of C_{60} in aqueous solution preserves the photosensitizing activity of fullerene.

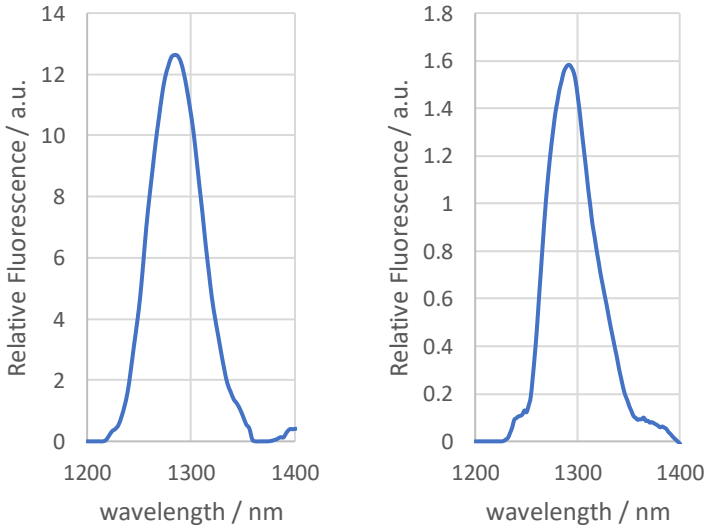

Figure 22. Corrected NIR emission of singlet oxygen produced upon excitation (λ = 514 nm) of C_{60} in toluene (left) and C_{60}@LSZ in water (right).

2.4.3 *In Vitro* Studies

PHOTODYNAMIC TREATMENTS

To evaluate the efficacy of C_{60}@LSZ hybrid system and its potential applications in photodynamic therapy, *in vitro* tests were performed (in collaboration with prof. Rapino group). Human cervical adenocarcinoma (HeLa) cell line was used as *in vitro* model to perform the experiments.

Exploring the range between 0.1 to 100 μM (final concentration) of C_{60}@LSZ and LSZ as reference, after one hour of irradiation with a low intensity visible light source (Figure 23), it was found that:

i. irradiated cells with C_{60}@LSZ showed a mortality level significantly higher than the analogues kept in dark;
ii. lysozyme (reference) did not affect the normal vitality of the cells, demonstrating that the protein itself is nontoxic in this range of concentrations;
iii. the half maximal inhibitory concentration (IC_{50}) value was identified for 3.75 μM of irradiated C_{60}@LSZ;

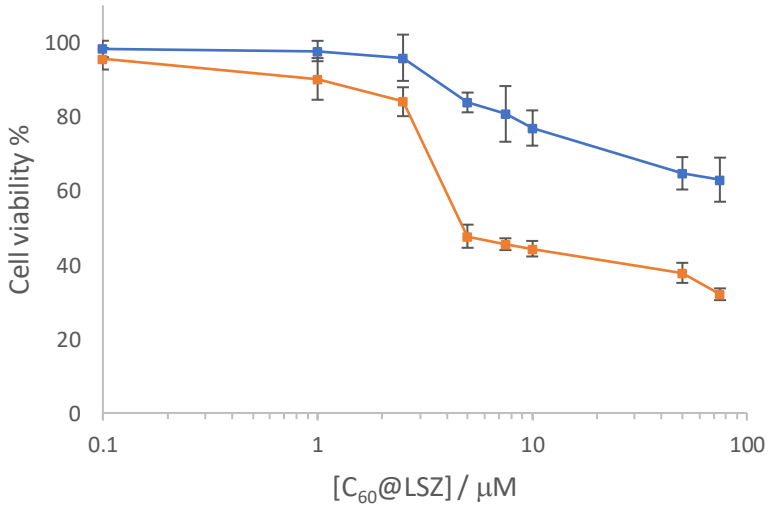

Figure 23. Concentration dependency of C_{60}@LSZ cytotoxicity in dark (blue) and under one hour of irradiation (orange), with a low power light source. Each value represents the mean value ± standard deviation of three experiments.

The choose of a low power intensity light source assured the neutral effect of the lamp during the irradiation. The potential application of C_{60}@LSZ hybrid system as photosensitizer in photodynamic therapy was better represented by an high power visible light, which permitted to be efficacy in a shorter irradiation time.

One sample without C_{60}@LSZ was used as control to monitor the possible toxic effect induced by the high intensity of irradiation, while in the other sample, 5 μM of C_{60}@LSZ was incubated. The cell viability in the control didn't show any variation upon 10 minutes of irradiation while in presence C_{60}@LSZ, after the same exposure time, a significant decrease of the cells viability was observed (Figure 24), corresponding to an average value of 37% (Figure 25).

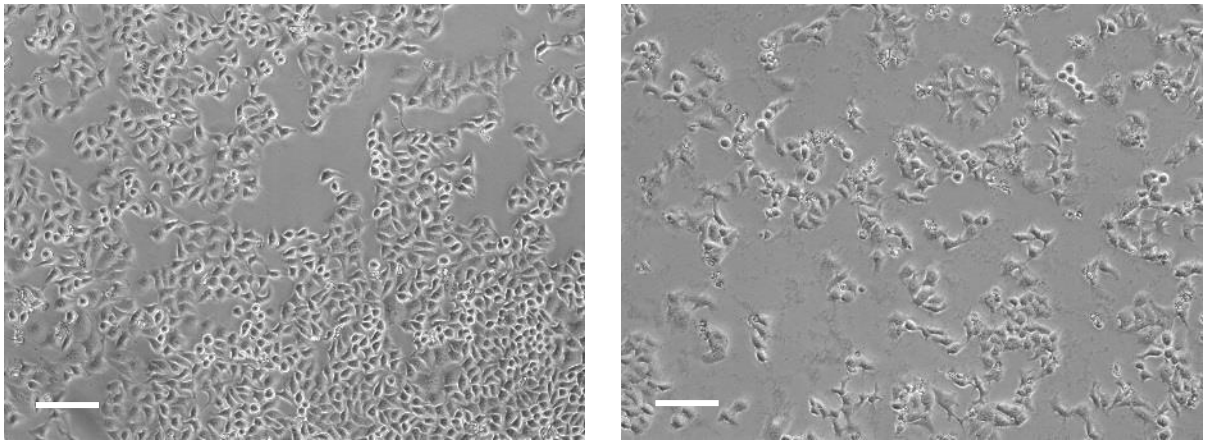

Figure 24. Phase contrast images of HeLa cells in absence (left) and in presence (right) of 5 μM of C_{60}@LSZ upon 10 min of irradiation. (Scale bar: 2.5 μm).*

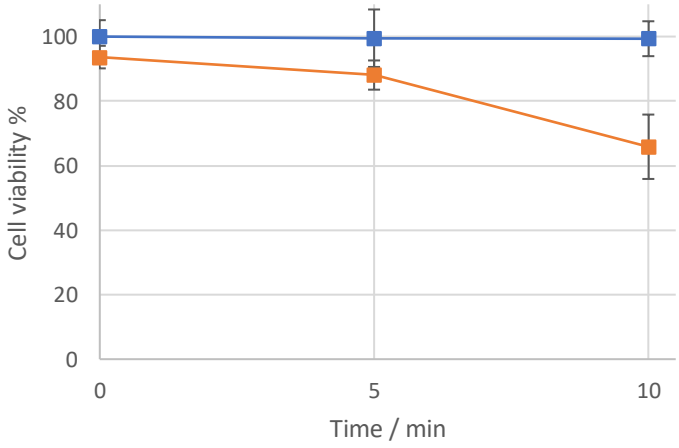

Figure 25. Effect on cell viability upon short time irradiation with high-power source. Samples are either in absence (cyan) or in presence (orange) of 5 μM of C_{60}@LSZ. Each value represents the mean value ± standard deviation of three experiments.*

Longer exposure times were also explored but the consecutive time points showed a decrease of the cell viability also for the untreated cells. Nevertheless, the cell viability gap between the control and the C_{60}@LSZ treated cells progressively increased for longer time of exposure.

MEASUREMENT OF REACTIVE OXYGEN SPECIES

The measurement of intracellular ROS was based on the oxidation of 2,7-dichlorohydrofluoroscein diacetate (DCFH-DA). 5µM of C_{60}@LSZ sensitizer and LSZ (reference) were incubated into the cells, which were then irradiated for 10 minutes with the high power light source, as well as for the untreated cells (blank). The same conditions were used for the non-irradiated samples (dark). The resulting fluorescence intensites estimates the amount of intracellular ROS produced. Among the explored conditions, the oxidative stress produced by C_{60}@LSZ to the cells upon irradiation was significantly higher than all the relative controls (Figure 26). As mentioned before, ROS sensitive fluorescent probes usually show a significant background signal.

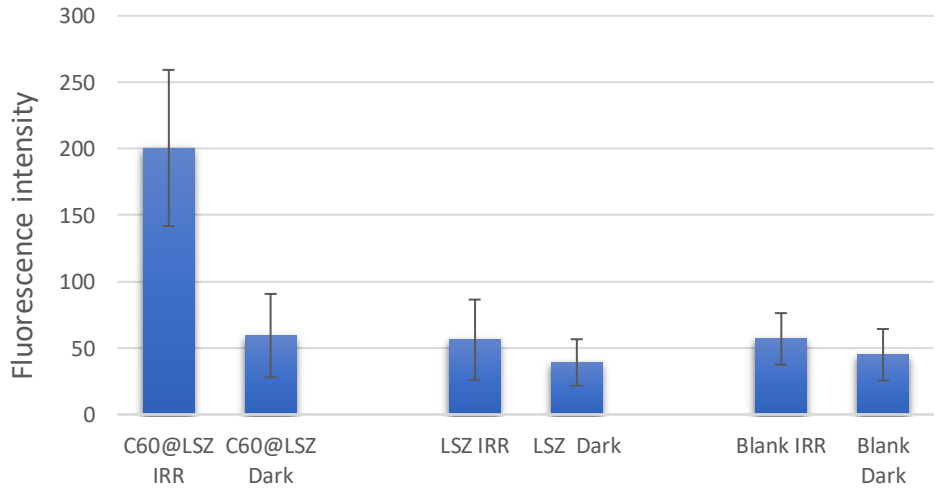

Figure 26. Fluorescence intensity of DCF acquired by fluorescence microscope (494 nm excitation, 518 nm emission filter) on treated (C_{60}@LSZ and LSZ) and untreated (Blank) cells. Each condition were performed in dark and under irradiation.*

*Thanks to Dr. Alice Soldà for *in vitro* tests

A positive control was obtained incubating 200 μM of H_2O_2 with the cells for 0.5, 1.5 and 3 hours (see experimental section, Figure S2). Comparing the fluorescence intensities, it was observed that the oxidative stress induced by C_{60}@LSZ to the HeLa cells upon irradiation was comparable to the effect obtained after 2 hours from the H_2O_2 incubation.

Performing the *in vitro* experiments it can be unambigously affirmed that C_{60}@LSZ hybrid system is an efficient sensitizer for photodynamic therapy. Its toxic effect resulted highly selective since C_{60}@LSZ showed an high production of reactive oxygen species only after the irradiation. The negative results showed by the uncomplexed protein demonstrated that the ROS production activity of the hybrid is ascribed to C_{60}.

2.5 New Fullerene@Protein Hybrids

Further improvements to fullerene@protein systems are under investigation. The goal is to obtain a new hybrid photosensitizer which is able to absorb in a wider range of visible light. Different approaches could be used for this scope:

i. Substituting C_{60} with other fullerenes which have a wider absorption spectra in the visible range;
ii. Functionalizing proteins with dyes acting as antennas for fullerene;
iii. Using fullerene@hemeproteins hybrid systems, that already contains a strong visible absorber (prosthetic heme group) and which could be needed as electron donor for fullerene.

Preliminary experiments carried out to produce new fullerene@protein hybrid photosensitizers will be briefly reported.

2.5.1 C_{70}@LYSOZYME

C_{70} shape as a rugby ball with a diameter included between 7 and 9 nanometers, so very similar to C_{60}. Nevertheless, their optical properties are slightly different: C_{70} shows an higher absorption coefficient in all the visible spectral range.

The same protocol was used to disperse C_{70} by lysozyme. The resultant UV-Vis spectrum (Figure 27) showed a similar behavior to C_{60}@LSZ, with the main advantage to absorb the light in most of the visible spectral range.

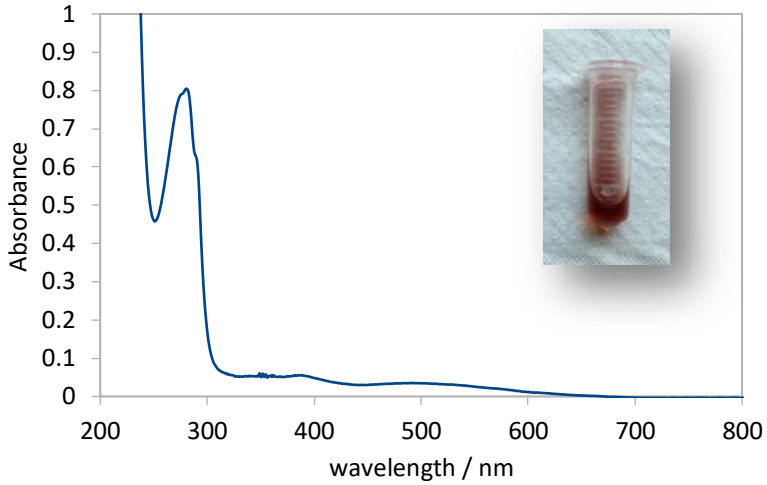

Figure 27. Absorption spectrum of C_{70}@lysozyme.

2.5.2 C_{60} DISPERSION BY ALTERNATIVE PROTEINS

A computational study carried out by Calvaresi et al.[47] used a validated reverse docking protocol to identify the best protein target candidates for C_{60} binding, picked up among the full list of the protein data bank (PDB).

An experimental screening test was performed on few of the top 10% listed proteins, choosing the most abundant, easy to purify and well characterized proteins. The preliminary screening was performed using the standard sonication and purification protocol, followed by the UV-Vis characterization to detect the possible presence of C_{60} dispersed in water.

The subsequent proteins were tested as potential carrier of C_{60}:

- ✓ Trypsin
- ✓ Thrombin
- ✓ Pepsin
- ✓ Human serum albumin

- ✓ Myoglobin
- ✓ Cytochrome C

- \- Lipase
- \- Papain

All the tested protein succeeded to disperse C_{60} except for lipase and papain. Observing the diagnostic band of fullerene (340 nm) it is clear that, among the first group, all the proteins showed a better tendency to bind C_{60} than lysozyme, except for thrombin (Figure 28).

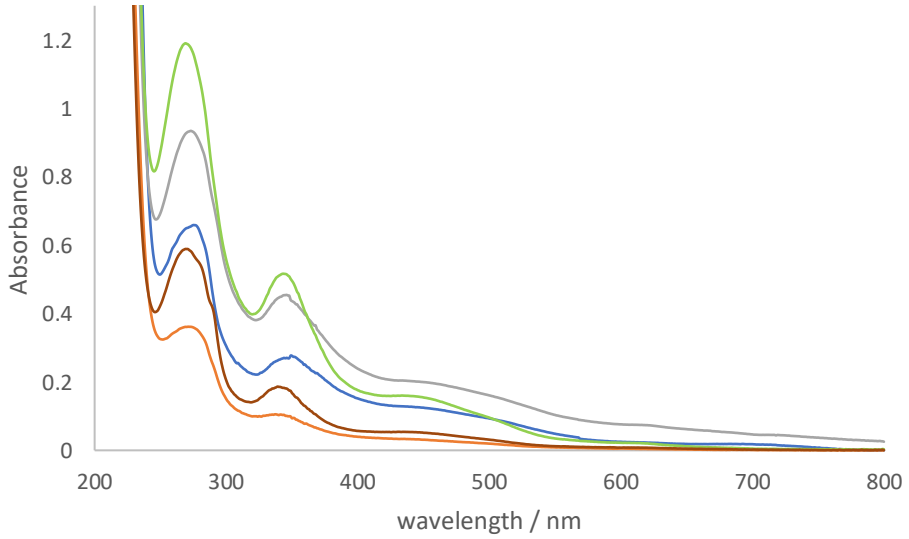

Figure 28. Absorption spectra of C_{60}@HSA (blue), C_{60}@thrombin (orange), C_{60}@trypsin (grey), C_{60}@pepsin (green), C_{60}@lysozyme (brown).

Myoglobin and cytochrome C are hemeproteins, so they show an intense absorption band (Soret band) around 420 nm (Figure 29). Both the proteins were able to disperse fullerene in water.

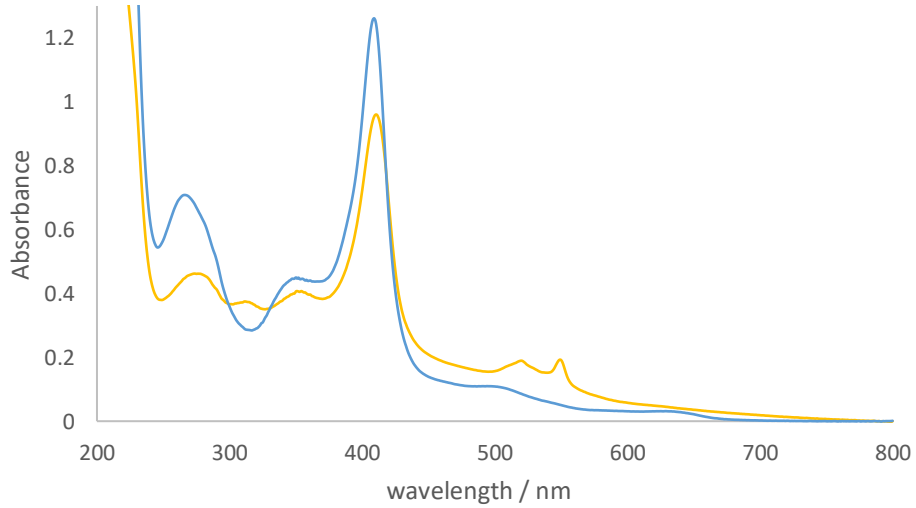

Figure 29. Absorption spectra of C_{60}@cytochrome C (yellow) and C_{60}@myoglobin (blue).

Subtracting the protein contribution to the absorption spectra, it is possible to compare the ability of each protein to assist the dispersion of C_{60} in water (Figure 30). Compared to γ-cyclodextrin, all the tested proteins resulted much more efficient to disperse fullerene. The subtracted spectra of a representative group of proteins and C_{60}@γ-cyclodextrin perfectly overlap, showing the contribute to the absorption spectra of the C_{60}.

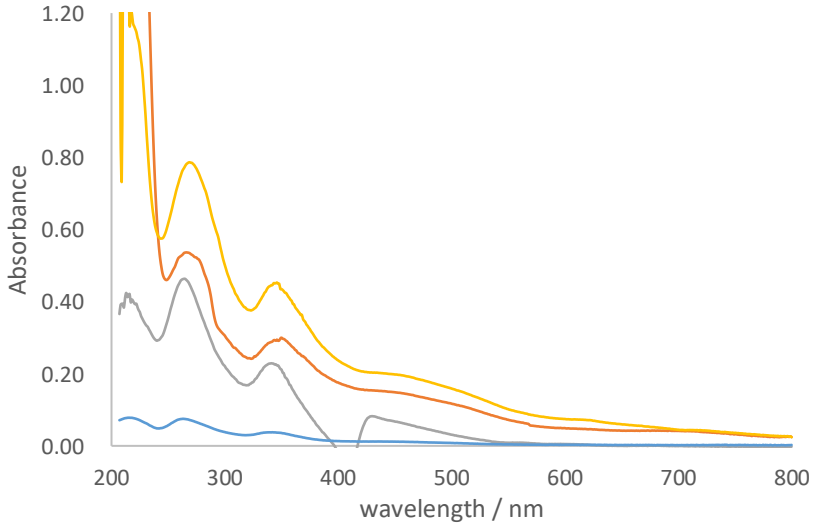

Figure 30. C_{60} absorption spectra obtained subtracting the protein contribution from the complexes: C_{60}@HSA (orange), C_{60}@myoglobin (grey), C_{60}@trypsin (yellow). C_{60}@γ-cyclodextrin is shown as reference (blue).

CONCLUSIONS

The unique photophysical, chemical and electrochemical properties of C_{60}, the most representative member of fullerenes category, made it a promising candidate for possible uses in different fields of biomedicine, in particular for photodynamic therapy. The lack of solubility in biological environment is the main obstacle in the development in this field, especially because fullerene properties and toxicity are strongly dependent to the aggregation phenomena.

In this work, non-covalent approach was used to disperse C_{60} in water by means of lysozyme. AFM, cryo-TEM and diffraction analysis demonstrated that C_{60}@LSZ hybrid is dispersed in water in monomolecular form. The stability of the adduct at different pH and ionic strength is governed by the protein. However, the fullerene properties as photosensitizer were still preserved also upon protein binding. Colorimetric and fluorimetric analysis were carried out to detect the production of reactive oxygen species (in particular, hydrogen peroxide and singlet oxygen) generated upon irradiation of C_{60}@LSZ.

To demonstrate the potential application of C_{60}@LSZ as sensitizer for photodynamic therapy, *in vitro* tests were performed on HeLa cells. The half maximal inhibitory concentration (IC_{50}) value was identified for 3.75 μM of irradiated C_{60}@LSZ, while in dark conditions the toxicity resulted much lower.

Lysozyme was used as model protein to understand the behavior of an hybrid fullerene@protein in aqueous media and to proof its ability to produce ROS upon light irradiation. New hybrids constituted by different fullerenes and different proteins are now under investigation to improve the sensitizing properties of the C_{60}@LSZ model.

The possibility to functionalize the protein with tags for cancer targeting (folate, RGD sequence), for imaging (fluorescent or MRI active tags) and for cell penetration (cell penetrating peptides), make the fullerene@protein bioconjugate a promising theranostic platform to detect, image and kill selectively cancer cells.

EXPERIMENTAL SECTION

C_{60}@lysozyme synthesis. C_{60}@lysozyme hybrid was prepared by mixing C_{60} powder (Sigma-Aldrich, used without further purifications) in excess (2:1) respect to the stoichiometric ratio, to 1 mL of 1 mM (14,4 mg/mL) solution of LSZ (Sigma-Adrich, purity 90%, used without further purification) in milliQ water.
The solution was sonicated using a probe tip sonicator (Hielsher UP200St, 200W, 26kHz), for 60 minutes at 30% of the maximum amplitude, refrigerating with an external ice bath.
The dark-brow turbid solution was then centrifugated at 10,000 rpm at 15°C (Eppendorf 5417R centrifuge supported by Eppendorf Fixed-angle Rotor F-45-30-11) to remove the excess of uncomplexed fullerene and possible aggregates.

Atomic Force Microscopy analysis. AFM images were collected with a Multimode VIII (Bruker, Santa Barbara,CA, US) equipped with a Nanoscope V electronics and operated in PeakForce Tapping mode. The cantilever used were ScanAsyst Air (Bruker, Santa Barbara, CA, US) with a nominal curvature radius of 5 nm and a nominal spring constant k=0.4 N/m.
To prevent aggregation phenomena induced by drying effects, the starting solution of C_{60}@LSZ was diluted 10,000 time before the drop deposition over the mica surface. The solution was then dried fluxing nitrogen gas and analyzed.

High-Resolution Powder X-ray Diffraction. HRPXRD analysis was carried out on the ID22 beamline of the European Synchrotron Radiation Facility (ESRF) in Grenoble. Powder samples were investigated at a wavelength of 0.39970(8)Å. All samples were measured in borosilicate 1 mm glass capillaries.

H_2O_2 detection by colorimetric (TMB) test. TMB test is a standard colorimetric test used for H_2O_2 quantification. Horseradish peroxidase catalyze the oxidation of a wide variety of substrates, including benzidine and other aromatic amines. 3,5,3',5'-tetramethylbenzidine is much less hazardous than benzidine itself and even more sensitive as an analytical reagent.[46]
Horseradish peroxidase, is capable of both one electron and two-electron oxidations, depending on the substrate employed. The blue oxidation product of TMB is either its one-electron oxidation

product (cation free-radical) or a complex of its two-electron oxidation product (diimine) with the parent diamine. This product can undergo further oxidation which produce the yellow colored diimine. According to the literature,[46] the UV chromophore of 3,5,3',5'-tetramethylbenzidine (λ_{max} = 285 nm) decreases to zero during the reaction, and no new UV peaks appear. In the visible region, two new bands appear initially, at 370 and 652 nm. These bands grow to a maximum and then decay, replaced by the band at 450 nm (figure S1). Using an excess of TMB, only the mono-oxidation reaction occurs. The absorption bands with maximums at 370 and 652 nm are diagnostic for hydrogen peroxide concentration.

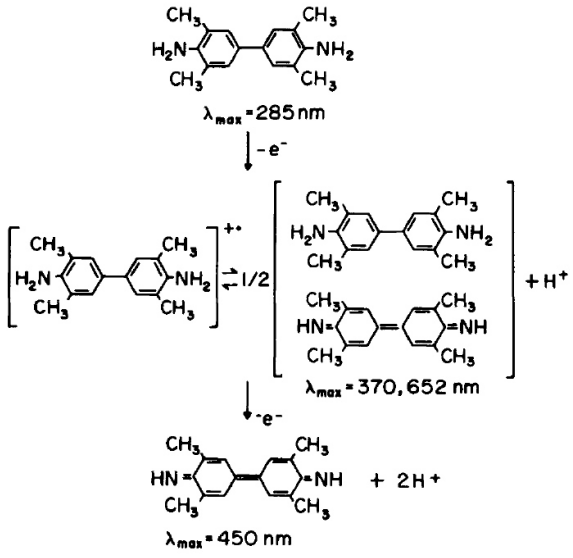

Figure S1. Schematic representation of two-step TMB oxidation reaction.

Quantification of H_2O_2 produced by C_{60}@LSZ irradiation. Stock solutions were prepared as follow:

i. 10 mg of TMB powder were dissolved in 1 mL DMSO in dark condition (it is insoluble in water and photosensitive);
ii. 1 mg of HRP was dissolved in 1 mL of PBS (pH 7.4);
iii. C_{60}@LSZ 1 mM was prepared using the standard protocol showed before.

The reagents was added in the following order, to obtain the relative final concentration:

i. C_{60}@LSZ 100 μM
ii. TMB 200 μM

iii. HRP 100 ng/mL

Each solution was prepared using PMMA semi-micro disposable cuvette (spectral range 280-800 nm) and irradiated for 30 minutes, using the same experimental conditions. The cuvettes were placed at a distance of 13 cm from the lamp. Absorption spectra were recorded by Agilent Cary 60 UV-Vis spectrophotometer supplemented by multicell holder and using a fast spectral acquisition. The H_2O_2 quantification were monitored following the absorbance of the mono-oxidized species at 650 nm.

Singlet oxygen detection. The luminescence spectra were recorded with a spectrofluorimeter Edinburgh FLS920 equipped with a photomultiplier Hamamatsu R928P for the visible region and a a Ge detector for emission in the NIR spectral region. Correction of the emission spectra for detector sensitivity in the 1200−1400 nm spectral region was performed. Quartz cuvette with optical path length of 1 cm were used (Hellma).

Singlet oxygen production of C_{60}@LSZ (in water) and C_{60} dispersed in toluene was measured. The emission spectra were acquired between 1200-1400 nm upon excitation at 514 nm.[19] The absorbance of each solution was previously normalized at 514 nm, to compare the fluorescence intensity.

Light Sources

Low-power energy source. Light-emission diode (LED) bulb (6W Non-Dimmable, 40W halogen equivalent). The LED 6W fluence rate is around 0.064 mW/cm^2 in 400 - 750 nm wavelength range. To have a homogeneous area of irradiation, the samples were placed under the LED source at distance of 25 cm during treatment.

High-power energy source. A SANOLUX HRC 300-280 E27 lamp operating in the 400 - 750 nm wavelength range purchased from Osram was used. To have a homogeneous area of irradiation the samples were placed under the light sources at the distance of 50 cm from the lamp providing a fluence rate of 1.6 mWcm^{-2} on the samples during treatment.

Cell Culture

Human cervical adenocarcinoma (HeLa) cell line was used as in vitro model. Cells were cultured in Dulbecco's Modified Eagle's Medium (DMEM) supplemented with 10% fetal bovine serum

(FBS) South-America, 2mM L-glutamine and 50 U/mL penicillin-streptomycin and sterilized by means of 0.45 μm filters (Millipore). Cells were kept in incubator at 37°C, 10% CO_2, 21% O_2 and were passed upon trypsin digestion every four days using a splitting ratio of 1:10 avoiding cells to reach full confluence.

Photodynamic treatments. To measure the photodynamic activity of C_{60}@LSZ complex, HeLa cells were plated at a density of 4×10^3 cells per well in 24-well plates. After growing overnight, the cells were incubated in free-serum and free-red phenol medium containing various concentrations of the photosensitizer. Then, some samples were exposed to the light source, while others were incubated in absence of any exposure to light (dark). Cell viability was conducted after 24 h of incubation upon photo-irradiation.

Cell viability studies. Cell viability was assessed by using erythrosine B exclusion assay. Cell survival was expressed as the percentage ratio of treated cells in comparison with untreated controls. For statistical elaboration and IC_{50} calculation, OriginPro Software was used. Data corresponded to mean value ± standard deviation (SD) from at least three different experiments.

Measurement of Reactive Oxygen Species. The measurement of intracellular ROS was based on the oxidation of 2,7-dichlorohydrofluoroscein diacetate (DCFH-DA). DCFH-DA passively enters the cells and then reacts with ROS to form a highly fluorescent compound dichlorofluorescein (DCF).

C_{60}@LSZ treatment. DCFDA - Cellular reactive oxygen species detection assay was tested on HeLa cells. HeLa cells were plated at a density of 6×10^3 cells per well in 35 mm Petri dishes. After growing overnight, the cells were washed with PBS buffer and incubated with 100 μM of DCFH-DA in PBS for 30 min, washed and overlaid with complete medium under strictly conditions for 30 min to avoid any nonspecific artifacts. Then, the cells were treated with 5 μM of C_{60}@LSZ in free-serum and free-red phenol medium and irradiated 10 min with the high-power energy light source. Cells were kept in incubation for other 30 min and then washed three times with PBS before analysis.

H_2O_2 treatment. HeLa cells were plated at a density of 6×10^3 cells per well in 35 mm Petri dishes. After growing overnight, the cells were washed with PBS buffer and incubated with a solution containing 200 µM of hydrogen peroxide for 30 min, 1,5 h, and 3h. Then, the cells were washed with PBS buffer and incubated with 100 µM of DCFH-DA in PBS for 30 min, washed and overlaid with complete medium under strictly conditions for 30 min to avoid any nonspecific artifacts (Chakravarty et al, 2008). Cells were washed three times with PBS before analysis.

The fluorescence of DCF was observed using 494 nm excitation and 518 nm emission filter sets. The fluorescence images of the treated cells were captured using a QImaging Retiga-2000RV CCD digital camera. The mean values of fluorescence intensity were estimated by using the histogram intensity profiles of the images, obtained with the same exposure settings, from at least thirty different cells (Figure S2). Statistical significance was established using one-way ANOVA test. P values < 0.05 (*), < 0.01 (**), < 0.001 (***) were considered as statistically significant.

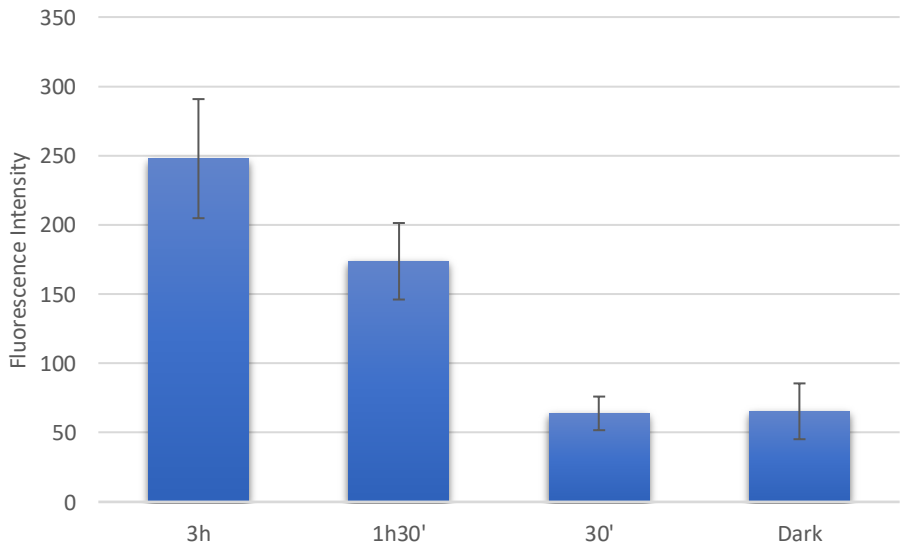

Figure S2. Fluorescence intensity of DCF acquired by fluorescence microscope (494 nm excitation, 518 nm emission filter) on cells treated with 200 µM of H_2O_2 for 3 hours (positive controls).

REFERENCES

1. Markovic, Z. & Trajkovic, V. Biomedical potential of the reactive oxygen species generation and quenching by fullerenes (C60). *Biomaterials* **29,** 3561–73 (2008).
2. Mroz, P. *et al.* in *Fullerenes as Photosensitizers in Photodynamic Therapy* 79–106 (2008). doi:10.1007/978-1-4020-6845-4_4
3. Calvaresi, M. & Zerbetto, F. Baiting proteins with C60. *ACS Nano* **4,** 2283–99 (2010).
4. Yang, S.-T. *et al.* Interaction of fullerenol with lysozyme investigated by experimental and computational approaches. *Nanotechnology* **19,** 395101 (2008).
5. Chaudhuri, P., Paraskar, A., Soni, S., Mashelkar, R. A. & Sengupta, S. Fullerenol−Cytotoxic Conjugates for Cancer Chemotherapy. *ACS Nano* **3,** 2505–2514 (2009).
6. Bolskar, R. D. in 157–180 (2008). doi:10.1007/978-1-4020-6845-4_8
7. Da Ros, T. in *Twenty Years of Promises: Fullerene in Medicinal Chemistry* 1–21 (2008). doi:10.1007/978-1-4020-6845-4_1
8. Guldi*, D. M. & Prato, M. Excited-State Properties of C60 Fullerene Derivatives. (2000). doi:10.1021/AR990144M
9. Jaesang Lee, John D. Fortner, Joseph B. Hughes, and & Kim*, J.-H. Photochemical Production of Reactive Oxygen Species by C60 in the Aqueous Phase During UV Irradiation. (2007). doi:10.1021/ES062066L
10. Zeng, Y., Biczok, L. & Linschitz, H. External heavy atom induced phosphorescence emission of fullerenes: the energy of triplet C60. *J. Phys. Chem.* **96,** 5237–5239 (1992).
11. Yanilkin, V. V. *et al.* Electrochemistry of Fullerenes and Their Derivatives. *Russ. J. Electrochem.* **39,** 1147–1165 (2003).
12. Guldi, D. M., Hungerbühler, H., Janata, E. & Asmus, K.-D. Radical-induced redox and addition reactions with C_{60} studied by pulse radiolysis. *J. Chem. Soc., Chem. Commun.* 84–86 (1993). doi:10.1039/C39930000084
13. Guldi, D. M. Capped Fullerenes: Stabilization of Water-Soluble Fullerene Monomers As Studied by Flash Photolysis and Pulse Radiolysis. (1997). doi:10.1021/JP9702863
14. Boudon, C. *et al.* Electrochemistry of Mono- through Hexakis-adducts of C60. *Helv. Chim. Acta* **78,** 1334–1344 (1995).
15. Wudl, F. The chemical properties of buckminsterfullerene (C60) and the birth and infancy of fulleroids. *Acc. Chem. Res.* **25,** 157–161 (1992).
16. Hamano, T. *et al.* Singlet oxygen production from fullerene derivatives: effect of sequential functionalization of the fullerene core. *Chem. Commun.* 21–22 (1997). doi:10.1039/a606335g

17. Dickinson, B. C. & Chang, C. J. Chemistry and biology of reactive oxygen species in signaling or stress responses. *Nat. Chem. Biol.* **7,** (2011).
18. Hu, B. *et al.* Surface plasmon-photosensitizer resonance coupling: an enhanced singlet oxygen production platform for broad-spectrum photodynamic inactivation of bacteria. *J. Mater. Chem. B* **2,** 7073–7081 (2014).
19. Yoko Yamakoshi, *,† *et al.* Active Oxygen Species Generated from Photoexcited Fullerene (C60) as Potential Medicines: O2-• versus 1O2. (2003). doi:10.1021/JA0355574
20. Sharma, S. K., Chiang, L. Y. & Hamblin, M. R. Photodynamic therapy with fullerenes in vivo: reality or a dream? doi:10.2217/nnm.11.144
21. Da Ros, T., Prato, M., Novello, F., Maggini, M. & Banfi, E. Easy Access to Water-Soluble Fullerene Derivatives via 1,3-Dipolar Cycloadditions of Azomethine Ylides to C(60). *J. Org. Chem.* **61,** 9070–9072 (1996).
22. Prato, M. Medicinal chemistry with fullerenes and fullerene derivatives. 663–669 (1999).
23. Susanna Bosi, † *et al.* Hemolytic Effects of Water-Soluble Fullerene Derivatives. (2004). doi:10.1021/JM0497489
24. Sundahl, M., Andersson, T., Nilsson, K., Wennerström, O. & Westman, G. Clusters of C60-fullerene in a water solution containing γ-cyclodextrin; A photophysical study. *Synth. Met.* **56,** 3252–3257 (1993).
25. Zhang, W. *et al.* Water-soluble inclusion complex of fullerene with g-cyclodextrin polymer for photodynamic therapy. doi:10.1039/c4tb00560k
26. Marconi, G., Mayer, B., Klein, C. T. & Köhler, G. The structure of higher order C60-fullerene-γ-cyclodextrin complexes. *Chem. Phys. Lett.* **260,** 589–594 (1996).
27. Ikeda, A. *et al.* Cyclodextrin Complexed [60]Fullerene Derivatives with High Levels of Photodynamic Activity by Long Wavelength Excitation. *ACS Med. Chem. Lett.* **4,** 752–756 (2013).
28. Shigeru Deguchi, *, Rossitza G. Alargova, and & Tsujii, K. Stable Dispersions of Fullerenes, C60 and C70, in Water. Preparation and Characterization. (2001). doi:10.1021/LA010651O
29. Moor, K. J., Snow, S. D. & Kim, J.-H. Differential Photoactivity of Aqueous [C 60] and [C 70] Fullerene Aggregates. doi:10.1021/acs.est.5b00100
30. Oberdörster, E., Zhu, S., Blickley, T. M., McClellan-Green, P. & Haasch, M. L. Ecotoxicology of carbon-based engineered nanoparticles: Effects of fullerene (C60) on aquatic organisms. *Carbon N. Y.* **44,** 1112–1120 (2006).
31. Deguchi, S., Mukai, S., Tsudome, M. & Horikoshi, K. Facile Generation of Fullerene Nanoparticles by Hand-Grinding. *Adv. Mater.* **18,** 729–732 (2006).

32. Makha, M., Purich, A., Raston, C. L. & Sobolev, A. N. Structural Diversity of Host–Guest and Intercalation Complexesof Fullerene C60. *Eur. J. Inorg. Chem.* **2006,** 507–517 (2006).
33. Konstantaki, M. *et al.* Optical limiting behaviour of the water-soluble C60/γ-cyclodextrin complex. *Chem. Phys. Lett.* **318,** 488–495 (2000).
34. Ratnikova, T. A., Nedumpully Govindan, P., Salonen, E. & Ke, P. C. In Vitro Polymerization of Microtubules with a Fullerene Derivative. *ACS Nano* **5,** 6306–6314 (2011).
35. Mashino, T. *et al. Human immunodeficiency virus-reverse transcriptase inhibition and hepatitis C virus RNA-dependent RNA polymerase inhibition activities of fullerene derivatives. Bioorganic & Medicinal Chemistry Letters* **15,** (2005).
36. Wolff, D. J., Barbieri, C. M., Richardson, C. F., Schuster, D. I. & Wilson, S. R. Trisamine C60-Fullerene Adducts Inhibit Neuronal Nitric Oxide Synthase by Acting as Highly Potent Calmodulin Antagonists. *Arch. Biochem. Biophys.* **399,** 130–141 (2002).
37. Pastorin, G. *et al.* Design and activity of cationic fullerene derivatives as inhibitors of acetylcholinesterase. *Org. Biomol. Chem.* **4,** 2556 (2006).
38. Belgorodsky, B. *et al.* Formation and Characterization of Stable Human Serum Albumin−Tris-malonic Acid [C_{60}]Fullerene Complex. *Bioconjug. Chem.* **16,** 1058–1062 (2005).
39. Calvaresi, M. *et al.* C60@Lysozyme: direct observation by nuclear magnetic resonance of a 1:1 fullerene protein adduct. *ACS Nano* **8,** 1871–7 (2014).
40. Nepal, D. & Geckeler, K. E. pH-Sensitive Dispersion and Debundling of Single-Walled Carbon Nanotubes: Lysozyme as a Tool. *Small* **2,** 406–412 (2006).
41. David T. Kim, Harvey W. Blanch, and & Radke*, C. J. Direct Imaging of Lysozyme Adsorption onto Mica by Atomic Force Microscopy. (2002). doi:10.1021/LA0256331
42. Li, D., Müller, M. B., Gilje, S., Kaner, R. B. & Wallace, G. G. Processable aqueous dispersions of graphene nanosheets. *Nat. Nanotechnol.* **3,** 101–5 (2008).
43. Fang, C.-Y. *et al.* The exocytosis of fluorescent nanodiamond and its use as a long-term cell tracker. *Small* **7,** 3363–70 (2011).
44. Markov, M. *Electromagnetic fields in biology and medicine*. (2015).
45. Gomes, A., Fernandes, E. & Lima, J. L. F. C. Fluorescence probes used for detection of reactive oxygen species. *J. Biochem. Biophys. Methods* **65,** 45–80 (2005).
46. Josephy, P. D., Eling, T. & Mason, R. P. The horseradish peroxidase-catalyzed oxidation of 3,5,3',5'-tetramethylbenzidine. Free radical and charge-transfer complex intermediates. *J. Biol. Chem.* **257,** 3669–75 (1982).
47. Calvaresi, M. & Zerbetto, F. Baiting Proteins with C_{60}. *ACS Nano* **4,** 2283–2299 (2010).

CHAPTER 3

NANODIAMONDS FOR BIOLOGICAL APPLICATIONS: STUDY OF THE INTERACTION WITH COMPLEX BIOLOGICAL FLUIDS

INTRODUCTION

3.1 NANODIAMONDS AS FLUORESCENT PROBE FOR *IN VIVO* IMAGING APPLICATIONS

Fluorescence bioimaging is a powerful technique for the investigation of the complex structure and functions of living organism in real time and space and, being poorly invasive, it is suitable for long-term observation of biological processes.[1]

The main limit showed by standard fluorescent probes for long-term detection, is the photobleaching that usually occurs upon long exposure to irradiation. From the photophysical point of view, inorganic nanoparticles can overcome this limit: this is the case of quantum dots (QDs). They are ultrastable, fluorescent contrast agents detectable even at the single nanoparticle level. QDs emission wavelength is size dependent and nanoprobes emitting in the near infrared (NIR) region are ideal for low background *in vivo* imaging. However, due to their intrinsic toxicity, their use *in vivo* is still controversial.[2]

Recent safety concerns enforced the search for a valid alternative for luminescent nanoprobes. Recent results demonstrated that fluorescent nanodiamonds (FNDs) show almost no photobleaching in a physiological environment.[3] Moreover *in vitro* and *in vivo* toxicity studies demonstrated their unique biocompatibility. FNDs are hence ideal diagnostic tools and promising non-toxic vectors for the delivery of therapeutic cargos.[1]

3.1.1 SYNTHESIS OF FLUORESCENT NANODIAMONDS

NDs show photoluminescence (PL) suitable for bioimaging only if they contain defects (color centers) in the structure that produce localized excited states upon light absorption. In most of the cases, emission of light arises from the presence of nitrogen atoms,[4] as dopants, in the carbon sp^3 structure.

Nitrogen atoms originate structurally and electronically different local defects[5] that absorb incident light and emit at characteristic wavelengths.[6] Nitrogen (N) content is a key parameter in the choice of the diamond precursors for FND preparation, since it limits the maximum density of color centers achievable in the nanomaterials, and consequently their potential brightness, as well as the probability of having defects containing two or more adjacent N atoms.[7]

Based on the relative abundance of nitrogen atoms into the crystal lattice, NDs can be classified as:[8]

i. type I, if diamonds contain nitrogen impurities;
ii. type II, if they do not contain measurable trace of nitrogen.

Only type I diamonds hence are suitable for producing luminescent probes. Moreover, type I diamonds are sub-classified into:

i. type Ia, containing N atoms up to 3000 ppm mainly in the form of aggregates (most natural diamonds belong to this category);
ii. type Ib containing less nitrogen and in the form of isolated atoms (most artificial diamonds).

High-energy ball milling of high-pressure high-temperature (HPHT) diamond microcrystals,[9] is the most used technique to prepare NDs for imaging applications. The general approach to the production of FNDs compatible with a physiological environment and suitable for bioconjugation is schematized in Figure 1.

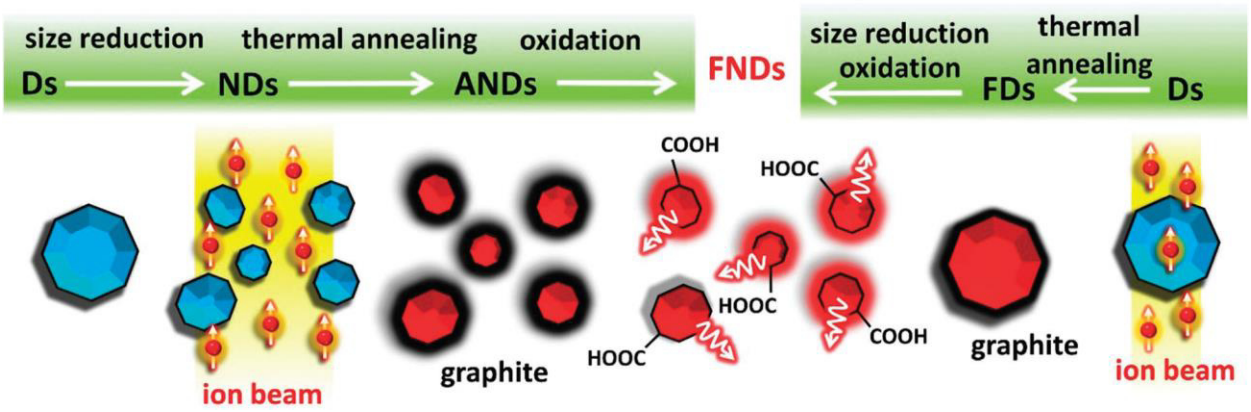

Figure 1. Schematic representation of the two main strategies for the preparation of aqueous dispersions of FNDs. Micro-sized diamonds (Ds) are reduced in size (from left to right) and ion beam damaged and then thermally treated to create color centers in the activated NDs (ANDs). Thermal annealing produces a surface graphitic layer which is eliminated by oxidation producing surface carboxylic groups together with other functions (anhydride and hydroxyl groups, not shown). In the alternative approach (from right to left). Microdiamonds are first activated to produce fluorescent diamonds (FDs) which are then reduced in size and oxidated.[1]

As prepared NDs show a weak fluorescence intensity since few color centers are present at this stage. Color centers (or defects) production involves the use of ion beam sources in high vacuum and can be hence accomplished only on dry materials.[10] Nowadays, the N-V defect centers (better discussed in the next section) in diamonds are produced by medium-energy (40 keV) He^+ beam radiation. This is a convenient alternative to the previous approaches (high-energy electron beam from a van de Graaff accelerator or a proton) since it produces high concentration of color centers in a setup that can be installed and operated safely in ordinary laboratories.[11] One further advantage of helium ions is their chemically inertness. As a consequence they do not alter the photophysical properties of the produced FNDs.

Independently of the ion source utilized, the exposed NPs need to undergo thermal annealing to induce vacancy migration and actual color center formation. As a side effect, thermal annealing (800°C) causes surface degradation, mostly in the form of graphitization. Surface graphite layers are detrimental to the photophysical properties of the FNDs and they have to be eliminated by oxidation in oxygen, air, ozone or nitric acid mixture in order to obtain bright materials and to enhance the ND water dispersibility, thanks to the formation of surface carboxylate groups.

An alternative approach consists in the activation performed directly on the microsized diamonds followed by pulverization and purification.

Separation techniques allow to obtain monodispersed diamond nanopowders but the size of the commercial products at the current stage can be hardly reduced below 10 nm.[12]

Bottom up approach is required to obtain smaller NDs. Detonation processes yield aggregates of NDs with sizes of 4−5 nm, embedded in a detonation soot composed of other carbon allotropes and impurities.[12] An explosive mixture (typically trinitrotoluene and hexogen) having an overall negative oxygen balance provides both a source of carbon and energy for the conversion. The detonation chamber reaches temperature as high as 3000−4000 °C and pressure of 20−30 GPa. Graphite is the most stable allotropic form of carbon at ambient temperature and pressure, hence, the fast cooling of the detonation products is crucial to avoid transformation of the diamond into graphitic phase. Formation of graphite (and other carbon allotropes) cannot be completely avoided, as well as the presence in the crude detonation "soot" of metals and oxide residuals.

The real challenge in producing FNDs is to obtain a stable aqueous colloidal suspension because of their strong propensity to aggregate. This lack of surface chemistry control might limit their application in bioimaging. Compatibility with an aqueous environment is in part favored by the modification occurring at the NDs surface during the purification process.

3.1.2 Photophysical Properties of Fluorescent Nanodiamonds Intended for Bioimaging

Although the FNDs can present different kinds of surface termination, including reconstruction to give sp^2 graphitic like shells (see chapter I), this shell is not directly involved in originating light emission.

As for analogous doped materials, the brightness of FNDs is dependent on the average number of emitting centers per particle. This parameter can be tuned by creating artificially the color sites in the synthetic or natural diamonds by radiation damaging with ion beams followed by thermal annealing. The former process produces stationary vacancies of carbon atoms in the lattice which, at 600 °C or above, become mobile and are trapped by nitrogen atoms to form color centers.

Vacancies in diamonds migrate primarily in their neutral charge state, while the color centers can exist either in the negatively charged state or in the neutral state.[13]

Defect related transitions in diamonds show characteristic zero phonon lines (ZPL) both in the absorption and luminescence spectra that give information about their nature and energies.

In the absence of nitrogen atoms indeed, simple vacancies of carbon atoms in the diamond lattice are non-paramagnetic color centers that adsorb light in the NIR region (ZPL = 741.2 nm). When excited these sites deactivate mainly via non-radiative pathways showing a PL quantum yield of ~1% (t = 2.55 ns) which makes them suitable for photothermal and photoacoustic applications.[14]

Indeed, starting from materials doped with a suitable level of nitrogen atoms (type I), it becomes possible to prepare FNDs emitting in the specific spectral region spanning from the NIR to green or blue depending on the nature of the formed color center.

From the biomedical imaging point of view, the most interesting FNDs are those whose emission spectrum belongs to the red-NIR range (Figure 2a,b). These color centers consist on negatively charged nitrogen-vacancy (N-V$^-$ centers), produced by ion beam damaging followed by thermal annealing, in type Ib diamonds together with their neutral counterpart NV^0.[15] As shown in Figure 2a, these centers correspond to the presence of a substitutional nitrogen atom adjacent to a carbon atom vacancy and show distinct ZPL at 637.6 nm and 575.4 nm for the negative and neutral defects respectively. Because of their NIR component, NV$^-$ emission matches well the transparency windows of living organism and it is hence well suited for in vivo optical imaging (Figure 2b).[16]

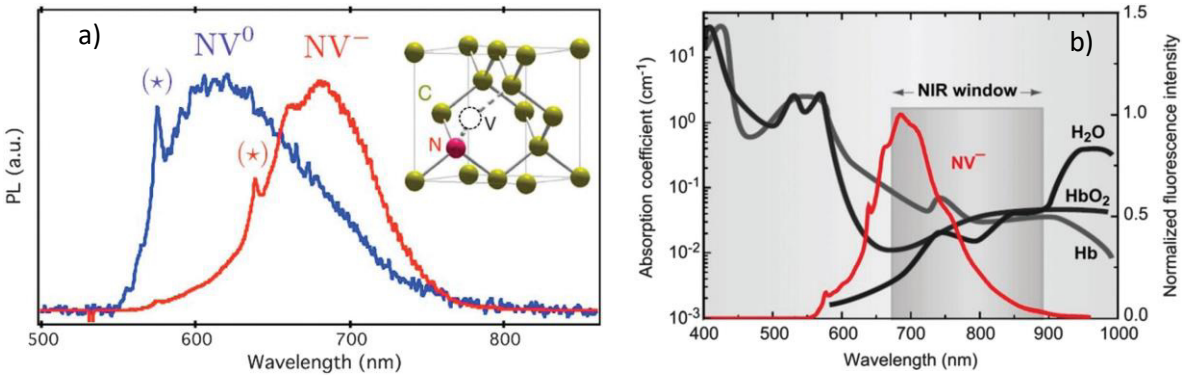

Figure 2. a) Normalized PL spectra of single NV$^-$ and NV^0 curve color centers in NDs. The zero-phonon line (*) symbols of NV$^-$ (637 nm), NV^0 (575 nm). The inset shows the atomic structure of the NV defect, consisting of a substitutional nitrogen atom N associated with a vacancy V in an adjacent lattice site of the diamond crystalline matrix.[15] b) Comparison of the fluorescence spectrum (red curve) of NV$^-$ centers in FNDs with the near-infrared (NIR) window of biological tissues. The black, dark gray, and light gray curves are the absorption spectra of H_2O, oxygen-bound hemoglobin (HbO_2), and hemoglobin (Hb), respectively.[16]

Negative centers are dominating in oxidized NDs being more than 80% of the total ones in type Ib NDs with diameters larger than 20 nm. NV^- centers show a unitary quantum yield, an excited state lifetime of ~12 ns. The electronic transition involved in the emission is the spin-allowed $^3E \rightarrow {}^3A_2$ one. The associated absorption band shows a broad phonon sideband at ~560 nm.[15]
Other nitrogen based defects can be produced in NDs, depending by the nature of the starting microcrystals and/or the irradiating conditions. Green and blue emitting nanodiamonds were produced and characterized. The first emission can be associated to the N-V-N defects, commonly produced in Ia type NDs while the second is originated by 3 nitrogen atom clusters.

The extreme photostability of the FNDs was demonstrated by comparing their emission with the one of 100 nm red fluorescent polystyrene carboxylated nanospheres under continuous excitation with a Hg lamp as shown in Figure 3. No sign of photobleaching was observed for FNDs, even after 8 hours of excitation; by contrast, the polymeric beads photobleached within 0.5 h under the same excitation conditions.[3]

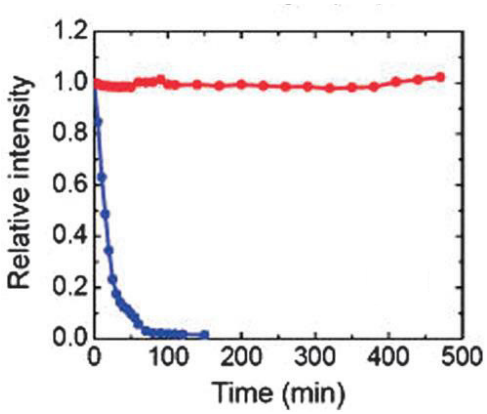

Figure 3. Photostability tests of FND (red) and fluorescent polystyrene nanospheres (blue) excited under the same conditions. The fluorescence intensity was obtained by integrating over the wavelength range of 590–900 nm for each sample.[3]

Kuo et al. demonstrated that it is possible to enhance the NV^- fluorescence lifetime to 20 ns.[17] Performing *in vivo* imaging, the lifetime is consistent with the picture that the fluorescent centers are embedded deep in the crystal and therefore their radiative relaxation dynamics is insensitive to environmental change and surface modification. The high photostability of FNDs, combined with their high compatibility allows to use time gating techniques (fluorescence lifetime imaging

microscopy) for long term *in vivo* imaging, with the main advantage to isolate the FNDs fluorescence from the cell components autofluorescent background.

Diamond has the highest refractive index of all transparent minerals, n = 2.42. This peculiar properties suggest to use ND also as optical scattering biomarker. It was theoretically estimated that the elastically scattered light from a single 55 nm ND particle is 300-fold brighter than that from a cell organelle of similar size.[18] Compared with metal-based scattering labels such as gold and silver particles, ND is advantageous in that it allows imaging of cellular events with less photodamage, thanks to the high optical transparency.[18]

3.1.3 FNDs IN PHYSIOLOGICAL ENVIRONMENT: LIMITATIONS AND STABILIZATION STRATEGIES

Beside of the graphitic surface removal, as said before, oxidation processes play a key role on FNDs stability. Carboxylate functional groups are mainly produced on the NPs surface during the purification. The hydrophilic nature and the negative charges of these functional groups (for pH values > 3.5, see Figure 4)[19] confer stability and improve the dispersibility on FNDs in water, making them suitable for functionalization.

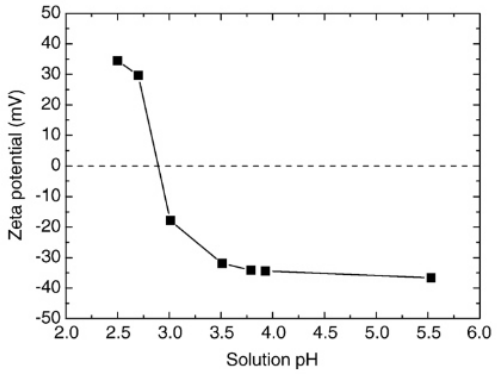

Figure 4. Zeta potential of oxidative-acid-treated diamonds (nominal size 100 nm) as function of solution pH. [19]

It is important to stress that, while these surface-oxidized FND particles are prone to precipitation in biological media such as phosphate-buffered saline (PBS) as shown in Figure 5, the particle

aggregation does not significantly change the fluorescence properties of FND since, contrary to the common organic emitting dyes, the light emitting NV centers are embedded deep in the diamond matrix.[20]

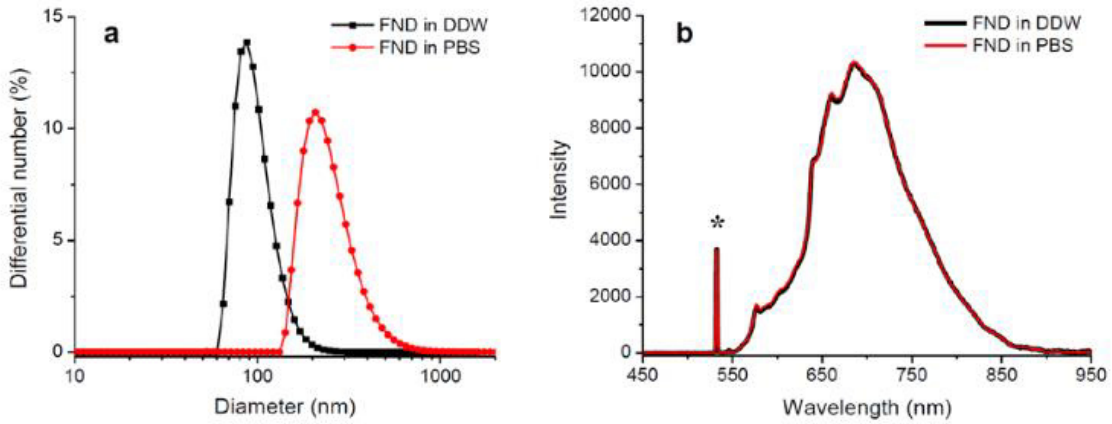

Figure 5. Characterization of the sizes (a) and fluorescence spectra (b) of FND particles in double distilled water (DDW) and PBS. The particles show good dispersibility in DDW with a mean size of 98 nm but form aggregates in PBS with size increasing to 255 nm. No significant differences between the spectra are found for particles suspended in DDW and PBS (concentration: 0.1 mg/mL). * in (b) denotes the residual excitation light at 532 nm.[20]

Oxidation induced functionalization does not suffice to stabilize the particles in physiological conditions.[20] The major difficulty using FNDs for bioimaging is to avoid their aggregation in a physiological environment. Two approaches are commonly used to overcome this limitation:

i. Covalent functionalization
ii. Non-covalent functionalization

In the first approach, the main advantage consists to have a well characterized surface, which does not change its chemical composition overtime. The drawback is the use of a multistep synthesis which usually entails the use of (toxic) organic solvents, therefore requiring an accurate purification before applications *in vitro* and *in vivo*.

A representative work on covalent functionalization of FNDs for targeted cellular imaging were realized by Weng et al.[21] In this work, covalent conjugation of transferrin to the carboxylate surface groups of 100 nm diameter red emitting diamond NPs was carried out. Chemical functionalization of FNDs with transferrin had a dual role: it prevented the re-aggregation of the particles and promoted the internalization, via receptor-mediated uptake mechanism, into the HeLa cells (where

transferrin receptors are over-expressed). They demonstrated that functionalized NDs were stable in physiological conditions and that transferrin receptors play a fundamental role in the trans-membrane permeation of the FNDs.[21]

In the latter approach (non-covalent functionalization), simple adsorption of water soluble molecules overcomes the limitations for the covalent counterpart but, at the same time, it makes more difficult the understanding of the surface composition in different physiological environments.

In general, polymeric surfactant and biopolymers are often used to enhance the colloidal stability of NPs.[22] The amphipathic nature and the high surface charge confer them the ability to interact, and make more stable hydrophobic objects in water. For example, core-shell Fe/Au nanoparticles are sufficiently charged to be stable against flocculation in low ionic strength media, but they require surface modification to be stably dispersed in elevated ionic strength media that are appropriate for biotechnological applications.[22] Nevertheless, aggregation phenomena could be completely prevented by using different synthetic surfactants (Pluonic F127 and F68), bovine serum albumin (BSA) and dextran to disperse the NPs (assisted by sonication), and then transferring the bioconjugate in high strength ionic media: the resulting colloidal system is stable for several days (Figure 6).[22]

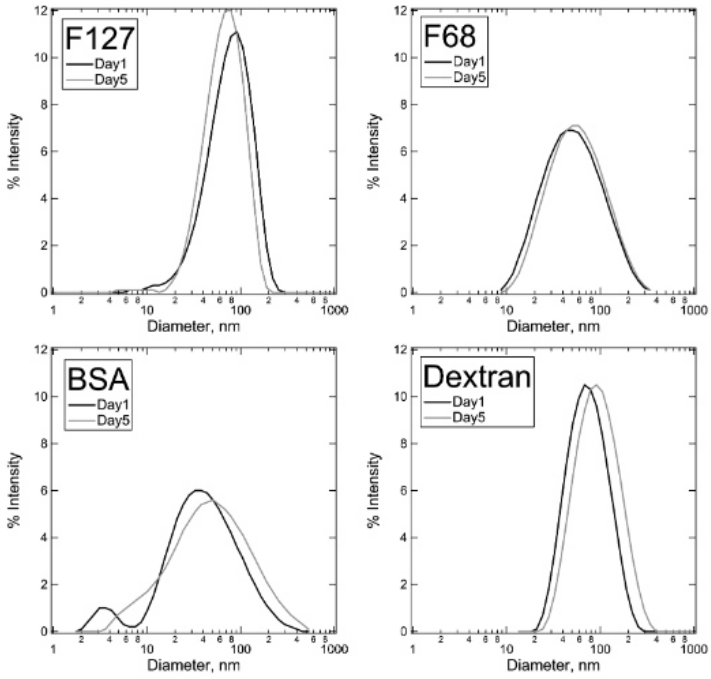

Figure 6. Intensity weighted DLS size distributions for Pluronic F127-, F68-, BSA- and dextran-coated Fe/Au NPs in PBS.[22]

Nowadays, the use of adsorbed biomolecules over the NDs surface to enhance their stability in physiological condition is becoming a necessary step to perform *in vitro* test, to prevent the aggregation. Because of the high biocompatibility, the abundance in plasma fluids and their surfactant-like behavior, proteins resulted the most used stabilizing agent for NDs.[19,23–25]

Using BSA and α-lactalbumin (a -LA) Tzeng et al.[23] showed that in both the cases it is possible to obtain a narrow distribution of the NDs size, allowing to perform high resolution imaging by confocal and stimulated emission depletion (STED) microscopy. The optimization of FNDs to protein concentration ratio, resulted a crucial parameter to preserve the particles monodispersity (Figure 7).

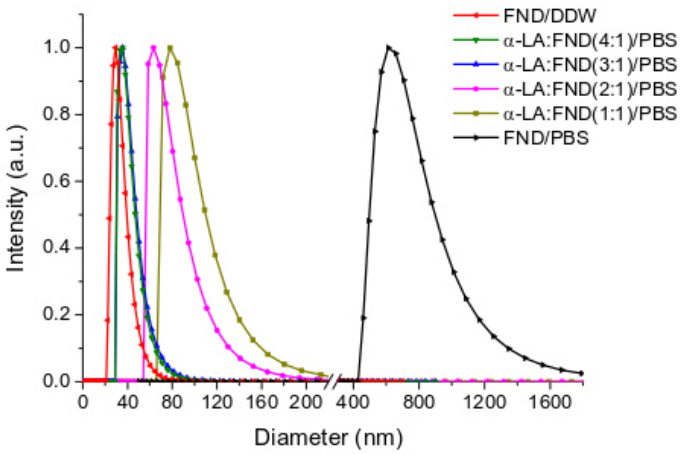

Figure 7. Size distribution of 30-nm FNDs measured with dynamic light scattering before and after noncovalent conjugation with α-LA at different weight ratios of α-LA:FND in DDW and PBS. The mean diameters of the particles with the size distributions from left to right are 30.0, 35.1, 35.4, 74.6, 93.0, 752.7 nm, respectively.[23]

Chang et al.[24] carried out *in vitro* experiments using FND noncovalently coated with glycoproteins or neoglycoproteins, in particular with BSA chemically modified with carbohydrate for targeting hepatocytes via carbohydrate receptors. Simple adsorption of these proteins on NDs surface, showed a potential applicability of the neoglycoprotein-coated FND for hepatic targeting, as demonstrated by the tests performed on HepG2 cell line. More in general, they demonstrated the dual ability of the adsorbed biomolecule to enhance the NDs stability and, at the same time, to address the FNDs toward a specific target.

Among the high number of works in this field, few representative and promising methods were reported. Very frequently, BSA was used to enhance the NDs stabilization in physiological conditions. Apart from the stabilization effect of BSA, the behavior of NDs in a complex media (e.g. serum) cannot be exhaustively understood simply investigating the interaction with a single kind of protein. Proteins size, tridimensional structure, protein-protein interaction and tendency to unfold upon adsorption, surface coverage and especially, the isoelectric point[19] are parameters which collectively affect the nanoparticle-protein adsorption processes.

The only characterization in this regard were performed before the incubation. Faklaris et al.[26] simulated the possible conditions of NDs in supplemented media, incubating the nanoparticle in DMEM (Dulbecco's Modified Eagle Medium) containing 10% FBS under sonication. Upon more

washing, FTIR and zeta potential measurements demonstrated the effective adsorption of protein over the NDs' surface. They demonstrated that the addition of FBS can mitigate the aggregation phenomena exacerbated by the cell medium DMEM. A step further could be addressed optimizing a protocol to disperse NDs in serum without the sonication assistance, with the aim to preserve the integrity of the proteins and hence simulate the conditions of *in vitro* studies

3.2 Nanomaterials Interactions with Relevant Biological Fluids: a New Biological Identity

All the materials show a higher free energy for the surface than the bulk itself. This behavior is exhibited independently by the size of the material but it become more important for high surface to volume ratio objects. For nanosized material, the high surface energy significantly influences their behavior. This means that the surface of nanoparticles will progressively and selectively adsorb biomolecule exposed to biological milieu[27]. The biomolecules surrounding the nanoparticles (the so-called " biomolecular corona") lowers their surface energy, promoting their dispersion.[28] The biomolecules presented in the biomolecular corona represent the final biological identity of the nanomaterial which are likely to interact with the biological machinery and determine the final fate of the nanomaterial intracellular trafficking (Figure 8a).[27,29,30] For most of the particles, a near-monolayer of biomolecules, named "hard" corona, binds tightly but not completely irreversibly, to the surface of nanoparticles. Over this layer, there are a more loosely associated and rapidly exchanging layer of biomolecules, defined "soft" corona (Figure 8b).[29]

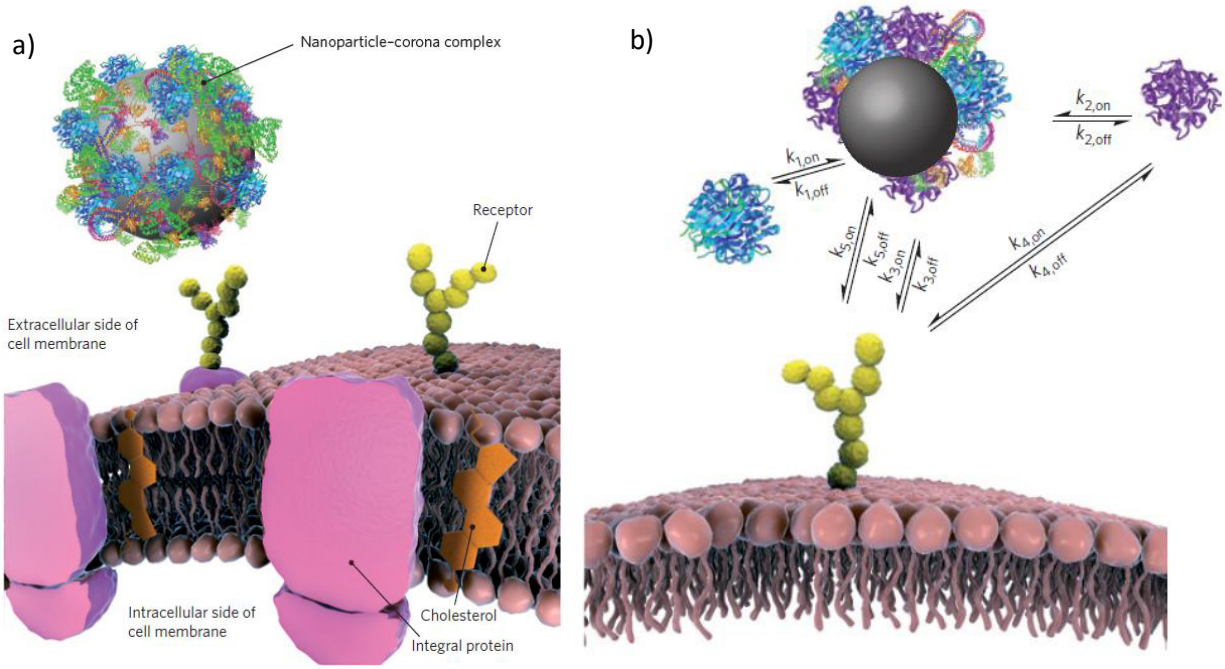

Figure 8 a) It is the nanoparticle–corona complex, rather than the bare nanoparticle, that interacts with biological machinery, here with a cell membrane receptor.[28]**.** b) Relevant processes (arrows), in both directions (on/off), for a nanoparticle interacting with a receptor. Biomolecules in the environment adsorb strongly to the bare nanoparticle surface (k_1), forming a tightly bound layer of biomolecules, the 'hard' corona, in immediate contact with the nanoparticle. Other biomolecules, the 'soft' corona, have a residual affinity to the nanoparticle–hard-corona complex (primarily to the hard corona itself), but this is much lower, so those molecules are in rapid exchange with the environment (k_2). If sufficiently long-lived in the corona, a biomolecule may lead to recognition of the nanoparticle–corona complex as a whole by a cell membrane receptor (k_3). The same biomolecule alone can also be recognized by the receptor (k_4). If present, the bare surface of the nanoparticle may also interact with cell surface receptors (k_5) or other constituents of the cell membrane.[28]

It is important to notice that only a few of the biomolecules available in typical biological environments are found in the hard corona.

Biological media contain thousands of molecules (for example, human blood plasma has 3,700 identified proteins) and they compete for limited space on a nanoparticle surface[31]. For a given nanoparticle, only few tens proteins bind in significant amounts and for long enough time to be biologically significant.[30] Furthermore, these tens of proteins rarely correspond to the most abundant proteins in plasma, and are not necessarily those with the highest individual affinity to the nanoparticle surface.[32]

Hard corona layer is significantly stable,[29,33] so any subsequent exposure of the NPs to a new environment could lead to a partial displacement of the original hard corona by new molecules.[34] The direct consequence of this behavior is that biomolecules which are not replaced would serve as corona "memory" of the nanoparticle's previous environment. Therefore, the corona composition could potentially depend not only on the current environment but on all environment it has moved through before.[34]

In light of all the studies performed on protein corona in the last 10 years, it is necessary to rethink the previous works which classified the substances according to "intrinsic" properties of bare material than the "extrinsic" properties defined from environment.

3.2.1 Biomolecular Corona Composition and Orientation : Parameters Affecting the Cellular Uptake

Nanoparticles (NPs) interact with cells (and living organisms in general) in a fundamentally different manner from small molecules. The latter, in fact, diffuse into and around the cell, partitioning freely according to near-equilibrium principles.[35]

In contrast, nanoparticles, because of their size, are processed and taken into the cell by active, energy-dependent processes.[29] Because of their size and surface, nanoparticle–corona complexes can engage with a wide range of endogenous cellular uptake and other processes, and potentially reach any cellular and organ compartments, interact with them, and initiate signalling processes.[28]

The interactions between NP-corona and the biological machinery are mediated by physical forces common to all molecular systems. It is more useful to distinguish these interactions considering if they involve non-specific physical interactions or specific biologic recognition. Such recognition can, for example, be driven either by the presence of specific peptide sequences (epitopes)[36] or it can be influenced by more subtle structural properties, such as curvature of the complex.[33] Recognition is expected to lead to well-regulated biological processing and functional impacts. In contrast, strong non-specific interactions between particles and cells could lead to a range of quite different, but equally complex, outcomes. For example, in several cases, such as carbon nanotubes[37], silica[38] and graphene oxide[39], it has been observed that cell damage occurs in the

absence of a protein corona (that is, cells exposed to particles in medium without proteins), but is mitigated in its presence.

Besides the intrinsic properties of bare nanoparticles, it is important to investigate the main factors which define the size, shape, structure and composition of protein corona and how this characteristics can confer a biological function to the nanoparticle.

Even if the NPs remain within the same biological compartment, the corona biomolecules must stay long enough on the surface of the nanoparticle to be biologically recognized at, for example, the outer plasma membrane of the cell. Thus, biological relevance is determined not only by the structure and composition of the corona but also from the dynamical exchange processes (Figure 8b). Collectively these particle-protein complexes constitute "what the cell sees". If the slowly exchanging proteins have sufficiently long residence times, then the effective biological unit is a nanoparticulate core and an associated biomolecule corona that is so strongly bound that the particle itself is merely the scaffold for the proteins.[29] For example, endocytosis of nanoparticles across the plasma membrane occurs within minutes, and consequently, a biomolecule must stay on the nanoparticle surface at least this long to be "seen" and processed by the endocytic machinery.

In the case of the much more rapidly exchanging outer soft corona, an exchange time of seconds or less is expected. This separation of timescales suggests that the key biological determinant for nanoparticles will often be the interface between the hard and soft corona. What the cell "sees" is a system in which the core nanoparticle is surrounded by a "hard" corona of slowly exchanging proteins and an outer (weakly interacting, and rapidly exchanging) collection of proteins.[29]

It is important to relate the structure and composition of the hard corona to the nature of the original nanoparticle surface. This is not an easy task because the corona is not at thermodynamic equilibrium. Indeed, the molecular dynamical exchange times of the hard-corona biomolecules can be many hours so this means that the composition and structure of the corona are not equilibrated on a timescale of typical biological experiments, and the nearly stationary composition and structure is actually a consequence of the very slow exchange. For example, in the absence of rapid exchange, some biomolecules arriving early to the nanoparticle surface may subsequently either

be displaced by those arriving later or, if they adhere strongly, may themselves play a role in determining the next set of proteins adsorbing (Figure 9).

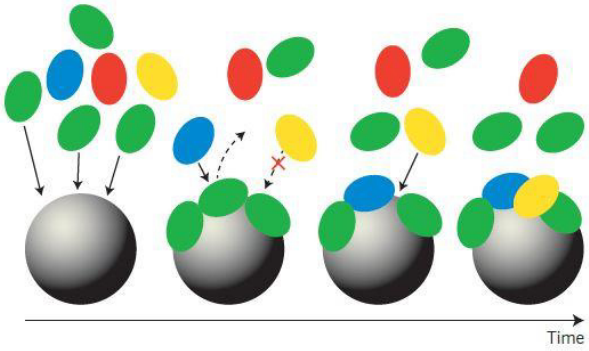

Figure 9. Formation of the biomolecular corona. From left to right: An initial corona forms from those biomolecules (in green) that arrive first to the surface (typically highly abundant proteins). An initially adsorbed molecule with low affinity (in green) is subsequently displaced by a different molecule with higher affinity (in blue) arriving later. A third molecule (in yellow), that initially had a low affinity for the bare surface, now adsorbs on the nanoparticle surface owing to favourable interactions with the adsorbed (green and blue) biomolecules. A different biomolecule (in red) does not adsorb at all.[28]

These processes are affected by the combination of different variables, such as: [40]

i. each biomolecule relative abundance;
ii. diffusion rate;
iii. affinity for the surface and/or other biomolecules already associated with the surface;
iv. nanoparticle–biomolecule and biomolecule–biomolecule interactions;
v. conditions in which the corona are formed.

Some factors that control the corona are now clear, for example, as with any surface-coverage phenomenon, the ratio of nanoparticle surface area to protein concentration.[27,33] Moreover, the radius of curvature of the nanoparticle is also a key parameter for several reasons.[27,32,41] The surface energy of a bare nanoparticle depends on the radius of curvature, because a highly curved surface causes local stresses on the microscopic organization of atoms at the surface. Indeed, the energy of a particle surface can be much larger than a flat surface of the same material.[42] The nanoparticle radius of curvature, if sufficiently high, will also affect the corona directly as large proteins seek to pack around small spaces.[41,43] For example, one expects radically different coronas in high-aspect-ratio materials (such as carbon nanotubes), where one of the lengths is typically

smaller than that of the abundant proteins.[44,45] In this case, biomolecules may align along the long axis to fit on the nanoparticle surface. Larger globular biomolecules, on the other hand, may simply not fit and hence be excluded from the corona.

Fine details of size, shape and bare-surface physicochemical properties can lead to different hard coronas. Therefore, the intrinsic properties of the nanoparticles may be insufficient to classify them into groups of similar particles in relation to, for example, their biological interactions.

For animal-derived biological media, those corona compositions known at present are largely composed of proteins[41,43] lipids[46] and sugars[47]. Most methods to determine the corona composition first separate all of the strongly adsorbed biomolecules from the particles into a single biomolecule sample, and then use mass spectrometry to identify the recovered proteins or other components. However, this analysis does not address their detailed organization on the nanoparticle surface, nor whether the molecules are presented appropriately to activate specific cellular processes, but is nevertheless suggestive of such possibilities.[48]

An exhaustive characterization of nanomaterials in biological environment will require a link between nanoparticle properties, biological milieu and biological pathways, and in particular a detailed description of the corona structure. For example, of the biomolecules grafted and adsorbed to nanoparticles, only a small fraction will have biologically relevant peptide sequences facing externally, away from the nanoparticle surface, making it difficult to predict how these nanoparticle–corona complexes might further interact with circulating molecules such as antibodies, scaffolding biopolymers and cell receptors.[36,48]

Recently, forefront approaches requiring the use of immunolabelling are addressed to detect, among the proteins composing the corona, the effective number of available epitopes potentially involved in a bio-recognition event. For example, using immunogold label it was possible to identify and evaluate the spatial organization of the exposed epitopes over the transferrin-grafted silica nanoparticles (SiO_2-PEG8-Tf), by means of transmission electron microscopy (Figure 10a,b).[48] A different approach was developed, labelling antibodies with quantum dots (QDs).[49] In this case, the fluorescence intensity of QDs was used to quantify the average number of exposed epitopes per particles, allowing the study of nanoparticles also *in situ* in realistic biological milieu (Figure 10c).

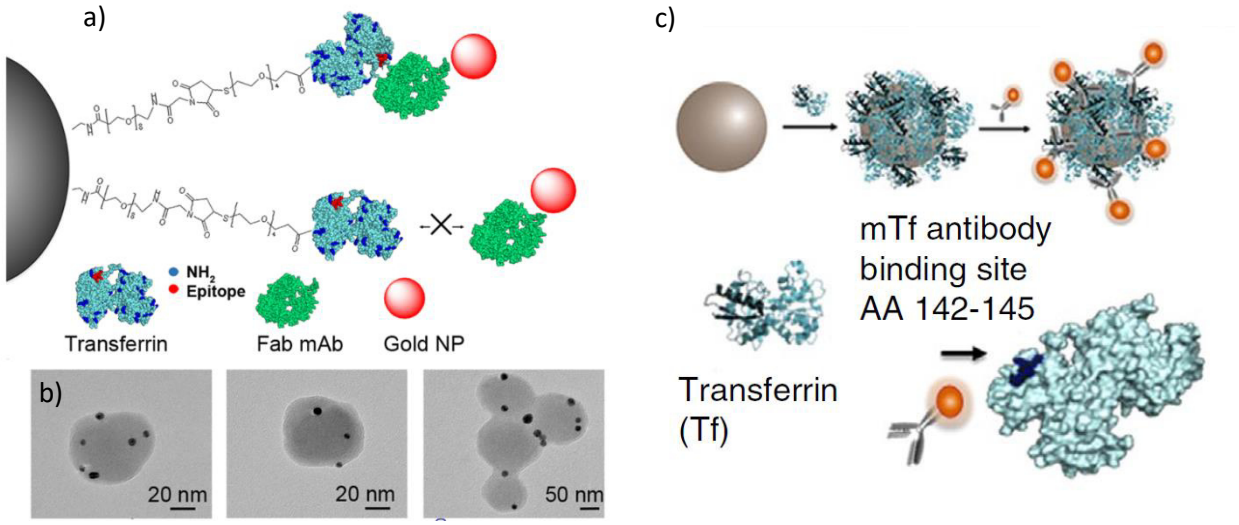

Figure 10. Left: a) Epitope mapping of SiO_2−PEG8−Tf nanoparticle surface. Schematic representation of the mechanism of interaction between Tf grafted silica nanoparticles and immunolabels b) Representative TEM micrographs of SiO_2−PEG8−Tf particles labeled with antibody fragments mAb IG at saturation.[48] Right: c) QDs functionalized with specific monoclonal antibodies used for fluorescent labelling to map out target relevant epitopes of the protein corona.[49]

The hard-corona structure can be studied by isolating the particle–corona complexes,[29] and using physical characterization methods that are well known from colloid and interface science,[50] for example:

- dynamic light scattering;[29]
- differential centrifugal sedimentation (DCS);[33,48]
- zeta-potential.[33]

The first two techniques are used to measure the hydrodynamic radius, and DCS sheds light on the distributions of such NP–corona complexes. It is also useful to perform average-size and zeta-potential measurements to monitor the corona formation when nanoparticles are added to biological media and characterize the quality of the resulting dispersion of these complexes (see appendix).

AIM OF THE STUDY

We strongly believe that protein stabilization could play a key role for NDs application for bioimaging, both *in vitro* than *in vivo*. *In vitro* tests are (mainly) performed in supplemented media, which consists in the addition of a percentage of serum (for example fetal bovine serum, FBS), necessary to promote the cells growth. Up to date there is a lack in the literature about the biomolecular surface coverage of nanodiamonds upon their addition in supplemented media.
The comprehension of the stabilization effect conferred by serum to NDs, require the still-missing identification of the composition of NDs protein corona. Moreover, the optimization of NDs dispersion procedure in physiological conditions is an important prerequisite to use them as a diagnostic probe for high resolution bioimaging applications. In fact, most of the NDs used for bioimaging *in vitro* and *in vivo* are not in the monodisperse form.

RESULTS AND DISCUSSION

3.3 SERUM PROTEINS AND NANODIAMONDS INTERACTION: THE BIOLOGICAL IDENTITY OF NANODIAMONDS

In this section, the first part of the work was addressed to the characterization of the commercial NDs to investigate their properties and limits in physiological conditions. The interactions with serum proteins was evaluated and then a suitable protocol for NDs stabilization in biological media was optimized. In the second part, the characterization of NDs protein corona was carried out, focusing more attention about their composition and to the orientation of specific proteins.

3.3.1 PRELIMINARY CHARACTERIZATION ON FNDS STABILITY

Commercial fluorescent nanodiamonds provided by Sigma-Aldrich were used for all the experiments shown in this chapter. The nominal sizes (from the vendor datasheet) of the nanoparticles were 70 and 120 nm (named ND-70 and ND-120 to distinguish them), having a color center number of 300 and 1200 NV/particle, respectively.

This materials do not require color centers activation or further purification. Based on the starting material and the experimental condition of irradiation, two kind of color center are contained in the lattice:

- N-V centers (red-NIR emission, Figure 11a)
- N-V-N center (green emission, Figure 11b)

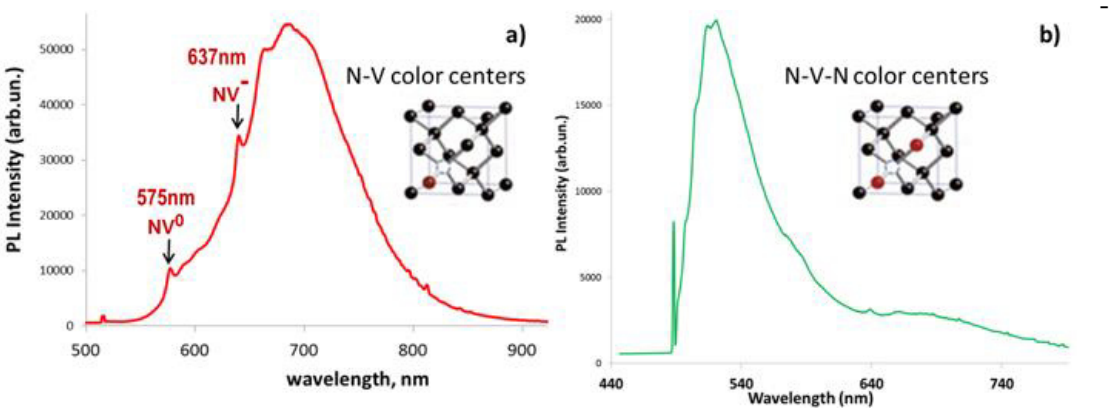

Figure 11. Emission spectra of ND particles containing N-V centers (a) and N-V-N centers (b) dispersed in water at a concentration of 1 mg/mL. Excitation wavelength is 532nm and 442nm, correspondingly. Peak at 488nm (b) corresponds to Raman shift of diamond. (Data provided by the vendor).

Preliminary studies about the stability of the commercial products were performed. Confocal microscopy confirmed the photophysical data provided by the vendor (Figure 12a,b), but the dispersion appeared highly aggregated (Figure 12a,b,c).

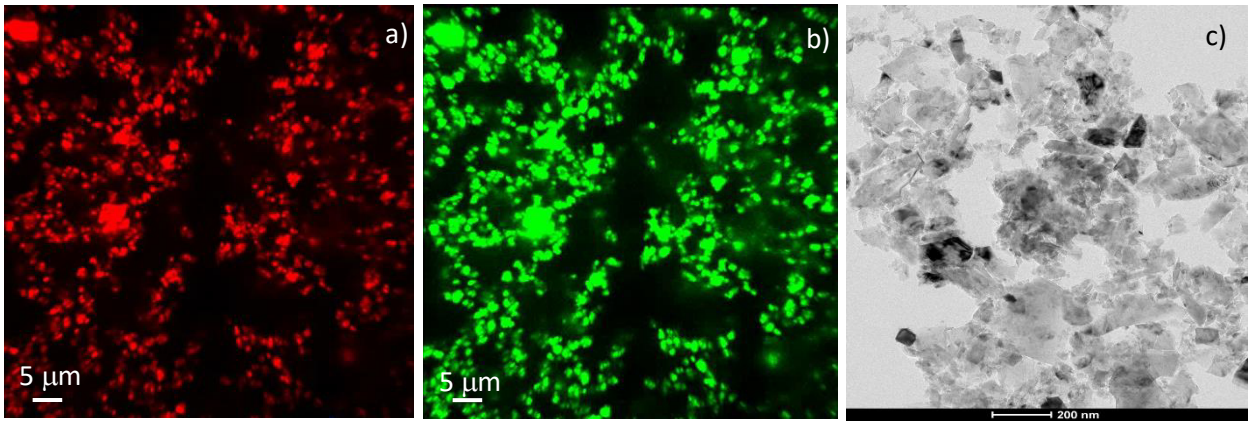

Figure 12. Confocal microscopy of ND-120 dispersion in water.* a) laser excitation at λ=560 nm. b) laser excitation at λ=488 nm. The fluorescence of diamond is based on color centers incorporated into the diamond lattice: nitrogen-vacancy centers (N-V), provide red fluorescence (left) and N-V-N (or H3 center) emit green light (right).
c) TEM acquisition on ND-120 deposited over the grid by drop casting.*
*Thanks to Diana Hudecz for confocal microscopy and to Luciana Herda for TEM analysis

Size characterizations were performed using both dynamic light scattering (DLS) and differential centrifugal sedimentation (DCS) analysis. DLS characterization confirmed the strong tendency of FNDs to the aggregation in milliQ water, showing also a wide distribution of population. Diluting the solutions, the medium size and the polydispersity didn't significantly changed. Furthermore, as expected, a fast coagulation was observed dispersing the particles in PBS (Figure 13).

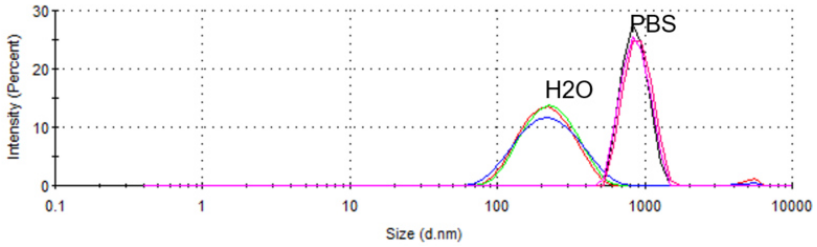

Figure 13. DLS analysis of FNDs 50 µg/mL (Sigma-Aldrich ND-120) performed in water and PBS.

Sonication process was conducted on NDs dispersed in water, to evaluate the possibility to disaggregate the preexisting clusters.
It was observed by DCS that after few minutes of treatment, a significant reduction of the nanoparticles average size occurred for ND-120 (Figure 14). Among 0 to 15 minutes, the average sizes shifted to smaller values. Longer sonication time did not show further effects on particle size

reduction. It is important to stress that sonication induced disaggregation is a reversible process, in fact, after few minutes NDs stick together again producing the original colloidal aggregate.

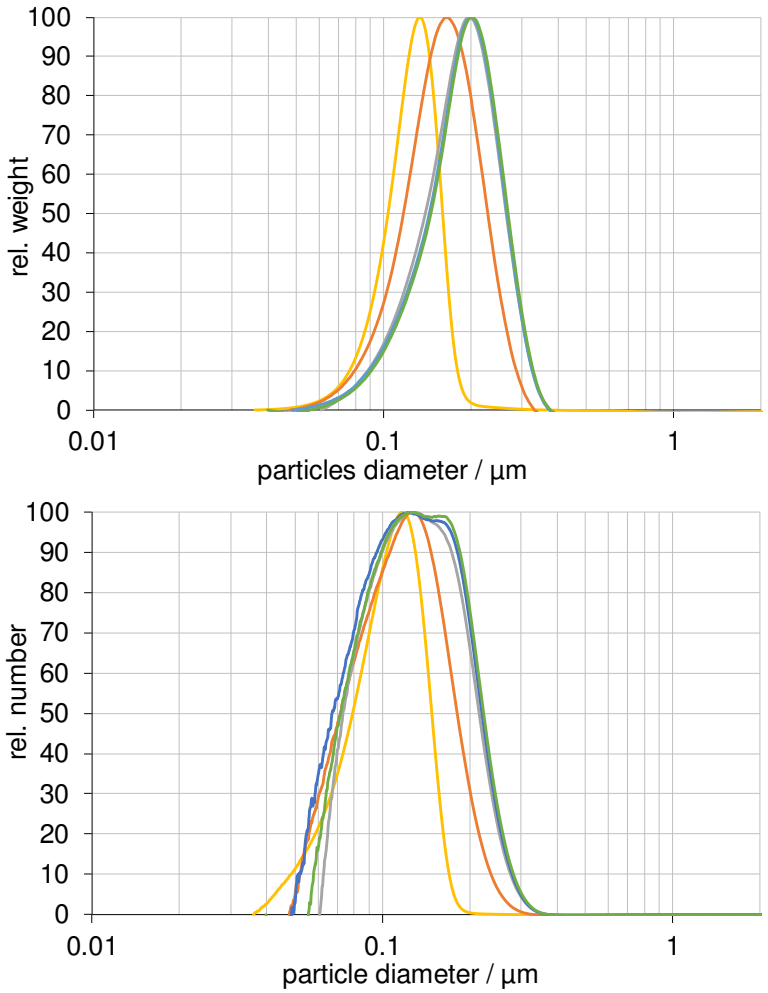

Figure 14. Sonication time effect on ND-120 average size, analyzed by DCS measurements, for 0 (green), 1 (blue), 3 (grey), 8 (orange),15 (yellow) minutes. Optical density expressed by relative weight (top) and relative number (bottom).

Contrary, for the smaller particles (70 nm) it was found a better stability which made unnecessary the sonication (Figure 15). However, sonication was performed for both the sizes to make the procedure as equal as possible.

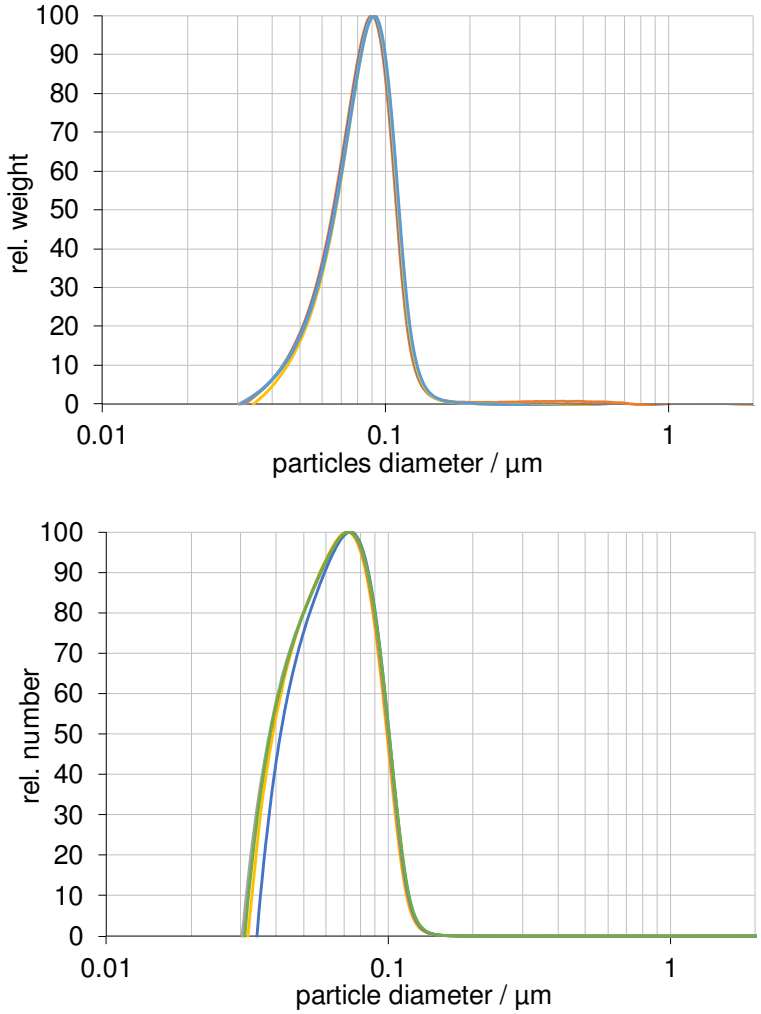

Figure 15. Sonication time effect on ND-70 average size, analyzed by DCS measurements, for 0, 1, 3, 8, 15 minutes (overlapped). Optical density expressed by relative weight (top) and relative number (bottom).

Using the Nanoparticle Tracking Analysis (NTA), the concentration of the particle was analyzed. NTA utilizes the properties of both light scattering and Brownian motion in order to obtain the particle size distribution of samples in liquid suspension and the relative particles number. ND-70 resulted about 2.5 times more concentrated than ND-120 (by number of particles) so a consequent dilution factor was considered in the experimental procedure.

Before to proceed to the protein corona characterization, few consideration has to be done.

i. Both DCS and DLS measurements were performed but, DCS measurement will be preferred as reference technique for size characterization: because of the high scattering properties of NDs, DLS slightly overestimates the NDs size.

ii. The incubation of the same volume of each NDs solution (ND-70 and ND-120) into the serum, originates a different ratio between proteins and particles. To compare the data, normalization of the particles was performed.

iii. Based on NPs geometrical factors, an estimation of the total surface area available for protein saturation was calculated. The main approximation consists into consider a representative protein (serum albumin) as a rigid structure adsorbing over the NP surface. This estimation is useful to understand if the order of magnitude of serum concentration is high enough to permit a complete coverage of all the particles. However, a large excess respect the calculated value is usually used to produce NPs protein corona.

3.3.2 NDs Protein Corona Preparation

In vivo and *in vitro* evidences suggest that the interaction between NPs and blood components is a determining factor driving the fate and impact of the particles. Certainly the adsorbed protein layer influences cellular uptake and may affect trafficking, while *in vivo*, specific binding of proteins may affect particle biodistribution.[33] For this reason, the identification of the serum protein composing the hard corona, could give indications about the possible fate of nanoparticles.

Nanoscale surface curvature strongly affects protein adsorption, so that protein-binding affinities for NPs surface are different than for their analogue bulk material and the coronas associated with NPs of the same material but of different size can vary in composition.[51] For this reason, two different sizes (70 nm and 120 nm) of NDs were used to evaluate a possible surface curvature effect on proteins adsorption.

A standard procedure developed by the Center for BioNano Interactions (CBNI) laboratory team[33] was used to produce and characterize NDs protein corona, adapting few conditions for the specific NPs. Two relevant biological fluids were used for the investigation: fetal bovine and human serum. The choice of the biofluid can deeply influence the composition of the corona.[52,53]

Structural and physical characterization of NDs-protein corona complexes have been performed on samples prepared following different procedures. Stock solution of ND-120 and ND-70 nm dispersed in milliQ (weighted by number of particles) were sonicated for 15 minute in the bath sonicator.

Taking advantage from the metastability of sonicated NDs, immediately after the sonication they were incubated with serum to evaluate the stabilization effect originated from protein adsorption (formation of hard corona). Different serum concentrations (10%, 50% and 80%) were used, diluting with PBS to obtain the desired final concentration (see experimental section). The protein concentration in HS (70 mg/mL) is higher than FBS (47 mg/ml), therefore a dilution was carried out to normalize the two concentrations. Each sample of resuspended particles were split in two different aliquots, necessary for the next characterizations (gel electrophoresis and DCS analysis).

3.3.3 DCS ANALYSIS OF FND-PROTEIN CORONA COMPLEXES

The NDs-protein corona complex free from serum excess were characterized by DCS, using a PBS based sucrose gradient (see experimental section). Each condition was performed in duplicate, conducing independent experiments in different days. The reproducibility is very high for both the sizes of NDs, in some cases the curve are superimposable. Representative peaks are reported in Figure 16.

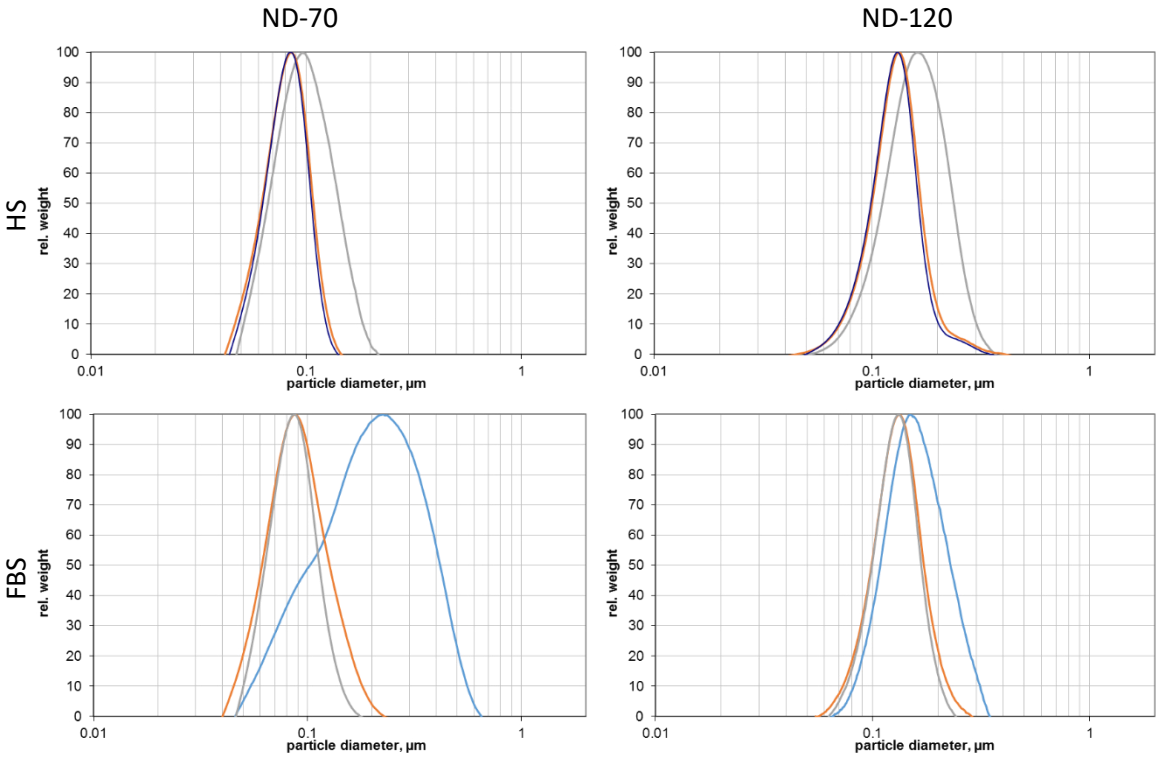

Figure 16. DCS experiments of ND-corona complexes free from excess serum and resuspended in PBS. Top: 10% (grey), 50% (orange), 80% (violet) HS. Bottom: 10% (cyan), 50% (orange), 80% (grey) FBS. Left ND-70 nm, right ND-120 nm.

The most evident results that can be deduced by DCS analysis were that serum concentration play a key role to prevent NDs aggregation. A similar behavior can be observed for all the explored conditions: for serum concentration equal or higher than 50%, the stabilizing effect is efficient. For 50% an 80% of serum, size distribution of NDs-corona complexes are superimposable.

Higher polydispersity was exhibited by the lowest serum concentration. Even though the minimum amount of proteins required for NPs saturation was guaranteed using an excess of serum proteins, a concentration dependency was still observed. It should be kept in mind that for most of the *in vitro* experiments, supplemented media consists on the addition 10% of serum proteins. For these sizes of NDs the use of an increased serum concentration will prevent the aggregation of the particles.

3.3.4 SDS-PAGE Analysis of Protein Corona

Immediately after the last centrifugation step the second aliquots of ND-protein corona pellet was re-suspended in protein loading buffer to perform SDS-PAGE analysis (see experimental section). In these denaturing conditions, the proteins get rid from NDs, and are able to run into the gel.
The same samples obtained by the two independent experiments analyzed by DCS were also used for SDS-PAGE characterization. Also in this case, the protocol resulted highly reproducible. Representative pictures of the gels, are shown in Figure 17 (HS) and Figure 18 (FBS).

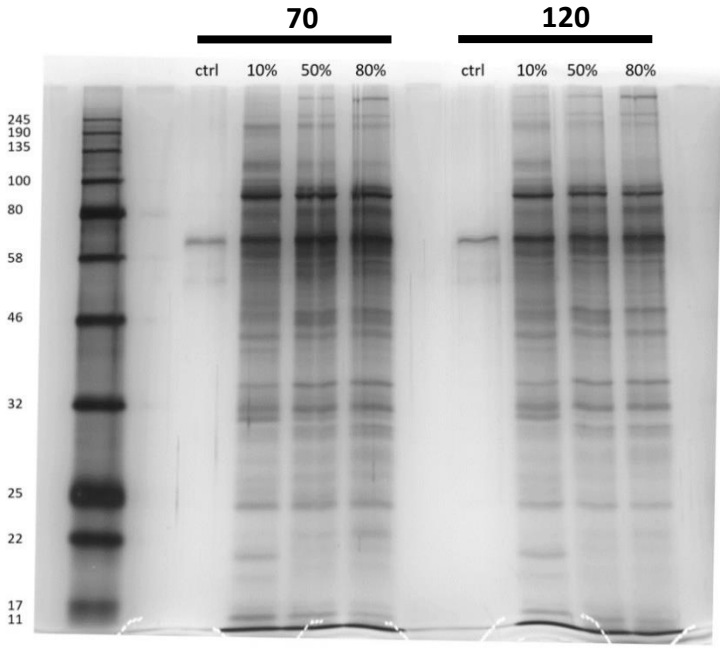

Figure 17. SDS-PAGE gel of human serum (HS) proteins obtained from ND-70 and ND-120 NP-protein complexes free from excess serum. The control is used to detect possible proteic residues from the excess serum. The Mw of the proteins in the standard ladder are reported on the left for reference.

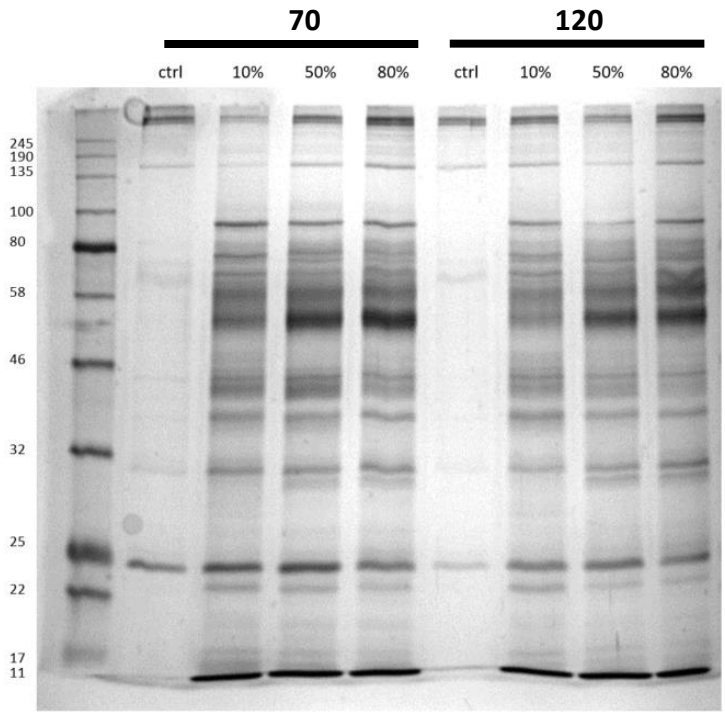

Figure 18. SDS-PAGE gel of fetal bovine serum (FBS) proteins obtained from ND-70 and ND-120 NP-protein complexes free from excess serum. The control is used to detect possible protein residues from the excess serum. The Mw of the proteins in the standard ladder are reported on the left for reference.

Considering the large number of biomolecules composing the serum, it is not easy to identify the proteins by observing the electrophoretic pattern obtained upon gel running. However some information can be provided by the relative comparison among the different samples (Figure 25 and 26). For example, for NDs corona obtained at higher plasma concentration the gel pattern and the relative intensity are almost equal. Indeed, for the lowest concentration (10%) it can be noticed that some bands appeared, respect to the others, and some other band changed in the intensity.
Among the conditions, the different behavior of the lowest serum concentration was already shown by DCS analysis. Two possible explanations can be suggested:

i. There is a lack of the minimum amount of protein which more specifically bind NDs. To complete the surface coverage, less specific interaction between proteins and NDs can occur.
ii. During the incubation, the kinetics of protein adsorption on NDs surface and NDs aggregation compete. In the case of lower protein concentration, the latter process is favored. The slight differences observed by SDS-PAGE analysis could be associated

to the different geometrical characteristics of NDs (monodispersed vs aggregates) which promotes a different proteins affinity for NDs. An analogues behavior was demonstrated using particles composed by the same material but with different sizes (and curvature).[33]

3.3.5 Protein Corona Identification by Mass Spectrometry

To understand which proteins constitute most to the overall protein coronas, collective results were classified calculating the normalized spectral counts (NSpC, see experimental section) on proteins and plotting the relative abundance as function of:

i. Molecular weight

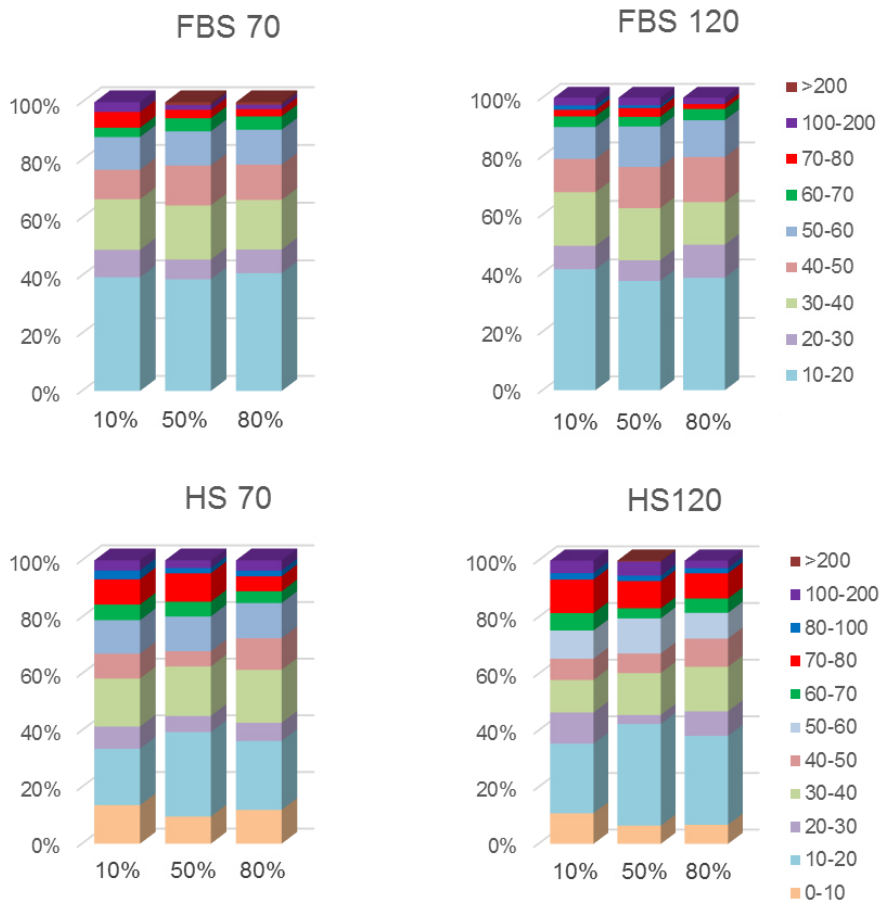

Figure 19. Distribution of molecular weight in FBS (top) and HS (bottom) corona, for ND-70 (left) a ND-120 (right), analyzed by LC-MS/MS. The abundance of protein groups is expressed as protein mass percentage of the total corona proteins.

ii. Classes of proteins

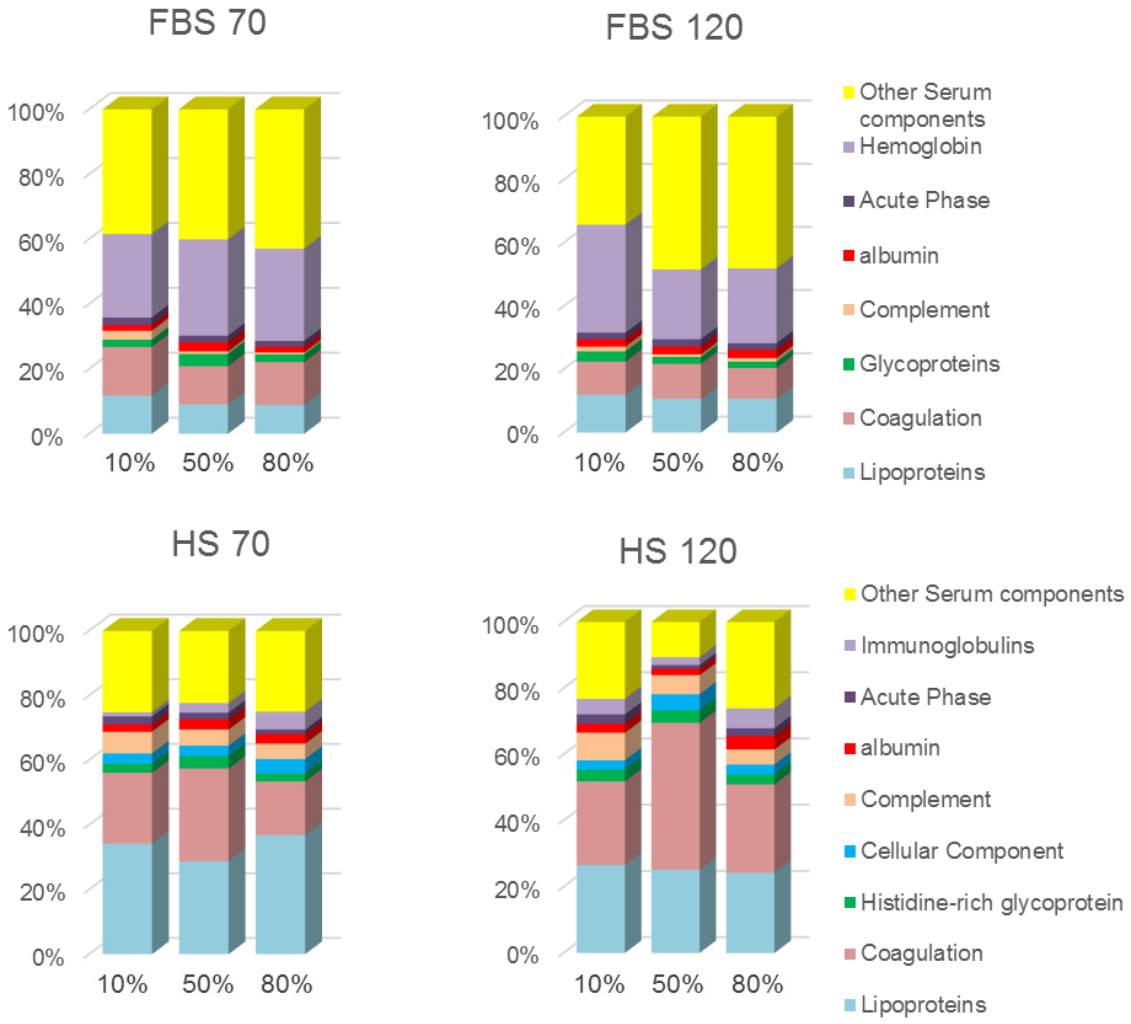

Figure 20. Distribution of protein groups in FBS (top) and HS (bottom) corona, for ND-70 (left) and ND-120 (right), analyzed by LC-MS/MS. The abundance of protein groups is expressed as protein mass percentage of the total corona proteins.

Distribution of molecular weight is a helpful visualization for the SDS-PAGE analysis interpretation. However, for these analysis, slight changes in protein relative abundance belonging to the different ranges of molecular weight are within the experimental error and no trends can be observed among the different plasma concentration. These results are obtained by single measurement for each condition (no replicates) so only qualitative considerations can be done.

Comparing the two sizes of nanodiamonds, it is evident that this parameter does not affect the molecular weight distribution of the proteins. NDs are produced grinding microcrystals, so the particles shape is highly irregular. Not being rounded shaped, it is realistic to think that the "radius" of the particles does not have a particular role on the protein corona composition (for the sizes under investigation).

More interesting is to observe the protein groups which confer the biological identity to the NDs. In fetal bovine serum proteins, hemoglobin abundance prevails respect to all others. It was found a relative concentration higher than 20% for all the explored conditions. High concentration can be detected also for coagulation proteins and lipoproteins. The sum of these groups of protein represent about 50% of the proteins composing the corona.
By the HS protein corona, more than 50% of the total proteins results composed by coagulation proteins and lipoprotein to the same extent. Excluding hemoglobin (which is absent in HS), the main components of protein corona are the same than FBS, but more concentrated. The sum of complement, immunoglobulins, albumin and histidine-rich glycoprotein compose more than 10% of the total proteins.

The most abundant proteins in the corona (for both FBS and HS) as identified by MS analysis based on Normalized spectral counts is reported in Table 2 (a more detailed list is reported in the experimental section, Tables S2 and S3).

Mw (kDa)	Human serum	Mw (kDa)	Fetal bovine serum
5.8767	*Apolipoprotein A-II*	15.184	*Hemoglobin subunit alpha*
30.777	***Apolipoprotein A-I***	15.859	*Hemoglobin fetal subunit beta*
36.154	***Apolipoprotein E***	52.347	*Antithrombin-III*
13.894	*Platelet basic*	35.979	*Apolipoprotein E*
52.602	*Antithrombin-III*	70.505	*Prothrombin*
59.578	*Histidine-rich glycoprotein*	167.57	*Alpha-2-macroglobulin*
10.845	*Platelet factor 4*	69.293	*Serum albumin*

187.15	*Complement C3*	30.276	*Apolipoprotein A-I*
54.305	*Vitronectin*	45.296	*Plasma serine protease inhibitor*
69.366	*Serum albumin*	34.015	*Insulin-like growth factor-binding protein 2*
45.398	*Apolipoprotein A-IV*	22.144	*Tetranectin*
8.647	*Apolipoprotein C-I*	140.37	*Complement factor H*
71.957	*Kininogen-1*	70.993	*Plasma kallikrein*
90.568	*Plasminogen*	248.98	*Coagulation factor V*
11.237	*Ig lambda-3 chain C regions;*	38.418	*Alpha-2-HS-glycoprotein*
70.036	*Prothrombin*	41.792	*Actin, cytoplasmic 2*
70.108	*Coagulation factor*	50.14	*Elongation factor 1-alpha 1*
23.742	*Peptidyl-prolyl cis-trans isomerase B*	35.868	*Glyceraldehyde-3-phosphate dehydrogenase*
16.55	*Angiogenin*	187.25	*Complement C3*

Table 1. Top 20 most abundant proteins identified in the protein corona of NDs assembled respect to FBS and HS (identified among the most common proteins found for both the sizes of NDs and all the serum concentrations).

Noteworthy behavior is shown by the presence of different apolipoproteins (underlined), which are found quite abundant on the surface of NDs incubated with both HS and FBS. For human serum, in particular, a high affinity of NDs for apolipoprotein A and apolipoprotein E was observed. Equally important is the complete absence of apolipoprotein B, which is commonly identified within protein corona of silica nanoparticles.[33]

Considering the ability of apolipoproteins adsorbed on NPs to promotes their prolonged circulation time in blood[33,54] and to interact with specific receptors (depending on the abundance of each apolipoprotein),[36] it can be affirmed that the distinguishing feature of NDs is associated to this class of proteins. However, specific binding with receptors require an appropriate orientation of the adsorbed proteins, hence immunoassay analysis were carried out to understand the targeting ability of NDs-protein corona, focusing the interest on apolipoproteins.

3.3.6 EPITOPE MAPPING OF APOLIPOPROTEINS - FNDS COMPLEX

Apolipoproteins are proteins that bind lipids to form lipoproteins. They transport the lipids through the lymphatic and circulatory systems. Because of their surfactant-like properties, apolipoproteins and other amphipathic molecules (such as phospholipids) can surround the lipids, creating the lipoprotein particle, and can thus be carried through the bloodstream.

There are two major types of apolipoproteins:

i. Apolipoproteins B form low-density lipoprotein (LDL) particles. These proteins have mostly beta-sheet structure and associate with lipids irreversibly.
ii. Most of the other apolipoproteins form high-density lipoprotein (HDL) particles and Apo A-I, in particular, is the main component. These proteins consist of alpha-helices and associate with lipids reversibly. They stabilize the complex by associating to the surface phospholipids. During binding to the lipid particles these proteins change their three-dimensional structure.

In lipid transport, apolipoproteins function as structural components of lipoprotein particles, cofactors for enzymes and ligands for cell-surface receptors. In particular, apoA-I is the major protein component of high-density lipoproteins (Figure 21), and apoE (which composes HDL too) is a blood plasma protein that mediates the transport and uptake of cholesterol and lipids by way of its high affinity interaction with different cellular receptors, including the low-density lipoprotein (LDL) receptor.[55]

The three-dimensional structure of the LDL receptor-binding domain of apoE indicates that the protein forms an unusually elongated four-helix bundle that may be stabilized by a tightly packed hydrophobic core that includes leucine zipper-type interactions and by numerous salt bridges on the mostly charged surface. Basic amino acids important for LDL receptor binding are clustered into a surface patch on one long helix.[56]

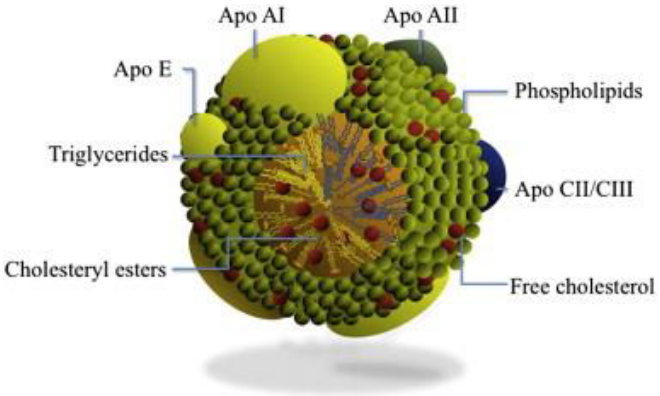

Figure. 21. Schematic representation of HDL structure. HDL are complex macromolecules formed by phospholipids and unesterified (free) cholesterol on the surface, and esterified cholesterol as well as triglycerides in the core. HDL include a heterogeneous group of lipoproteins, which have in common apo AI as the distinctive apolipoprotein.[57]

From mass spectrometry analysis, a high percentage of apolipoproteins was identified into the hard corona composition. However, the only identification of these proteins doesn't give any information about the organization on the nanoparticle surface. More in general, of the biomolecules grafted and adsorbed to nanoparticles, only a small fraction will have biologically relevant peptide sequences facing externally, away from the nanoparticle surface, making difficult to predict how these nanoparticle–corona complexes might further interact with circulating molecules such as antibodies, scaffolding biopolymers, cell receptors, or key structures in organs such as the liver.[48]

In this section the epitope availability of apolipoprotein A-I and apolipoprotein E was investigated using immuno-dot blot and immuno-QD mapping assays[49] As proof of concept, we selected only the ND-corona complexes obtained in human serum.

IMMUNO-DOT BLOT ASSAY

Dot blot assay was used as qualitative test to estimate the relative abundance of available epitopes. Two independent experiments, showed the same intensity trend. Comparing the spots intensity (Figure 22) of the positive reference (top, right), the higher intensity observed for ApoA-I depends by the higher relative abundance of ApoA-I than ApoE in serum.

Bovine serum albumin (BSA) and transferrin (Tf) spots, used as negative references, did not show detectable fluorescence signals, confirming the specificity of the antibody.

The higher intensity signal associated to ApoE compared to ApoA-I suggests a higher number of exposed epitopes for the first.

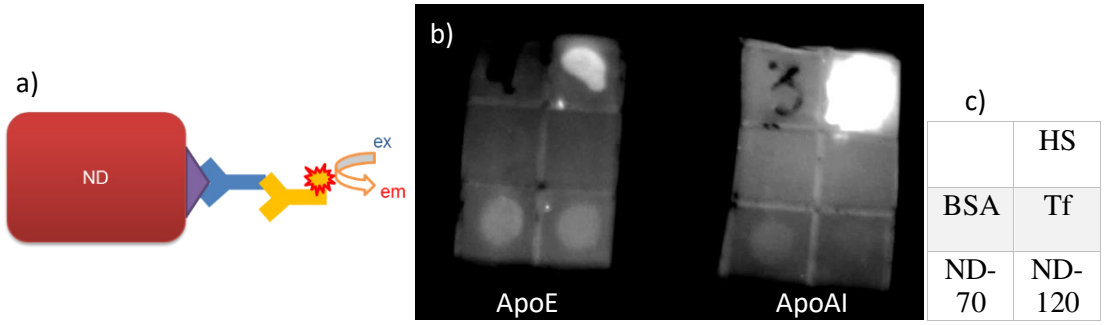

Figure 22. a) Schematic representation of immune dot blot assay. ND (red), exposed epitopes (violet), primary antibody (blue), Alexa 488-labeled secondary antibody (yellow). b) Fluorescence scanning of dot blot experiments carried out on ApoE (left) and ApoA-I (right). c) schematic representation of each spot content, equal for both the membranes.

This is in accordance to mass spectrometry analysis, where apoE resulted more abundant than apoA-I (Table 2). It should be stressed that this correspondence cannot be assumed *a priori*, because the quantification of the adsorbed protein is not necessarily associated to the relative number of accessible epitopes.[48]

	70	120
ApoE	5.00%	3.78%
ApoA-I	4.19%	2.57%

Table 2. Normalized spectral counts of ApoE and ApoA I identified my mass spec analysis for NDs-corona complexes obtained upon incubation into 80% HS.

IMMUNO-QD MAPPING ASSAYS

This technique differs from the previous approach because it only use immunolabelled primary antibody. Anti-Apolipoprotein A-I and anti-Apolipoprotein E monoclonal antibodies were conjugated with an CdTe quantum dot (QD) fluorescent label (Figure 23a).

The synthesis of red emitting CdTe quantum dots, and the following conjugation to the antibody, were carried out at CBNI laboratory by Cristina Lo Giudice and Dr. Ester Polo, following their own developed procedure, recently published.[49]

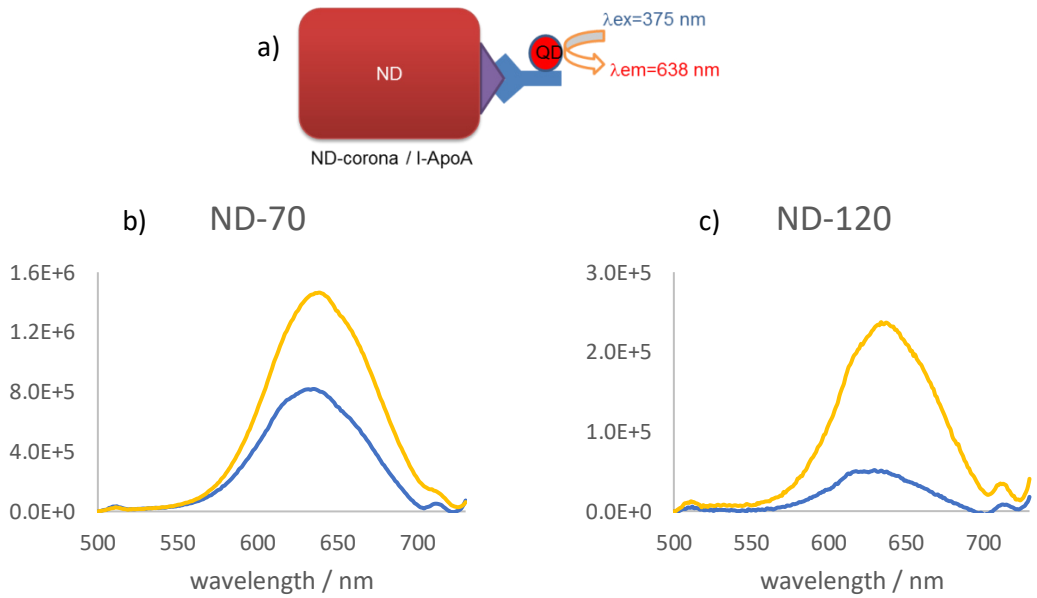

Figure 23. a) Schematic representation of immune-QD assay. ND (red), exposed epitopes (violet), QD-labelled antibody (blue). b,c) Emission spectra of immuno-QDs interacting with ApoA-I (blue) and Apo E (yellow) exposed epitopes, upon excitation at $\lambda = 375$ nm.

Considering that the stoichiometry antibody : QD is 1:1, based on the calibration curve performed on immuno-QD (see experimental section) the quantification of the average number of available epitopes was achieved (Table 3).

ND-HS 80%	**ApoAI**	**ApoE**
70 nm	15.6	25.1
120 nm	12.6	17.8

Table 3. Average number of accessible epitopes (ApoA-I and ApoE) per particle, detected by immuno-QD mapping.

The similar trend suggested by dot blot immunoassay was measured by immuno-QD mapping method. It confirmed that the smaller particles showed an higher number of exposed epitopes. Among the explored conditions, the average number of available epitopes for ApoA-I and ApoE belongs to the same order of magnitude.

In biological fluids, a high affinity between apolipoproteins and ND surface was found, in particular for ApoA-I and ApoE. Furthermore, upon protein-ND interaction, a (residual) number of epitopes involved on cell receptor recognition resulted accessible from the environment.

3.3.7 LONG TERM STABILITY TEST FOR *IN VITRO* STUDIES

So far, most of the characterization were addressed to improve the dispersibility of NDs in biological fluid a many improvements were achieved. A step further is required prior to perform *in vitro* tests, and concern the evaluation (and the possible optimization) of NDs stability in biological media, for a timescale which is compatible with cells culture experiments.

ND-corona complexes were produced with the only difference concerning the use the minimum essential media (MEM) instead of PBS. Taking into account that the minimum serum concentration needed to prevent aggregation was 50%, this concentration was used to carry out the experiments. In order to simulate the real conditions of *in vitro* experiments, after the last wash (in PBS), the samples were recovered in MEM, split in 3 identical tubes e kept incubated at 37 °C in static conditions (no shaking). The triplicate sample assure to perform DCS analysis for each of them at 3 different times points (0, 4, 24 hours) without to interfere with the residual solution, necessary for the next injection.

Essentially, the first time point consists in the immediate measurement upon resuspension in MEM. As expected, the distribution reflects the previous analysis. Except for one condition (70 nm in FBS) after 4 hours of incubation, a significant increase of the average size occurred and consequently, after 24 hours NDs are mostly aggregated (Fig. 24).

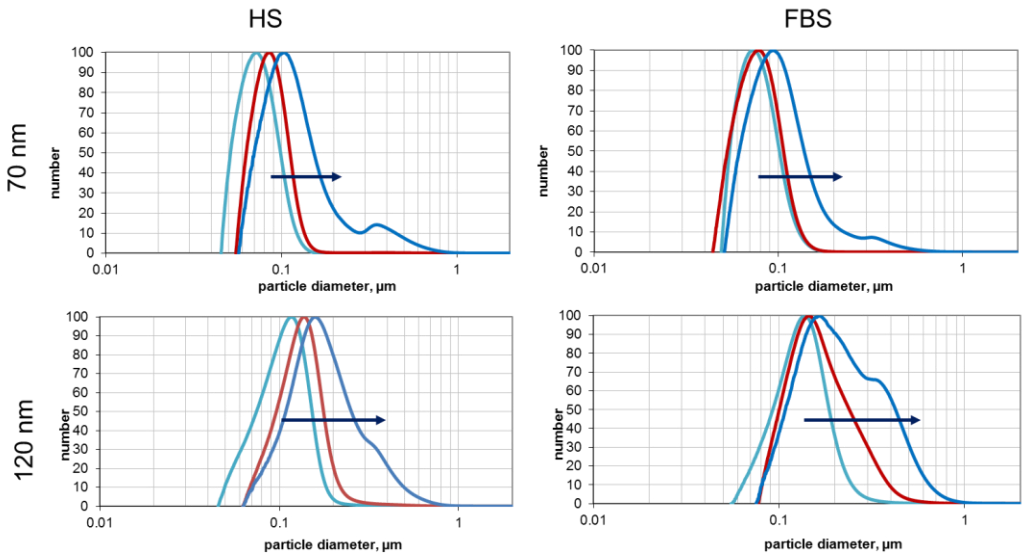

Figure 24. DCS experiments of ND-corona complexes free from excess plasma, resuspended in MEM and kept incubated at 37 °C in static conditions for the following times: 0 (cyan), 4 (red), 24 (blue) hours.

A possible explanation for this behavior could be ascribed to the he high gradient concentration between the ND surface (protein corona) and the serum-free media, acting as driving force to promote proteins desorption. The equilibrium between protein corona and the surrounding proteins plays an important role on hard corona stability and composition, so in this case that equilibrium is lost.

Based on this hypothesis, the same experiment was replicated but resuspending the ND-corona complex in supplemented media (10% and 50% HS). Single point DCS analysis was performed after 24 hours of static incubation at 37 °C. For both of the concentration used to supplement the media, ND-corona complexes resulted stable after 24 hours (Figure 25).

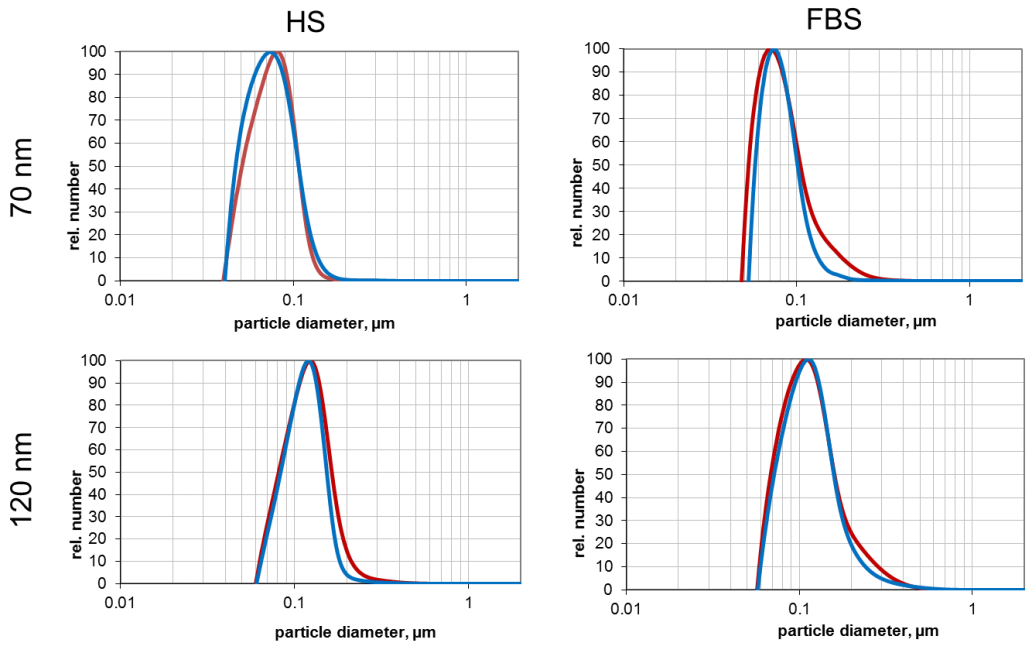

Figure 25. DCS experiments of ND-corona complexes free from excess plasma, resuspended in supplemented MEM (10% HS in red, 50% HS in blue) and kept incubated at 37 °C in static conditions for 24 hours.

The second incubation of the particles in a "fresh" solution could modify the relative abundance of protein corona composition since some protein exchange might occur. SDS-PAGE test was hence performed to check if a significant changes occurred.

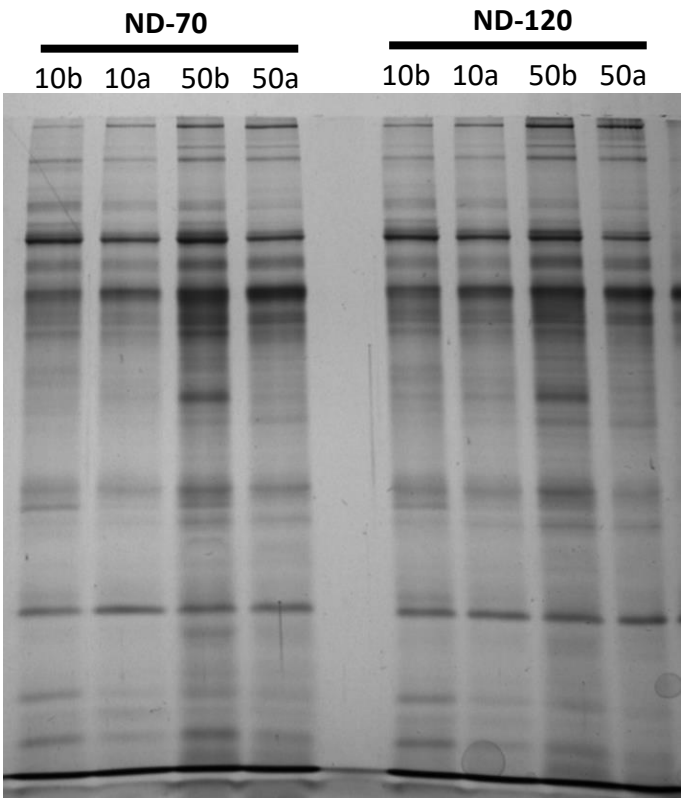

Figure 35. SDS-PAGE gel of FBS proteins obtained from ND-70 and ND-120 NP-protein complexes free from excess serum, resuspended in supplemented MEM (10% and 50% FBS) and kept incubated at 37 °C in static conditions for 24 hours. The b and a subscripts identify the sample obtained before and after the second incubation into the supplemented medium, respectively.

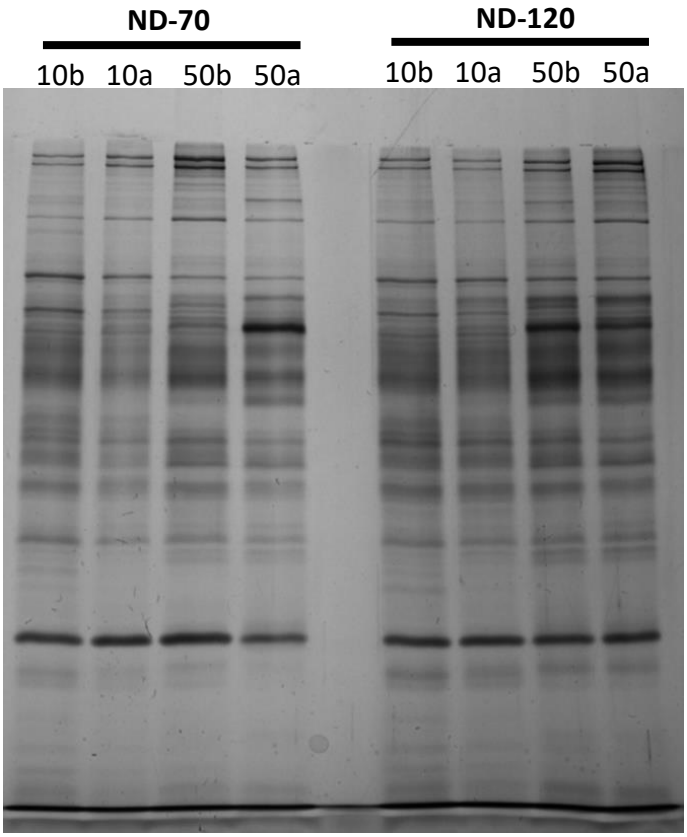

Figure 36. SDS-PAGE gel of HS proteins obtained from ND-70 and ND-120 NP-protein complexes free from excess serum, resuspended in supplemented MEM (10% and 50% HS) and kept incubated at 37 °C in static conditions for 24 hours. The b and a subscripts identify the sample obtained before and after the second incubation in the supplemented medium, respectively.

Considering the longer time of NDs incubation with serum (24 hours) respect to the incubation time usually used to prepare ND-corona complexes a further equilibration can occur. However, apart from few isolated variations, upon the second incubation the overall composition of ND-protein corona was preserved.

CONCLUSIONS

In this work, a protocol for NDs (two sizes: 70 and 120 nm of diameter) dispersion in physiological conditions was set out. DLS and DCS measurements were used to detect the final particles size. The formation of the hard corona, which confers stability to ND and prevents their re-aggregation, was obtained by the incubation of NDs in different concentration of plasma serum (HS and FBS). Stability tests carried out by ND-corona complexes resuspended in supplemented media and incubated for 24 hours demonstrated that the particles sizes were preserved. A step further to the current literature has already been done because the developed protocol permits to use NDs in biological media overcoming the aggregation phenomena typically observed during *in vitro* experiments.

In addition, the interacting proteins were identified by SDS-PAGE and Mass Spectrometry analysis and no significant changes in protein composition related to the different size of the NDs were observed.

Based on Mass Spectrometry analysis, it can be affirmed that the distinguishing feature of NDs-protein corona complex is associated to the high concentration of apolipoproteins. Focusing the interest on two of the most abundant apolipoproteins: apoA-I and apoE, epitopes mapping was performed, using immune-dot blot and immuno-QDs assays. The significant number of exposed epitopes was detected, suggesting that apolipoproteins contribute to the overall biological identity of nanodiamonds.

EXPERIMENTAL SECTION

Differential Centrifugal Sedimentation. Bath sonicator (Ultrasonic Cleaner Elmasonic PH350EL, 100W, 37 kHz, 100% power) has been used to reduce the average size of NDs and the resulting dispersions were then characterized by DCS, using a CPS disc centrifuge DC24000. A 8−24% sucrose density gradient (suitable for the nanoparticle density range used) in milliQ water was used with a disk speed of 20,000 rpm. The particles were measured between 0.001 and 2 μm, with each measurement being calibrated with a PVC standard with a nominal size of 483 nm (Analytic Ltd.). Size distribution of NDs-protein corona complexes were characterized by DCS using the same conditions, but using 8−24% sucrose density gradient in PBS instead of milliQ water.

NDs-protein corona complexes preparation. Two sizes of NDs (ND-70 and ND-120, normalized by number) were incubated with different concentrations of serum solutions (FBS and HS, 10%, 50%, 80% v/v, as shown in Table S1) under continuous shaking for one hour at 37 °C. The samples were centrifuged to pellet the particle-protein complexes and separated from the supernatant. The pellet was then resuspended in 500 μL of PBS and centrifuged again for 15 minutes at 18 krcf at 4°C to pellet the particle-protein complexes. The procedure consists of three successive washing-steps before resuspension of the final pellet to the desired concentration. This treatment allows to get rid of the proteins with low affinity for the NP surface (the soft protein corona).

Fetal Bovin Serum (FBS)		Human Serum (HS)	
NDs 120 nm	NDs 70 nm	NDs 120 nm	NDs 70 nm
100 μg/mL 10% serum	40 μg/mL 10% serum	100 μg/mL 10% serum*	40 μg/mL 10% serum*
100 μg/mL 50% serum	40 μg/mL 50% serum	100 μg/mL 50% serum*	40 μg/mL 50% serum*
100 μg/mL 80% serum	40 μg/mL 80% serum	100 μg/mL 80% serum*	40 μg/mL 80% serum*

Table S1. Cheat sheet of samples prepare to produce ND-protein corona complexes. *HS concentration is normalized to FBS concentration.

SDS-PAGE. ND-protein corona pellet was re-suspended in protein buffer (62.5 mM Tris-HCl pH 6.8, 2% (w/v) SDS, 10% glycerol, 0.04 M DTT and 0.01% (w/v) bromophenol blue), it was then

boiled for 5 minutes at 100 °C and loaded in 4-12% gradient polyacrylamide gel. Gel electrophoresis was performed at 120V, 40 mA for about 60 minutes each, until the proteins neared the end of the gel. The gels were stained following the standard procedure of a silver stain kit, provided by the vendor (CosmoBio). The gels were then scanned using G:Box Chemi XT4 (Syngene).

Mass Spectrometry. Bands of interest from SDS-PAGE gels (12%) were excised and digested in-gel with trypsin according to the method of Shevchenko et al.[58] The resulting peptide mixtures were re-suspended in 0.1% formic acid and analyzed by electrospray liquid chromatography mass spectrometry (LC MS/MS). An HPLC (Surveyor, ThermoFinnigan, CA) was interfaced with an LTQ Orbitrap (ThermoFinnigan, CA). Chromatography buffer solutions (Buffer A, 0.1% formic acid; Buffer B, 100% acetonitrile and 0.1% formic acid) were run using a 72 minute gradient. A flow rate of 150 μL/min was used at the electrospray source. Spectra were searched using BioworksBrowser 3.3.1 SP1 (ThermoFisher Scientific) using Sequest Uniprot/Swiss-Prot database (www.expasy.org).

MS/MS raw files were exported into Microsoft Excel. If the same protein identity was detected in multiple bands from the same sample condition, their SpCs were summed to get the total protein amount. Semi-quantitative analysis was performed converting the spectral counts of the most abundant proteins determined in the NP coronas into normalized spectral counts (NSpC). The SpC of each protein identity was normalized to the protein mass and expressed as the relative protein quantity by applying the following equation:

$$NSpC_k = \left(\frac{\left(\frac{SpC}{M_w}\right)_k}{\sum_{i=1}^{n} \left(\frac{SpC}{M_w}\right)_i} \right) \times 100$$

where $NSpC_k$ is the percentage normalized spectral count for protein k, SpC is the spectral count identified, and M_w is the molecular weight in kDa for protein k. This correction takes into account the protein size and evaluates the real contribution of each protein to the hard corona composition.[59]

Dot-blot immunoassay. ND-corona (80% HS), negatives (BSA and transferrin) an positive (HS) controls were spotted on each of the polyvinylidene fluoride membranes (PVDF). The blots were

blocked in 5 % skimmed milk in PBS for 1 hour at room temperature, washed three times in PBS and incubated with 2 µg/mL of the corresponding antibody, purchased by Santacruz biotechnology (Ab mouse monoclonal anti apo A-I sc-13549, Ab mouse monoclonal anti Apo E sc-393302). After 1 h incubation with the antibody solution in PBS at room temperature, the blots were washed three times for 10 minutes, and incubated with a 1 µg/mL solution of Alexa 488-labeled secondary antibody for 1 hour at room temperature. The blots were washed 5 times, dried and scanned for fluorescence using a G:Box Chemi XT4 (Syngene) to detect the presence of the primary antibody bound to the spots on the membranes.

Immuno-QD mapping. For the immunolabelling experiments 20 µL of ND-corona complex (ND-70 and ND-120, 80% HS) purified by the serum proteins excess, were incubated with an excess of immuno-QDs in PBS (pH 7.4), at 37 °C, for 1 h under constant agitation. After the incubation, the samples were washed by centrifuging at 20,000 rcf and re-suspending in fresh PBS twice, to remove the unbound immunoprobes. The interaction between the immuno-QDs and the nanoparticles coated with the proteins was studied by steady-state fluorescence spectroscopy (Horiba Jobin Yvon Fluorolog-3 fluorimeter using a 45 ml quartz Ultra-Micro cuvette of 3mm path length, Hellma Analytics). For each sample, the emission spectra were recorded at 500-750 nm range (max emission 630 nm), exciting at $\lambda = 375$ nm from a Xenon lamp source.

A set of samples of known QD concentration was measured in the spectrofluorimeter to get a calibration curve for the QD signal in fluorescence spectroscopy (Figure S1).

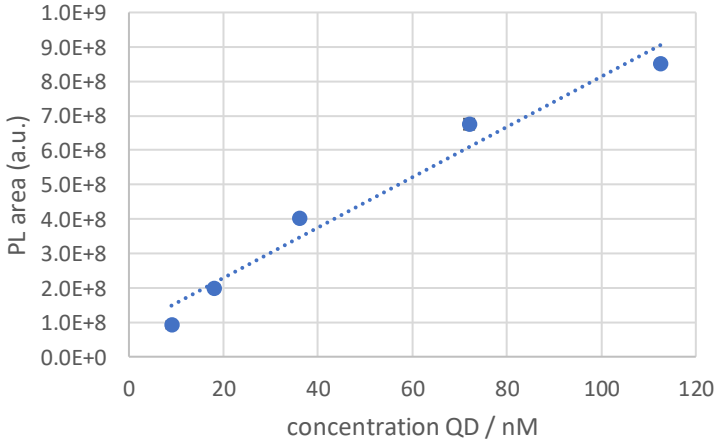

Figure S1. Calibration curve of QDs obtained by steady-state fluorescence spectroscopy. In the vertical axes, the integrated area of the emission bands.

Protein names	weighted counts
ND-70 HS 10%	NSpC
Apolipoprotein A-I	5.89%
Apolipoprotein A-II	5.74%
Apolipoprotein E	5.36%
Antithrombin-III	3.69%
Apolipoprotein C-I	3.41%
Apolipoprotein A-IV	2.88%
Vitronectin;	2.41%
Cystatin-A	2.30%
Histidine-rich glycoprotein	2.12%
Complement C3	1.76%
Serum albumin	1.70%
Prothrombin	1.69%
Protein S100-A8	1.56%
Platelet factor 4	1.56%
Platelet basic protein	1.52%
Dermcidin	1.49%
Insulin-like growth factor-binding protein 3	1.45%
Kininogen-1	1.41%
Clusterin	1.30%

Protein names	weighted counts
ND-120 HS 10%	NSpC
Apolipoprotein A-II	4.23%
Apolipoprotein A-I	3.74%
Apolipoprotein E	3.44%
Platelet basic protein	2.44%
Antithrombin-III	2.23%
Histidine-rich glycoprotein	2.20%
Platelet factor 4	1.87%
Complement C3	1.81%
Vitronectin	1.79%
Serum albumin	1.73%
Apolipoprotein A-IV	1.69%
Apolipoprotein C-I	1.57%
Kininogen-1	1.48%
Plasminogen	1.45%
Ig lambda-3 chain C regions	1.41%
Prothrombin	1.39%
Coagulation factor XI	1.35%
Peptidyl-prolyl cis-trans isomerase B	1.24%
Angiogenin	1.23%

ND-70 HS 50%	NSpC
Apolipoprotein E	5.42%
Platelet basic protein	4.99%
Apolipoprotein A-I	4.90%
Apolipoprotein A-II	4.11%
Platelet factor 4	3.34%
Antithrombin-III	2.92%
Histidine-rich glycoprotein	2.84%
Serum albumin	2.35%
Vitronectin	2.33%
Kininogen-1	2.18%
Apolipoprotein C-I	2.09%
Complement C3	1.98%
Coagulation factor XI	1.98%
Prothrombin	1.90%
Apolipoprotein A-IV	1.86%
Plasminogen	1.37%
Carboxypeptidase B2	1.30%
Ig kappa chain C region	1.18%
Dermcidin	1.07%

ND-120 HS 50%	NSpC
Platelet factor 4	17.17%
Platelet basic protein	12.51%
Apolipoprotein A-I	8.07%
Apolipoprotein A-II	6.34%
Vitronectin	4.80%
Complement C3	3.98%
Kininogen-1	3.80%
Apolipoprotein E	3.78%
Histidine-rich glycoprotein	3.75%
Coagulation factor XI	3.01%
Apolipoprotein C-III	2.29%
Apolipoprotein A-IV	2.19%
Antithrombin-III	2.12%
Serum albumin	1.97%
Prothrombin	1.95%
Clusterin	1.53%
Ig kappa chain C region	1.45%
Plasminogen	1.23%
Complement component C9	1.18%

ND-70 HS 80%	NSpC
Apolipoprotein E	5.00%
Apolipoprotein A-II	4.39%
Apolipoprotein A-I	4.19%
Apolipoprotein C-I	3.28%
Vitronectin	2.90%
Apolipoprotein A-IV	2.73%
Antithrombin-III	2.36%
Ig lambda-3 chain C regions	2.07%
Serum albumin	1.94%
Platelet basic protein	1.86%
Complement C3	1.78%
Histidine-rich glycoprotein	1.56%
Hemoglobin subunit alpha	1.52%
Clusterin	1.43%
Prothrombin	1.29%
Alpha-1-antitrypsin	1.22%
Platelet factor 4	1.19%
Coagulation factor XI	1.14%
Angiogenin	1.09%

ND-120 HS 80%	NSpC
Platelet basic protein	4.70%
Apolipoprotein E	3.78%
Platelet factor 4	3.08%
Ig lambda-3 chain C regions	2.57%
Apolipoprotein A-I	2.57%
Serum albumin	2.43%
Apolipoprotein A-II	2.33%
Antithrombin-III	1.85%
Vitronectin	1.79%
Histidine-rich glycoprotein	1.78%
Prothrombin	1.60%
Complement C3	1.59%
Apolipoprotein A-IV	1.54%
Kininogen-1	1.20%
Coagulation factor XI	1.17%
Plasminogen	1.07%
Apolipoprotein C-I	1.05%
Four and a half LIM domains protein 1	1.05%
Alpha-1-antitrypsin	1.04%

Table S2. Top 20 most abundant proteins identified on ND-70 (left) and ND-120 (right) protein corona (Human Serum).

Protein names	weighted counts
ND-70 FBS 10%	NSpC
Hemoglobin subunit alpha	18.03%
Hemoglobin fetal subunit beta	10.75%
Antithrombin-III	6.61%
Apolipoprotein E	4.88%
Apolipoprotein A-I	4.61%
Plasma serine protease inhibitor	3.65%
Tetranectin	3.27%
Alpha-2-HS-glycoprotein	2.15%
Serum albumin	2.09%
Insulin-like growth factor-binding protein 2	1.97%
Alpha-1-antiproteinase	1.68%
Actin, cytoplasmic 2	1.48%
Glyceraldehyde-3-phosphate dehydrogenase	1.44%
Gelsolin	1.28%
Histone H2B type 1-K	1.12%
Thrombospondin-1	1.08%
Alpha-2-antiplasmin	1.04%
Prothrombin	1.03%
Hemoglobin subunit beta	0.97%

Protein names	weighted counts
ND-120 FBS 10%	NSpC
Hemoglobin subunit alpha	10.38%
Hemoglobin fetal subunit beta	9.44%
Antithrombin-III	6.62%
Apolipoprotein E	4.49%
Apolipoprotein A-I	3.77%
Tetranectin	3.74%
Plasma serine protease inhibitor	3.31%
Prothrombin	3.19%
Actin, cytoplasmic 2	2.55%
Insulin-like growth factor-binding protein 2	1.85%
Histone H2B type 1-K	1.70%
Glyceraldehyde-3-phosphate dehydrogenase	1.54%
Serum albumin	1.48%
Apolipoprotein A-II	1.41%
Alpha-1-antiproteinase	1.28%
Plasma kallikrein	1.28%
Hemoglobin subunit beta	1.23%
Alpha-2-macroglobulin	1.13%
Alpha-2-HS-glycoprotein	1.13%

ND-70 FBS 50%	NSpC
Hemoglobin fetal subunit beta	8.31%
Hemoglobin subunit alpha	7.68%
Antithrombin-III	6.29%
Apolipoprotein E	3.94%
Plasma serine protease inhibitor	3.80%
Apolipoprotein A-I	3.52%
Actin, cytoplasmic 2	2.18%
Histone H2A.J	2.17%
Glyceraldehyde-3-phosphate dehydrogenase	1.98%
Serum albumin	1.97%
Prothrombin	1.87%
Histone H2B type 1-K	1.83%
Alpha-1-antiproteinase	1.65%
Elongation factor 1-alpha 1	1.62%
Ras-related protein Rap-1A	1.45%
Tetranectin	1.37%
Histone H4	1.34%
Hemoglobin subunit beta	1.27%
Eukaryotic translation initiation factor 5A-1	1.20%

ND-120 FBS 50%	NSpC
Hemoglobin subunit alpha	14.54%
Hemoglobin fetal subunit beta	7.59%
Antithrombin-III	5.56%
Apolipoprotein E	4.18%
Plasma serine protease inhibitor	3.77%
Apolipoprotein A-I	3.15%
Alpha-2-HS-glycoprotein	3.00%
Serum albumin	2.32%
Alpha-1-antiproteinase	1.96%
Actin, cytoplasmic 2	1.92%
Glyceraldehyde-3-phosphate dehydrogenase	1.82%
Histone H2B type 1-K	1.81%
Histone H4	1.77%
Prothrombin	1.49%
Elongation factor 1-alpha 1	1.30%
Hemoglobin subunit beta	1.26%
Tetranectin	1.13%
Carboxypeptidase B2	1.13%
Secreted phosphoprotein 24	0.87%

ND-70 FBS 80%	NSpC
Hemoglobin fetal subunit beta	9.25%
Hemoglobin subunit alpha	8.58%
Antithrombin-III	5.60%
Apolipoprotein E	3.77%
Plasma serine protease inhibitor	3.60%
Apolipoprotein A-I	3.59%
Histone H2A.J	2.32%
Actin, cytoplasmic 2	2.08%
Serum albumin	2.04%
Histone H2B type 1-K	1.96%
Alpha-1-antiproteinase	1.77%
Ras-related protein Rap-1A	1.55%
Elongation factor 1-alpha 1	1.52%
Glyceraldehyde-3-phosphate dehydrogenase	1.51%
Integrin-linked protein kinase	1.37%
Cysteine and glycine-rich protein 1	1.32%
Prothrombin	1.31%
Flavin reductase (NADPH)	1.23%
Carboxypeptidase B2	1.11%

ND-120 FBS 80%	NSpC
Hemoglobin subunit alpha	11.15%
Hemoglobin fetal subunit beta	10.38%
Antithrombin-III	6.38%
Apolipoprotein E	4.18%
Plasma serine protease inhibitor	3.43%
Apolipoprotein A-I	2.95%
Histone H4	2.48%
Histone H2A.J	2.01%
Glyceraldehyde-3-phosphate dehydrogenase	1.97%
Actin, cytoplasmic 2	1.91%
Prothrombin	1.53%
Serum albumin	1.49%
Histone H2B type 1-K	1.36%
GTP-binding nuclear protein	1.35%
Alpha-2-HS-glycoprotein	1.35%
Alpha-1-antiproteinase	1.22%
Hemoglobin subunit beta	1.18%
Elongation factor 1-alpha 1	1.13%
Tetranectin	1.06%

Table S3. Top 20 most abundant proteins identified on ND-70 (left) and ND-120 (right) protein corona (Fetal Bovine Serum).

REFERENCES

1. Montalti, M., Cantelli, A. & Battistelli, G. Nanodiamonds and silicon quantum dots: ultrastable and biocompatible luminescent nanoprobes for long-term bioimaging. *Chem. Soc. Rev.* **44,** 4853–921 (2015).

2. Tsoi, K. M., Dai, Q., Alman, B. A. & Chan, W. C. W. Are Quantum Dots Toxic? Exploring the Discrepancy Between Cell Culture and Animal Studies. *Acc. Chem. Res.* **46,** 662–671 (2013).

3. Shu-Jung Yu, Ming-Wei Kang, Huan-Cheng Chang, Kuan-Ming Chen, and & Yu, Y.-C. Bright Fluorescent Nanodiamonds: No Photobleaching and Low Cytotoxicity. (2005). doi:10.1021/JA0567081

4. Vaijayanthimala, V. & Chang, H.-C. Functionalized fluorescent nanodiamonds for biomedical applications. *Nanomedicine* **4,** 47–55 (2009).

5. Bradac, C. *et al.* Observation and control of blinking nitrogen-vacancy centres in discrete nanodiamonds. *Nat. Nanotechnol.* **5,** 345–349 (2010).

6. Tisler, J. *et al.* Fluorescence and Spin Properties of Defects in Single Digit Nanodiamonds. *ACS Nano* **3,** 1959–1965 (2009).

7. Bradac, C. *et al.* Effect of the Nanodiamond Host on a Nitrogen-Vacancy Color-Centre Emission State. *Small* **9,** 132–139 (2013).

8. Walker, J. Optical absorption and luminescence in diamond. *Reports Prog. Phys.* **42,** 1605–1659 (1979).

9. Boudou, J.-P. *et al.* High yield fabrication of fluorescent nanodiamonds. *Nanotechnology* **20,** 235602 (2009).

10. Campbell, B., Choudhury, W., Mainwood, A., Newton, M. & Davies, G. Lattice damage caused by the irradiation of diamond. *Nucl. Instruments Methods Phys. Res. Sect. A Accel. Spectrometers, Detect. Assoc. Equip.* **476,** 680–685 (2002).

11. Chang, Y.-R. *et al.* Mass production and dynamic imaging of fluorescent nanodiamonds. *Nat. Nanotechnol.* **3,** 284–288 (2008).

12. Mochalin, V. N., Shenderova, O., Ho, D. & Gogotsi, Y. The properties and applications of nanodiamonds. *Nat. Nanotechnol.* **7,** 11–23 (2011).

13. Davies, G., Lawson, S. C., Collins, A. T., Mainwood, A. & Sharp, S. J. Vacancy-related centers in diamond. *Phys. Rev. B* **46,** 13157–13170 (1992).

14. Wang, L. V. & Hu, S. Photoacoustic Tomography: In Vivo Imaging from Organelles to Organs. *Science (80-.).* **335,** (2012).

15. Rondin, L. *et al.* Surface-induced charge state conversion of nitrogen-vacancy defects in nanodiamonds. *Phys. Rev. B* **82,** 115449 (2010).

16. Vaijayanthimala, V. *et al.* The long-term stability and biocompatibility of fluorescent nanodiamond as an in vivo contrast agent. *Biomaterials* **33,** 7794–7802 (2012).

17. Kuo, Y., Hsu, T.-Y., Wu, Y.-C. & Chang, H.-C. Fluorescent nanodiamond as a probe for the intercellular transport of proteins in vivo. *Biomaterials* **34,** 8352–60 (2013).

18. Smith, B. R., Niebert, M., Plakhotnik, T. & Zvyagin, A. V. Transfection and imaging of diamond nanocrystals as scattering optical labels. *J. Lumin.* **127,** 260–263 (2007).

19. Nguyen, T.-T.-B., Chang, H.-C. & Wu, V. W.-K. Adsorption and hydrolytic activity of lysozyme on diamond nanocrystallites. *Diam. Relat. Mater.* **16,** 872–876 (2007).

20. Fang, C.-Y. *et al.* The exocytosis of fluorescent nanodiamond and its use as a long-term cell tracker. *Small* **7,** 3363–70 (2011).

21. Weng, M.-F., Chiang, S.-Y., Wang, N.-S. & Niu, H. Fluorescent nanodiamonds for specifically targeted bioimaging: Application to the interaction of transferrin with transferrin receptor. *Diam. Relat. Mater.* **18,** 587–591 (2009).

22. Lim, J. K., Majetich, S. A. & Tilton, R. D. Stabilization of Superparamagnetic Iron Oxide Core−Gold Shell Nanoparticles in High Ionic Strength Media. *Langmuir* **25,** 13384–13393 (2009).

23. Tzeng, Y.-K. *et al.* Superresolution imaging of albumin-conjugated fluorescent nanodiamonds in cells by stimulated emission depletion. *Angew. Chem. Int. Ed. Engl.* **50,** 2262–5 (2011).

24. Chang, B.-M. *et al.* Highly Fluorescent Nanodiamonds Protein-Functionalized for Cell Labeling and Targeting. *Adv. Funct. Mater.* **23,** 5737–5745 (2013).

25. X. L. Kong *et al.* High-Affinity Capture of Proteins by Diamond Nanoparticles for Mass Spectrometric Analysis. (2004). doi:10.1021/AC048971A

26. Faklaris, O. *et al.* Photoluminescent Diamond Nanoparticles for Cell Labeling: Study of the Uptake Mechanism in Mammalian Cells. doi:10.1021/nn901014j

27. Cedervall, T. *et al.* Understanding the nanoparticle-protein corona using methods to quantify exchange rates and affinities of proteins for nanoparticles. *Proc. Natl. Acad. Sci. U. S. A.* **104,** 2050–5 (2007).

28. Monopoli, M. P., Åberg, C., Salvati, A. & Dawson, K. A. Biomolecular coronas provide the biological identity of nanosized materials. *Nat. Nanotechnol.* **7,** 779–786 (2012).

29. Walczyk, D., Bombelli, F. B., Monopoli, M. P., Lynch, I. & Dawson, K. A. What the Cell 'Sees' in Bionanoscience. *J. Am. Chem. Soc.* **132,** 5761–5768 (2010).

30. Lynch, I., Salvati, A. & Dawson, K. A. Protein-nanoparticle interactions: What does the cell see? *Nat. Nanotechnol.* **4,** 546–547 (2009).

31. Cedervall, T. *et al.* Detailed Identification of Plasma Proteins Adsorbed on Copolymer Nanoparticles. *Angew. Chemie Int. Ed.* **46,** 5754–5756 (2007).

32. Zhang, H. *et al.* Quantitative proteomics analysis of adsorbed plasma proteins classifies nanoparticles with different surface properties and size. *Proteomics* **11,** 4569–4577 (2011).

33. Monopoli, M. P. *et al.* Physical−Chemical Aspects of Protein Corona: Relevance to in Vitro and in Vivo Biological Impacts of Nanoparticles. *J. Am. Chem. Soc.* **133,** 2525–2534 (2011).

34. Lundqvist, M. *et al.* The Evolution of the Protein Corona around Nanoparticles: A Test Study. *ACS Nano* **5,** 7503–7509 (2011).

35. Salvati, A. Experimental and theoretical comparison of intracellular import of polymeric nanoparticles and small molecules: towards models of uptake kinetics. *Nanomed. Nanotechnol. Biol. Med.* **7,** 816–826 (2011).

36. Lara, S. *et al.* Identification of Receptor Binding to the Biomolecular Corona of Nanoparticles. doi:10.1021/acsnano.6b07933

37. Ge, C. *et al.* Binding of blood proteins to carbon nanotubes reduces cytotoxicity. *Proc. Natl. Acad. Sci. U. S. A.* **108,** 16968–73 (2011).

38. Lesniak, A. *et al.* Effects of the Presence or Absence of a Protein Corona on Silica Nanoparticle Uptake and Impact on Cells. *ACS Nano* **6,** 5845–5857 (2012).

39. Hu, W. *et al.* Protein Corona-Mediated Mitigation of Cytotoxicity of Graphene Oxide. *ACS Nano* **5,** 3693–3700 (2011).

40. Lacerda, S. H. D. P. *et al.* Interaction of Gold Nanoparticles with Common Human Blood Proteins. *ACS Nano* **4,** 365–379 (2010).

41. Tenzer, S. *et al.* Nanoparticle Size Is a Critical Physicochemical Determinant of the Human Blood Plasma Corona: A Comprehensive Quantitative Proteomic Analysis. *ACS Nano* **5,** 7155–7167 (2011).

42. Nanda, K. K., Maisels, A., Kruis, F. E., Fissan, H. & Stappert, S. Higher surface energy of free nanoparticles. *Phys. Rev. Lett.* **91,** 106102 (2003).

43. Lundqvist, M. Nanoparticle size and surface properties determine the protein corona with possible implications for biological impacts. *Proc. Natl Acad. Sci. USA* **105,** 14265–14270 (2008).

44. Chakraborty, S. Contrasting effect of gold nanoparticles and nanorods with different surface modifications on the structure and activity of bovine serum albumin. *Langmuir* **27,** 7722–7731 (2011).

45. Dutta, D. Adsorbed proteins influence the biological activity and molecular targeting of nanomaterials. *Toxicol. Sci.* **100,** 303–315 (2007).

46. Kapralov, A. A. Adsorption of surfactant lipids by single-walled carbon nanotubes in mouse lung upon pharyngeal aspiration. *ACS Nano* **6,** 4147–4156 (2012).

47. Zeng, Z. Synthetic polymer nanoparticle-polysaccharide interaction: a systematic study. *J. Am. Chem. Soc.* **134,** 2681–2690 (2012).

48. Kelly, P. M. *et al.* Mapping protein binding sites on the biomolecular corona of nanoparticles. *Nat. Nanotechnol.* **10,** 472–479 (2015).

49. Lo Giudice, M. C., Herda, L. M., Polo, E. & Dawson, K. A. In situ characterization of nanoparticle biomolecular interactions in complex biological media by flow cytometry. *Nat. Commun.* **7,** 13475 (2016).

50. Hunter, R. J. Foundations of Colloid Science. (2001).

51. Shang, W. *et al.* Cytochrome *c* on Silica Nanoparticles: Influence of Nanoparticle Size on Protein Structure, Stability, and Activity. *Small* **5,** 470–476 (2009).

52. Mirshafiee, V., Kim, R., Mahmoudi, M. & Kraft, M. L. The importance of selecting a proper biological milieu for protein corona analysis in vitro: Human plasma versus human serum. *Int. J. Biochem. Cell Biol.* **75,** 188–195 (2016).

53. Corbo, C. *et al.* Personalized protein corona on nanoparticles and its clinical implications. *Biomater. Sci.* **5,** 378–387 (2017).

54. Kreuter, J. Influence of the Surface Properties on Nanoparticle-Mediated Transport of Drugs to the Brain. *J. Nanosci. Nanotechnol.* **4,** 484–488 (2004).

55. Saito, H., Lund-Katz, S. & Phillips, M. C. Contributions of domain structure and lipid interaction to the functionality of exchangeable human apolipoproteins. *Prog. Lipid Res.* **43,** 350–380 (2004).

56. Wilson, C., Wardell, M. . R. R. R., Weisgraber, K. . H. H. H., Mahley, R. . W. W. W. & Agard, D. A. A. A. A. Three-dimensional structure of the LDL receptor-binding domain of human apolipoprotein E. *Science* **252,** 1817–1822 (1991).

57. Pérez-Méndez, Ó., Pacheco, H. G., Martínez-Sánchez, C. & Franco, M. HDL-cholesterol in coronary artery disease risk: Function or structure? *Clin. Chim. Acta* **429,** 111–122 (2014).

58. Shevchenko, A., Wilm, M., Vorm, O. & Mann, M. Mass Spectrometric Sequencing of Proteins from Silver-Stained Polyacrylamide Gels. *Anal. Chem.* **68,** 850–858 (1996).

59. Walczyk, D., Baldelli Bombelli, F., Monopoli, M. P., Lynch, I. & Dawson, K. A. What the cell 'sees' in bionanoscience. *J. Am. Chem. Soc.* **132,** 5761–5768 (2010).

CHAPTER 4

CALCITE - GRAPHENE NANOCOMPOSITES FOR TECHNOLOGICAL APPLICATIONS

INTRODUCTION

Among CNMs, because of its distinctive mechanical features (high strength and toughness) and physicochemical properties (high surface area, electrical and thermal conductivities, low weight), graphene is a promising material for the fabrication of novel carbon-based nanocomposites.[1–3]
Biominerals formed in the process of biomineralization are also nanocomposites:[4–6] for example $CaCO_3$ is found as skeletal parts in many organisms such as echinoderms, mollusks and crustaceans. The inclusion of biological macromolecules within the $CaCO_3$ lattice generates complex composites with enhanced mechanical and optical properties.[7–11] These intra-crystalline organic macromolecules are responsible for the sophisticated morphologies and the increased fracture toughness of these biogenic crystals.[12–15] They usually form 2D periodic layers inside the host crystals.[16–18]
Taking advantage of the high capability of calcite to interact with a wide variety of molecules, in this work, the incorporation of graphene into the crystalline lattice of single crystals of calcite was performed, following a biological inspired synthetic procedure. Because of the hydrophobic nature of graphene, two approaches were used to disperse it in water:

i. Covalent: using water dispersible graphene oxide (section 4.1);
ii. Non-covalent: exfoliating graphite with tryptophan or N-acetyl-D-glucosamine to produce graphene/biomolecule stable adducts (section 4.2).

In both the cases it was possible to incorporate the 2D materials within a 3D crystal lattice, producing a new material possessing new optical and mechanical properties. The morphology of calcite host resulted altered when the carbon-based dopant was introduced into its lattice.

4.1. BIOINSPIRED NANOCOMPOSITES: ORDERED 2D MATERIALS WITHIN A 3D LATTICE

This chapter is based on a peer-reviewed publication:
Adv. Funct. Mater., 26: 5569–5575. doi:10.1002/adfm.201601318

Matteo Di Giosia, Iryna Polishchuk, Eva Weber, Simona Fermani, Luca Pasquini, Nicola M. Pugno, Francesco Zerbetto, Marco Montalti, Matteo Calvaresi, Giuseppe Falini*, Boaz Pokroy*

RESULTS AND DISCUSSION

The hybrid GO/calcite crystals that we grew were characterized structurally, spectroscopically, and mechanically in order to investigate the mechanism by which the intercalation of a 2D material into a 3D lattice alters the chemical and physical properties of both the host and the guest.

First, we developed an optimal procedure for entrapping GO sheets into the single crystals of calcite (see Experimental Section). Once the hybrid crystals were successfully grown we used high-resolution scanning electron microscopy (HRSEM) to study their morphologies. Figure 1 shows some GO sheets and flakes emerging from the hybrid crystals (see arrows in Figure 1B,D). This was confirmed by energy-dispersive X-ray spectroscopy (EDS) performed directly on those regions that are clearly carbon rich (35.55 ± 0.62 wt% of carbon as compared to 8.74 ± 0.42 wt% on the regions without GO flakes). In contrast to the sharp edges of the pure calcite crystals that serve as a control (Figure 1A), the GO/calcite crystals demonstrate a layered structure, possibly indicating a layered distribution of the GO sheets entrapped within the crystal (Figure 1B,D).

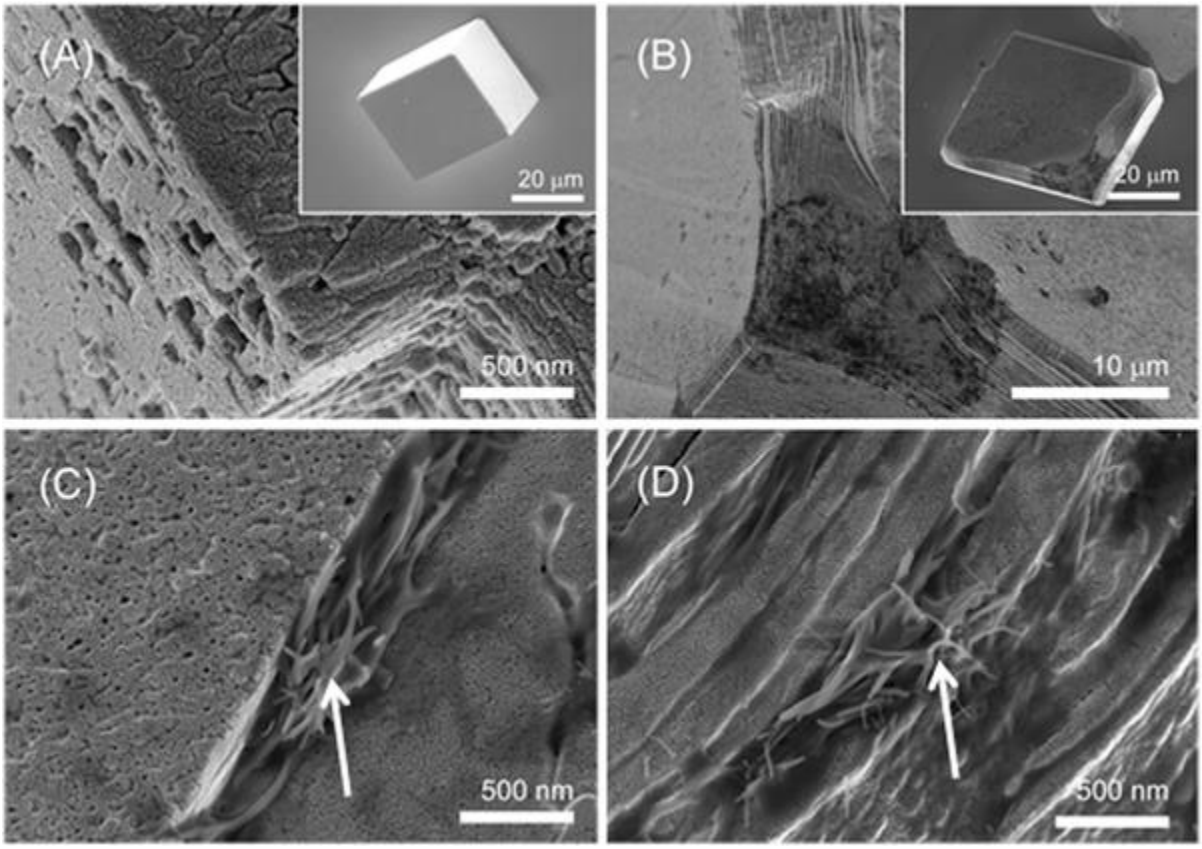

Figure 1. Representative HRSEM images of calcite single crystals. A) Pure calcite crystal grown in the absence of an additive. The crystal exhibits a stepped surface as a result of the extensive washing process in deionized water that gently etches the surface. GO/Calcite hybrid single crystal imaged at different magnifications on C) the surface and at B–D) the edge regions. Insets show corresponding images at low magnification. Arrows indicate GO flakes emerging from the crystal.

The crystal structure of GO/calcite crystals at the atomic scale was further studied by means of state-of-the-art high-resolution aberration-corrected transmission electron microscopy (HRTEM). Our findings indicated that individual calcite crystals grown in the presence of GO are indeed single crystalline. HRTEM image (Figure 2A) demonstrates lattice fringes with a *d*-spacing of 3.9 Å, which corresponds to the {012} planes. The inset in Figure 2A displays the fast Fourier transforms (FFT) of the corresponding TEM image. As can be seen the FFT generated fits that of a single crystal (inset in Figure 2A). To investigate the apparent distribution of occluded GO sheets on the nanometer scale, we further employed scanning-TEM (STEM) coupled with a high-angle annular dark-field imaging (HAADF) detector, thus enabling imaging with chemical contrast. HAADF-STEM images obtained for the hybrid GO/calcite crystals elegantly revealed a layered distribution of the GO sheets, imaged here as darker stripes owing to their lower atomic number

(*Z*) than that of the calcite matrix (Figure 2B, arrows). Imaging of the control calcite by the same technique revealed no such contrast (Figure 2C). The striped distribution of GO sheets observed on the HAADF-STEM images of the GO/calcite sample correlates well with the layered structure of the hybrid crystal edges observed on HRSEM (Figure 1D).

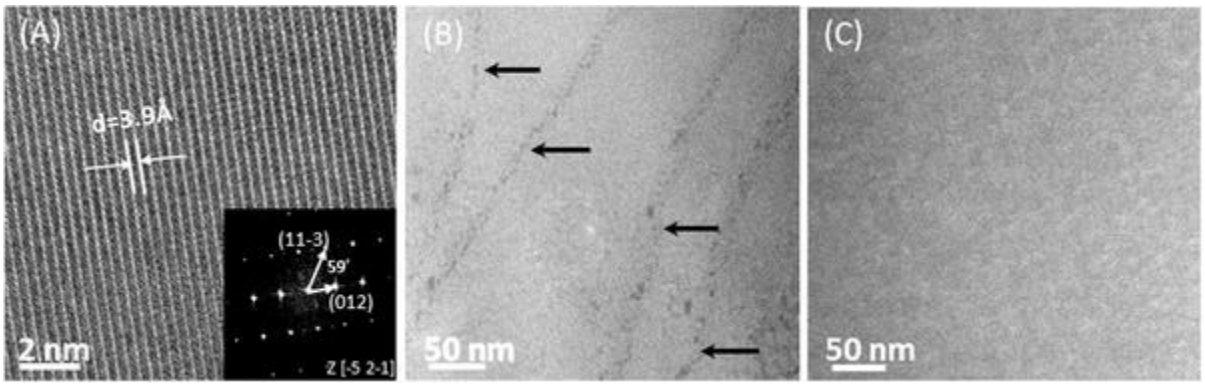

Figure 2. A) HRTEM image of GO/calcite thin sample prepared by FIB and the corresponding fast Fourier transform (FFT) over the entire region. B) HAADF-STEM image of calcite with embedded GO sheets appearing as dark stripes (see indicating arrows), and of pure calcite showing no C) Z-contrast.

Incorporation of various organic molecules into an inorganic host is widely accepted to lead to lattice distortions and unique microstructures.[19] Therefore, to determine plausible effects of the inclusion of GO on the calcite crystal lattice we performed high-resolution synchrotron powder X-ray diffraction (HRPXRD) at a dedicated synchrotron beam line (ID22 of the European Synchrotron Research Facility (ESRF), Grenoble, France) at a wavelength of 0.39970(8)Å. Both the control and the composite crystals exhibited a pure calcite phase (Figure 3A). Diffraction patterns revealed considerable structural differences between the lattice parameters of GO/calcite and those of the pure $CaCO_3$. The observed shift in XRD peak positions towards smaller 2θ values, shown here only for the {111} reflection (Figure 3B), strongly supports incorporation of GO into the calcite crystal lattice. Similar behavior associated with incorporation phenomena was previously demonstrated on different synthetic calcite systems occluding various types of organic matter.[3,20,21]

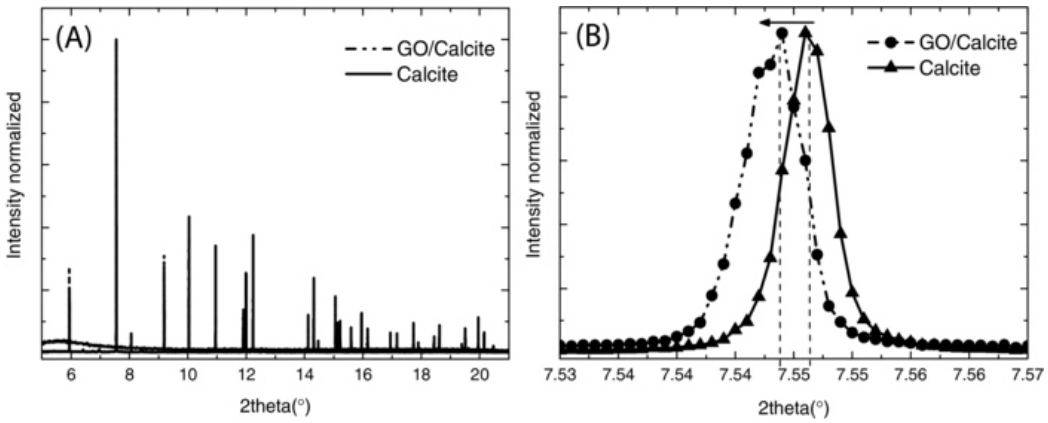

Figure 3. A) HRPXRD patterns of pure calcite (solid line) and hybrid GO/calcite (dashed line) crystals. B) Difference between the {104} reflection of the hybrid GO/calcite crystal relative to the control sample.

Rietveld structure refinement of the experimental data enabled us to precisely extract the lattice parameters and estimate the magnitude of the lattice distortions produced after entrapment of the GO sheets. The observed increase in the *c*-parameter of the hybrid calcite crystal resulted in positive lattice distortions of $4.23*10^{-4}$ relative to the pure $CaCO_3$. By contrast, the slight decrease in *a,b*-parameters led to negative lattice distortions with a significantly lower magnitude of $-9.32*10^{-5}$ (Table 1).

Sample	*a, b*-parameter [Å]	Distortions *a,b*-axes	*c*-parameter [Å]	Distortions *c*-axis	Unit cell volume [Å^3]	χ^2
Calcite	4.990914(6)	–	17.065653(8)	–	368.14	2.259
GO/calcite	4.990449(4)	−9.32E-05	17.072865(5)	4.23E-04	368.23	1.606

Table 1. Lattice parameters, induced lattice distortions, unit cell volume, and goodness of fit parameter

We next investigated the emission properties of GO upon its inclusion within the calcite crystals. Figure 4A shows the emission spectrum of a GO/calcite hybrid single crystal. The spectrum fits well to the GO emission reported in aqueous solvents.[22,23] Notice that the emission spectrum was recorded locally on the crystal collecting the emission that arises from a section of ≈2 μm in diameter and that it did not change significantly when collected from different points on the crystal. Using time-correlated single photon counting (TCSPC), we also investigated the excited-state decay upon pulsed laser excitation at 405 nm. A multi-exponential decay was obtained, as shown in Figure B. The trace was fitted with a tri-exponential model that derived lifetimes of τ_1 = 1.0 ns (48%), τ_2 = 9.3 ns (13%), τ_3 = 3.8 ns (39%), and hence an average lifetime

of 3.2 ns. The 9.3 ns component of the decay is considerably longer than that previously observed for GO, which was in the range of picoseconds to a maximum of 2 ns.[22] Such an increase in the decay time might result from either the effect of the crystal's local polarity or the matrix rigidity that slows down the non-radiative deactivation rates of GO.[22,24]

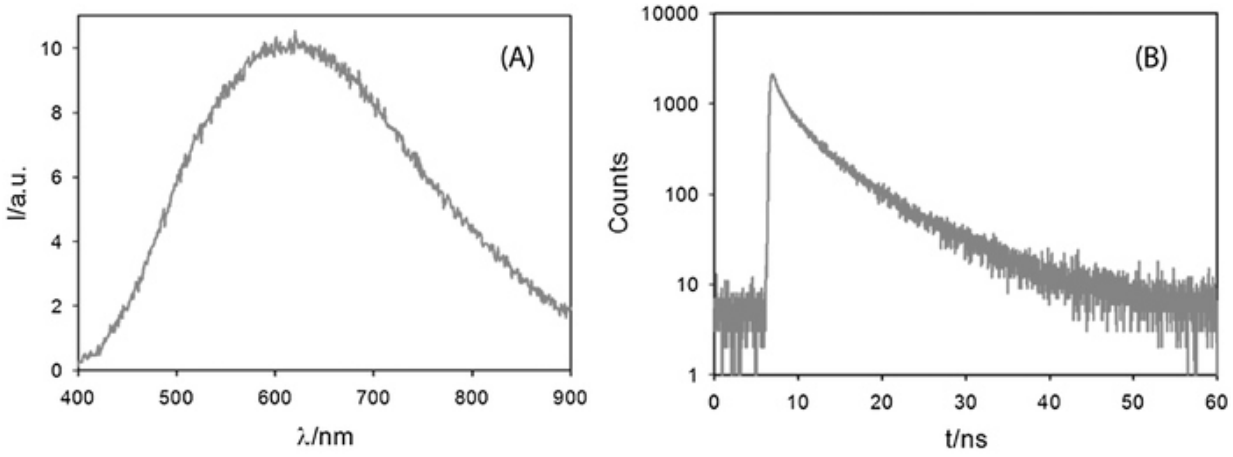

Figure 4. A) Local fluorescence spectrum of GO-doped calcite upon excitation at 405 nm. B) Excited-state decay of fluorescence in a GO-doped calcite crystal.

Transmission optical and fluorescence images of calcite crystals grown in the absence and in the presence of GO are compared in Figure 5. In the fluorescence detection mode, pure calcite shows almost no signal (Figure 5D), whereas fluorescence is clearly detectable in the GO/calcite hybrid single crystal (Figure 5B). We performed these experiments utilizing an electron-multiplying charge coupled device (EMCCD) camera for image acquisition. A steady-state fluorescence spectroscope and a TCSPC apparatus were coupled with the optical microscope to record the local emission spectrum of GO in the crystals.

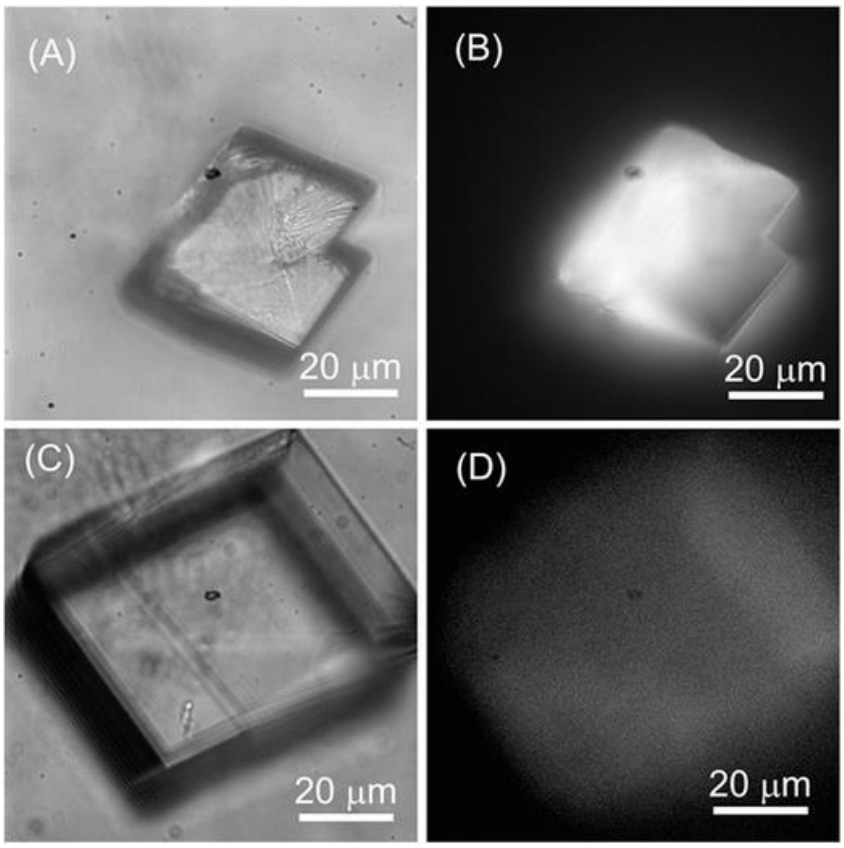

Figure 5. Transmission optical images of calcite crystals grown in the presence A) and in the absence C) of GO. On the right B) and D) are the corresponding transmission fluorescence images upon excitation at 405 nm.

These fluorescence imaging experiments again clearly indicate that GO is incorporated into the single crystal of calcite, and show that GO confers a new property on the calcite host. An optical micrograph and its corresponding crossed polarizer optical micrograph of several calcium carbonate single crystals precipitated in the presence of GO are observed. This experiment is yet another proof of the single crystallinity nature of the hybrid crystals.

Finally, we examined the mechanical properties of GO/calcite single crystals by nanoindentation testing[25] and analyzed the findings in comparison to those of control calcite crystals. To determine the elastic modulus (E_{IT}) and hardness (H_{IT}) as functions of the indentation depth, we analyzed the load/depth oscillations superimposed on the loading portion of the curve. Maximum indentation depths were measured at 200, 300, or 400 nm. From the data reported in Table 2, it appears that the two samples exhibited different values of E_{IT} and H_{IT}. The presence of GO in the crystalline lattice produced an average decrease in E_{IT} of about 12.5% and an increase in H_{IT} of about 12.8%.

This change was not affected by the indentation depth. Similar trends of decrease in elastic modulus and increase in hardness have been observed in an artificial biomineral.[12]

	E_{IT} [GPa]			H_{IT} [GPa]		
Material	**200**	**300**	**400**	**200**	**300**	**400**
GO/calcite	59.3 ± 4.5	55.7 ± 3.4	53.3 ± 3.7	4.40 ± 0.84	4.12 ± 0.85	4.16 ± 0.89
Calcite	67.3 ± 2.7	63.9 ± 2.3	61.2 ± 2.4	3.82 ± 0.42	3.70 ± 0.49	3.72 ± 0.53
Δ%	−11.9	−12.8	−12.8	15.0	11.4	11.9

Table 2. EIT and HIT values calculated at indentation depths of 200, 300, or 400 nm, averaged over a set of five different crystals (five control and five hybrid crystals). Recorded are the percentages of variation (Δ%) in EIT and in HIT from calcite to GO/calcite at the different indentation depths. The uncertainty reported in the table is the standard deviation

The reduction in elastic modulus can be explained by the fact that the GO layers are well oriented along the interface perpendicular to the direction of indentation (along the cleavage planes). It is therefore the out-of-plane Young's modulus, E_{33}, that has the main influence. Since the E_{33} of graphite is smaller than that of calcite, and because the GO is incorporated in the direction perpendicular to the indentation, thus forming an alternating series of calcite and GO bundles, a softening of calcite is indeed expected. Accordingly, applying an inverse rule of mixture for the Young's modulus, as imposed by our in-series stacking ($1/E_{(Calcite/GO)} = 1/E_{(Calcite)} * (1-f) + 1/E_{(GO)} * f$), and assuming a minimum GO content of $f = 0.027$ in volume fraction (as deduced from the TEM image in Figure 2B), we deduce that E_{33} for GO is 11.2, 9.9, or 9.4 GPa at 200, 300, or 400 nm of indentation, respectively.

On the other hand, the increase in hardness of the GO/calcite composite might suggest that both GO and the strain fields in the surrounding calcite lattice provide an obstacle to the motion of deformation twinning and the dislocation-mediated propagation of plastic deformation in the crystalline slip system. Moreover, applying the general shape/size-effect law for nanoindentation proposed in Pugno et al.,[26] we obtain (minimum)

$$H(h) = H_0*(1+h_0/(h+h_1))^{(1/2)}$$

where H is the hardness, h is the indentation depth, H_0 is the macroscopic hardness, and h_0 and h_1 are the characteristic lengths. For H_0 we find 3.8 GPa for the GO/calcite or 3.6 GPa for the

calcite. We also derive h_0 = 63.6 nm and $h_1 \cong 0$ for GO/calcite or h_0 = 28.8 nm and $h_1 \cong 0$ ($R^2 \cong 1$) for pure calcite.

CONCLUSIONS

Our results showed that GO sheets can indeed become incorporated into calcite single crystalline hosts, allowing for the fabrication of graphene-based composite materials with enhanced properties. We demonstrated a layered distribution of GO sheets entrapped within the calcite host. These hybrid single crystals show new optical properties: in contrast to pure calcite, the hybrid crystals become fluorescent and are spectroscopically characterized by the presence of three lifetimes, one of which is considerably longer than that observed for bare GO in solution. Moreover, the mechanical properties of the calcite host are manipulated upon introduction of a carbon-based nanomaterial into its lattice. Compared to pure calcite, the composite GO/calcite crystals exhibit lower elastic modulus and higher hardness.

This study thus demonstrates that by incorporating 2D materials within a 3D crystal lattice we can obtain hybrid crystals possessing several new properties.

EXPERIMENTAL SECTION

Materials: Graphene oxide was purchased from Cheap Tubes Inc. (USA) and was used as supplied (lateral dimension 300−800 nm, thickness 0.7−1.2 nm, purity 99 wt%). Cao et al.[27]characterized this source of GO by X-ray photoelectron spectroscopy (XPS) and found that the carbon-to-oxygen ratio is approximately 4:1. The functional composition of the bulk GO was determined as follows: sp^2 carbon (71.4%), hydroxyl groups (19.3%), carboxyl groups (9.3%). Dihydrate calcium chloride and granular anhydrous calcium chloride (for drying) were from Merck. Ammonium carbonate was supplied by Sigma-Aldrich. Solutions were prepared using water of Millipore grade (18.2 MΩ).

Synthesis: The pH-controllable dispersion of GO is favored mainly by alkaline conditions. Whereas the presence of Ca^{2+} facilitates GO aggregation, the dispersion of GO is assisted by ultrasonication. By optimization of these parameters, the optimal dispersion of GO was achieved in 10×10^{-3} M $CaCl_2$ at pH 5.4 under ultrasonication for 60 min at 40% of the maximum amplitude of 120 μm (tip diameter 13 mm) and frequency of 20 kHz.

Calcite single crystals were precipitated at room temperature by controlled diffusion of CO_2 and NH_3 vapors into the 10×10^{-3} M $CaCl_2$ solution containing previously dispersed GO in a concentration of 0.6 mg mL^{-1}. This simple method has the advantage of inducing slow nucleation and growth of calcite single crystals under the low supersaturation conditions that favor the additive incorporation.[28]

Scanning Electron Microscopy: A high-resolution scanning electron microscope (HR-SEM, ULTRA Plus, Zeiss, Oberkochen, Germany) was used to characterize the crystal shape and morphology. Samples were mounted on carbon tape and coated with carbon (Quorum Q150T ES, East Grinstead, UK). Images were obtained in high vacuum mode at 4 kV.

Transmission and Scanning Transmission Electron Microscopy: This was done with a Titan 80–300 FEG-S/TEM (FEI) microscope coupled with a HAADF detector. The microscope was operated at 300 kV. The sample analyzed by STEM and TEM analysis was prepared utilizing an FEI Strata400S Dual-Beam focused ion beam (FIB).

High-Resolution Powder X-ray Diffraction: HRPXRD analysis was carried out on the ID22 beamline of the ESRF. Powder samples were investigated at a wavelength of 0.39970(8)Å. All samples were measured in borosilicate 1 mm glass capillaries. Crystal lattice parameters were assessed by the Rietveld refinement method with GSAS software and the EXPGUI interface.[29]

Fluorescence Microscopy: Entrapping of GO within the calcite crystals causes changes in the spectroscopic properties of the hybrid crystals. The emission properties of GO upon its inclusion in calcite crystals were investigated by fluorescence microscopy using an inverted optical microscope IX-71 and a xenon lamp for excitation. An electron multiplying charge coupled device (EMCCD) camera (Princeton Instruments, PhotonMAX 512) was used for imaging acquisition. A

steady-state fluorescence spectroscope and a time-correlated single photon counting (TCSPC) apparatus were coupled to the microscope to record the local emission spectrum of GO in the crystals.

Optical Microscopy: Leica transmission optical microscopy was used in order to obtain images of $CaCO_3$ crystals grown in the presence of GO. Samples were placed on a microscope slide beneath a standard glass coverslip and observed under bright-field conditions with crossed polarizers. Images were captured with a CCD digital camera and recorded using the LAS EZ software supplied by Leica Microsystems.

Nanoindentation Analysis: The mechanical properties of single crystals of pure calcite and of GO/calcite were measured with a nanoindentation tester model TTX-NHT (CSM Instruments), equipped with a Berkovich diamond tip and operating in continuous stiffness mode. Measurements were taken up to a maximum applied load of 30 mN. Using Oliver and Pharr dynamic analysis of the loading portion of the curve, we determined the instrumented (IT) values of the elastic Young's modulus (E_{IT}) and hardness (H_{IT}) as well as the stiffness S as functions of indentation depth.[22] Crystals were embedded at room temperature using fast curing, cold polymerizing resins based on methyl methacrylate (Technovit 5071 (Buehler)), and were then lightly polished using colloid alumina, average size 1 μm (PACE Technologies) to yield a clean, smooth, flat surface for indentation.

4.2. Morphological Changes of Calcite Single Crystals Induced by Graphene-Biomolecule Adducts

This chapter is based on a peer-reviewed publication:
Adv. Funct. Mater., 26: 5569–5575. doi:10.1002/adfm.201601318

Matteo Calvaresi, Matteo Di Giosia*, Alessandro Ianiro, Francesco Valle, Simona Fermani, Iryna Polishchuk, Boaz Pokroy, Giuseppe Falini

Results and discussion

Graphene/biomolecules adducts

Liquid-phase exfoliation (LPE) of graphite is a common technique used to obtain exfoliated graphene sheets.[30] Graphene/biomolecules adducts were successfully synthesized by ultrasonication of graphite in the presence of tryptophan or N-acetyl-D-glucosamine (Figure 6). Among the amino acids, tryptophan possesses the highest affinity for carbon nanomaterials,[31–33] while direct exfoliation of graphite was carried out with chitosan, a polymer constitute by N-acetyl-D-glucosamine and D-glucosamine.[34]

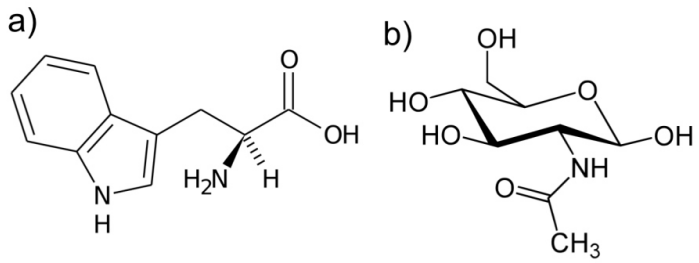

Figure 6 Molecular structure of a) Tryptophan; b) N-acetyl-D-glucosamine

The dispersion of graphene products in water was evident by the color of the dispersion that appeared grey. This dispersion was stable for several weeks. In the absence of the biomolecules no graphite exfoliation was observed. The characterization of the dispersion products was carried out by AFM. The results obtained by the observation of samples obtained in the presence of N-acetyl- D-glucosamine or tryptophan are illustrated in Figure 7.

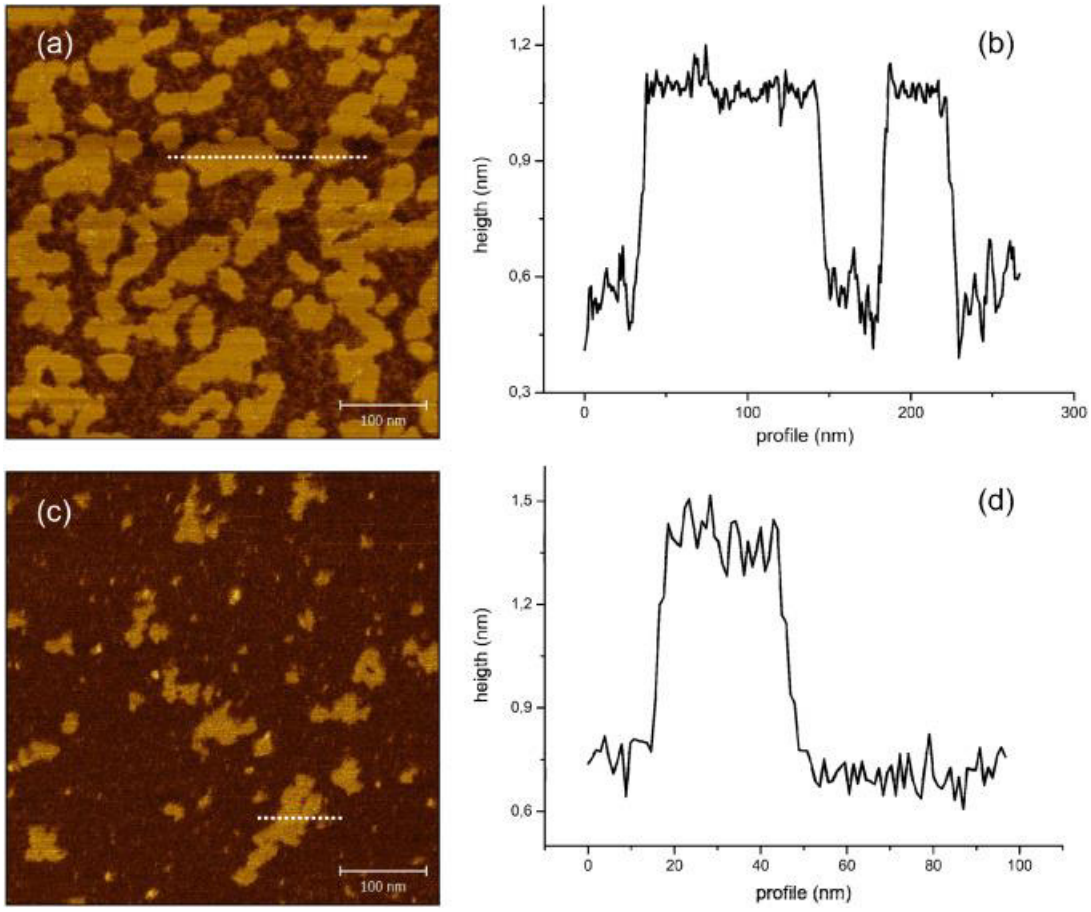

Figure 7 AFM image of graphene obtained by exfoliation of graphite in the presence of (a) N-acetyl-D-glucosamine or (c) tryptophan. The corresponding height profile of a single flake of graphene (marked by a dotted line) is reported in (b) and (d), respectively.

The analysis of the AFM images show that irregular shaped flakes of graphene are produced. The flakes show a wide varieties of geometry and their maximum length is around 100 nm, in the presence of both biomolecules. Despite this irregularity in shape the thickness of the flakes is quite regular and is about 0.6 nm for both N-acetyl-D-glucosamine and tryptophan, respectively. Considering that the interplanar distance in graphite is of 0.33 nm this means that in average each flake of graphene contains 2 layers.

Tip sonication of graphite flakes in the presence of the biomolecules led to the exfoliation of the graphite into graphene flakes. The biomolecules adsorbed on the surface of graphene flakes prevent them from re-stacking.

CALCITE/GRAPHENE/BIOMOLECULE ADDUCTS HYBRID CRYSTALS

The precipitation of calcium carbonate was carried out by the vapor diffusion techniques using a fixed volume of 2.0 mM, 10.0 mM or 50.0 mM of $CaCl_2$ solution at which was added a fixed volume of the saturated dispersion of the graphene/biomolecule adduct obtained using 10 mM tryptophan or N-acetyl-D-glucosamine solution. Control experiments in the presence of each biomolecule were carried out as well. In all precipitation experiments only calcite formed.

In the control experiments the additive/Ca^{2+} molar ratio reduced increasing the Ca^{2+} concentration. This is reflected on the morphological modification induced in the calcite crystals.

In the presence of N-acetyl-D-glucosamine the calcite crystals appear almost as prefect rhombohedra showing {10.4}faces and only when a 2.0 mM Ca^{2+} solution was used the presence of {18.0}faces were observed together with {10.4}faces (Fig. 8). When the graphene/N-acetyl-D-glucosamine adduct was used, a different morphological scenario was observed. The effect of the starting Ca^{2+} concentration was less marked compared with the control experiment graphene free. The presence of graphene favors the action of N-acetyl-D-glucosamine as crystal morphology modifier. The graphene/N-acetyl-D-glucosamine adduct favored the formation of {hk.0} faces not observed in the presence of N-acetyl-D-glucosamine. These faces become more and more {10.4} stepped as the starting concentration of Ca^{2+} increased.

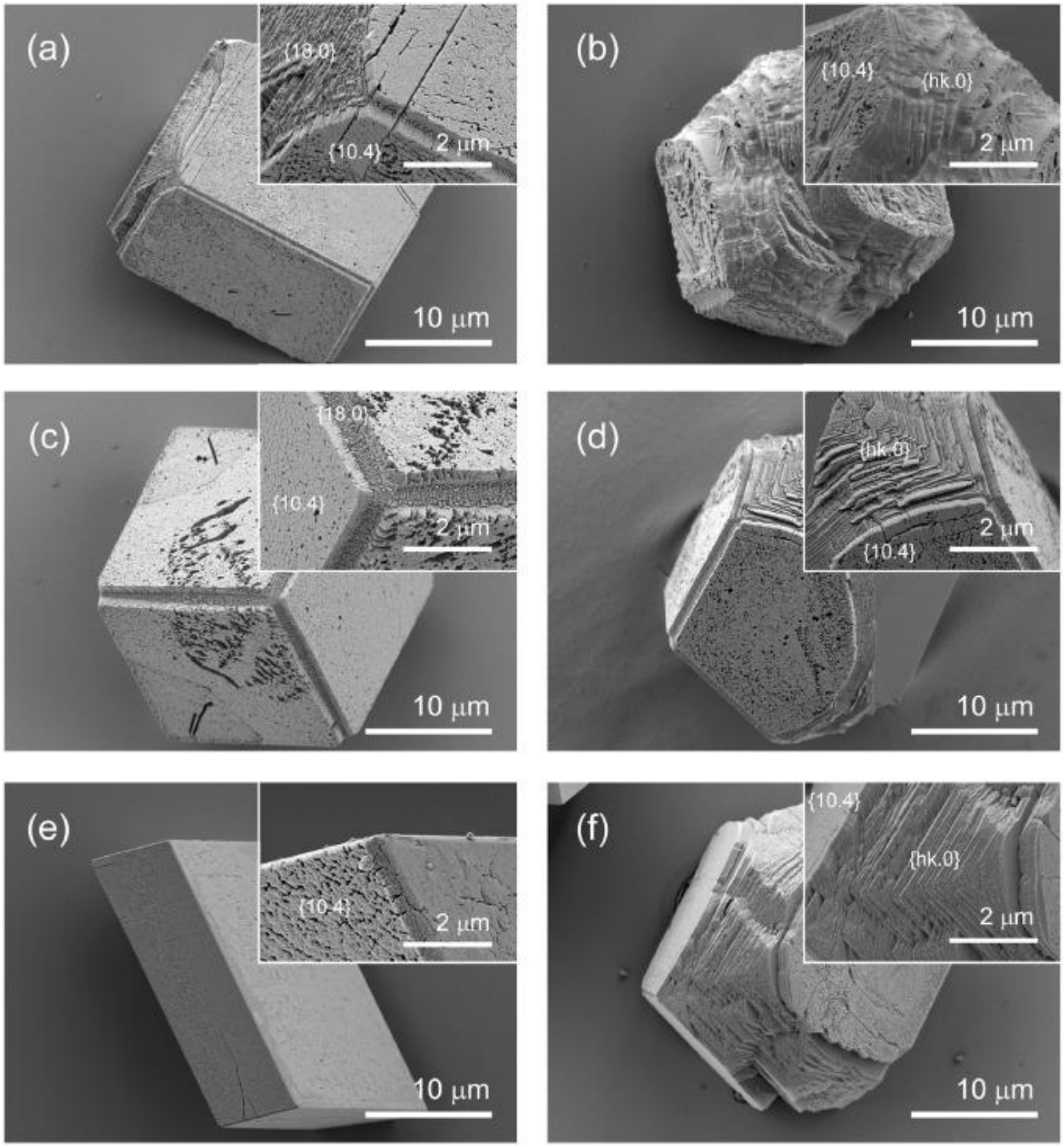

Figure 8 Scanning electron microscope images of calcite crystals grown using a 2.0 mM (a. b), 10.0 mM (c, d) and 50.0 mM Ca^{2+} solution (e, f). In (a), (c) and (e) the crystal are grown in the presence of 10 mM N-acetly-D-glucosamine. In (b), (d) and (f) the crystals were grown in the presence of 375 μL of the graphene/N-acetly-D-glucosamine adduct added to 375 μL of each Ca^{2+} solution. In the inset is shown a high magnification of the crystals edged and the Miller indexes of the crystalline faces are indicated.

In the presence of tryptophan a similar scenario was observed (Fig. 9). The only presence of the amino acid does not change drastically the morphology of the rhombohedral crystals. Indeed, they show only {10.4} and the face {18.0} appears only at the highest aminoacid/Ca^{2+} molar ratio value.

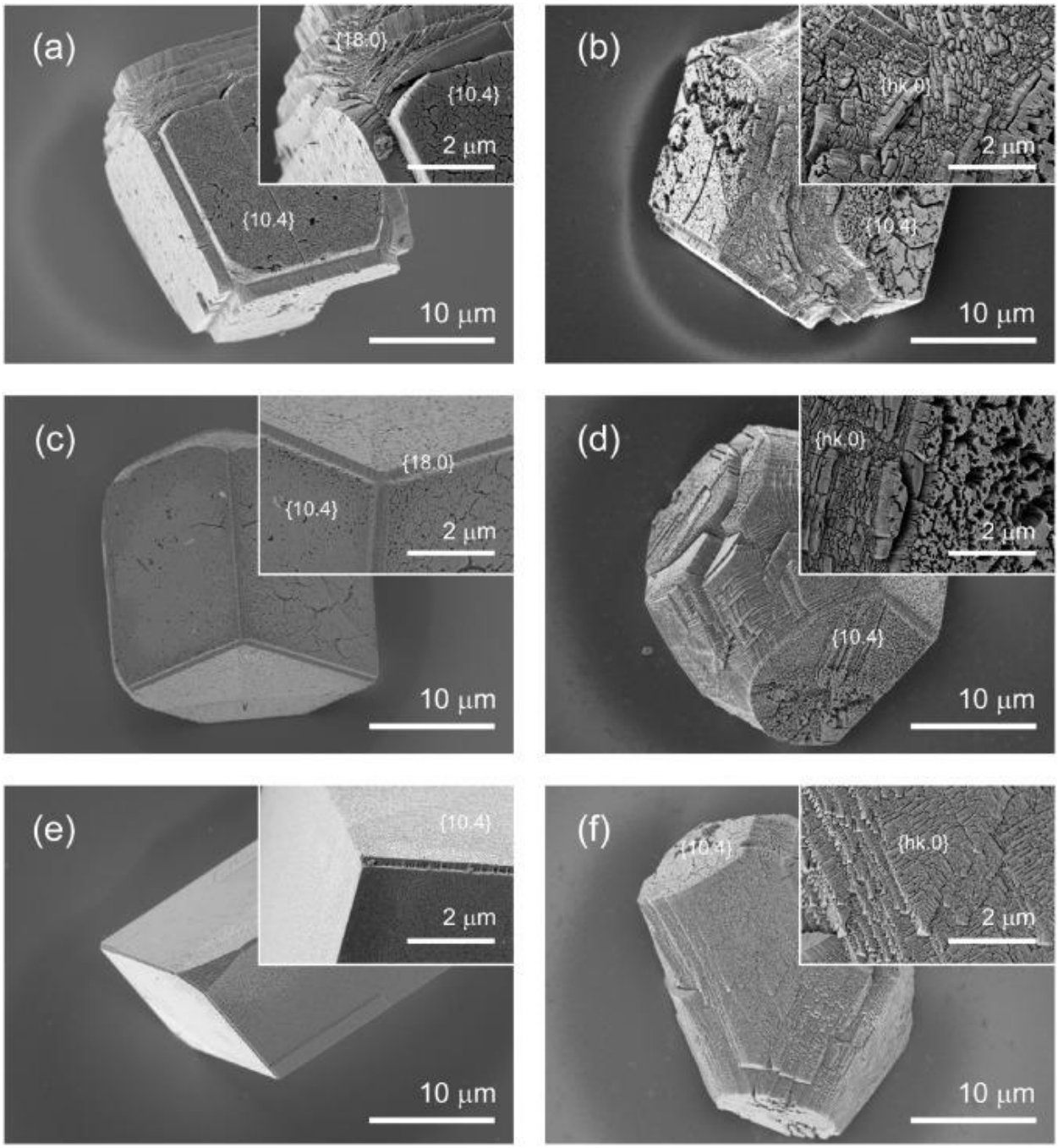

Figura 9 Scanning electron microscope images of calcite crystals grown using a 2.0 mM (a. b), 10.0 mM (c, d) and 50.0 mM Ca^{2+} solution. In (a), (c) and (e) the crystal are grown in the presence of 10 mM tryptophan. In (b), (d) and (f) the crystals were grown in the presence of 375 μL of the graphene/tryptophan adduct added to 375 μL of each Ca^{2+}

solution. In the inset is shown a high magnification of the crystals edged and the Miller index of the crystalline faces are indicated.

When the tryptophan was adsorbed to the graphene flakes, the calcite morphological scenario changed. The stabilization of the {hk.0} occurred while the {10.4} faces reduced their exposed surfaces. Interestingly this effect was more marked on the crystal grown using the highest concentration of Ca^{2+}.

These morphological observations, which are a proxy of the additive/calcite interaction, highlight some important considerations linked to the capability of graphene to adsorb on its surface the biomolecules. First the biomolecules has a minimal stabilization of the {18.0} faces while the graphene/biomolecules adducts stabilize the {hk.0} faces. These two families of faces show a completely different packing of carbonate and calcium ions. Along the {hk.0} faces there is the alternation of calcium and carbonate layers, while the {18.0} faces are locally less charged.

The stabilization of the {hk.0} requires the presence of locally organized charged regions on the graphene/biomolecules adduct surfaces. Accordingly it can be supposed specific interaction between graphene and tryptophan/N-acetyl-D-glucosamine. The relative extent of the stabilized surfaces, {hk.0} vs {18.0} strongly indicates that the 2D spatial organization of the biomolecules on the graphene surface increases the capability to act as crystal morphology modifies, with respect to when the biomolecules is free in solution.

This observation has relevant implications in biological mineralization, where structures surfaces act as mineral inhibitors or nucleators.

CONCLUSIONS

In this research it was shown that graphite can be exfoliated by tryptophan or N-acetyl-D-glucosamine biomolecules under ultrasonication. A stable dispersion of graphene sheets is obtained by the adsorption of the biomolecules on the surface of graphene flakes that prevent them from restacking.

The graphene/biomolecules adduct layers have a strong capability to interact with growing crystals of calcite. Doing this the stabilization of {hk.0} faces occurs. Very importantly the only presence

of tryptophan or N-acetyl-D-glucosamine biomolecules almost does not affect the morphology of calcite crystals, which show only the typical {10.4}.

EXPERIMENTAL SECTION

Preparation of the graphene/biomolecules adducts. Liquid-phase exfoliation (LPE) of graphite was performed using Misonix XL2020 tip sonicator (500 W, 20 kHz, standard tip probe 12.7 mm diameter). In a scintillation vial a water solution of tryptophan (or N-acetyl-D-glucosamine) 10 mM and insoluble graphite powder (1.5 mg mL-1) were sonicated for one hour at 40% of the maximum amplitude.

After sonication the solution was centrifuged for 10 minutes at about 5000 g to remove unsuspended graphite and graphene aggregates. The collected supernatant was used for the crystallization process.

Crystallization of calcium carbonate in the presence of graphene/biomolecules adducts. A 30 cm× 30 cm × 50 cm crystallization chamber was used for the crystallization experiments of calcium carbonate. Two 25 mL beakers each containing about 20 g of $(NH_4)_2CO_3$ (Sigma -Aldrich,) the source of NH_3 and CO_2 vapours, and two Petri dishes (d = 8 cm), each containing about 10 g of anhydrous $CaCl_2$ (Fluka), a hygroscopic agent that controls humidity, were placed inside the chamber. Microplates for cellular culture (Microplate 24 well with Lid, IWAKI) containing a round glass cover slip in each well were used. Into each well, 750 μL of a 2.0, 10.0 or 50.0 mM $CaCl_2$ solution in a 9/1 H2O–EtOH mixture were poured. The additive, the graphene/biomolecules adduct, was dissolved in the $CaCl_2$ solution. The microplate was covered with aluminum foil and a hole was made over every well. After 4 days, the obtained crystals were washed three times with the 9/1 H2O–EtOH mixture, three times with milli-Q water (with a resistivity of 18.2 MΩ cm at 25 °C, filtered through a 0.22 μm membrane) and one time with ethanol; then they were air-dried and analyzed. All of the experiments were conducted at room temperature. Each crystallization trial was replicated at least three times.

Characterization of the calcium carbonate crystals. A Leica transmission optical microscope was used to obtain images of $CaCO_3$ crystals. A microscope slide containing the sample was placed beneath a standard glass cover slip and observed under bright-field conditions with crossed polarizers. Images were captured with a CCD digital camera and recorded using the software (LAS EZ) supplied by Leica Microsystems. Image analysis was conducted on the crossed polarized optical micrographs to obtain info on crystallite birefringence. The dried glass cover slips covered with crystals were glued to the SEM aluminum stubs.

A high-resolution scanning electron microscope (HR-SEM, ULTRA Plus, Zeiss, Oberkochen, Germany) was used for characterization of crystal shape and morphology of the gold-sputtered crystals.

The X-ray powder diffraction patterns were obtained using a Philips X'PertPro diffractometer. The diffraction patterns were collected using a voltage of 40 kV and a current of 40 mA. A diffraction region between 20° and 60° of 2θ was scanned. The measurements were carried out directly on the microscope slide on which particles were deposited.

REFERENCES

1. Huang, X., Qi, X., Boey, F. & Zhang, H. Graphene-based composites. *Chem. Soc. Rev.* **41,** 666–86 (2012).
2. Ferrari, A. C. *et al.* Science and technology roadmap for graphene, related two-dimensional crystals, and hybrid systems. *Nanoscale* **7,** 4598–4810 (2015).
3. Weber, E. *et al.* Incorporation of a Recombinant Biomineralization Fusion Protein into the Crystalline Lattice of Calcite. *Chem. Mater.* **26,** 4925–4932 (2014).
4. Addadi, L. & Weiner, S. Control and Design Principles in Biological Mineralization. *Angew. Chemie Int. Ed. English* **31,** 153–169 (1992).
5. Mann, S. Biomineralization - Stephen Mann - Oxford University Press. (2001).
6. Lowenstam, H. A. (Heinz A. & Weiner, S. *On biomineralization*. (Oxford University Press, 1989).
7. Fratzl, P., Gupta, H. S., Fischer, F. D. & Kolednik, O. Hindered Crack Propagation in Materials with Periodically Varying Young's Modulus—Lessons from Biological Materials. *Adv. Mater.* **19,** 2657–2661 (2007).
8. Tai, K., Dao, M., Suresh, S., Palazoglu, A. & Ortiz, C. Nanoscale heterogeneity promotes energy dissipation in bone. *Nat. Mater.* **6,** 454–62 (2007).
9. Nudelman, F. & Sommerdijk, N. A. J. M. Biomineralization as an inspiration for materials chemistry. *Angew. Chem. Int. Ed. Engl.* **51,** 6582–96 (2012).
10. Kunitake, M. E., Mangano, L. M., Peloquin, J. M., Baker, S. P. & Estroff, L. A. Evaluation of strengthening mechanisms in calcite single crystals from mollusk shells. *Acta Biomater.* **9,** 5353–5359 (2013).
11. Kim, S., Ku, S. H., Lim, S. Y., Kim, J. H. & Park, C. B. Graphene-biomineral hybrid materials. *Adv. Mater.* **23,** 2009–14 (2011).
12. Kim, Y.-Y. *et al.* An artificial biomineral formed by incorporation of copolymer micelles in calcite crystals. *Nat. Mater.* **10,** 890–896 (2011).
13. Herman, A., Addadi, L. & Weiner, S. Interactions of sea-urchin skeleton macromolecules with growing calcite crystals—a study of intracrystalline proteins. *Nature* **331,** 546–548 (1988).
14. Pokroy, B. *et al.* Anisotropic lattice distortions in biogenic calcite induced by intra-crystalline organic molecules. *J. Struct. Biol.* **155,** 96–103 (2006).
15. Weber, E. *et al.* Intracrystalline inclusions within single crystalline hosts: from biomineralization to bio-inspired crystal growth. *CrystEngComm* **17,** 5873–5883 (2015).
16. Pokroy, B., Fitch, A. & Zolotoyabko, E. The Microstructure of Biogenic Calcite: A View by High-Resolution Synchrotron Powder Diffraction. *Adv. Mater.* **18,** 2363–2368 (2006).
17. B. Pokroy, †, A. N. Fitch, ‡ and & E. Zolotoyabko*, †. Structure of Biogenic Aragonite (CaCO3). (2007). doi:10.1021/CG060842V

18. Borukhin, S. *et al.* Screening the Incorporation of Amino Acids into an Inorganic Crystalline Host: the Case of Calcite. *Adv. Funct. Mater.* **22,** 4216–4224 (2012).

19. Weber, E. & Pokroy, B. Intracrystalline inclusions within single crystalline hosts: from biomineralization to bio-inspired crystal growth. *CrystEngComm* **17,** 5873–5883 (2015).

20. Pokroy, B., Quintana, J. P., Caspi, E. N., Berner, A. & Zolotoyabko, E. Anisotropic lattice distortions in biogenic aragonite. *Nat. Mater.* **3,** 900–902 (2004).

21. Magnabosco, G. *et al.* Calcite Single Crystals as Hosts for Atomic-Scale Entrapment and Slow Release of Drugs. *Adv. Healthc. Mater.* **4,** 1510–1516 (2015).

22. Shang, J. *et al.* The origin of fluorescence from graphene oxide. *Sci. Rep.* **2,** 792 (2012).

23. Loh, K. P., Bao, Q., Eda, G. & Chhowalla, M. Graphene oxide as a chemically tunable platform for optical applications. *Nat. Chem.* **2,** 1015–24 (2010).

24. Vempati, S. *et al.* Fluorescence from graphene oxide and the influence of ionic, π–π interactions and heterointerfaces: electron or energy transfer dynamics. *Phys. Chem. Chem. Phys.* **16,** 21183–21203 (2014).

25. Oliver, W. C. & Pharr, G. M. An improved technique for determining hardness and elastic modulus using load and displacement sensing indentation experiments. *J. Mater. Res.* **7,** 1564–1583 (1992).

26. Pugno, N. M. A general shape/size-effect law for nanoindentation. *Acta Mater.* **55,** 1947–1953 (2007).

27. Cao, C., Daly, M., Singh, C. V., Sun, Y. & Filleter, T. High strength measurement of monolayer graphene oxide. *Carbon N. Y.* **81,** 497–504 (2015).

28. Ihli, J., Bots, P., Kulak, A., Benning, L. G. & Meldrum, F. C. Elucidating Mechanisms of Diffusion-Based Calcium Carbonate Synthesis Leads to Controlled Mesocrystal Formation. *Adv. Funct. Mater.* **23,** 1965–1973 (2013).

29. Toby, B. H., G., U. A. & D., B. I. *EXPGUI* , a graphical user interface for *GSAS*. *J. Appl. Crystallogr.* **34,** 210–213 (2001).

30. Ciesielski, A. & Samorì, P. Graphene via sonication assisted liquid-phase exfoliation. *Chem. Soc. Rev.* **43,** 381–398 (2014).

31. Calvaresi, M. & Zerbetto, F. The devil and holy water: protein and carbon nanotube hybrids. *Acc. Chem. Res.* **46,** 2454–63 (2013).

32. Calvaresi, M. *et al.* C60@Lysozyme: direct observation by nuclear magnetic resonance of a 1:1 fullerene protein adduct. *ACS Nano* **8,** 1871–7 (2014).

33. Calvaresi, M., Bottoni, A. & Zerbetto, F. Thermodynamics of Binding Between Proteins and Carbon Nanoparticles: The Case of C 60 @Lysozyme. *J. Phys. Chem. C* **119,** 28077–28082 (2015).

34. Demitri, C., Moscatello, A., Giuri, A., Raucci, M. & Esposito Corcione, C. Preparation and Characterization of EG-Chitosan Nanocomposites via Direct Exfoliation: A Green Methodology. *Polymers (Basel).* **7,** 2584–2594 (2015).

SIDE PROJECT

GAINS AND LOSSES OF CORAL SKELETAL POROSITY CHANGES WITH OCEAN ACIDIFICATION ACCLIMATION

This chapter is based on a peer-reviewed publication:
Nat. Commun. 6:7785 doi: 10.1038/ncomms8785 (2015)

Paola Fantazzini*, Stefano Mengoli, Luca Pasquini, Villiam Bortolotti, Leonardo Brizi, Manuel Mariani, Matteo Di Giosia, Simona Fermani, Bruno Capaccioni, Erik Caroselli, Fiorella Prada, Francesco Zaccanti, Oren Levy, Zvy Dubinsky, Jaap A. Kaandorp, Pirom Konglerd, Jörg U. Hammel, Yannicke Dauphin, Jean-Pierre Cuif, James C. Weaver, Katharina E. Fabricius, Wolfgang Wagermaier, Peter Fratzl, Giuseppe Falini* & Stefano Goffredo*

My contribution to this project concerns the mechanical characterization of the corals carried out by means of the nanoindenter.

INTRODUCTION

Climate change is among the biggest threats to the health of marine ecosystems. Rising atmospheric carbon dioxide partial pressure (pCO_2)[1] increases ocean surface pCO_2 due to CO_2 diffusion across the air-water interface, leading to ocean acidification (OA)[2]. Since global warming and OA are coupled and are predicted to act synergistically[3,4], the future health of marine ecosystems and their corresponding long-term economic impacts on human coastal populations

remain uncertain.[5–7] It is therefore of great interest to understand how increasing atmospheric CO_2 concentrations will affect these marine habitats and the species that inhabit them.

Since the early 1800s, ocean pH has decreased from 8.2 by *ca.* 0.1 U[8] and, if CO_2 emissions continue at their current rates, the average sea surface pH is predicted to drop to 7.8 by the year 2100. The Mediterranean Sea, with its closed circulation patterns and limited water exchange with the adjacent Atlantic Ocean, has already undergone a larger decrease in surface pH compared with the global average[9], making it an ideal site for OA studies.[10–13]

Near Panarea Island, off the southwestern coast of Italy, lies a series of active volcanic vents in the seabed releasing CO_2 emissions that acidify the surrounding seawater, making this location an ideal natural laboratory for OA studies. The underwater CO_2 emissions generate a stable pH gradient with levels matching several Intergovernmental Panel on Climate Change (IPCC) sea surface pH predictions associated with different atmospheric CO_2 emission scenarios for the end of the century.[1]

The present study investigates the effects of environmental pH on skeletal structures and growth at multiple length scales in the solitary scleractinian coral *Balanophyllia europaea* living along the pH gradient. We studied 74 corals of similar age (mean age of 12 years) that had spent their lives at the CO_2-pH gradient. Using a combination of scanning electron microscopy (SEM), atomic force microscopy (AFM), small-angle X-ray scattering (SAXS), micro computed tomography (μCT), nanoindentation, hydrostatic weight measurement and time-domain nuclear magnetic resonance (TD-NMR), we document the skeletal mass, bulk volume, pore volume, porosity, biomineral density, bulk density, hardness, stiffness (ratio between elastic stress and strain), biometry data, net calcification rate and linear extension rate for each coral. Weight measurements combined with TD-NMR data represent a non-destructive technique for quantifying skeletal porosity over length scales spanning from tens of nanometers to tens of micrometres,[14,15] whereas μCT analysis permits a detailed large-scale quantitative 3D analysis of skeletal architecture, including the interseptal regions.

We show that in response to depressed calcification at lower pH, corals increase their skeletal porosity maintaining constant linear extension rate, which is important for reaching critical size at sexual maturity. However, higher skeletal porosity and reduced bulk density and stiffness may contribute to reduced mechanical strength, increasing damage susceptibility, which could result in increased mortality in an acidic environment.

RESULTS

STUDY SITE AND SEAWATER CARBONATE CHEMISTRY

The four sites around the main vent are reported in Figure 1. Site 1 (S1) has an average total scale pH (pH_{TS}) of 8.1, equivalent to the average surface pH of modern oceans. S2's average pH_{TS} of 7.9 aligns with IPCC's predictions of a conservative CO_2 emissions scenario (Representative Concentration Pathway (RCP6.0)), and the average pH_{TS} of 7.7 for S3 fits the predictions of the 'business-as-usual' CO_2 emissions scenario (RCP8.5). Since no corals were found at S4 (within the vent crater, pH_{TS}7.4), only S1–3, which had growing coral populations and pH_{TS} values ranging from 8.1 to 7.7, were included in the present study. Of the measured parameters at the three sites along the pH gradient (pH_{TS}, total alkalinity, temperature and salinity), only pH_{TS} differed significantly across sites (N=103–110; P<0.001, Kruskal–Wallis χ^2-test). The changing pH was accompanied by significant shifts in carbonate–bicarbonate equilibria, with aragonite saturation (Ω_{arag}) decreasing by >30% from S1 to S3 (Figure 1).

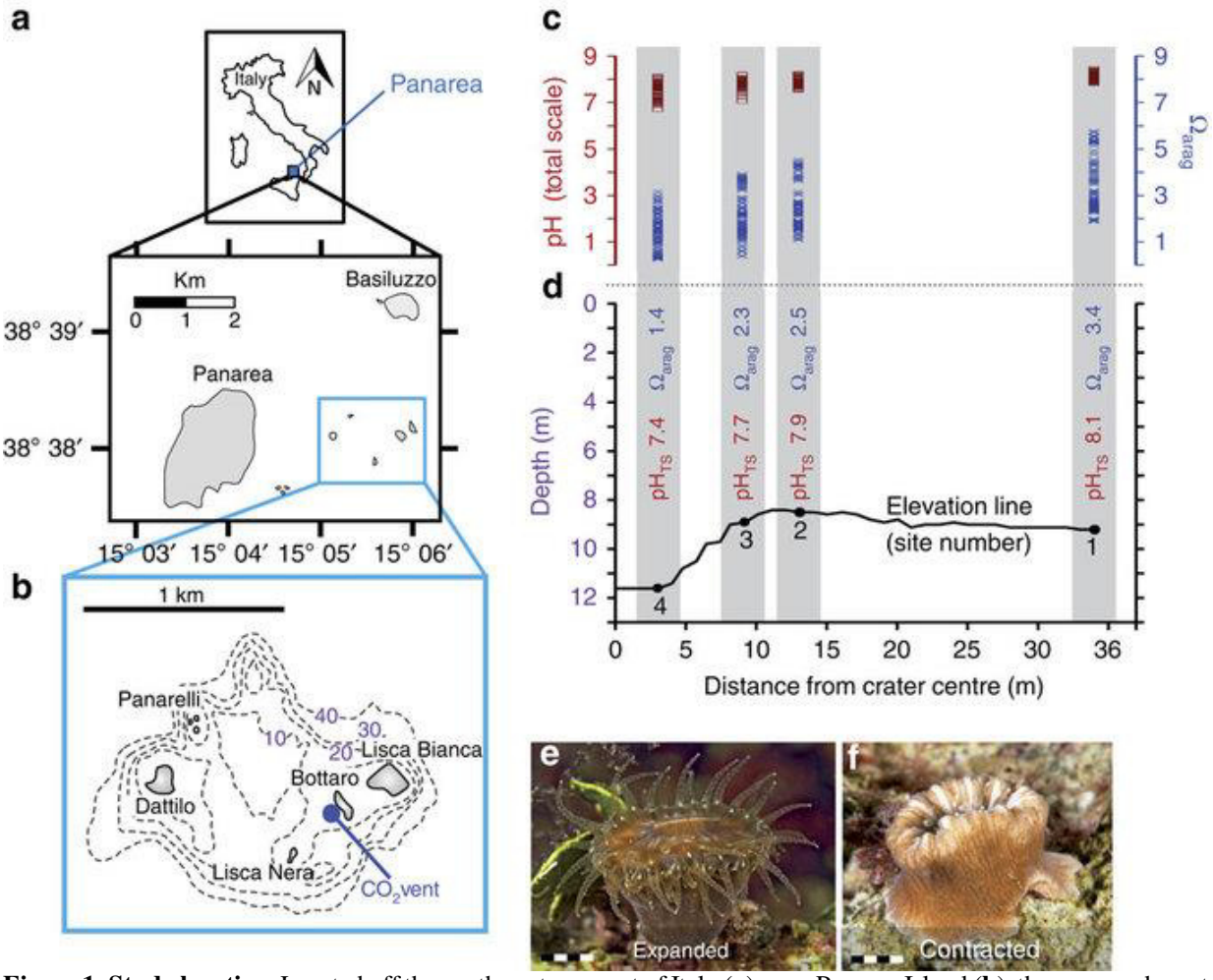

Figure 1: Study location. Located off the southwestern coast of Italy (**a**), near Panarea Island (**b**), there are underwater volcanic vents releasing persistent gaseous emissions (98–99% CO_2 without instrumentally detectable toxic compounds), resulting in a stable pH gradient. Four sites at various distances from the primary vent were initially selected for study. No temperature difference exists among the four study sites throughout the year. (**c**) Ranges of measured pH_{TS} (number of observations [*n*]=103–110 per site) and Ω_{arag} (*n*=96–104 per site) values at the four sites, showing consistent increases in both pH_{TS} and Ω_{arag} from the vent crater to its periphery. (**d**) Bathymetric profile of the sites with associated mean pH_{TS} and Ω_{arag}values. No corals were found at Site 4, characterized by the lowest pH (mean pH_{TS} 7.4). Living specimens of *Balanophyllia europaea*, photographed at night with expanded tentacles (**e**) and during the day with contracted tentacles (**f**); marker 5 mm.

Combined results of SEM, μCT, AFM and TD-NMR skeletal analyses of corals growing at each study site revealed the detailed, multi-scale structural organization of the skeletons of *B. europaea* (Figure 2).

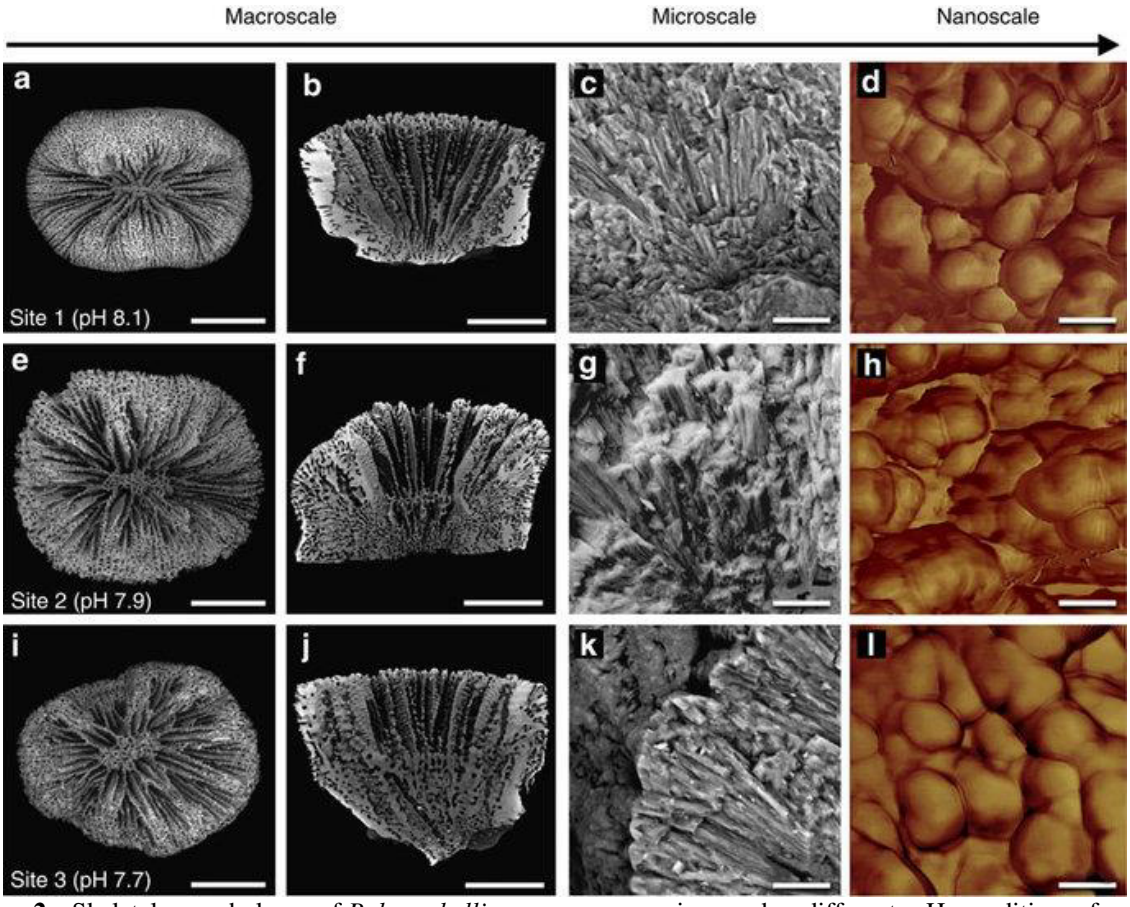

Figure 2: Skeletal morphology of *Balanophyllia europaea* growing under different pH conditions from the macroscale to the nanoscale. Each row in the figure corresponds to a different study site and sample age is 9–11 years. Images are representative of all observed skeletons. (a,e,i) Low magnification SEM images of coral skeletons, marker 5 mm. (b,f,j) Internal sections of corallites from μCT images, marker 5 mm. (c,g,k) SEM images of entire skeletal fibres from fractured septae, marker 10 μm. (d,h,l) AFM images of mineral grains on the skeletal fibre surfaces, marker 50 nm.

At the macroscale (relating to feature sizes >10 μm), linear extension rate (averaging *ca.* 1 mm per year) did not vary among sites, whereas net calcification rate (N=44; P<0.01, robust t-statistics test) and skeletal bulk density (N=44, P<0.001, robust t-statistics test) significantly declined and skeletal porosity and macroscale porosity increased (N=44; P<0.001, robust t-statistics test). The

differences between S1 and S3 were *ca.* −18% for net calcification rate, *ca.* −7% for bulk density, *ca.*+21% for porosity and *ca.*+30% for macroscale porosity. The corallite interseptal volume fraction from μCT showed a difference among sites (N=30; P<0.05, F and Kruskal–Wallis χ^2-tests) but no significant dependence on pH. The biometric data for the corallites did not vary among sites.

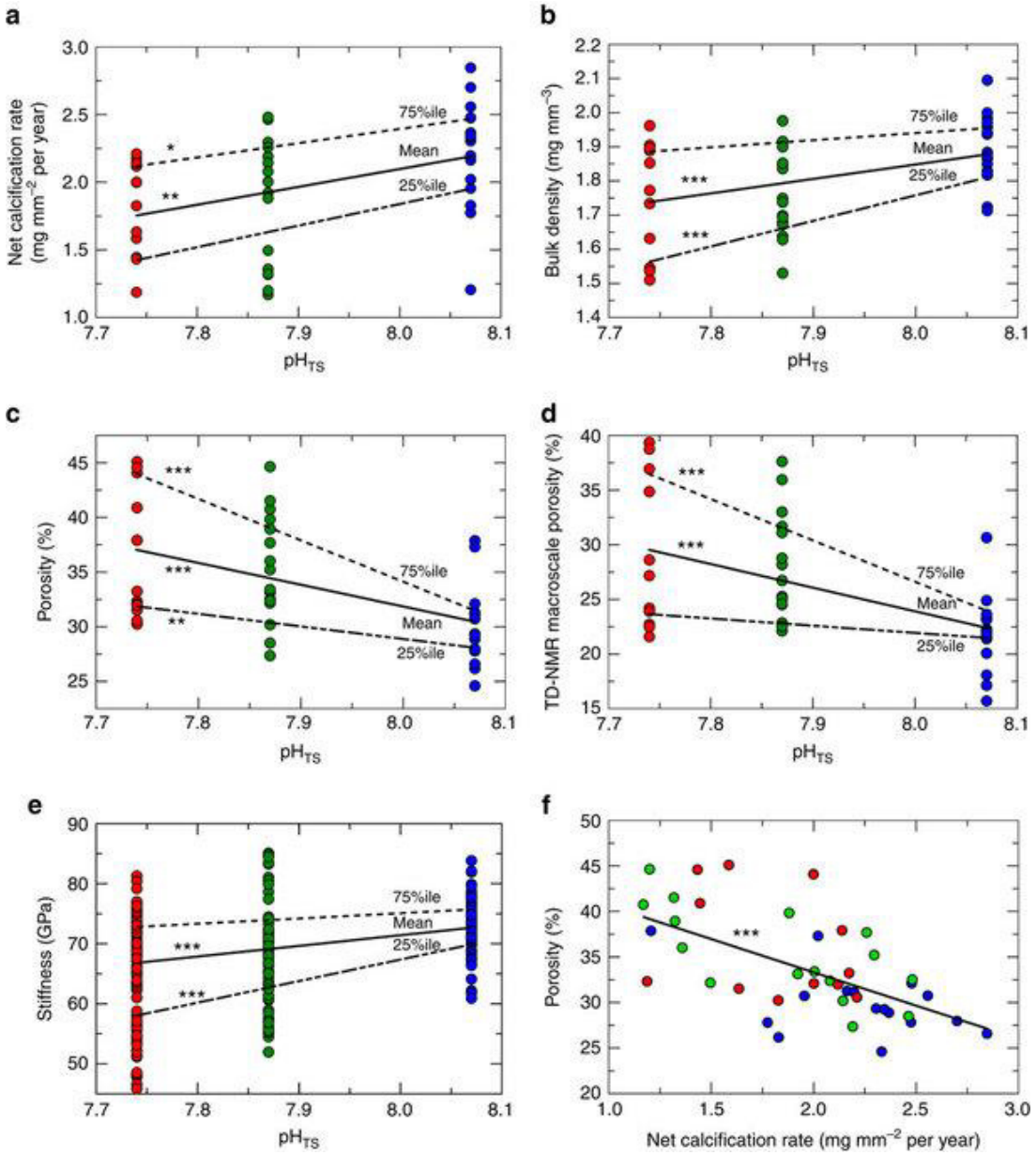

Figure 3: Scatterplots of skeletal parameters, and correlation analysis between porosity and net calcification rate. Site 1=blue, Site 2=green, Site 3=red. Straight lines represent the best-fit linear regression (mean, solid line), 25% quantile and 75% quantile (dashed lines). (**a**–**e**) Skeletal parameters (*y*-axes) plotted against pH_{TS}. (**f**) Scatterplot of porosity (P_A) versus net calcification rate in corals from Sites 1 to 3. For **a**–**d**,**f** N=44; for **e** n=122. ***P<0.001; **P<0.01; *P<0.05, robust t-statistics test.

At the micro/macroscale, skeletal stiffness significantly declined with decreasing pH (n=122; P<0.001, robust t-statistics test, Figure 3, Figure 4 , Table 1), whereas skeletal microscale porosity did not vary among sites.

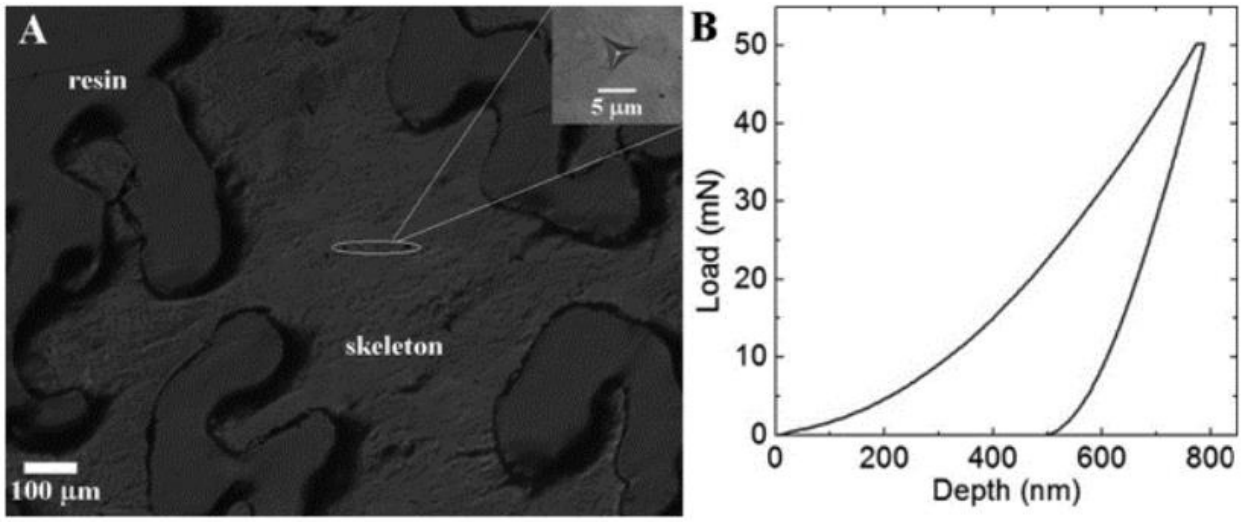

Figure 4. (A) Optical micrograph of a typical skeletal section used for nanoindentation measurements. The white ellipse highlights an area with a sequence of five indentations. The top right inset displays a higher magnification view of one indentation's residual imprint. The apparent roughness arises from optical contrast between differently oriented fibers. (B) Typical load-depth curve at 50 mN maximum load (corresponding to a depth of about 800 nm), loading/unloading rate = 100 mN/min, hold period at maximum load = 10 s).

	Site 1: d=34 m pCO_2=423 µatm pH=8.07				Site 2: d=13 m pCO_2=698 µatm pH=7.87				Site 3: d=9 m pCO_2=922 µatm pH=7.74				
	N	***n***	**mean**	**se**	***N***	***n***	**mean**	**se**	***N***	***n***	**mean**	**se**	**statistical significance**
Skeletal hardness (MPa)	3	37	5109	51	3	37	5170	88	3	48	5171	60	NS
Skeletal stiffness (GPa)	3	37	70.8	0.8	3	37	66.4	1.0	3	48	63.8	1.6	***
SAXS nanopore volume (a.u.)	3	31	11 10^{-3}	1 10^{-3}	3	34	12 10^{-3}	1 10^{-3}	3	31	3 10^{-2}	1 10^{-2}	NS
µCT corallite interseptal volume fraction (%)	Entire 10 corallite volume		63.4	1.7	Entire 10 corallite volume		69.1	0.8	Entire 10 corallite volume		66.7	1.5	*

Table 1. Skeletal parameters by different techniques for corals from the three study sites. N = number of corals; n = number of observations or tests; se = standard error; d = distance in meters from the vent to the study site; a.u.=arbitrary units. The values of F-test and Kruskal-Wallis χ 2 equality-of-populations rank tests suggest highly significant differences among sites only for stiffness. NS = not significant; ***p<0.05.

At smaller length scales (at the micro and nanoscales), SEM and AFM showed that the organization of the aragonite fibre bundles (Figure 2c,g,k) and the morphology and packing of the constituent mineral grains (Figure 2d,h,l) appeared similar among corals from the three different sites, confirming that the basic biomineralization products were not affected by reduced pH[13] (Figure 2). Skeletal biomineral hardness did not change among sites (Figure 5, Table 1).

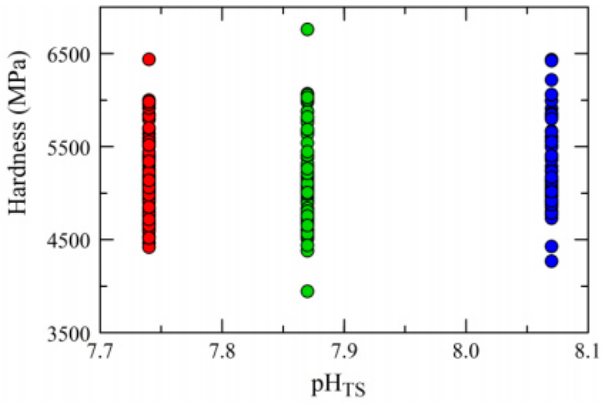

Figure 5. Scatterplot of skeletal hardness measured by nanoindentation in corals from the three study sites. Site 1 = blue, Site 2 = green, Site 3 = red.

Also, skeletal biomineral density values were similar across sites and consistent with those measured in previous studies.[16] Similar results were obtained from both SAXS and TD-NMR analyses, which revealed that nanoscale porosity did not change significantly with changing pH.

The principal component analysis identified three major components: growth, skeletal porosity and biomineral density. Only the first two components depended significantly on pH.

In summary, skeletal nano and microstructural features, linear extension rate, interseptal volume fraction and corallite biometry of *B. europaea* did not change significantly with decreasing pH, despite a clear reduction in net calcification rates. This reduction in net calcification rate was accompanied by an increase in skeletal porosity (Figure 3f, N=44; P<0.001, robust t-statistics test) and a consequent decrease in skeletal bulk density and stiffness.

DISCUSSION

Results of the present study complement previous research on *B. europaea* at this same vent site, which revealed no changes in skeletal calcium carbonate polymorph, organic matrix content, aragonite fibre thickness and skeletal hardness in corals growing along the pH gradient.[13] There was, however, a significant reduction in population density along the pH gradient, decreasing by a factor of 3 with increasing proximity to the vent crater centre (that is, from S1 to S3).[13]

Figure 6 summarizes these results at the ocean, population, macro, micro and nanoscales for *B. europaea*. At the macroscale, increasing acidity was associated with a reduction in net calcification rate and a parallel increase in skeletal porosity, coupled with a decrease in skeletal bulk density. Linear extension rate and corallite shape (biometry and interseptal volume fraction) did not depend on pH, probably as a result of the compensation of reduced net calcification rate by increased skeletal porosity. At the micro/macroscale, the declining skeletal stiffness with decreasing pH could be coupled to an increased volume fraction of pores having a size comparable to the indentation area (that is, at the border between the micro and macroscales). At the nanoscale, porosity, biomineral hardness and density were not significantly affected by pH. These results, bolstered by qualitative SEM and AFM analyses, suggest that the 'building blocks' produced by the biomineralization process are substantially unaffected, but the increase in skeletal porosity is both a gain and a loss for the coral. In fact, in an acidic environment, where the net calcification is depressed, enhanced macroporosity keeps linear extension rate constant, potentially meeting functional reproductive needs (for example, the ability to reach critical size at sexual maturity); however, it also reduces the mechanical strength of the skeletons, increasing damage susceptibility, which could result in increased mortality and the observed population density decline.[13]

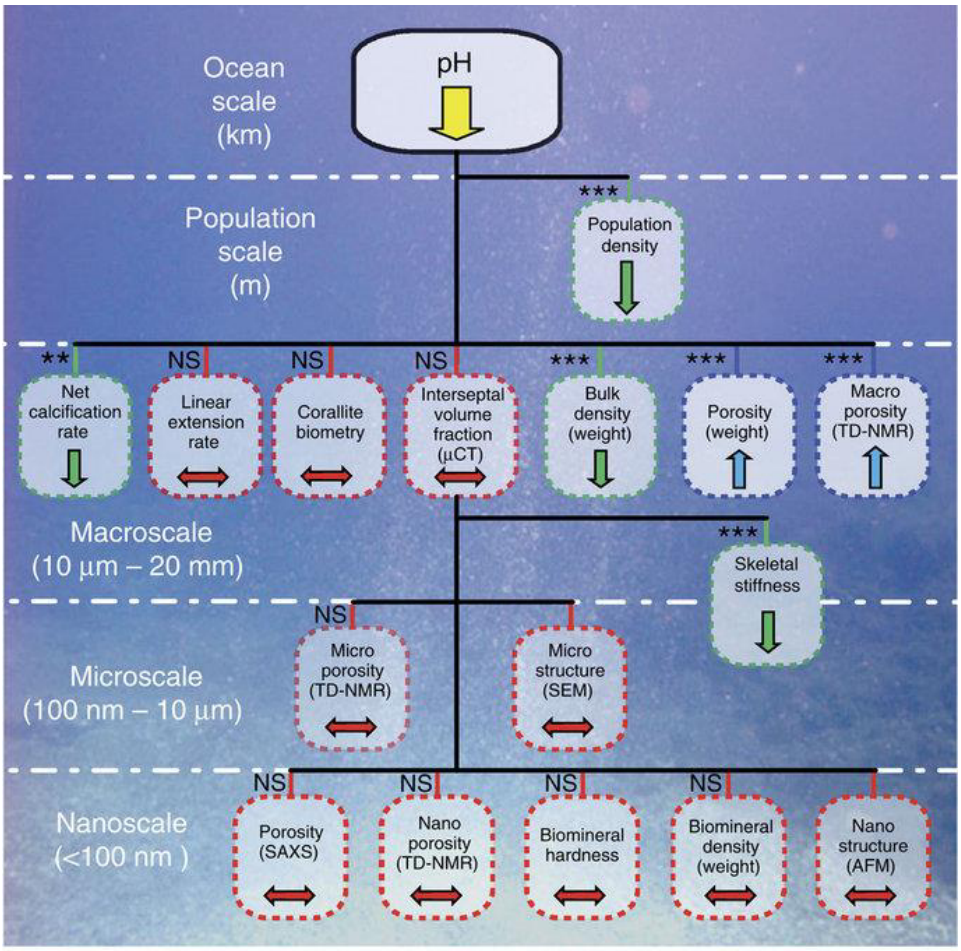

Figure 6: Summary of responses in *Balanophyllia europaea* skeletal parameters as a function of pH from the ocean to the nanoscale. The significant decline in population density with pH was measured in previously published research13. Net calcification rate and bulk density decrease with decreasing pH, whereas porosity (PA) increases, preserving the linear extension rate and corallite shape (biometry and interseptal volume fraction as measured by µCT do not correlate with pH). The increase in porosity is associated with a decrease in skeletal stiffness. At the nanoscale, the 'building blocks' (the fundamental structural components of the coral skeleton, aragonite fibre bundles and their constituent mineral grains) produced by the biomineralization process are substantially unaffected by increased acidity. Green boxes denote parameters found to have a direct relationship with pH, blue boxes denote parameters that have an inverse relationship and red boxes denote parameters found to have no relationship with pH. The significances of the regression of each parameter (dependent variable) with pH (independent variable) are indicated; ***P<0.001; **P<0.01; NS indicates no significance. Micro and nanoscale structure observations by SEM and AFM represent qualitative data.

While the results reported here for *B. europaea* may not be representative of the generalized response of all coral species to OA, they are consistent with field observations made on other reef-

building scleractinians. For example, while maintaining constant skeletal linear extension, decreased rates of calcification and losses in bulk skeletal density as a function of reduced aragonite saturation have been observed in *Montasraea annularis*[17] and *Porites astreoides*.[18] While low aragonite saturation as a sole driver for the observed reduction in coral calcification has been discussed,[19] our conclusions regarding a balance between reduced net calcification rate and increased macroporosity to maintain constant linear extension can explain the outcomes of those studies.[17,18] In fact bulk density depends both on biomineral density and porosity. Our multi-scale analysis shows that all the skeletal features at the nano and microscales, including biomineral density, are unchanged. The decrease of bulk density with decreasing pH depends on the increase of macroporosity, leaving the linear extension rate constant.

Our findings, together with the well-described detrimental effects of heat stress on the scleractinian zooxanthellate coral *B. europaea*,[16,20–23] provide several independent and consistent clues regarding the sensitivity of this species to global climate change predicted for the coming decades. Together with results from previous studies,[24] we demonstrate that the almost universally employed measure of coral biomineralization, namely the rate of linear extension, might not be a reliable metric for assessing coral health and resilience in a warming and acidifying ocean. Indeed, although the coral's ability to maintain linear extension rate and gross skeletal morphology under conditions of decreasing oceanic pH could allow it to reach sexual maturity, it could reduce skeletal resistance to environmental challenges, affecting the long-term survivability of the species.

METHODS

Study site. Off the southwestern coast of Italy, near the island of Panarea, an area delimited by the islets of Dattilo, Bottaro, Lisca Nera and Lisca Bianca (Figure 1) is characterized by underwater volcanic CO_2 vents. The main vent, a crater measuring 20 m × 14 m and ~10-m deep, generates a persistent column of CO_2 bubbles that rise from the seabed to the sea surface. In this hydrothermally stable setting with ambient temperature, CO_2 emissions establish a pH gradient that extends ~34 m from the centre of this crater to its periphery.[13] Three sites along this pH gradient were chosen for study. Distances (d) from the main crater centre and mean pH_{TS} values of the three sites from which corals were collected are: S1 (the control site), d=34 m, pH_{TS}=8.07;

S2, d=13 m, pH_{TS}=7.87; S3, d=9 m, pH_{TS}=7.74. Water depth varies from 11.6 m within the crater to 8.8 m at the crater edge (S2) to 9.2 m at the outer margins (S1), where the local pH matches that of the surrounding seawater. The study site has stable hydrothermal–chemical properties.[25]

The corals. B. europaea (Figure 1) is a solitary zooxanthellate scleractinian coral endemic to the Mediterranean Sea found at depths ranging from 0 to 50 m.[26] Specimens of *B. europaea* were randomly collected by SCUBA diving at the three study sites along the pH gradient (26 from S1, 26 from S2 and 22 from S3) between November 2010 and May 2013. This sample size was chosen to limit damage on the natural population, which significantly diminishes in the most acidic sites[13], and was considered suitable for properly describing the skeletal properties, as shown in previous studies. [13,14] Biometric data were recorded for the specimens (that is, width-to-length, width-to-height and height-to-length ratios). Nanoindentation, hydrostatic weight measurement, SEM, AFM, SAXS, μCT and TD-NMR analyses were performed on a subsample of specimens from each site.

Coral sample cleaning. Coral skeletons were submerged in 1% solution of sodium hypochlorite for 3 days to dissolve polyp tissue. After washing with deionized water and drying at 50 °C for 3–4 days, each coral was examined under a binocular microscope to remove fragments of sediment, rock and encrusting organisms.[16]

Weight measurements. The buoyant method, usually applied for corals,[27–29] was used to measure the total volume occupied by the coral skeleton (called bulk volume, V_B), the bulk density (d_b, ratio of the mass to V_B), the biomineral density (d_r, ratio of the biomineral mass to biomineral volume, excluding pore volume connected to the external surface, also called real density or micro-density) and the apparent porosity (or effective or connected porosity, P_A)[30] (ratio of the pore volume connected to the external surface (V_A) to V_B). This method is based on the Archimedean principle applied to a specimen after full saturation with the same fluid in which it is submerged (water in our case). It is worth to underline that the pore volume (V_A) measured by the buoyant method is only the volume of the pores that can be saturated with water, that is, connected with the external surface. Pores inside the biomineral that are not connected to the external surface (occluded pores) are not measured. An estimate of the occluded porosity gave a negligible maximum value of ~3%

(in porosity units), which was homogeneous among sites. For coherence with coral literature, for the apparent porosity we use the term porosity.

The skeletons were weighed with a precision balance to determine the dry mass (m) and then placed inside a dryer chamber and evacuated with a rotary mechanical pump down to a vacuum of 10^{-2} mbar. After 6 hours, water was gently introduced to fully saturate the samples. The pump was switched off, the chamber was vented to the ambient atmosphere, and the masses of the fully water-saturated samples (m_s) determined. With a hydrostatic balance, the masses of saturated samples fully immersed in water (m_h) were determined. The skeletal parameters were calculated by means of the following operational definitions: ρ_w=water density, $V_A=(m_s-m)/\rho_w$; $V_B=(m_s-m_h)/\rho_w$; $P_A=V_A/V_B=(m_s-m)/(m_s-m_h)$; $d_b=m/V_B$; $d_t=m/(V_B-V_A)$.

After weight measurement, the fully saturated samples were removed from the water container and rapidly placed on wet paper to remove excess water on the external surface. Each specimen was then placed in the bottom of a glass tube, which was then sealed for TD-NMR measurements.

TD-NMR method and parameter definitions. This technique was applied to obtain skeletal 'pore-size' distributions by the analysis of quasi-continuous distributions of the transverse relaxation time T_2 by means of the algorithm UPEN,[31] implemented in the UpenWin software. T_2 distributions for specimens of *B. europaea*, showed in all cases, that the slope of the distribution presented a strong increase at a specific T_2 value, the "cutoff", revealing a sharp boundary between two distinct pore classes. This point was chosen as the boundary between smaller (shorter T_2) and larger (longer T_2) pores. The ratio of the area under the distribution for T_2 larger than the cutoff to the total area under the distribution, called "macroscale pore volume fraction", indicates the fraction as a percentage of the pore volume in the macroscale. On the basis of the comparison with mercury intrusion porosimetry data, the sizes of pores in the macroscale pore volume fraction, corresponding to the major fraction of pores, are >10–20 μm. The tail in the distribution is about 3 orders of magnitude long and should correspond to smaller pore sizes up to tens of nanometres.[14] The distribution with T_2 <3 ms was chosen to identify the signal corresponding to water in the smallest pores or size-scale, which we refer to here as 'nanoscale pore volume fraction'. The remaining fraction of the distribution is called 'microscale pore volume fraction'. The nano, micro and macroscale pore volume fractions multiplied by the skeletal porosity produced the TD-NMR nano, micro and macroscale porosities, respectively.

TD-NMR apparatus and data acquisition. A homebuilt relaxometre based on a 0.2 T permanent magnet operating at 8 MHz was used for acquisition of the transverse relaxation curve of the ^{1}H nuclei of water molecules saturating the cleaned coral skeletons. The relaxometer was equipped with a coil ~2 cm in diameter to analyse the entire coral and a Spinmaster console (Stelar, Mede, Pavia, Italy) for automatic pulse sequence transmission and data acquisition. The transverse relaxation data were acquired by using the Carr–Purcell–Meiboom–Gill sequence[32] with a 200 μs echo time. Sixteen corals from S1, 16 corals from S2 and 12 corals from S3 were analysed.

SEM images. To investigate the meso and macroscale organization of the aragonite fibre bundles, SEM analyses were performed. The cleaned coral skeletons were mounted (uncoated) to conductive carbon tape and examined with a Tescan Vega3 GMU (Czech Republic) variable pressure scanning electron microscope. Three corals per site were analysed.

Evaluation of net calcification rate. The age of each coral was determined based on growth band analysis via computerized tomography.[22,33] The linear extension rate was obtained by dividing the length of each sample (maximum axis of the oral disc) by its age. The net calcification rate was calculated as: net calcification rate=bulk density × linear extension rate.[21,34]

μCT analysis. To compute the corallite interseptal volume fraction (ratio of the total pore space volume inside the corallite to the total volume occupied by the corallite itself), μCT analyses were acquired and the convex hull approach was followed. μCT scans of coral skeletons were performed with a GE phoenix X-ray Nanotom S. The voxel sizes in the scans varied from 2.91 to 13.25 μm depending on the actual size of the investigated coral sample. All image processing steps in the analysis were performed with the open source software FIJI.[35]

Nanoindentation. To analyse mechanical properties of the coral skeletons, skeletal stiffness (Young's modulus) and hardness were determined by Oliver–Pharr analysis of load-depth curves,[36] using a Nanoindentation Tester, model NHT-TTX by CSM Instruments, Switzerland, equipped with a Berkovich diamond tip (opening angle=142.3°). On each sample, a minimum of 10 indentation tests were carried out, in the oral region, with a minimum distance of 30 μm between two tests (the total number of tests for each site is reported in Table 1). To avoid influence from

the embedding resin, a minimum distance of 100 μm from the skeleton/resin boundaries was always maintained.

SAXS analysis. To obtain information on skeletal porosity at the nanoscale, SAXS analyses were performed on three corals per site. Sections were mounted onto a laboratory SAXS apparatus with a rotating anode X-ray generator (Bruker, AXS, Karlsruhe, Germany) operating with a copper anode.

AFM analysis. To study the morphology and packing of skeletal mineral grains at the nanoscale, AFM images were acquired. Samples were lightly polished using diamond paste, cleaned with milli-Q water and observed using a Veeco AFM Dimension 3100 Nanoscope III, Plainview, NY. The probe consisted of a cantilever with an integrated silicon nitride tip. Samples were imaged at room temperature and in air using tapping mode phase contrast imaging.

Statistical analysis. Statistical analyses (analysis of variance, multivariate, principal components and quantile analysis) were performed using the Statistical Package STATA 9.0 (StataCorp LP). To test the significance of the differences among sites, parametric (F) or non-parametric (Kruskal–Wallis χ^2) tests were run. Non-parametric tests were performed for data that did not assume normal distributions. Multivariate regression analyses were performed to investigate the relationships between one dependent and one or several independent variables, using ordinary least squares robust to outliers. The model is described by the following equation:

$$y_i = a + \sum_{j=1}^{M} b_j x_{i,j} + \varepsilon_i$$

where the index i refers to the i-observation, x_j is an independent variable, y_i is the value of the dependent variable and ε_i is the corresponding error. The constants a, b_j (j=1, M) are the best-fit parameters, to be determined by the best fit. Quantile analysis was performed to study the previous relationships for homogeneous groups of values of the dependent variable. This analysis was used to give a more comprehensive picture of the effect of the independent variable (pH) on the dependent variables of Figure 3, as it can show different effects of the independent variable in different ranges of the dependent variable.

REFERENCES

1. Stocker, T. F. Climate Change 2013: The Physical Science Basis (Cambridge Univ. Press, 2013). *Clim. Chang. 2013 Phys. Sci. Basis* (2013).
2. Sabine, C. L. The oceanic sink for anthropogenic CO2. *Science.* **305,** 367–371 (2004).
3. Six, K. D. Global warming amplified by reduced sulphur fluxes as a result of ocean acidification. *Nat. Clim. Chang.* **3,** 975–978 (2013).
4. Rodolfo-Metalpa, R. Coral and mollusc resistance to ocean acidification adversely affected by warming. *Nat. Clim. Chang.* **1,** 308–312 (2011).
5. Hoegh-Guldberg, O. Coral reefs under rapid climate change and ocean acidification. *Science.* **318,** 1737–1742 (2007).
6. Pandolfi, J. M., Connolly, S. R., Marshall, D. J. & Cohen, A. L. Projecting coral reef futures under global warming and ocean acidification. *Science.* **333,** 418–422 (2011).
7. Dove, S. Future reef decalcification under a business-as-usual CO2 emission scenario. *Proc. Natl Acad. Sci. Usa* **110,** 15342–15347 (2013).
8. Orr, J. C. Anthropogenic ocean acidification over the twenty-first century and its impact on calcifying organisms. *Nature* **437,** 681–686 (2005).
9. Touratier, F. & Goyet, C. Impact of the Eastern Mediterranean transient on the distribution of anthropogenic CO2 and first estimate of acidification for the Mediterranean Sea. *Deep Sea Res. I* **58,** 1–15 (2011).
10. Yilmaz, A. Impact of acidification on biological, chemical and physical systems in the Mediterranean and Black Sea Mediterranean. *Mediterr. Sci. Comm. (Ciesm), Monogr. Ser.* **36,** 124 (2008).
11. Calvo, E. Effects of climate change on Mediterranean marine ecosystems: the case of the Catalan Sea. *Clim. Res.* **50,** 1–29 (2011).
12. Ziveri, P. Research turns to acidification and warming in the Mediterranean Sea, IMBER (Integrated Marine Biogeochemistry and Ecosystem Research). (2012).
13. Goffredo, S. Biomineralization control related to population density under ocean acidification. *Nat. Clim. Chang.* **4,** 593–597 (2014).
14. Fantazzini, P. Time-Domain NMR study of Mediterranean scleractinian corals reveals skeletal-porosity sensitivity to environmental changes. *Environ. Sci. Technol.* **47,** 12679–12686 (2013).
15. Laine, J., Labady, M., Albornoz, A. & Yunes, S. Porosities and pore sizes in coralline calcium carbonate. *Mater. Charact.* **59,** 1522–1525 (2008).
16. Caroselli, E. Environmental implications of skeletal micro-density and porosity variation in two scleractinian corals. *Zoology* **114,** 255–264 (2011).
17. Carricart-Ganivet, J. P. Sea surface temperature and the growth of the West Atlantic reef-building coral Montastraea annularis. *J. Exp. Mar. Biol. Ecol.* **302,** 249–260 (2004).
18. Crook, E. D., Cohen, A. L., Rebolledo-Vieyra, M., Hernandez, L. & Paytan, A. Reduced

calcification and lack of acclimatization by coral colonies growing in areas of persistent natural acidification. *Proc. Natl Acad. Sci. Usa* **110,** 11044–11049 (2013).

19. Iglesias-Prieto, R., Galindo-Martinez, C. T., Enriquez, S. & Carricart-Ganivet, J. P. Attributing reductions in coral calcification to the saturation state of aragonite, comments on the effects of persistent naturals acidification. *Proc. Natl Acad. Sci. Usa* **111,** E300–E301 (2014).

20. Goffredo, S., Caroselli, E., Mattioli, G., Pignotti, E. & Zaccanti, F. Variation in biometry and demography of solitary corals with environmental factors in the Mediterranean Sea. *Mar. Biol.* **152,** 351–361 (2007).

21. Goffredo, S. Inferred level of calcification decreases along an increasing temperature gradient in a Mediterranean endemic coral. *Limnol. Ocean.* **54,** 930–937 (2009).

22. Goffredo, S., Caroselli, E., Mattioli, G., Pignotti, E. & Zaccanti, F. Relationships between growth, population structure and sea surface temperature in the temperate solitary coral Balanophyllia europaea (Scleractinia, Dendrophylliidae). *Coral Reefs* **27,** 623–632 (2008).

23. Airi, V. Reproductive efficiency of a Mediterranean endemic zooxanthellate coral decreases with increasing temperature along a wide latitudinal gradient. *P Lo S One* **9,** e91792 (2014).

24. Wooldridge, S. A. Assessing coral health and resilience in a warming ocean: Why looks can be deceptive. *Bioessays* **36,** 1041–1049 (2014).

25. Capaccioni, B., Tassi, F., Vaselli, O., Tedesco, D. & Poreda, R. Submarine gas burst at Panarea Island (southern Italy) on 3 November 2002: A magmatic versus hydrothermal episode. *J. Geophys. Res.* **112,** B05201 (2007).

26. Zibrowius, H. Les. scleractiniaires de la Méditerranée et del'Atlantique nord-oriental. *Mem. Inst. Ocean.* **11,** 1–284 (1980).

27. Jokiel, R. L., Maragos, J. E. & Franzisket, L. Coral Reef Research Methods .(eds Stoddart, D. R. & Johannes, R. E.) 5 529–542 (UNESCO, 1978). *Coral Reef Res. Methods* 529–542 (1978).

28. Davies, P. S. Short-term growth measurements of corals using an accurate buoyant weighing technique. *Mar. Biol.* **101,** 389–395 (1989).

29. Walsh, S.-J. Proceedings of 12th International Coral Reef Symposium,Cairns, Australia, 9–13 July 2012.

30. Manger, G. E. Porosity and bulk density of sedimentary rocks. *Geol. Surv. Bull*

31. Borgia, G. C., Brown, R. J. S. & Fantazzini, P. Examples of marginal resolution of NMR relaxation peaks using UPEN and diagnostics. *Magn. Reson. Imaging* **19,** 473–475 (2001).

32. Cowan, B. Nuclear Magnetic Resonance and Relaxation (Cambridge Univ.Press, 1997). *Nucl. Magn. Reson. Relax.* (1997).

33. Goffredo, S., Mattioli, G. & Zaccanti, F. Growth and population dynamics model of the Mediterranean solitary coral Balanophyllia europaea (Scleractinia Dendrophylliidae). *Coral Reefs* **23,** 433–443 (2004).

34. Lough, J. M. & Barnes, D. J. Environmental controls on growth and of the massive coral Porites. *J. Exp. Mar. Biol. Ecol.* **245,** 225–243 (2000).

35. Schindelin, J. Fiji: an open-source platform for biological-image analysis. *Nat. Methods* **9,** 676–682 (2012).

36. Oliver, W. C. & Pharr, G. M. An improved technique for determining hardness and elastic modulus using load and displacement sensing indentation experiments. *J. Mater. Res.* **7,** 1564–1583 (1992).

APPENDIX

METHODS AND TECHNIQUES

ATOMIC FORCE MICROSCOPY

Atomic Force Microscopy is a scanning probe technique. The main component of the instrumentation consists in a sharp tip placed at the extremity of the cantilever. The force applied to the tip from the surface produces a deflection of the cantilever. Measuring the bending of the cantilever it is possible to evaluate the tip-surface interaction forces.

Different settings of the feedback loop allow to the piezoelectric scanner to maintain constant the tip-sample force or the tip height, to obtain height or force informations, respectively.

The AFM head includes an optical detection system. A laser beam is focused and centered on the rear side of the reflective cantilever. In this way the deflection of the cantilever is monitored, projecting the reflected beam to a dual element photodiode (Figure 1). The difference between the two elements gives information about the cantilever deflection. Feedback system instantaneously receives the information and acts to maintain constant the force (or the height) above the sample.

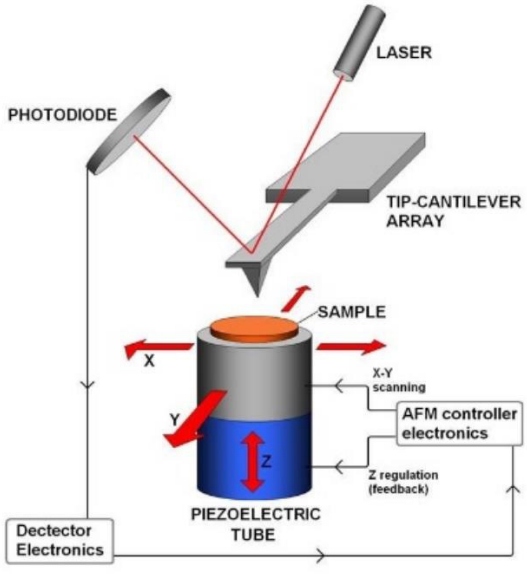

Figure 1. Schematic representation of the main components of the atomic force microscope.

Modes of operation

The dominant interactions at short probe-sample distances in the AFM are Van der Waals (VdW) interactions. However long-range interactions (i.e. capillary, electrostatic, magnetic) are also relevant further away from the surface. The latter are important in other SPM modes of operation and analysis. In contact with the sample, the probe predominately experiences repulsive Van der Waals forces (contact mode). This leads to the cantilever positive deflection. As the tip moves away from the surface attractive Van der Waals forces become dominant (non-contact mode) Figure 2 and the cantilever deflect in the negative direction.

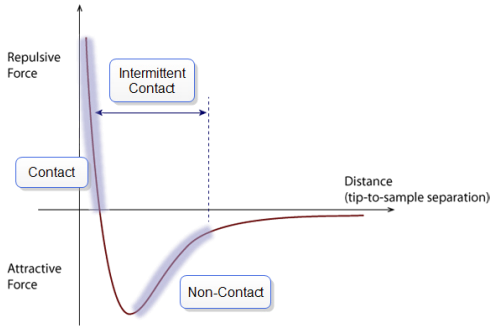

Figure 2. The effect of tip-to-sample distance on the force interaction between tip and sample.

Contact mode. The tip is in direct contact with the surface. The force of interaction between the tip and the sample is balanced by the elastic force produced by the cantilever deflection. Cantilevers used for contact mode require an elastic constant relatively small, offering higher sensibility and reducing the risk of excessive interactions between tip and sample.

Non-contact mode. The cantilever oscillate with a small amplitude (about 1 nanometer). During the approaching, the cantilever is affected by attractive forces (Van der Waal interactions) applied by the surface. To detect the amplitude and phase variations produced on the cantilever, high sensitivity and high stability of the electronic feedback system is required.

Tapping mode. It is more common to use the semi-contact or tapping mode. In this case, the imposed oscillations of the cantilever are tuned close to its resonance frequency, with a resulting oscillation amplitude which range from 10 to 100 nanometers. The cantilever during the oscillation come in contact with the surface, in the repulsive force region (Figure 2). During the scanning,

amplitude and phase variation are measured and the feedback system compensate the variations maintaining the oscillation frequency constant.

ZETA POTENTIAL

Zeta-potential is one of the physical properties exhibited by any particle in suspension. It can be used for the formulation and study of suspensions and emulsions. The scientists Derjaguin, Verwey, Overbeek and Landau worked out a theory (DVLO), which relates the stability of a particle in suspension with its total potential energy function V_T.

$$V_T = V_A + V_R + V_S$$

V_S is the potential energy due to the interaction with solvent. Generally it is negligible as it involves very short distances for which its weight on the total potential in a colloid is minimum. Much more important is the balance between the attractive V_A and repulsive V_R contributions (Figure 3). They operate over a much larger distance.

$V_A = -A/(12\pi D^2)$

A	Hamaker constant
D	particle separation

$V_R = 2\,\pi\,\varepsilon\,a\,\zeta^2\exp(-\kappa D)$

a	particle radius
π	solvent permeability
κ	function of the ionic composition ($1/\kappa$ = double layer thickness)
ζ	zeta potential

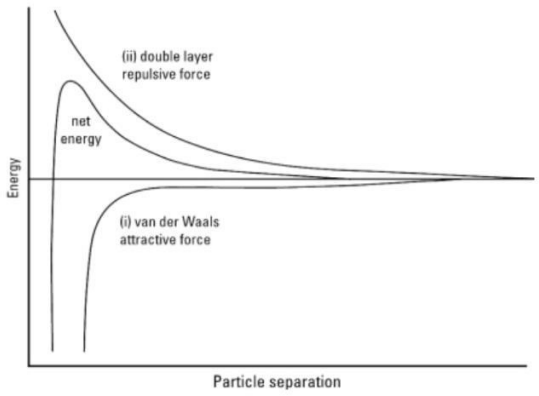

Figure 3. Trend of attractive and repulsive potential energy and sum of the two contributions. The presence of a barrier due to the repulsive forces prevents the aggregation of the particles. If the particles collide with enough energy to overcome the barrier, the attractive forces prevail, causing the contact and thus irreversible adhesion between the particles.

In order to have a stable colloidal system, repulsive forces must prevail. Electrostatic or charge stabilization have the advantage to be modulated in a reversible manner by varying the ions concentration in the system. The magnitude of the surface charge depends on the acidic or basic strengths of the surface groups and the pH. In case of negatively charged surface (Figure 4), the net charge can be reduced to zero by decreasing the pH (suppressing the surface ionization) and *vice versa*.

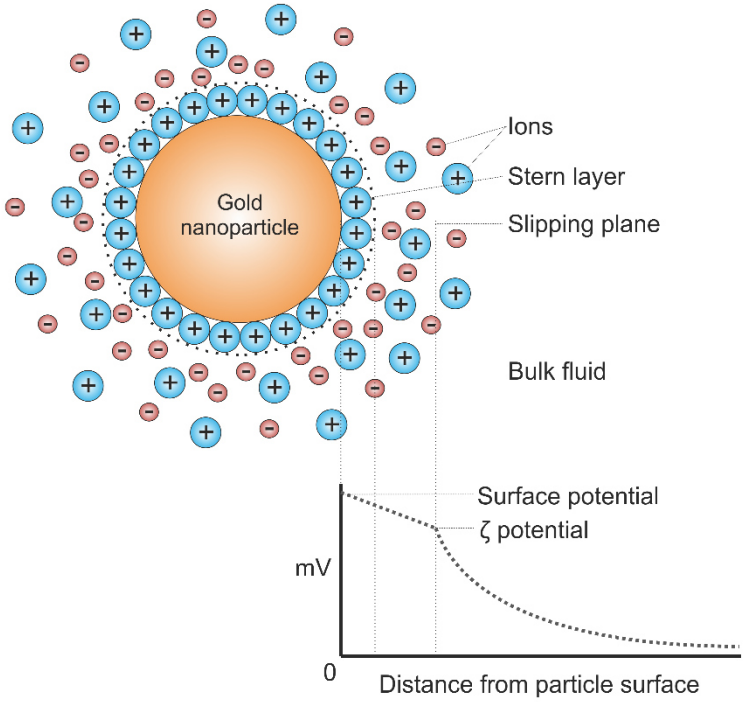

Figure 4. Representation of a negatively charged particle in suspension. In "contact" with the surface there is a shell of positive ions whose thickness have approximately the same size of the solvated cation. The trend of the potential within the thickness of this "shell" (Stern Layer) linearly decrease (electric double layer). It follows an exponential decay of the potential in a "shell" consisting of predominantly positive ions (diffuse layer). The volume of the sphere containing the charged species moving together with the negative particle is between the center of the particle and the slipping plane. At this distance it corresponds a specific potential which is, by definition, the zeta potential.

The thickness of the double layer ($1/\kappa$) depends by the ionic concentration of the solution. For high ionic strength, the double layer is more compressed on the surface. Even the valence of the ion influence the thickness of the double layer, for example a trivalent ion compresses the double layer more than a monovalent ion. The zeta potential value that ideally separates the stability from the instability regions of a colloidal system is considered +30 or -30 mV, for positively or negatively charged particles, respectively.

The existence of the electrical charge over the surface of the particles, implies their interaction with an applied electric field. These effects are collectively defined as electrokinetic effects. Electrophoresis is the effect used to perform zeta potential measurements and it measures the mobility of charged species. The particle is attracted to the electrode having opposite charge.

Viscous forces acting on the particles tend to oppose this movement. When equilibrium is reached between these two opposing forces, the particles move with constant velocity. The velocity of a particle in an unit electric field is defined as electrophoretic mobility. Zeta potential is related to the electrophoretic mobility by the Henry equation:

$$U_E = 2\,\varepsilon\,\zeta\,\, f(\kappa a) / 3\eta$$

U_E	electrophoretic mobility
ζ	zeta potential
ε	dielectric constant
η	viscosity
$f(\kappa a)$	Henry's function

The measurements were carried out on Malvern Zetasizer Nano Series. It uses the combination of a Doppler analyzer and a phase diode laser velocimeter (633 nm) based on light scattering (PALS) to measure the electrophoretic mobility of the particles. The essence of a classical microelectrophoresis system is a capillary cell with electrodes at either end to which a potential is applied. The system is thermostatically controlled.

DIFFERENTIAL CENTRIFUGAL SEDIMENTATION

Differential Centrifugal Sedimentation (or DCS) is a widely used analysis method that produces extremely high resolution size distributions of microscopic to sub-microscopic particles. The normal measurement range for the method is from about 10 nanometers to about 50 microns, though it is possible with some types of materials to extend the range to below 3 nanometers or up to 120 microns or more.

The DCS has many advantages over other NP sizing techniques; for example, respect to the DLS, it is capable of resolution of multiple peaks in polydisperse samples (where DLS shows only one broad peak). Another advantage of DCS is its capacity to perform measurements of NPs in complex biological fluids, where optical methods such as DLS are affected by high scattering of the free proteins in the sample.

The DCS operates by measuring the sedimentation time of a particle of known density under centrifugal force in the sucrose gradient inside of rotating disc (Figure 5).

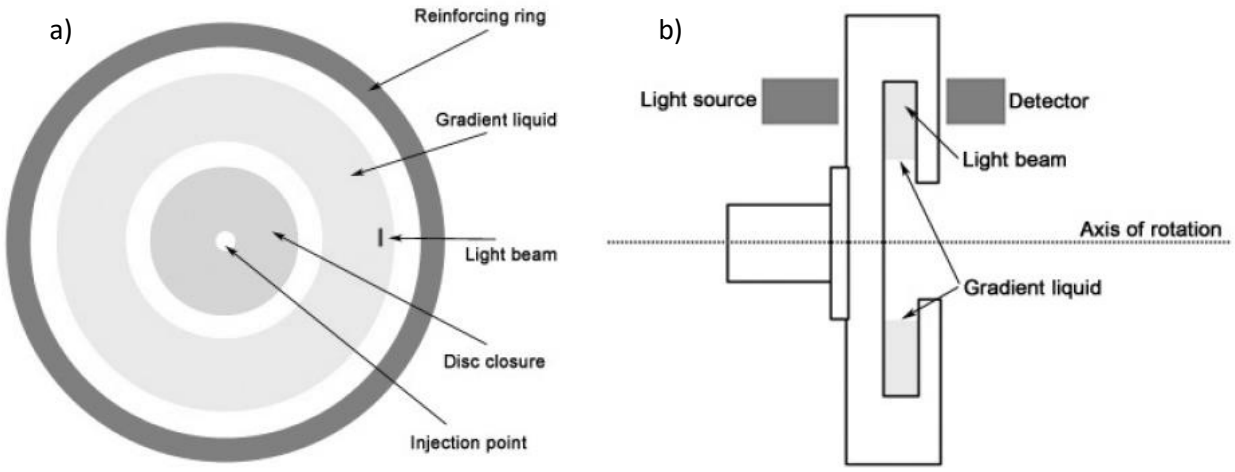

Figure 5. a) Schematic of the DCS disk with the sucrose density gradient built on the outer wall of the disk, position of the light detector and injection point; b) Cross section of the DCS disk.

The nanoparticle diameter is then calculated according to the formula:

$$D = \sqrt{\frac{(18\mu \ln(R_f/R_0))}{(\rho_p - \rho_f)\omega^2 t}} \qquad (1)$$

Which can also be expressed as:

$$D = K / t^{1/2}$$

Where:

D	is the particle diameter
μ	is the fluid viscosity
t	is the measured sedimentation time
ω	is the rotational speed
R_0 & R_f	are the starting and final radii of rotation respectively
ρ_p & ρ_f	are the densities of the particles and the fluid respectively.

For a centrifuge running at constant speed and temperature, the K coefficient does not need to be theoretically calculated, because it is determined experimentally by the calibration measurement of the sedimentation time, using standard nanoparticles of known density and diameter. Since all the measurements are calibrated to the same standard, the results are directly comparable and are not affected by fluctuations of the measurement conditions (e.g. changes in the gradient density or temperature).

Sucrose density gradient

The sucrose gradient is prepared injecting a series of sucrose solutions into the DCS spinning disk in motion. The first injection consists in the higher concentration of sucrose solution. Progressively lower concentrations of sucrose solutions are injected, one by one.

The concentrations range of the gradient depends on the density of analyzed NPs and is indicated in the official manual of the manufacturer. The injected fluid portions, under high centrifugal force, form layers on the outer wall of the disk (Fig. 5a,b). The resulting gradient is capped with a thin layer of dodecane to prevent evaporations during prolonged measurements. An equilibration of the gradient for 30 minutes is required. During this time, the starting differences in the sucrose concentration (step like trend) between the layers are "smoothed" thanks to the sucrose diffusion (Figure 6).

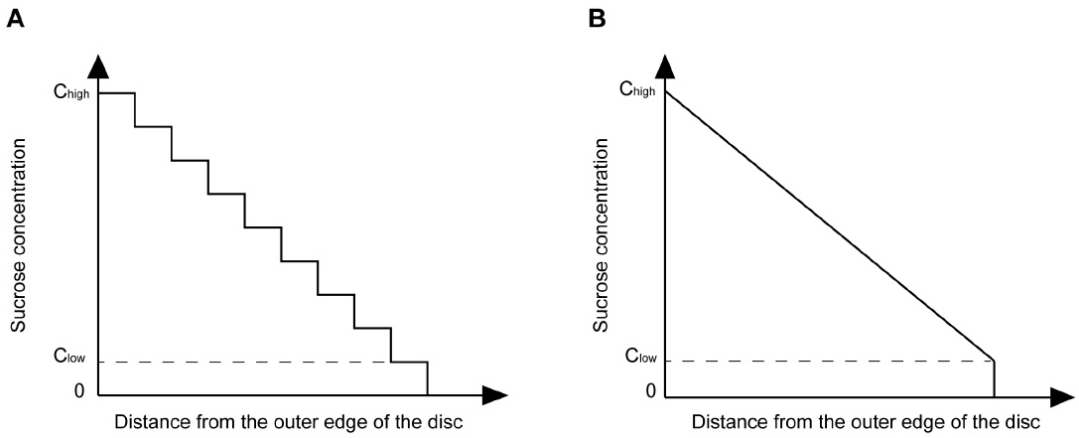

Figure 6. Equilibration of the sucrose density gradient; A. Scheme of theoretical sucrose concentration in the density gradient at time=O; B. Scheme of theoretical sucrose concentration in the ideally equilibrated density gradient.

Samples are prepared for analysis by dilution in a fluid of slightly lower density than the least dense fluid in the disc (in this work we used water or PBS). The lower density fluid used for the

sample reduces initial mixing of the fluid inside the disc with the sample. When a sample is injected (Figure 5), it strikes the back inside face of the disc, and forms a thin film, which spreads as it accelerates radially toward the surface of the fluid. When the sample dispersion reaches the fluid surface, it quickly spreads over the surface, because it is of lower density (it "floats" on the higher density fluid). Once a sample is on the fluid surface, sedimentation of individual particles begins. The injection of a sample is rapid (typically <50 milliseconds), so the starting time for an analysis is well defined, and the precision of sedimentation time is quite good.

As the nanoparticles run through the gradient (therefore increasing density and viscosity), a reduction of the sedimentation velocity occurs, allowing a good separation of the nanoparticles having different sizes. If the NPs are composed by the same material (same density and refractive index), the big nanoparticles sediment faster than the smaller one. The low sedimentation rate occurring close to the edge of the disc (high sucrose concentration) allows to obtain and high precision and resolution detection of the particles sizes. NPs absorb and scatter the light during their pass through the detector beam, allowing for their detection based on attenuation of the light.

DCS Samples

The DCS is a powerful NP sizing technique capable of analyzing different kinds of samples such as bare NPs or NP/protein corona complexes. In particular, DCS has a significant advantage for analysis of in situ samples, without the need to separate the NPs from the excess biological fluid. This characteristic, provides the opportunity to analyze the nanomaterials as they are in biologically relevant conditions.

The main samples analyzed in this project (3rd chapter) were protein-coated NDs "hard corona", where bare NDs were incubated in biological relevant fluids (human and bovine serum) and subsequently separated (altogether with biomolecules strongly bound to their surface) from excess serum (see experimental section, chapter 3).

After the preparation, the NP samples were injected into the spinning disk of DCS (following the calibration run of standard polystyrene NPs), and their sedimentation time were measured.

DCS results

During the sedimentation, the concentration of particles of each size is determined by continuous measurement of the turbidity of the fluid (sucrose gradient) close to the external edge of the

transparent rotating disc (Figure 5a,b). Using the equation (1) this raw data is represented as absorption distribution (light absorbed/scattered plotted against diameter). Specific algorithms which consider the physical properties of the particles and geometrical parameters, are used to convert the raw (optical absorption) signal to weight, volume and number distributions of the NPs.

SDS-PAGE

A very common method for separating proteins by electrophoresis uses a discontinuous polyacrylamide gel as a support medium and sodium dodecyl sulfate (SDS) to denature the proteins. The method is called sodium dodecyl sulfate polyacrylamide gel electrophoresis (SDS-PAGE).

The negative charges on SDS destroy most of the complex structure of proteins, and are strongly attracted toward an anode (positively-charged electrode) in an electric field.

Polyacrylamide gels restrain larger molecules from migrating as fast as smaller molecules. Because the charge-to-mass ratio is nearly the same among SDS-denatured polypeptides, the final separation of proteins is dependent almost entirely on the differences in relative molecular mass of polypeptides. In a gel of uniform density the relative migration distance (R_f) of a protein is negatively proportional to the log of its mass. If proteins of known mass are run simultaneously with the unknowns, the relationship between R_f and mass can be plotted, and the masses of unknown proteins estimated.

Protein separation by SDS-PAGE can be used to estimate relative molecular mass, to determine the relative abundance of major proteins in a sample, and to determine the distribution of proteins among fractions. The purity of protein samples can be assessed and the progress of a fractionation or purification procedure can be followed. Different staining methods can be used to detect rare proteins and to learn something about their biochemical properties.

Polyacrylamide gels for SDS-PAGE

The preparation of the gel consists of the casting of two different layers of acrylamide between glass plates. The lower layer (running or resolving gel) is responsible for actually separating polypeptides by size. The upper layer (stacking gel) includes the sample wells. It is designed to

sweep up proteins in a sample between two moving boundaries so that they are compressed (stacked) into micrometer thin layers when they reach the separating gel.

Preparing SDS Gels

A gel of given acrylamide concentration separates proteins effectively within a characteristic range. Very large polypeptides cannot penetrate far into a gel and thus their corresponding bands may be too compressed for resolution. Polypeptides below a particular size are not restricted at all by the gel, and regardless of mass they all move at the same pace along with the tracking dye. Gel concentration (%T) should be selected so that the proteins of interest are resolved.

A typical gel of 7% acrylamide composition nicely separates polypeptides with molecular mass between 45 and 200 kDa. Polypeptides below the cutoff of around 45 kDa do not resolve. A denser gel, say 14%T, usually resolves all of the smallest polypeptides in a mix. A good compromise to analyze the entire profile of a fraction that contains heavy and light polypeptides, consists of the use of an average concentration of 10%T.

Running Gel Preparation (10% acrylamide)

Casting stands are used to prepare the mini-slab gels. The cassettes are staked upright in the stand with the bottoms of the cassettes tight to the bottom of the stand. The total volume between the plates of the gel cassettes is 10 mL, so this volume of separating gel mix per cassette is required. The separating gel components used in this work consists of:

i. 3.7 mL Tris-HCl 1 M, pH 8.9,
ii. 3.6 mL H_2O milliQ
iii. 100 μL 10% SDS,
iv. 2.5 mL acrylamide 40%
v. 50 μL APS
vi. 5 μL TEMED

The polymerization is initiated by adding freshly prepared ammonium persulfate (APS) to the mix followed by N, N, N', N'-tetramethylethylenediamine (TEMED). Once the catalysts are added, polymerization occurs quickly. After swirling to mix, the solution is poured into the space occupied by the cassettes.

Immediately after pouring the gel mix, it must be overlaid with isopropanol to an additional height of few mm. The purpose of isopropanol is to produce a smooth, completely level surface on top of the separating gel, so that bands are straight and uniform.

Stacking gel preparation (4% acrylamide)

The stacker is simply designed to perform as a matrix through which samples will pass as they are caught up between moving boundaries. It is not designed for uniform separation of proteins. The stacking gel components used in this work consists of:

i. 2.7 mL Tris-HCl 0.4 M, pH 6.9,
ii. 2.8 mL H_2O milliQ
iii. 50 µL 10% SDS,
iv. 500 µL acrylamide
v. 50 µL APS
vi. 5 µL TEMED

Before adding the final two components, which will start polymerization, the isopropanol should be poured off the separating gel. After adding APS and TEMED the mix is poured it into the cassettes to the tops of the plates. The comb is inserted on the top, taking care not to catch bubbles under the teeth.

Sample denaturation

Denaturation of the sample is obtained incubating proteins (or NPs-protein corona complex) with commercial SDS-Blue 3x which contains:

i. 187,5 mM Tris-HCl pH 6.8
ii. 6% SDS
iii. 30% glycerol
iv. 0.03% bromphenol blue

A reducing agent such as 1,4-dithiothreitol (DTT) is also added to obtain the same final concentration (3x).

The Tris-HCl acts as a buffer, which is very important since the stacking process in discontinuous electrophoresis requires a specific pH. Glycerol makes the sample more dense than the sample

buffer, so the sample will remain in the bottom of a well rather than float out. The dye allows the investigator to track the progress of the electrophoresis.

SDS, DTT, and heat are responsible for the actual denaturation of the sample. SDS breaks up the two- and three-dimensional structure of the proteins by adding negative charge to the amino acids. Since like charges repel, the proteins are more-or-less straightened out, immediately rendering them functionless. Many proteins have significant hydrophobic properties and may be tighly associated with other molecules, such as lipids, through hydrophobic interaction.

Heating the samples to at 100 °C under shaking for 5 minutes, allows SDS to bind in the hydrophobic regions and complete the denaturation (Figure 7).

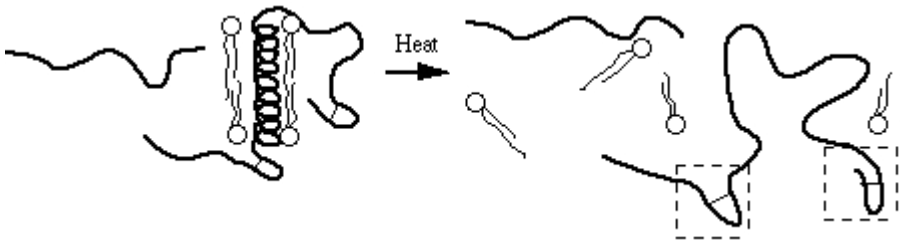

Figure 7. Disruption of secondary, tertiary and quaternary structure upon SDS and heating treatment. Dashed squares indicate folds caused by disulfide (covalent) bonds.

The amino acid cysteine contains a sulfhydryl (-SH) group that spontaneously forms a disulfide bond (-S-S-) with another sulfhydryl group under normal intracellular conditions. Disulfide bonding is covalent and is not disrupted by SDS. DTT is a strong reducing agent. Its specific role in sample denaturation is to remove the last portions of tertiary and quaternary structure by reducing disulfide bonds.

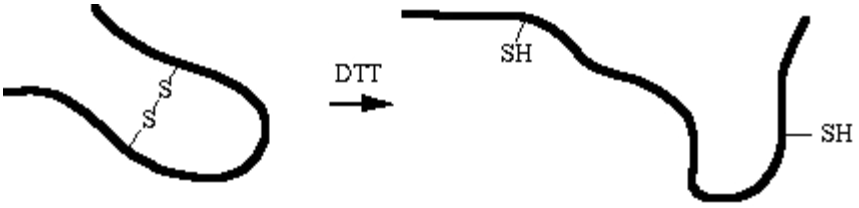

Figure 8. Reduction of disulfide bonds by means of DTT.

Assembling, Loading, and Running Gels

Cassettes should be rinsed free of any excess liquid, leaving the combs in place. The top of the cassette must be continuous with an upper buffer chamber and the bottom must be continuous with

a lower chamber so that current will run through the gel itself. Both the upper and lower buffer compartments have to be filled with an electrode buffer (running buffer) consisting of:

i. 3 g/L Tris-HCl
ii. 14,4 g/L glycine
iii. 1g/L SDS

The comb has to be removed from the gel before filling the upper buffer compartment.

Specific gel loading tips are usually used for loading samples into the wells. Ideally, the glycerol in a sample causes it to sink neatly to the bottom of the well, allowing as much as 20 µl or even more to be loaded.

The anode (+ electrode) must be connected to the bottom chamber and the cathode to the top chamber. The negatively-charged proteins will move toward the anode. Gels are usually run at a voltage that will run the tracking dye to the bottom as quickly as possible without overheating the gels. We run our gels at 120 volts.

Disassembly and staining

When the dye front is nearly at the bottom of the gel it is time to stop the run. The plates are then separated and the gel is dropped into a staining dish containing deionized water. After a quick rinse, the water is poured off and stain added.

Staining protein gels

For detection of proteins migration by polyacrylamide gel electrophoresis, silver staining is now being highlighted as a sensitive staining method. The standard staining procedure consists of multistep washes and incubations of the gel in different solutions (reagents COSMOBIO), described as follow:

1. Fixing solution I: 50% MeOH, 10% acetic acid;
2. Fixing solution II: 30% MeOH, 10% acetic acid, 5% fixing reagent (thiourea);
3. Pretreatment solution: 50% MeOH, 5% pretreatment reagent (DTT, Glutaraldehyde, Thiourea)
4. Silver staining solutions: 5% solution A ($AgNO_3$) + 5% solution B (NH_4OH, NaOH)
5. Developer: 5% concentrated developer (citric acid, folmaldehyde, NaOH)
6. Stopper: diluted citric acid solution

Washing steps with milliQ water and incubation times are intentionally omitted. The detailed procedure is available on the website of the vendor (COSMOBIO).

ACKNOWLEDGMENTS

At the end of my PhD experience, I want to thank many people which helped and supported me during the years.
Foremost, I would like to thank my supervisors Prof. Marco Montalti, Prof. Giuseppe Falini and Dr. Matteo Calvaresi for their scientific and personal support during this period. Working with them has been a stimulating experience.
I thank all the members of the biocrystallography lab I worked with during these years, Simona Fermani, Michela Reggi, Giulia Magnabosco, Devis Montroni and Alessandro Ianiro.
I thank the people of the cantina lab, Stefania Rapino, Alice Soldà and Andrea Cantelli, for their help and their friendly attitude. It's a pleasure to work with all of you.
I thank all the collaborators from Bologna. Among them, a special thank is addressed to Francesco Valle, Marianna Barbalinardo and to all the ISMN-CNR group.

I'm really glad of my abroad experiences carried out during my PhD. I found very special people which welcomed me and made me feel part of the group. I thank prof. Boaz Pokroy and his group, which hosted me at the Technion Institute (Haifa, Israel).
I thank prof. Kennet Dawson which gave me the opportunity to spend six months in the Centre for BioNano Interaction at UCD (Dublin, Ireland). A special thanks is addressed to Valentina, which spent time and patience to train me. Many thanks also to all friends and colleagues from CBNI, in particular to Ester, Cristina, Raul, Luca, Luciana, Stephanie, Potti, Sandra, Francesco...
I'm also grateful to my friends which made the Irish experience unforgettable. In particular, the "little Italy" group, Lucia, Valeria, Francesca Giulia, Marinella, Marco, Riccardo and Andrea.

I owe a lot to Bologna. This city welcomed me ten years ago and I loved it from the beginning. Here I met very special people, coming from all over the world. The list is too long, but I'd like to thank all of them, acquaintances, strangers, colleagues and friends.
I owe eternal gratitude to all the teachers and mentors which transmitted to me their enthusiasm and curiosity toward learning. Among them, I'd like to thank Domenico Priori and Stella Allevi.
Thanks to my old friends from Caselle, Stefano, Andrea, Giuseppe, Marco, Mauro, Diana, Giorgio and Jessica. Even though we are spread out, we're still close.

Thanks to my parents Paolo and Anna, my brother Daniele and all my family for their continuous support. I'm really grateful to Chiara which gave me a huge help during these years, especially during the last months.
Thanks to all the people that I didn't mention here, you know that you are important to me.

I dedicate this thesis to my cousin Massimo.